UNIVERSIDADE DA CORUÑA

DOCTORAL THESIS

Crashworthiness analysis and design optimization of hybrid impact energy absorbers

Miguel Costas Piñó
Ingeniero de Caminos, Canales y Puertos

SUPERVISORS
Luis Esteban Romera Rodríguez
Dr. Ingeniero Industrial

Jacobo Díaz García
Dr. Ingeniero de Caminos, Canales y Puertos

Programa de doctorado en Ingeniería Civil

2015

Preface

This dissertation has been submitted for the degree of *doctor ingeniero de caminos, canales y puertos* (doctor of philosophy in civil engineering) at Universidade da Coruña. The research described herein was conducted under the supervision of Professor Luis E. Romera Rodríguez and Professor Jacobo Díaz García, at the Group of Structural Mechanics, Department of Construction Technology, between October 2011 and November 2015.

This work is original to the best of the author's knowledge, except where acknowledgments and references are made to previous research. Several original publications have been hitherto derived from this thesis, and a patent has been granted. These publications are listed in Chapter 1.

Despite concise proofreading and corrections, this book may still contain errors. Attentive readers are encouraged to report them to the author.

Miguel Costas Piñó
November 17, 2015

Acknowledgments

The author wants to thank some people and institutions which have been helpful or essential during these four years of work. First, and foremost, the excellent supervision work carried out by Dr. Luis Romera Rodríguez and Dr. Jacobo Díaz García must be recognized and thanked. Not only did they provide insightful ideas and recommendations but they also kept the work flow in the right lane, which sometimes can be even more important. The author is, and will always be, thankful for four years of superb guidance and goal-orientated supervision. In the same vein, the author is also very thankful to the director of the Group of Structural Mechanics (GME), Dr. Santiago Hernández Ibáñez, for providing him the opportunity to work at one of the leading research groups in Universidade da Coruña.

Thanks must be also given to all the workmates at GME, including professors, PhD candidates, research engineers, research fellows, IT tech and secretary during these four years. A very nice and happy work environment is due 100 % to them.

A part of this work is based on the research project “Hybrid Body” carried out in close cooperation with CTAG (Centro Tecnolóxico da Automoción de Galicia). The extremely value collaboration of this industrial partner, through Alberto Tielas and Raquel Ledo, must be highlighted and thanked as deserved.

Forfattern ønsker å uttrykk også sin ærligste takknemlighet til de menneskan som har våre sjefan og arbeidskollegane sine i løpet av oppholjdet sitt på 6 måna på Sturctural Impact Laboratory (SIMLab) ved NTNU i Trondhjæm (Norge). For det første e det nødvendig å fremhev denj fremragende jobben med tilsyn gjort av Magnus Langseth og David Morin, som forfattern skylder denj tydelige suksessen i jobban som har blitt gjort i løpet av oppholjdet, og muligheten til å få bli midlertidig en del av en av de bæste (om itj den bæste) forskningsgrup-

pan innenfor støt-ingeniørarbeid i verden. Det e også obligatorisk å takk for hjelpa som e fått av professoran i gruppa, spesielt til Odd Sture Hopperstad og Tore Børvik, samt denj hyggelige stæmninga på jobben og i fritida, oppnådd av doktorgradstudentan som æ har truffet på (Jens, Lars, Petter, Arne, Vincent, Vegard, Marius, Martin, Dmitry, Mikhail, Erik, Joakim og Johan) og som æ ønsker my suksess og Hiroshima til! Sist, men ikke minst, en stor takk t labingeniøran Tore Wisth og Trond Auestad for uvurderlig hjælp i forbindels med forberedelse og gjennomføring av labforsøk.

Funding for this work, including the research stay in Norway, has to be acknowledged to Xunta de Galicia, Fundación Barrié and CEAGA. The author is fully thankful for the support received.

A very special, warm thank you also for Prof. Dr. Yury A. Popov for the past, present and upcoming years of extraordinary guidance at the piano and Music in general. This counterpoint has been truly helpful for the development of the present work.

The author takes this opportunity to thank also the very valuable, strictly scientific contribution by Carlos, Denís, Hadrián, Hugo, Marina, Matías, Óscar, Rocío, Sanni and Vítor. Discussions with them on the challenging field of advanced computational continuum mechanics have definitely put the wind in the sails of this work. Thanks to the staff at Rif Rock as well for providing an inspirational environment for such scientifically thriving debates.

Last but not least, the support by my close family is obviously thanked.

As an extra entry, the author thanks parking enforcement officers in A Coruña for keeping his working hours somewhat stable.

Abstract

Extensive research has been done on the energy absorption, crash performance and optimization of different protective structures, helped by recent advances in computational modeling and simulation. When it comes to road vehicles, research on occupant protection has been emphasized since the 1990s due to increasing society's concerns. Head-on collisions are particularly fatal for occupants, and therefore, special focus has been put on the energy absorption and structural performance of the vehicles' front parts. This effort led to structural designs where the front members are axially crushed in a controlled and progressive way, absorbing a remarkable amount of kinetic energy by means of plastic dissipation of metals, collapse of foams or degradation and fracture of composite materials. Nowadays, steel or aluminum profiles are vastly employed in industry, whereas other materials are also suitable. In particular, one way to improve the behavior of these structural elements is to combine several materials into a single design, so that the best characteristics of each one contribute to the component's overall performance.

This thesis presents the investigations into the energy absorption and crashworthiness of structural members made of a metal tube and different non-metallic inner reinforcements. Experimental and numerical tests were performed on components filled with carbon or glass fiber reinforced polymers, polyethylene terephthalate foam or a cork agglomerate, in order to assess their crash performance.

A test campaign involving the numerical and experimental axial crushing of filled components made from a spot-welded steel profile is first presented, which was carried out in close collaboration with the research center CTAG (Centro Tecnolóxico da Automoción de Galicia) under the research project "Hybrid Body", publicly funded by the regional government of Galicia. Results of GFRP-filled or foam-filled tubes showed a particularly good result in terms of different crashworthiness metrics, and a parametric study was performed afterwards in order to look closer to the performance of the GFRP-filled component and the influence of the spacing and distribution of the spot welds on the flanges of the steel profiles. Given the previous results, GFRP-filled tubes were subjected to an optimization procedure to obtain the optimum designs for two simultaneous objective functions, load ratio and specific energy absorption, by means of an optimization strategy which was run on metamodels of the objective functions. A gradient-based and a genetic optimization algorithms were run on a multivariate adaptive regression splines metamodel (MARS) and tested against each other. It was observed that the performance of this GFRP-filled tube could be improved if the GFRP plates in the inner reinforcement were somehow confined inside the tube, given that some parts were dislodged after the first fractures occurred. To that end, a design consisting of an aluminum tube filled with a GFRP skeleton embedded in PET foam was tested numerically and experimentally. This work was done during a six-monthly research stay at the Structural Impact Laboratory (SIMLab) of the NTNU in Trondheim, Norway. Some interesting results were obtained, given that the interaction between both filler materials indeed improved the crashworthiness of the design. This interaction was analyzed and quantified by terms of Hanssen's formula for foam-filled aluminum sections, modified in this thesis to account for the interaction between two reinforcement parts. A finite element model was then build to simulate the performance of this last design, assisted by a material testing campaign. The behavior of the finite element model was validated against the experimental test, showing a very good agreement. Additionally, an alternative design with a DDQ steel instead of aluminum was also considered and simulated. A MARS surrogate model was fit to a large sample of these models considering several crashworthiness metrics to be used then as objective functions in a multi-objective optimization problem. The foam density and the GFRP and metal thicknesses were chosen as design variables for the optimization problem, solved by the previously tested genetic algorithm.

Results showed that the crashworthiness of steel or aluminum tubes can be improved at a larger extent with inner GFRP structures and PET foam than with other materials. Optimum pairs were obtained for selected designs considering different crashworthiness metrics as objective functions. From the optimization phases, it can be concluded that an evolutionary algorithm was slightly more effective than a conjugate-gradient method in finding the optimum designs of the models, given that the metamodel was more concisely explored by the former. The interaction between GFRP plates and PET foam reinforcements placed together inside a metal tube was found to be very relevant for the energy absorption of the component, and was conveniently quantified.

Resumen

En el campo de investigación del diseño y la optimización de estructuras de protección y absorción de energía, se ha experimentado un importante avance gracias a las rápidas mejoras de las herramientas de modelado y simulación computacionales. En lo relativo a vehículos de carretera, este énfasis se ha notado desde los años 1990, motivado por las preocupaciones y necesidades de la sociedad. Las colisiones frontales son especialmente fatales para los ocupantes y, por lo tanto, se ha prestado especial atención a la absorción de energía y comportamiento frente a impacto de las partes frontales de los vehículos. Este esfuerzo ha conducido a diseños estructurales en los que los elementos frontales se aplastan longitudinalmente de forma progresiva y controlada, absorbiendo una considerable cantidad de energía cinética por medio de mecanismos de disipación plástica en metales, aplastamiento de espumas o degradación y fractura de materiales compuestos. Hoy en día, se utilizan muy habitualmente en la industria perfiles de acero o aluminio, aunque existen otros materiales igualmente adecuados. En particular, una forma de mejorar el comportamiento de estos elementos estructurales es combinar varios materiales en un único diseño, de forma que las mejores características de cada uno contribuyan al comportamiento global del componente.

Esta tesis doctoral presenta una investigación acerca de la absorción de energía y el comportamiento frente a impacto de elementos estructurales consistentes en una combinación de un tubo metálico y diferentes refuerzos internos en materiales no metálicos. Se han realizado ensayos experimentales y simulaciones computacionales de elementos rellenos de láminas de fibra de carbono o fibra de vidrio, espuma de tereftalato de polietileno y un aglomerado de corcho para evaluar su comportamiento frente a impacto.

En primer lugar, se presenta una campaña de ensayos experimentales y numéricos del aplastamiento axial de componentes rellenos hechos de un perfil de acero ensamblado mediante soldadura por puntos, trabajo hecho en colaboración con el centro de investigación CTAG (Centro Tecnolóxico da Automoción de Galicia) en el marco del proyecto “Hybrid Body”, financiado con fondos públicos de la Xunta de Galicia. Los resultados de los componentes rellenos con placas de fibra de vidrio o espuma mostraron un comportamiento particularmente bueno en términos de distintas métricas usadas para su evaluación. Se realizó asimismo un estudio paramétrico para examinar con mayor precisión el comportamiento de los componentes rellenos de fibra de vidrio, así como la influencia del espaciado y distribución de los puntos de soldadura en los resultados. A la vista de lo anterior, se procedió a optimizar los tubos rellenos de placas de fibra de vidrio con el objetivo de obtener los diseños óptimos para dos funciones objetivo simultáneas: la absorción específica de energía y la relación de carga. Esta optimización se ejecutó sobre metamodelos de las funciones objetivo. Se utilizaron para este fin un algoritmo de gradiente conjugado y un algoritmo genético, que fueron ejecutados sobre un metamodelo de regresión de splines adaptativas multivariadas (MARS) y comparados entre sí. Se observó que el comportamiento de este componente se podría mejorar si las placas internas de fibra de vidrio se confinasen de alguna manera en el interior del tubo, dado que algunos pedazos se desprenden con las primeras fracturas. Para ello, un nuevo diseño consistente en un tubo de aluminio relleno con placas de fibra de vidrio embebidas en espuma sintética se ensayó numérica y computacionalmente. Este trabajo se realizó durante una estancia de investigación de seis meses en el laboratorio de impacto estructural (SIMLab) de la NTNU en Trondheim, Noruega. Se obtuvieron algunos resultados de interés propiciados por el hecho de que la interacción entre los dos materiales de refuerzo mejoró, en efecto, el comportamiento del elemento estructural. Esta interacción fue analizada y cuantificada por medio de la fórmula de Hanssen para secciones de aluminio rellenas de espuma, que fue modificada pertinentemente en esta tesis para tener en cuenta la interacción entre dos refuerzos. Después de estos ensayos experimentales, se construyó un nuevo modelo de elementos finitos basado en una campaña de ensayos de materiales para simular el comportamiento de este último diseño. El comportamiento de este modelo se validó con los ensayos experimentales, mostrando una excelente correlación. Se construyó también un modelo adicional considerando acero en lugar de aluminio para el tubo exterior. Se ajustó un metamodelo MARS a un muestreo de resultados computacionales considerando distintas métricas de absorción de impactos, que fueron usadas posteriormente en un problema de optimización multi-objetivo. Como variables de diseño se tomaron la densidad de la espuma y los espesores de la fibra de vidrio y los metales. El problema se resolvió con el algoritmo genético probado con anterioridad.

Los resultados muestran que el comportamiento frente a impacto de tubos de acero o aluminio puede ser mejorado en gran medida con refuerzos internos de fibra de vidrio y espuma de tereftalato de polietileno. Se han obtenido diseños óptimos para elementos seleccionados considerando distintas funciones objetivo relevantes. De la fase de optimización se concluye que un algoritmo evolutivo trabaja sensiblemente mejor que uno de gradiente conjugado en este tipo de problemas, dado que el primero fue capaz de explorar los metamodelos más concienzudamente que el segundo. Se ha descubierto asímismo que la interacción entre placas de fibra de vidrio y espuma de tereftalato de polietileno colocadas en el interior de un tubo metálico es de gran importancia para una mayor absorción de energía del diseño, siendo convenientemente cuantificada.

Resumo

No eido do deseño e a optimización de estruturas de protección e absorción de enerxía, experimentouse un importante avance grazas ás rápidas melloras das ferramentas de modelado e simulación computacionais. No relativo aos automóbiles, esta énfase notouse desde os anos 1990, motivada polas preocupacións e necesidades da sociedade. As colisións frontais son especialmente fatais para os ocupantes e, por tanto, prestouse especial atención á absorción de enerxía e comportamento fronte a impacto das partes frontais dos vehículos. Este esforzo conduciu a deseños estruturais nos que os elementos frontais esmáganse lonxitudinalmente de forma progresiva e controlada, absorbendo unha considerable cantidade de enerxía cinética por medio de mecanismos de disipación plástica en metais, esmagamento de escumas ou degradación e fractura de materiais compostos. Hoxe en día, empréganse a cotío na industria perfís de aceiro ou aluminio, aínda que existen outros materiais igualmente adecuados. En particular, unha forma de mellorar o comportamento destes elementos estruturais é combinar varios materiais nun único deseño, de forma que as mellores características de cada un contribúan ao comportamento global do compoñente.

Esta tese doutoral presenta unha investigación acerca da absorción de enerxía e o comportamento fronte a impacto de elementos estruturais consistentes nunha combinación dun tubo metálico e diferentes reforzos internos en materiais non metálicos. Realizáronse ensaios experimentais e simulacións computacionais de elementos recheos de láminas de fibra de carbono ou fibra de vidro, escuma de tereftalato de polietileno e un aglomerado de cortiza para avaliar o seu comportamento fronte a impacto.

En primeiro lugar, preséntase unha campaña de ensaios experimentais e numéricos do esmagamento axial de compoñentes recheos feitos dun perfil de aceiro ensamblado mediante soldadura por puntos, traballo feito en colaboración co centro de investigación CTAG (Centro Tecnolóxico da Automoción de Galicia) no marco do proxecto “Hybrid Body”, financiado con fondos públicos da Xunta de Galicia. Os resultados dos compoñentes recheos con placas de fibra de vidro ou escuma mostraron un comportamento particularmente bo en termos de distintas métricas usadas para a súa avaliación. Realizouse así mesmo un estudo paramétrico para examinar con maior precisión o comportamento dos compoñentes recheos de fibra de vidro, así como a influencia do espaciado e distribución dos puntos de soldadura nos resultados. Á vista do anterior, procedeuse a optimizar os tubos recheos de placas de fibra de vidro co obxectivo de obter os deseños óptimos para dúas funcións obxectivo simultáneas: a absorción específica de enerxía e a relación de carga. Esta optimización executouse sobre metamodelos das funcións obxectivo. Utilizáronse para este fin un algoritmo de gradiente conxugado e un algoritmo xenético, que foron executados sobre un metamodelo de regresión de splines adaptativas multivariadas (MARS) e comparados entre si. Observouse que o comportamento deste compoñente poderíase mellorar se as placas internas de fibra de vidro se confinasen dalgún xeito no interior do tubo, dado que algúns pedazos despréndense coas primeiras fracturas. Para iso, un novo deseño consistente nun tubo de aluminio recheo con placas de fibra de vidro embebidas en escuma sintética ensaiouse numérica e computacionalmente. Este traballo realizouse durante unha estancia de investigación de seis meses no laboratorio de impacto estrutural (SIMLab) da NTNU en Trondheim, Noruega. Obtivéronse algúns resultados de interese propiciados polo feito de que a interacción entre os dous materiais de reforzo mellorou, en efecto, o comportamento do elemento estrutural. Esta interacción foi analizada e cuantificada por medio da fórmula de Hanssen para seccións de aluminio recheas de escuma, que foi modificada axeitadamente nesta tese para ter en conta a interacción entre dous reforzos. Despois destes ensaios experimentais, construíuse un novo modelo de elementos finitos baseado nunha campaña de ensaios de materiais para simular o comportamento deste último deseño. O comportamento deste modelo validouse cos ensaios experimentais, mostrando unha excelente correlación. Construíuse tamén un modelo adicional considerando aceiro en lugar de aluminio para o tubo exterior. Axustouse un metamodelo MARS a unha mostraxe de resultados computacionales considerando distintas métricas de absorción de impactos, que foron usadas posteriormente nun problema de optimización multi-obxectivo. Coma variables de deseño tomáronse a densidade da escuma e os espesores da fibra de vidro e os metais. O problema resolveuse co algoritmo xenético probado con anterioridade.

Os resultados mostran que o comportamento fronte a impacto de tubos de aceiro ou aluminio pode ser mellorado en gran medida con reforzos internos de fibra de vidro e escuma de tereftalato de polietileno. Obtivéronse deseños óptimos para elementos seleccionados considerando distintas funcións obxectivo relevantes. Da fase de optimización conclúese que un algoritmo evolutivo traballa

sensiblemente mellor que un de gradiente conxugado neste tipo de problemas, dado que o primeiro foi capaz de explorar os metamodelos máis concienzudamente que o segundo. Descubriuse tamén que a interacción entre placas de fibra de vidro e escuma de tereftalato de polietileno colocadas no interior dun tubo metálico é de gran importancia para unha maior absorción de enerxía do deseño, sendo convenientemente cuantificada.

Contents

List of Figures

List of Tables

Notation

Greek letters

α	Courant number, step length in a conjugate-gradient method, shape factor for Deshpande model, interaction parameter (Hanssen's formula).
β	Parameter for the flow potential of Deshpande model, vector of least-squares estimates in a Gaussian process, interaction parameter (Hanssen's formula).
γ	Gaussian correlation function.
δ	Axial crushing distance.
δ_{e}	Effective crushing length of a lobe in a collapse mechanism.
δ_{max}	Bottoming-out length (maximum crushing distance).
ε	True strain, stationary error model.
ε_θ	Circumferential strain.
ε_{D}	Ultimate strain for damage model.
$\varepsilon_{\mathrm{tol}}$	Tolerance.
ε_{u}	Ultimate tensile strain.
ε^{p}	Plastic strain.

$\dot{\varepsilon}$	Strain rate.
$\dot{\varepsilon}_0$	Reference strain rate.
ϵ	Levi-Civita symbol.
η_c	Structural effectiveness.
θ	Angle of a plastic hinge, correlation parameter for GP model.
$\dot{\lambda}$	Plastic multiplier.
$\hat{\lambda}$	Effective Lamé's constant.
$\hat{\mu}$	Effective Lamé's constant.
ν	Elastic Poisson's ratio.
ν^p	Plastic Poisson's ratio.
ρ	Density.
σ	True stress, auto-covariance function.
σ_eq	Equivalent (von Mises) stress.
σ_f	Foam yield stress (Hanssen's formula).
σ_H	Hydrostatic stress.
σ_u	Ultimate stress.
σ_y	Yield stress (sometimes σ_0).
σ^*	Stress triaxiality ratio.
σ^2	Variance.
$\sigma_\mathrm{H}^\mathrm{C}$	Yield stress in hydrostatic compression.
$\sigma_\mathrm{H}^\mathrm{T}$	Yield stress in hydrostatic tension.
σ_y^0	Initial yield stress.
$\boldsymbol{\sigma}$	Cauchy stress tensor.
$\boldsymbol{\sigma}^{\nabla\mathrm{G}}$	Green-Naghdi stress rate.
$\boldsymbol{\sigma}'$	Deviatoric stress tensor.

ϕ	Solidity ratio.
ψ	Energy-absorbing effectiveness factor.
Ω	Cross-sectional area enclosed by the middle line of the cross section, number of input dimensions for GP model.

Roman letters

A	Cross-sectional area, initial yield strength in Johnson-Cook model, parameter for the pressure fit in triaxial tests, shape parameter for Deshpande model.
A_{f}	Foam cross-sectional area (Hanssen's formula).
a	Coefficient of the MARS power basis functions.
$\mathbf{a}$	Nodal accelerations.
B	Isotropic hardening parameter in Johnson-Cook model, MARS power basis function, parameter for the pressure fit in triaxial tests, shape parameter for Deshpande model.
b	Side length in square section, parameter for Voce model, outer diameter (Hanssen's formula).
C	Viscosity exponent, parameter for the membrane deformability fit in triaxial tests.
C_{avg}	Main interaction parameter (Hanssen's formula).
c_{d}	Stress wave speed.
$\mathbf{C}^{\mathrm{damp}}$	Matrix of damping coefficients.
D	Diameter, parameter for Cowper–Symonds overstress power law, parameter for the membrane deformability in triaxial tests.
$\mathbf{D}$	Strain rate tensor.
$\mathbf{D}^{\mathrm{e}}$	Elastic part of the strain rate tensor.
$\mathbf{D}^{\mathrm{p}}$	Plastic part of the strain rate tensor.
E	Young's modulus.

E_a	Absorbed energy.
e	Engineering strain.
F	Crushing force.
F_avg	Average crushing force.
F_avg^0	Average crushing force of an empty extrusion (Hanssen's formula).
F_V	Vertical load in triaxial test.
f	Yield criterion, mass-scaling factor, generic objective function, flange width.
$\hat{f}$	Metamodel of the function f.
$\hat{f}'$	Mono-objective optimization function.
$\hat{\mathbf{f}}$	Values of the metamodel of the function f.
$\mathbf{f}^\mathrm{damp}$	Viscous forces.
$\mathbf{f}^\mathrm{ext}$	External nodal forces.
$\mathbf{f}^\mathrm{int}$	Internal nodal forces.
G	Shear modulus.
g	Flow potential.
g_I	Boundary conditions.
$\mathbf{g}$	Vector of basis functions in a Gaussian process.
h	Half-lobe length in collapse mechanism, element size, wall thickness (Hanssen's formula).
I_σ	First stress invariant.
$\mathbf{I}$	Identity tensor.
J_2	Second stress invariant.
J_3	Third stress invariant.
k	Parameter for Deshpande model.
k_c	Parameter for Deshpande model.

k_{t}	Parameter for Deshpande model.
L	Component length, correlation length for GP.
L_{e}	Effective crushing length, characteristic element length.
L_{min}	Smallest element dimension in a finite element model.
M	Number of divisions of the design space for LHS.
M_0	Collapse moment per unit circumferential length.
M_{b}	Number of MARS basis functions.
M^{C}	Generic consistent matrix.
M^{D}	Generic diagonal matrix.
m	Mass.
$\mathbf{M}$	Mass matrix.
$\mathbf{f}$	Nodal unbalanced forces, values of the function f obtained from FE sampling.
N	Number of contributing flanges in a multi-cell cross section, number of variables for LH sampling.
N_{p}	Size of the data set for the correlation coefficient R^2.
N_{V}	Number of terms for a Voce law.
n	Isotropic hardening parameter in Johnson-Cook model, parameter for Cowper–Symonds overstress power law.
n_{c}	Number of boundary conditions.
$n_{\mathrm{T}I}$	Total number of increments.
P	Vertical pressure in triaxial tests.
P_{m}	Mean crushing force.
P_{peak}	Initial peak crushing force.
R^2	Correlation coefficient.
p	Equivalent plastic strain.

p_{D}	Ultimate equivalent plastic strain.
$\dot{p}$	Equivalent plastic strain rate.
$\dot{p}_0$	Reference equivalent plastic strain rate.
Q	Parameter for Voce model (saturation hardening stress).
R	Radius, isotropic hardening function, stress ratio for Cowper–Symonds overstress power law, anisotropy ratio.
r	Stationary autocorrelation function for GP model.
S	Total perimeter of the cross section.
S_{E}	Stroke efficiency.
s	Engineering stress.
$\mathbf{s}$	Search direction for a conjugate-gradient method.
t	Thickness, time.
t_{E}	Total simulation time.
Δt^{crit}	Critical time increment in an explicit analysis.
$\mathbf{u}$	Nodal displacements.
V	Volume.
$\mathbf{v}$	Nodal velocities.
W	Work or energy.
W_{ext}	External energy.
W_{int}	Internal energy.
W_{kin}	Kinetic or inertial energy.
w	Weight for the weighted model of multi-objective optimization.
x_{m}	Half-lobe length in Abramowicz and Jones model.
$\mathbf{x}$	Generic variables vector.

Acronyms

ASTM	American Society for Testing Materials.
CFE	crush force efficiency.
CFRP	carbon-fiber reinforced polymer.
DDQ	deep drawing quality.
DIC	digital image correlation.
FE	finite element.
GFRP	glass-fiber reinforced polymer.
GP	Gaussian process.
HIC	head injury criterion.
LHS	Latin hypercube sampling.
LR	load ratio.
LVDT	linear variable differential transformer.
MARS	multivariate adaptive regression splines.
PEEK	polyether ether ketone.
PET	polyethylene terephthalate.
PLC	Portevin-Le Chatelier.
PVC	polyvinyl chloride.
SAE	Society of Automotive Engineers.
SBGO	surrogate-based global optimization.
SEA	specific energy absorption.
SEM	scanning electron microscope.
SHPB	Split-Hopkinson pressure bar.

1

Introduction

This thesis investigated the axial crushing of frontal energy absorbers made of a combination of steel or aluminum with composite materials or foams, by means of experimental and numerical tests and different optimization strategies. Therefore, it can be considered to be part of the wide research topic of structural crashworthiness and crash safety. The developed work was focused on structural elements that, for their dimensions, are suitable to be used in cars. However, the results are applicable to any other type of vehicle. This introductory chapter presents these research fields, with an introduction to vehicle occupant protection issues where the different safety layers are stated. Frontal energy-absorbing members are highlighted as a part of this system. The main research goals of the work are stated next, together with a list of the experimental and numerical methods employed to achieve them. A brief outline of each chapter is also presented, whose essential contents are shortly described. Finally, a list of the peer-reviewed publications and conference communications hitherto derived from this PhD thesis is also provided at the end of the chapter.

1.1 Motivation

In the field of protective structures, vehicle occupant safety has established itself as an essential characteristic of modern cars, trains and aircraft. Over the past two decades, many crashworthiness features have been added to vehicles motivated by new legislation and society's demands, usually classified into active and passive: active safety refers to technology assisting in the prevention of a crash, whereas passive safety refers to components of the vehicle (airbags, seat belts, structure, etc.) which help to protect occupants during a crash event. Regarding the car structure, these passive safety features include, for example, rigid steel occupant-cells surrounded by strategically-placed energy absorbing components, areas of controlled deformation, reinforcements, etc.

As an example of the efficiency of these improvements, fatalities were reduced by 24.5 % in USA from 2006 to 2013 [1]. It is important to recall that frontal crashes produce nowadays 50-70 % of the fatalities by car accidents in developed countries [2], so any safety improvement in this field has a direct effect on the occupant safety levels.

In Europe, the drive for improved crashworthiness accelerated from the 1990s onwards, with the 1997 advent of the car safety performance assessment programme Euro NCAP. This agency publishes standards for crash testing and rating of modern vehicles in Europe, like the frontal impact testing protocol [3]. These standards are partly responsible of cars becoming much safer: tests results are commonly presented by motor press, and in turn greatly influence the consumer preferences. It is interesting to comment here that nowadays, most car producers get a five-star score in the frontal impact tests against a flexible barrier. Due to this, the Euro NCAP protocol has been modified very recently to include an additional test consisting of an impact against a rigid barrier, which is far more demanding [4].

Moreover, the increasing importance of the economical cost of cars and requirements on CO_2 emissions have made that weight savings in the automotive industry are increasingly approaching the importance they have, for example, in the aeronautical industry. Thus, protection systems and components should be developed so that a weight reduction is pursued.

The structural design of the car should protect the occupants during a crash event. The protection limits arise from bio-mechanics, based on the limits of acceleration that a human body can withstand, which can be translated to energies, forces and displacements. These values have to be considered during the vehicle design phase. This design primarily consists of a stiff, theoretically undeformable safety cage where the occupants are placed. Around this cage, a series of specifically-designed deformable systems must absorb the impact energy in a controlled way (see Figure 1.1). From outside inwards, these parts are the following:

- The bumper is designed to cope with low velocity impacts (up to 8-10 km/h [5]) with as little damage as possible. It also distributes the crash forces from the point of impact to both sides of the car, ideally. It consists of an inner steel or aluminum beam covered with a thermoplastic shell containing ribs which fold together [6].
- The crash boxes and front rails should be activated with more serious collisions which cause permanent damage to the structure. They are designed to deform axially under the loads transmitted by the bumper. Crash boxes

are usually placed so that they can be replaced if the crash does not affect the engine.

- Progressively stiffer elements dedicated for severe collisions, which contact the safety cage. This includes the region from the shock towers to the safety cage.

A schematic representation of all these safety layers is provided in Figure 1.1, taken from [5].

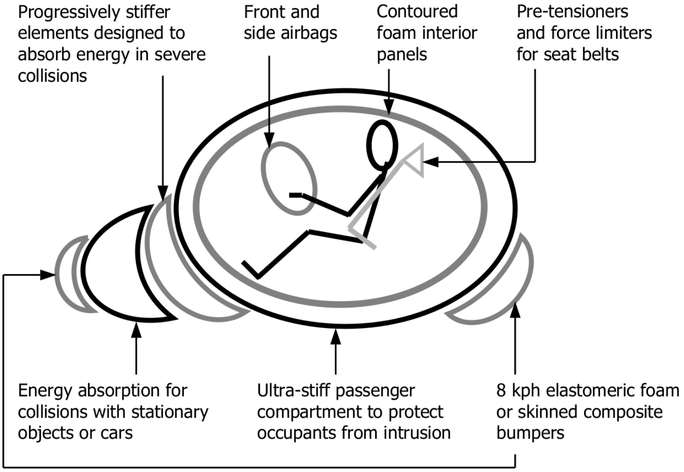

Figure 1.1: Simplified representation of car safety layers [5].

As an example of the importance that collision safety has nowadays in the car industry, Figure 1.2 depicts the concept of automotive body structure design developed by Honda, named ACE (Advanced Compatibility Engineering). This idea consists on the evenly distribution of the crash forces on the body structure and their redirection away from the passenger compartment, while minimizing damage to other impacted vehicles at the same time.

Regarding the materials employed to build the main frame of cars, different steels and aluminums can be found. The former have higher energy-absorbing characteristics than the latter, in exchange for a density three times higher than aluminum. A view of the body-in-white of a modern 2011 Audi A8 built in aluminum is presented in Figure 1.3, where different building materials are highlighted. In the detail view, two bi-tubal rectangular crash boxes can be observed with a triggering mechanism, whose function will be discussed later.

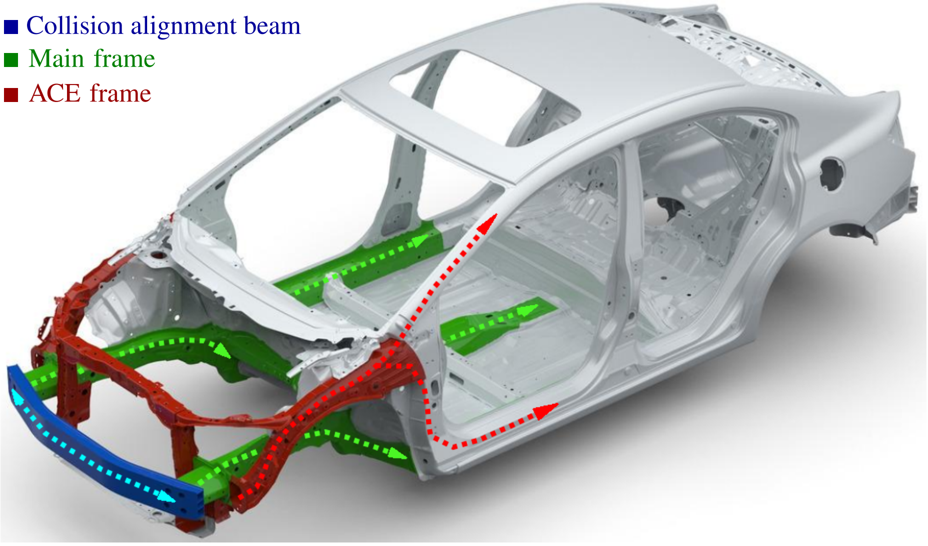

Figure 1.2: ACE body structure design by Honda. Relevant structural members and load paths. Taken and modified from [7].

The frontal members depicted in Figure 1.3b, designed to absorb part of the kinetic energy of the impact event by axial progressive crushing, are usually built in steel or aluminum. Furthermore, extensive research has been done with other alternative materials, as will be discussed in Chapter 2. However, there is still room for improvement regarding the combinations of innovative materials with classic metallic structures, and also regarding the use of new bonding techniques for the correct assembly of these new materials with an adequate response to impact loads and fatigue.

1.2 Contributions of this thesis

The present thesis contributes focusing on the lightweight design and optimization of energy absorbing systems, more specifically, frontal crash boxes, made of a combination of metals, composite materials, foam and cork. In particular:

1. This work investigated the crashworthiness of non-conventional crash boxes consisting of an outer metal tube made of steel or aluminum filled with either composite structures or a solid padding of PET foam or cork agglomerate.

2. Different optimization strategies were tested under the challenging task of

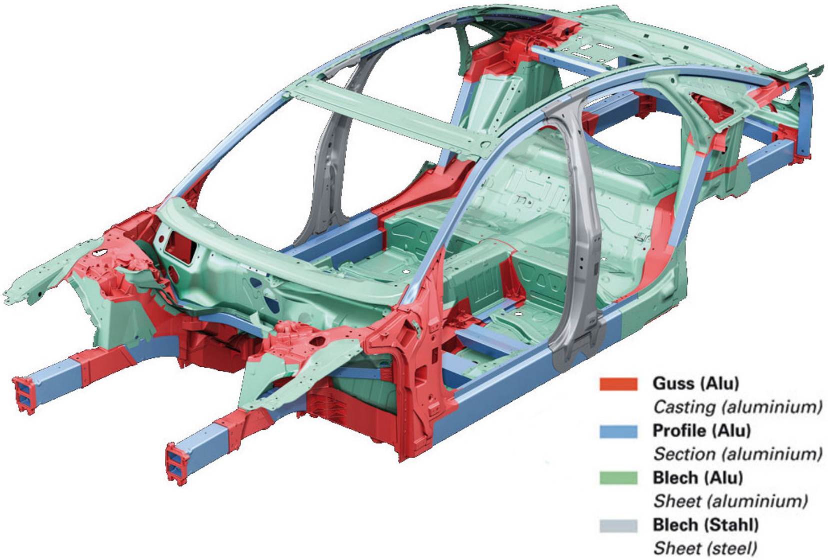

(a) Body structure of a 2011 Audi A8, different materials are highlighted. Taken form [8].

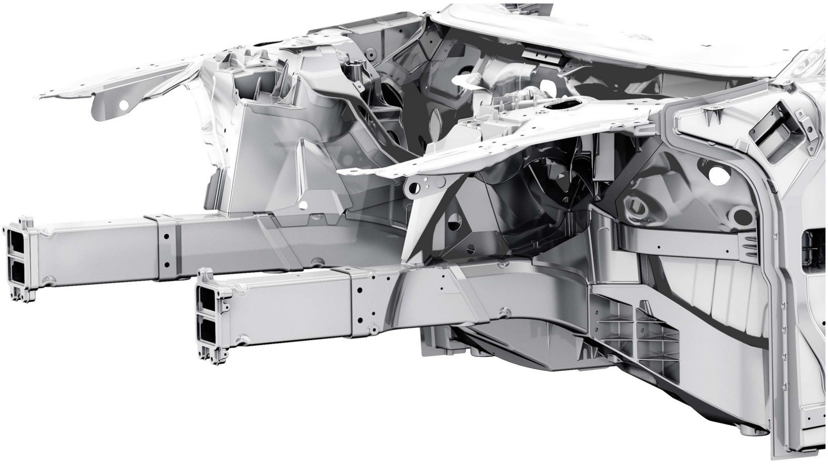

(b) Detail view of the frontal structural system dedicated to energy absorption. Bi-tubal crash boxes with their triggering mechanisms can be identified. Original image copyrighted by AUDI AG [9].

Figure 1.3: Body-in-white aluminum structure of a 2011 Audi A8.

performing a successful and reliable optimization of the aforementioned designs, which required the use of surrogate models (also assessed here).

3. Finite element models for the new designs were validated for their further usage.
4. The interaction effect between two simultaneous filler materials (glass fiber plates and PET foam) was investigated.

1.3 Research aims and methodology

The research aims are as follows:

- To generate research information and scientific understanding about the static and dynamic axial crushing of some unexplored material combinations to be used as possible energy absorbing structural systems. These materials include, at a first stage, glass and carbon fiber reinforced polymers, polyethylene terephthalate (PET) foam and a cork agglomerate, all of them used as fillers for steel or aluminum tubes. This includes both experimental and numerical work via finite element modeling, and the analysis of possible interaction effects between materials.
- To achieve the structural optimization of the studied components through the application of different optimization methods and algorithms using computational simulations of the calibrated finite element models. The optimization process will generate some understanding about how materials are working and which are more worthy for this application, and some useful results about the optimum dimensions, thicknesses and material distribution.

These goals were achieved using the following methods, tools and procedures:

- Experimental methods:
  - Material testing:
    - Tensile testing on smooth and notched specimens.
    - Low-rate compression tests.
    - Drop-tower tests.
  - Component testing:
    - Quasi-static compression tests.
    - Drop tower impact tests.

    - Pendulum accelerator impact tests.

- Computational methods:
  - High-end finite element modeling of the involved materials and components, using Abaqus Explicit controlled by scripts written in Python and user material subroutines.
  - Simulation of the quasi-static and dynamic experimental tests, using the aforementioned tools.
  - Optimization algorithms based on surrogate modeling. The optimization framework DAKOTA was utilized to build in the metamodels from FE samplings and run different optimization algorithms, like gradient-based and evolutionary.

1.4 Outline

This work is based on a series of research publications by the author, thus the seven chapters are arranged so that they can be even read in their own right. The contents of each chapter are mentioned below.

Chapter 2 reviews the current state of the art in dedicated energy absorbing systems. After a brief lecture on impact mechanics and crashworthiness, the work elaborates fully on the most used materials for crash boxes and their combinations, and on the analysis methods for their design.

Chapter 3 includes the experimental and numerical assessment of the crashworthiness of several innovative fillers for steel cold-formed tubes: a structure of a glass-fiber reinforced polyamide, corrugated prepregs of a carbon-fiber reinforced polymer, a PET-based foam and a cork agglomerate. The relative merits of each design are highlighted and a parametric study is performed for the best-performing alternative. Finally, the welding scheme of the steel parts is studied.

Chapter 4 contains the application of different optimization schemes to the previous GFRP-steel design. Gradient-based and meta-heuristic optimization algorithms are run on metamodels fit to samples obtained by finite element simulations, in order to obtain the optimum design for different simultaneous objective functions: specific energy absorption, load ratio, peak forces, etc.

Chapter 5 reports the experimental work carried out to asses the crashworthiness of a design combining a GFRP structure and a PET-foam filler inside an aluminum cylinder. The component is studied quasi-static and dynamically, and the interaction effect between foam and glass fiber is assessed from a scientific point of view.

Chapter 6 describes the finite element modeling of the component studied in Chapter 5 and its optimization for aluminum and steel casings based on what was learned from Chapters 3 and 4.

Chapter 7 closes this work and rounds it off with a final summary, conclusions and some discussion and recommendations for further work.

The six appendices contain supplementary information: material tests are described in Appendix A, some microscope views of material samples are presented in Appendix B, manufacturer's datasheets are provided in Appendix C and the national patent derived from this work is reproduced in Appendix D. In accordance with the regulations of Universidade da Coruña, two extended summaries of this thesis are provided in Spanish (Appendix E) and Galician (Appendix F).

The source of this monograph is a series of research works by the author, which have been partially or totally included here. As the main author, the following peer-reviewed works are highlighted:

- M. Costas, J. Díaz, L. E. Romera, S. Hernández and A. Tielas. "Static and dynamic axial crushing analysis of car frontal impact hybrid absorbers". *International Journal of Impact Engineering* 62 (2013), pp. 166-181 [10].
- M. Costas, J. Díaz, L. E. Romera and S. Hernández. "A multi-objective surrogate-based optimization of the crashworthiness of a hybrid impact absorber". *International Journal of Mechanical Sciences* 88 (2014), pp. 46-54 [11].
- M. Costas, D. Morin, M. Langseth, L. Romera and J. Díaz. "Axial crushing of aluminum extrusions filled with PET foam and GFRP. An experimental investigation". *Thin-Walled Structures*, 99 (2016), pp. 45-57 [12].
- M. Costas, D. Morin, M. Langseth, J. Díaz and L. Romera. "Computational modeling and multi-objective crashworthiness optimization of aluminum extrusions filled with PET foam and GFRP". To be submitted for possible publication.

Furthermore, the following publications closely related to this thesis' topic have been co-authored by the author:

- J. Paz, J. Díaz, L. E. Romera and M. Costas "Crushing analysis and multi-objective crashworthiness optimization of GFRP honeycomb-filled energy absorption devices". *Finite Elements in Analysis and Design* 91 (2014), pp. 30-39 [13].
- M. Cid Montoya, M. Costas, J. Díaz, L. E. Romera and S. Hernández "A multi-objective reliability-based optimization of the crashworthiness of a metallic-GFRP impact absorber using hybrid approximations". *Structural and Multidisciplinary Optimization* 52 (2015), pp. 827-243 [14].
- J. Paz, J Díaz, L. E. Romera and M. Costas. "Size and shape optimization of aluminum tubes with GFRP honeycomb reinforcements for crashworthy aircraft structures". *Composite Structures* 133 (2015), pp. 599-507 [15].

Finally, several conference contributions derived from this work were presented, including:

- M. Costas, J. Díaz, L. Romera, S. Hernández and R. Ledo. "Influence of welded joints on the crashworthiness response of hybrid structural elements". *SAE 2013 World Congress and Exhibition, paper 13B-0036/2013-01-0755* (2013) [16].
- M. Costas, L. Romera, J. Díaz, S. Hernández and A. Tielas. "Computational and experimental analysis of a hybrid car impact absorber". *Computational Methods and Experimental Measurements XVI, WIT Press, C.A. Brebbia. G.M. Carlomagno and S. Hernández (eds.)* 2013, pp. 367-378 [17].
- L. Romera, J. Paz, M. Costas, J. Díaz and S. Hernández. "Crashworthiness response of honeycomb-metallic-GFRP energy absorption devices". *HPSM/OPTI 2014, The 2014 International Conference on High Performance and Optimum Design of Structures and Materials* 2014 [18].
- J. Díaz, M. Costas, L. Romera, J. Paz and S. Hernández. "Surrogate-based multi-objective optimization of glass-fiber–steel crash absorbers". *35th FISITA World Automotive Congress, Maastrich (Netherlands)* 2014 [19].
- L. Romera, M. Costas, J. Díaz, J. Paz and S. Hernández. *Reduction of the frontal crash peak forces in a car using size optimization tools. 35th FISITA World Automotive Congress, Maastrich (Netherlands)* 2014 [20].

References

[1] National Highway Traffic Safety Administration - NHTSA. *Early estimate of motor vehicle traffic fatalities for the first half (January-June) of 2013.* Tech. rep. U.S. Department of Transportation, 2013.

[2] National Highway Traffic Safety Administration - NHTSA. *Fatalities in Frontal Crashes despite Seat Belts and Air Bags.* Tech. rep. U.S. Department of Transportation, 2009.

[3] *Frontal Impact Testing Protocol, Version 6.0.* European New Car Assessment Programme (Euro NCAP), 2012.

[4] *Full Width Rigid Barrier.* `http://www.euroncap.com/en/vehicle-safety/the-ratings-explained/adult-occupant-protection/full-width-rigid-barrier/`.

[5] J. De Kanter. “Energy absorption of monolithic and fibre reinforced aluminium cylinders”. PhD thesis. Faculty of Aerospace Engineering - Delft University of Technology, 2006.

[6] G. Nagel. “Impact and energy absorption of straight and tapered rectangular tubes”. PhD thesis. School of Civil Engineering, Queensland University of Technology, 2005.

[7] *Image of the Honda ACE system.* `http://www.quazoo.com/q/Advanced_Compatibility_Engineering`.

[8] *Image of the body-in-white of an Audi A8, 2011 version.* `http://www.boronextrication.com/2010/04/29/2010-audi-a8-uk-body-structure/`.

[9] *Detail of the body-in-white of an Audi A8, 2011 version.* `https://www.audi-mediacenter.com/en/photos/detail/audi-ultra-lightweight-construction-9223`.

[10] M. Costas, J. Díaz, L. Romera, S. Hernández, and A. Tielas. “Static and dynamic axial crushing analysis of car frontal impact hybrid absorbers”. *International Journal of Impact Engineering* 62 (2013), pp. 166–181.

[11] M. Costas, J. Díaz, L. Romera, and S. Hernández. “A multi-objective surrogate-based optimization of the crashworthiness of a hybrid impact absorber”. *International Journal of Mechanical Sciences* 88 (2014), pp. 46–54.

[12] M. Costas, D. Morin, M. Langseth, L. Romera, and J. Díaz. “Axial crushing of aluminum extrusions filled with PET foam and GFRP. An experimental investigation”. *Thin-Walled Structures* 99 (2016), pp. 45–57.

[13] J. Paz, J. Díaz, L. Romera, and M. Costas. “Crushing analysis and multi-objective crashworthiness optimization of GFRP honeycomb-filled energy absorption devices”. *Finite Elements in Analysis and Design* 91 (2014), pp. 30–39.

[14] M. Cid Montoya, M. Costas, J. Díaz, L. Romera, and S. Hernández. “A multi-objective reliability-based optimization of the crashworthiness of a metallic-GFRP impact absorber using hybrid approximations”. *Structural and Multidisciplinary Optimization* 52 (2015), pp. 827–843.

[15] J. Paz, J. Díaz, L. Romera, and M. Costas. “Size and shape optimization of aluminum tubes with GFRP honeycomb reinforcements for crashworthy aircraft structures”. *Composite Structures* 133 (2015), pp. 499–507.

[16] M. Costas, J. Díaz, L. Romera, S. Hernández, and R. Ledo. “Influence of welded joints on the crashworthiness response of hybrid structural elements”. In: *SAE 2013 World Congress and Exhibition, paper 13B-0036/2013-01-0755.* 2013.

[17] M. Costas, L. Romera, J. Díaz, S. Hernández, and A. Tielas. “Computational and experimental analysis of a hybrid car impact absorber”. In: *Computational Methods and Experimental Measurements XVI, WIT Press, C.A. Brebbia, G. M. Carlomagno and S. Hernandez (eds.)* 2013, pp. 367–378.

[18] L. Romera, J. Paz, M. Costas, J. Díaz, and S. Hernández. “Crashworthiness response of honeycomb metallic-GFRP energy abpsortion devices”. In: *HPSM/OPTI 2014, The 2014 International Conference on High Performance and Optimum Design of Structures and Materials.* 2014.

[19] J. Díaz, M. Costas, L. Romera, J. Paz, and S. Hernández. “Surrogate-based multi-objective optimization of glass-fiber - steel crash absorbers”. In: *35th FISITA World Automotive Congress, Maastrich (Netherlands).* 2014.

[20] L. Romera, M. Costas, J. Díaz, J. Paz, and S. Hernández. “Reduction of the frontal crash peak forces in a car using size optimization tools”. In: *35th FISITA World Automotive Congress, Maastrich (Netherlands).* 2014.

2

Structural crashworthiness and impact energy absorption

This chapter introduces some basis of structural crashworthiness and energy absorption, starting with the analysis of a car crash from a theoretical point of view, focusing on the contribution and performance of the frontal energy absorption. This gives an idea about how the dissipative devices work and their consequences on the injury risks for passengers. Afterwards, the term «crashworthiness »is defined and some useful metrics are described. Then, the current state of the art of the usage of different materials and geometries for these members is presented, including the theory behind the axial crushing of standard geometries of metal tubes, composite tubes, foam-filled sections, corks and honeycombs. The chapter closes with an introduction to the explicit computational method for finite element models applied to the simulation of axial progressive crushing.

2.1 Structural impact mechanics

In this development, adapted from [21], the following event is studied: a car with a mass m_1 traveling at an initial velocity v_1 impacts an stationary vehicle with mass m_2 equipped with a deformation zone in the front (see Figure 2.1):

Perfectly inelastic collision is assumed, i.e., both cars will have the same velocity after the crash. Car m_1 is assumed rigid, thus all deformation will take place in car m_2. Car m_2 has a deformation zone in the front where two front members will absorb the energy. The response of these members consists of a constant force-displacement response curve with value F_0, depicted in Figure 2.2.

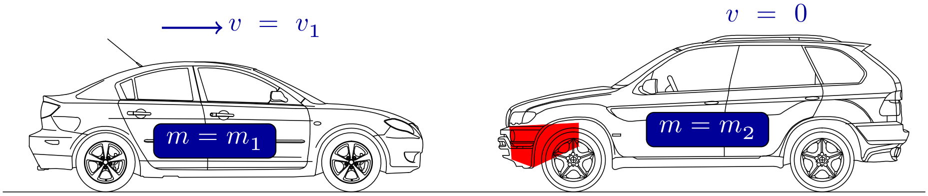

Figure 2.1: Initial configuration of the theoretical analysis of a car crash: car 1 impacts car 2, which is provided with deformable body (red).

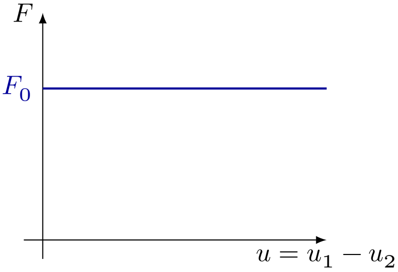

Figure 2.2: Force-displacement response of a simplified crash box.

If dynamic equilibrium is imposed during the crash:

$$\text{car 1}: \qquad -F_0 = m_1 \ddot{u}_1 \implies \ddot{u}_1 = -\frac{F_0}{m_1}, \tag{2.1a}$$

$$\text{car 2}: \qquad F_0 = m_2 \ddot{u}_2 \implies \ddot{u}_2 = \frac{F_0}{m_2}. \tag{2.1b}$$

The relative acceleration $\ddot{u}$ can be obtained by subtracting the previous equations:

$$\ddot{u} = \ddot{u}_1 - \ddot{u}_2 = -F_0 \left(\frac{1}{m_1} + \frac{1}{m_2} \right). \tag{2.2}$$

Integrating twice over time gives the relative velocity and deformation:

$$\dot{u} = -F_0 \left(\frac{1}{m_1} + \frac{1}{m_2} \right) t + A, \tag{2.3a}$$

$$u = -F_0 \left(\frac{1}{m_1} + \frac{1}{m_2} \right) t^2 + At + B. \tag{2.3b}$$

The boundary conditions can now be applied to determine A and B:

$$\dot{u}\,(t = 0) = \dot{u}_1\,(t = 0) = v_1 \implies A = v_1, \tag{2.4a}$$

$$u\,(t = 0) = 0 \implies B = 0. \tag{2.4b}$$

Therefore, the relative deformation u can be expressed as

$$u = -F_0 \left(\frac{1}{m_1} + \frac{1}{m_2} \right) t^2 + v_1 t. \tag{2.5}$$

The maximum deformation after the crash u_{max} can be found by setting $\mathrm{d}u/\mathrm{d}t = 0$. This gives

$$u_{\mathrm{max}} = \frac{{v_1}^2}{2F_0} \frac{m_1 m_2}{m_1 + m_2} \tag{2.6}$$

at

$$t_{\mathrm{max}} = \frac{v_1}{F_0} \left(\frac{1}{m_1} + \frac{1}{m_2} \right). \tag{2.7}$$

The velocities of both cars during the crash can be obtained as

$$\ddot{u}_1 = -\frac{F_0}{m_1}, \tag{2.8a}$$

$$\dot{u}_1 = -\frac{F_0}{m_1} t + C, \tag{2.8b}$$

$$\dot{u}_1 \left(t = 0 \right) = v_1 \implies C = v_1, \tag{2.8c}$$

$$\dot{u}_1 = v_1 - \frac{F_0}{m_1} t, \tag{2.8d}$$

and

$$\ddot{u}_2 = \frac{F_0}{m_2}, \tag{2.9a}$$

$$\dot{u}_2 = \frac{F_0}{m_2} t + D, \tag{2.9b}$$

$$\dot{u}_2 \left(t = 0 \right) = 0 \implies D = 0, \tag{2.9c}$$

$$\dot{u}_2 = \frac{F_0}{m_2} t. \tag{2.9d}$$

If Equation (2.7) is applied to the previous expressions, it is straightforward to check that both cars have the same velocity when the front members reach $u = u_{\mathrm{max}}$ (perfectly inelastic collision). The value of this final velocity v_{f} is

$$v_{\mathrm{f}} = v_1 \frac{m_1}{m_1 + m_2}. \tag{2.10}$$

In order to illustrate these results, the velocity histories for both cars during the crash event are plotted in Figure 2.3. Notice that, for the represented scenario, $m_1 > m_2$ and therefore v_{f} is closer to v_1.

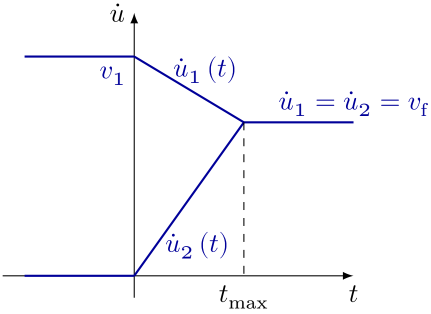

Figure 2.3: Velocity histories for cars 1 and 2 during a perfectly inelastic collision.

In view of these results a couple of questions may arise: if the final velocity of the vehicles does not depend on F_0, what about the energy absorption?; and where does F_0 come into play? To answer the first question the hypothesis of *perfectly inelastic collision* must be recalled. This implies that the dissipated energy is exactly the amount required to make both cars move together after the crash event. This amount matches what is usually referred as *maximum available kinetic energy.* If the absorbed energy was less than this quantity, then some elastic energy would be returned to the cars and the collision would not be *perfectly* inelastic. In this simplified example, the energy dissipated by the frontal crash boxes E_a can be found using the equation of conservation of energy applied to the perfectly inelastic case:

$$\frac{1}{2} m_1 {v_1}^2 = \frac{1}{2}\left(m_1 + m_2\right) {v_\mathrm{f}}^2 + E_\mathrm{a}. \tag{2.11}$$

Combining Equations (2.10) and (2.11), the absorbed energy can be obtained as:

$$E_\mathrm{a} = \frac{1}{2} {v_1}^2 \frac{m_1 m_2}{m_1 + m_2}, \tag{2.12}$$

and given that $E_\mathrm{a} = \int_0^{u_\mathrm{max}} F \mathrm{d}u = F_0 u_\mathrm{max}$ (see Figure 2.2), the same result for the maximum displacement than in Equation (2.6) is obtained.

Once the expression of the absorbed energy was obtained, the role of F_0 can be looked into. Its contribution is particularly evident considering Equation (2.7): it can be seen that the duration of the crash event is inversely proportional to the crushing force of the crash boxes, always under conditions of perfect inelasticity. Given that the final speed v_f is immediately determined once the initial speed and the car masses are known, the value F_0 controls how fast the transition from the initial to the final states takes place, i.e., the acceleration or deceleration of both vehicles. The lower the crushing force, the lower the accelerations (as t_max

increases). This has obviously a drawback: as the crushing force decreases, longer crash boxes are required to absorb the same amount of energy.

If the accelerations in absolute value are plotted versus time for one of the cars, Figure 2.4 is obtained.

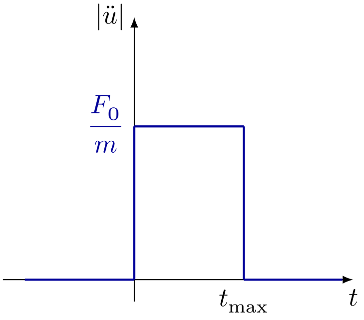

Figure 2.4: Acceleration pulse for one car in a perfectly inelastic collision.

Accelerations are among the most important factors to consider when it comes to occupant safety. They are related to the likelihood of severe or fatal injuries arising from an impact by means of the *injury criteria*. Many of these criteria have been proposed or enhanced over the years for different parts of the human body. One of the most relevant is the head injury criterion (HIC) [22], defined as:

$$\mathrm{HIC} = \max_{0 \le t_1 \le t_2 \le \Delta} \left\{ \left[\frac{1}{t_2 - t_1} \int_{t_1}^{t_2} a\,(t)\,\mathrm{d}t \right]^{2.5} (t_2 - t_1) \right\}. \tag{2.13}$$

The HIC estimates the likelihood of head injury arising from a crash, relating the acceleration $a\,(t)$ at the gravity center of the head, in g units, and its duration. The latter is relevant as larger accelerations can be tolerated for short durations. The HIC is obtained by applying Equation (2.13) for different time intervals $t_2 - t_1$ up to a certain limit Δ, which is usually 36 or 15 ms[1]. Figure 2.5 provides a graphical representation of the curve for HIC= 1000 (usual value) and a constant acceleration pulse like Figure 2.4.

The example for can be now particularized for $m_1 = 1000\,\mathrm{kg}$, $m_2 = 1500\,\mathrm{kg}$ and $F_0 = 200\,\mathrm{kN}$; and assuming that the accelerations in the head are equal to

---

[1] This value varies in different consulted standards and test protocols, which choose either 15 or 36 ms.

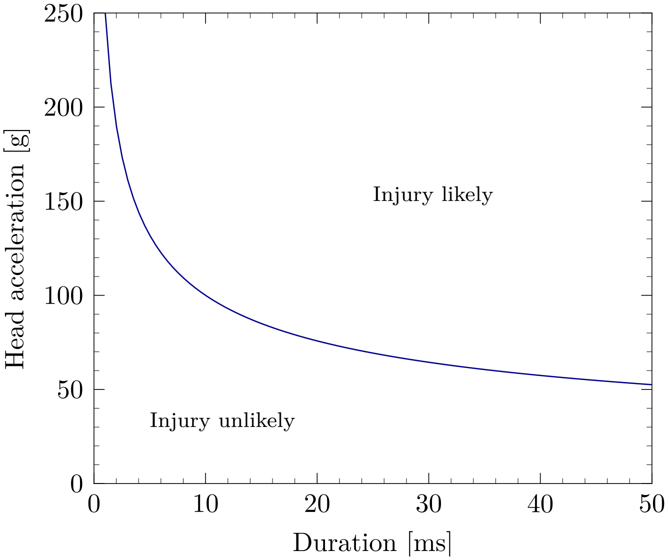

Figure 2.5: Head acceleration vs. time for HIC = 1000.

the accelerations of the whole car. This leads to $t_{\max} = 0.0298\,\text{s}$, $\ddot{u}_1 = 34\,\text{g}$ and $\ddot{u}_2 = 14\,\text{g}$, both values being in the safe side of Equation (2.13).

To sum up, the inclusion of the energy-absorbing system increases the duration of the event and keeps the acceleration levels in a tolerable range. The ideal absorber would have infinite length and a very low crushing force F_0, but since this is not possible, for a given length two ideas can be pointed out:

- The lower the force, the lower the accelerations suffered by the occupants; but a smaller amount of energy is absorbed and the remaining part will have to be dissipated by other structural parts or eventually transmitted to the occupants.
- The higher the force, the higher the accelerations experimented by the occupants; but higher levels of energy absorption are achieved and less remaining energy is transmitted to other members or to the occupants.

Therefore, the crushing force should be as high as allowed by the human tolerance limits, and high peak forces should be avoided since they can be transmitted to the passenger's cage. This is related to the concept of crashworthiness, described next.

2.2 Crashworthiness and its evaluation

Structural crashworthiness refers to the performance of a structure under impact loading, and has recently become an integral part in the design of vehicular structures (road vehicles, trains, aircraft, ...) where passengers or valuable cargo are involved. In this scenario, the capacity of the structure to withstand impact forces and protect the passengers or cargo has to be ensured. Lu and Yu [23] provide a definition for crashworthiness as:

> *...the quality of response of a vehicle when it is involved in or undergoes an impact. The less damaged the vehicle and/or its occupants and contents after the given event, the higher the crashworthiness of the vehicle or the better its crashworthy performance.*

As long as the term crashworthiness refers to a global, qualitative and unmeasurable property of a protective structure, some metrics have been typically used to assess and quantify the performance and efficiency of impact-absorbing structural designs. These metrics are used as criteria to judge and compare different designs, or even as objective functions in a possible optimization of the design. The most relevant are presented next.

2.2.1 Absorbed energy

This value represents the amount of kinetic energy that a structure absorbs by means of thermal dissipation (plasticity and friction) or fracture phenomena. The absorbed energy E_{a} is obtained as the area under the force-displacement curve over the collapsed length:

$$E_{\mathrm{a}} = \int_0^{\delta_{\max}} F(\delta)\ \mathrm{d}\delta. \tag{2.14}$$

In the previous equation, $\delta_{\max}$ is the total crushing length along the axial direction and $F(\delta)$ represents the value of the crushing force along the axial direction. The absorbed energy is tagged as ① in Figure 2.6.

2.2.2 Specific energy absorption

This parameter is a measure of the efficiency of a structural design in terms of the absorbed energy for a given mass. It is therefore of particular interest for comparing different designs made of different materials, or materials themselves,

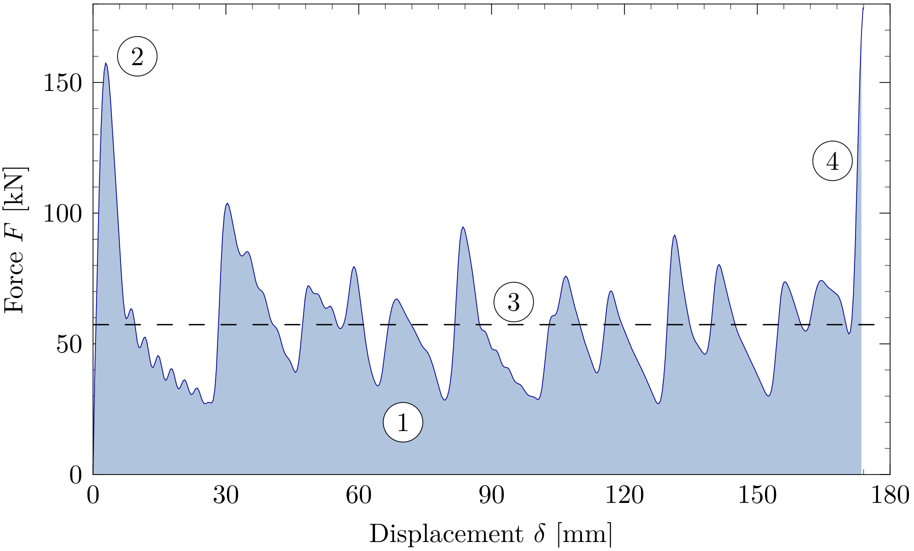

Figure 2.6: Typical force-displacement curve produced in the axial crushing of a thin-walled metal tube. 1: Absorbed energy E_{a}, 2: peak force P_{peak}, 3: mean crushing force P_{m}, 4: bottoming-out phase at $\delta = \delta_{\mathrm{max}}$.

specially if a weight reduction is desired. The *SEA* is given as the ratio of the absorbed energy E_{a} to the component mass m:

$$SEA = \frac{E_{\mathrm{a}}}{m}. \tag{2.15}$$

Some values of specific energy absorption for different materials are presented in Figure 2.7, taken from [24]. These are just indicative values, since the test conditions varied from one material to another.

Two important facts about the specific energy absorption are worth mentioning. The first is of particular importance for metallic tubes: the *SEA* is strongly dependent on the collapse mode developed during the axial crushing. This means that two identical metal tubes will absorb a different amount of energy if different modes are triggered. As an example, the axial crushing of two identical steel cylindrical tubes can be considered. If they are triggered to develop a concertina and diamond modes respectively[2], the later would absorb more energy than the former since larger plastic strains are developed. The second word of caution regarding the *SEA* is that a design with a higher value does not necessarily imply

---

[2] The axial collapse modes of cylindrical shells are explained in Section 2.3.1.

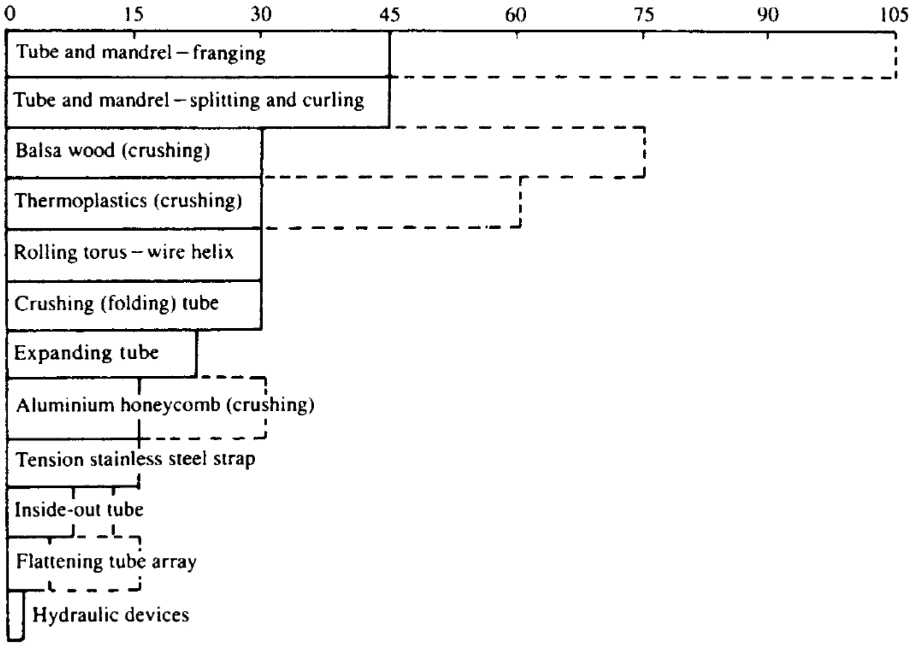

Figure 2.7: Specific energies for some energy absorbers in kJ/kg [24]

that a smaller component can be used to absorb the same amount of energy. As an example, if two identical tubes of aluminum and steel are compared, higher *SEA* values will be obtained for the aluminum due to its lower density. However, a longer aluminum tube will be required if the same amount of energy has to be absorbed. This can be illustrated with Table 2.1, adapted from [25], where the authors obtained the length required to absorb 31.7 kJ by a tube with a nominal diameter of 100 mm and a nominal wall thickness of 2.5 mm.

Therefore, what stands out of Table 2.1 is that even though the steel has the lowest value of *SEA*, a much shorter member is required to absorb the same amount of energy compared to an AA6009-T6 aluminum alloy. This is one of the reasons why designers still prefer steel to aluminum or composite materials for the design of crash boxes, since a smaller space is needed for the structural system.

2.2.3 Peak crushing load

The peak crushing load P_{peak} is the maximum axial load observed during a crushing test before bottoming-out occurs. The latter consists of a rapid increment in

Material	Density [kg/cm^3]	*SEA* [kJ/kg]	Mass needed to absorb 31.7 kJ [kg]	Unit mass [kg/cm]	Length needed to absorb 31.7 kJ [cm]
Mild 1024 steel	7.86	15	2.11	61.7	34.2
AA6009-T6	2.71	30	1.06	21.3	49.8
Glass/epoxy	1.90	60	0.53	14.9	35.6
Kevlar/epoxy	1.45	75	0.42	11.4	36.8
Graphite/epoxy	1.58	80	0.40	12.4	32.3

Table 2.1: A survey of various energy absorption devices, adapted from [25]. The geometry is a hollow circular tube with a nominal diameter of 100 mm and a nominal wall thickness of 2.5 mm.

the crushing force levels due to the complete compression of the member. The crushable distance up to this point is δ_{max}. The peak force is usually produced at the beginning of the test when the collapse starts. This can be also due to the elastic buckling of the tube, but in the range of slendernesses of this research this phenomenon does not occur. The peak crushing load is tagged as ② in Figure 2.6.

When it comes to the design of vehicle crash boxes, this parameter is particularly interesting for two main reasons. In first place, it is very important to avoid high force levels at the beginning of the impact, since they could lead to a plastic collapse of other parts in the car body. These parts should collapse only after the previous elements have reached their maximum energy absorption levels. As an illustrative example, if the front rails develop a plastic hinge with significant rotation before the crash boxes are crushed, the latter will experience a rigid-body rotation and the crushing will be not axial. The second reason to avoid high peak forces is that the impact force levels are proportional, to some extent, to the acceleration levels the occupants have to withstand. However, this is not completely true since the occupant active retaining systems will be generally triggered later than this peak force, so if the peak force lasts short enough the occupants will only experience a small relative displacement with respect to the vehicle.

2.2.4 Load ratio

This parameter is defined as the ratio of the peak load P_{peak} to the mean crushing force P_{m} (see ③ in Figure 2.6).

$$LR = \frac{P_{\mathrm{peak}}}{P_{\mathrm{m}}} \tag{2.16}$$

The mean crushing force is the mean value of the axial force from the beginning of the test until the bottoming-out of the component happens. When it comes to the protection of occupants, the load ratio is specially important, since strong variations in the crushing force can be transmitted through the crash boxes to the passenger compartment and exceed the acceleration tolerances of the passengers. With the aim of reducing the load ratio of crash boxes, indentations or triggers have been traditionally introduced. These consist of induced imperfections in the undeformed configuration of the box, which concentrate the stresses and deformations as the load starts to apply, thus reducing the initial peak force. Later in this chapter, it will be discussed the importance of triggers in order to guarantee that the desired collapse modes are developed.

As an illustration of the effect that triggering a metal profile has in the force-displacement curves, Figure 2.8 (taken from [26]) is offered, where a remarkable reduction of the initial peak force is achieved. Collapse-triggering mechanisms are present in modern crash boxes, as the one depicted in Figure 2.9. Sometimes the uniformity of the crush force is also referred to as crush force efficiency (*CFE*), defined as the inverse of the load ratio:

$$CFE = \frac{1}{LR}. \tag{2.17}$$

2.2.5 Stroke efficiency

When a crash box is axially crushed, folds are developed up to a crushing distance in which there is no more length available for folding. At this point, densification and bottoming-out causes that the force levels increase rapidly as the compressed absorber is now elastically loaded in compression (see ④ in Figure 2.6). If this distance is called δ_{max}, the stroke efficiency S_{E} is given as

$$S_{\mathrm{E}} = \frac{\delta_{\mathrm{max}}}{L}, \tag{2.18}$$

where L is the undeformed length of the crash box.

Therefore, the stroke efficiency measures how much length of the crash box is actually used up in energy absorption. This becomes a specially useful criterion

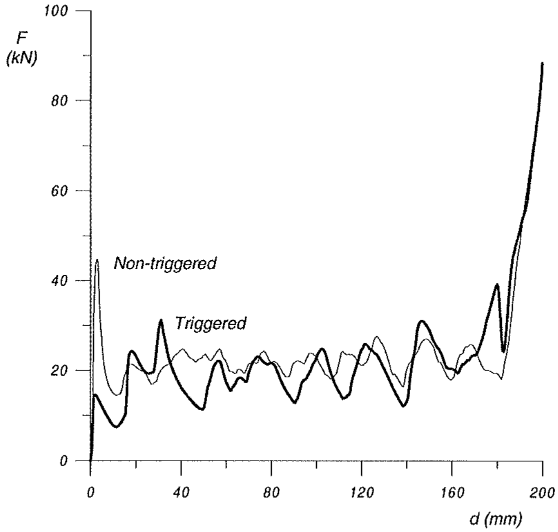

Figure 2.8: Force-displacement curves showing the difference in the initial peak load for triggered and non-triggered profiles, taken from [26].

Figure 2.9: Real life crash box with alternate indentations in the outer walls to trigger a stable crushing mechanism, courtesy of J. K. Holmen (SIMLab).

when spatial restrictions are present, as usually happens in the frontal parts of road vehicles.

Some values of stroke efficiency for several devices are presented in Figure 2.10, taken from [24].

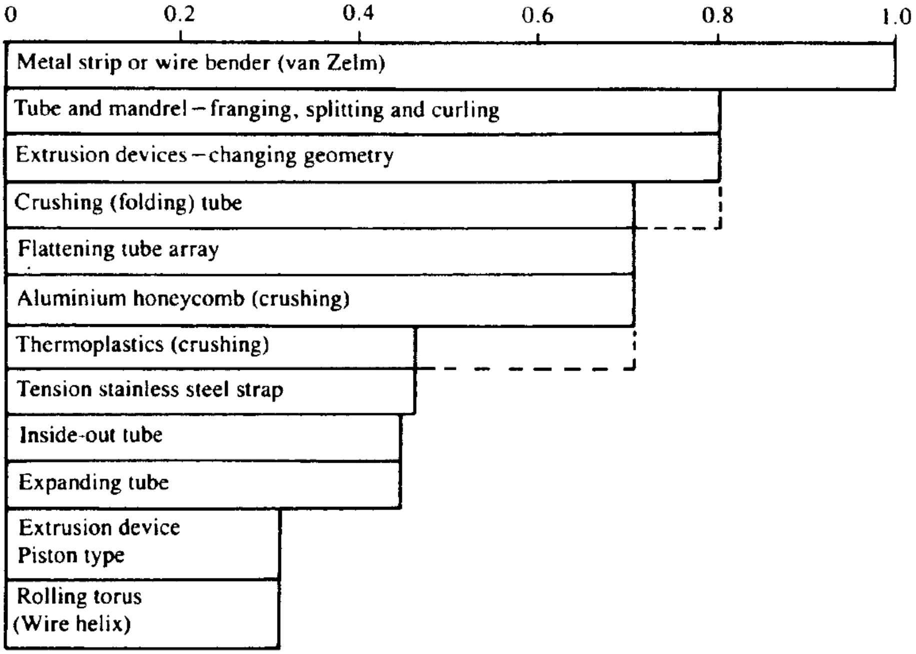

Figure 2.10: Stroke efficiencies for some energy absorbers [24].

2.2.6 Energy-absorbing effectiveness factor

This relatively recent indicator was proposed by Jones [27] in order to allow comparisons of the effectiveness of different designs made from different materials. The energy-absorbing effectiveness factor ψ is the ratio of the total energy absorbed by the system to the maximum energy up to failure of a normal tensile specimen made from the same volume of material (or compressive in the particular case of crushable foams or other cellular materials). Therefore, this criterion allows to estimate how efficiently the material in a crash box is being used in energy absorption.

2.3 Structural systems for impact energy absorption

In the previous section, various evaluation criteria were established to allow the assessment and comparison of different energy absorbers. This section offers a literature review of the main types of absorbers studied over the last 50 years, most notably thin-walled metal columns, fiber-reinforced plastic columns, fiber-reinforced metal tubes, extrusions filled with cellular materials (plastic or aluminum foams and cork agglomerates), and honeycombs.

2.3.1 Metal tubes: steel and aluminum

The capacity of metals to undergo severe plastic deformations and the simplicity of thin-walled tubes have made that axially-crushable metal tubular profiles have been vastly employed as crash boxes and impact energy absorbers in general. Countless studies have been carried out on the crashworthiness of these structures, depending on the geometrical properties of the system, the applied loads and the metal itself. These members have been traditionally built in steel or aluminum, and it is nowadays a matter of market prices and desired cost which makes designers to opt for one metal or another. They are usually employed behind car bumpers and train buffers, but also in aircraft, bases of elevator shafts, etc.

Circular tubes - theoretical models

Axially compressed circular metal tubes can undergo one of more of the following collapse modes:

- Global or Euler buckling.
- Concertina progressive collapse mode.
- Diamond progressive collapse mode.

Which of these three modes is developed under axial crushing depends on its diameter to thickness and length to wall thickness ratios. Global buckling is undesirable for energy absorption purposes since only a small part of the materials develops plasticity phenomena. Concertina and diamond collapse modes undergo local, progressive deformation patterns and more material is promoted to develop plastic deformations. Therefore, the absorbed energy is much higher.

Figure 2.11 provides a side view of the axial crushing of aluminum tubes with two different diameter to thickness ratios developing concertina and diamond collapse modes. The shape of the lobes in the diamond mode can vary depending on the geometry of the tube, but it usually consists of two alternate triangles (so that a top view looks like a hexagram).

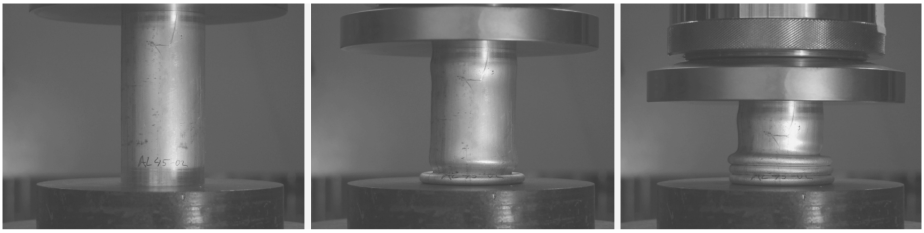

(a) Concertina collapse mode of an aluminum tube.

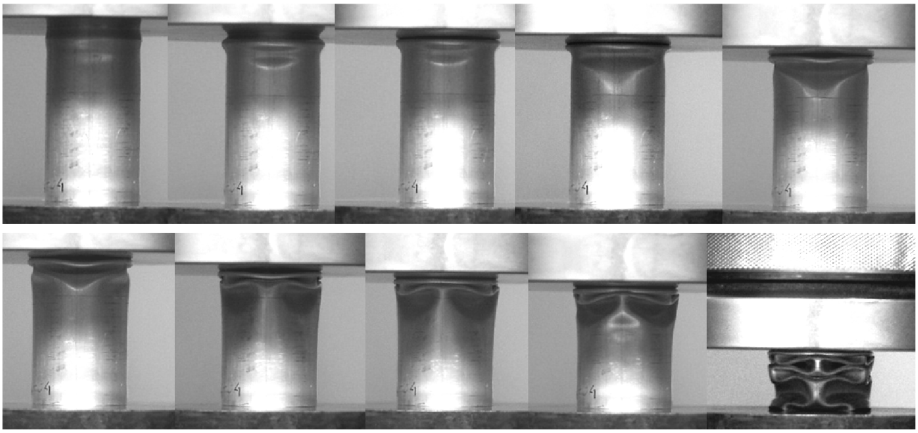

(b) Diamond collapse mode of an aluminum tube.

Figure 2.11: Collapse modes of thin-walled circular metal sections, source: [5].

The axial crushing of thin-walled circular tubes has been the focus of many theoretical studies since the beginning of the 20th century. To the author's knowledge, the first reference on the axial crushing of metal tubes dates from 1908 with a publication by Mallock [28], where the author described geometrically the three possible collapse modes for cylindrical metal sheets, i.e., concertina, two-lobe diamond and three-lobe diamond. This publication focused only on the collapse modes and did not provide any expression to calculate the mean crushing load (and therefore the absorbed energy) of the tubes. In 1958, Pugsley [29] proposed an early expression for the ratio of the mean crushing load to the initial peak load of mild steel and soft aluminum circular tubes undergoing a diamond collapse mode ($R/t > 50$), depending on the wall thickness t and the radius of the tube R. This first expression reads as

$$\frac{P_{\mathrm{m}}}{P_{\mathrm{peak}}} = 5\frac{t}{R} + 0.13, \tag{2.19}$$

where the initial peak load is obtained as $P_{\mathrm{peak}} = 2\pi R t \sigma_0$, where σ_0 is the yield stress for the wall material.

In 1960, an early work by Alexander [30] presented an approximate theoretical analysis for the axial crushing of circular tubes under three basic hypotheses:

- The metal is a perfect-plastic material.
- The tube folds according to the simplified antisymmetric collapse mode depicted in Figure 2.12, where the areas between the hinges behave rigidly.
- The developed hinges are stationary.

If these points are assumed, the principle of virtual works can be applied to calculate the mean crushing force P_{m}. If the collapse moment per unit circumferential length is called $M_0 = \sigma_0 t^2/4$, for an increment $\mathrm{d}\theta$ of the angle θ, the increment of bending work W_1 done by the hinges is

$$\mathrm{d}W_1 = M_0 \mathrm{d}\theta \left(2\pi D + 2\pi h \sin\theta\right). \tag{2.20}$$

Alexander assumed a plane strain state in the circumferential direction, which is actually only true for the upper and lower hinges in Figure 2.12 as long as no circumferential strain occurs there. He adopted the von Mises yield criterion and a plastic Poisson's ratio for isochoric plasticity ($\nu^{\mathrm{p}} = 1/2$). Thus, the plastic collapse moment M_0 reads as

$$M_0 = \frac{2}{\sqrt{3}} \sigma_{\mathrm{y}} t^2/4. \tag{2.21}$$

The middle hinges in Figure 2.12 suffer a circumferential strain which extends the metal between the hinges. For a $\mathrm{d}\theta$, the mean circumferential strain ε_θ is

$$\varepsilon_\theta = \frac{\pi\left(D + h\sin\left(\theta + \mathrm{d}\theta\right)\right) - \pi\left(D + h\sin\theta\right)}{\pi\left(D + h\sin\theta\right)} = \frac{h\mathrm{d}\theta\cos\theta}{D + h\sin\theta}. \tag{2.22}$$

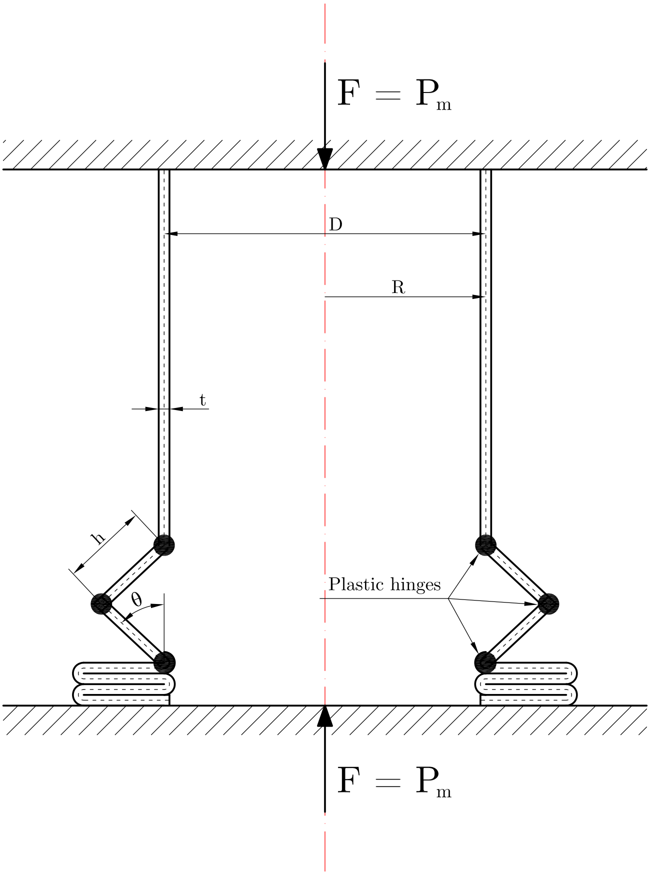

Figure 2.12: Alexander stationary hinge collapse model.

The incremental work done by this extension is

$$\mathrm{d}W_2 = \sigma_\mathrm{y}\varepsilon_\theta = \sigma_\mathrm{y}\frac{h\mathrm{d}\theta\cos\theta}{D + h\sin\theta}\pi\left(D + h\sin\theta\right)2ht = 2\pi\sigma_\mathrm{y}h^2t\mathrm{d}\theta\cos\theta. \tag{2.23}$$

If Equation (2.20) and Equation (2.23) are now summed and the incremental works for θ are integrated increasing from 0 to 90° (one complete fold), the total work W done in collapsing one convolution is obtained:

$$W = \int\left(\mathrm{d}W_1 + \mathrm{d}W_2\right) = \int_0^{\pi/2}\left[M_0 4\pi\left(D + h\sin\theta\right) + 2\pi\sigma_\mathrm{y}h^2t\cos\theta\right]\mathrm{d}\theta. \tag{2.24}$$

This must be made equal to the external work done by the mean force P_m. Alexander neglects here the space occupied by the wall thickness, making this external work equal to P_m multiplied by $2h$. Thus,

$$\frac{P_\mathrm{m}}{M_0} = \pi^2 \frac{D}{h} + 2i\pi + 2\pi\sqrt{3}\frac{h}{t}. \tag{2.25}$$

In the previous equation, $i = 1$ for the analyzed outward folding and $i = -1$ for the inward folding. Alexander obtained the folding length h by minimizing the value of the mean load in Equation (2.25), giving

$$h = \sqrt{\frac{\pi}{2\sqrt{3}}}\sqrt{Dt} = 0.952\sqrt{Dt}. \tag{2.26}$$

He assumed that the actual collapse mode lies somewhere in between the two modes (inward and outward folding), so he adopted the mean value of Equation (2.25) ($i = \pm 1$), i.e.

$$\frac{P_\mathrm{m}}{M_0} = \pi^2 \frac{D}{h} + 2\pi\sqrt{3}\frac{h}{t}. \tag{2.27}$$

Finally, if Equation (2.26) is introduced in Equation (2.27), the expression of the mean load results

$$\frac{P_\mathrm{m}}{M_0} = 20.73\sqrt{\frac{D}{t}}, \tag{2.28}$$

so the mean load becomes a function of the thickness t and diameter D exclusively.

In 1978, Pugsley reviewed his former work to account for the transition from diamond to concertina collapse mode [31], improving the description of the geometry of the folding process involved. A first approximate expression for the average crushing load in a diamond deformation mode was derived by T. Wierzbicki in 1983 [32], reading

$$\frac{P_\mathrm{m}}{M_0} = 86.14\sqrt[3]{\frac{D}{t}}. \tag{2.29}$$

Alexander's model for axisymmetric folding was later modified by Abramowicz and Jones [33] in 1984. Two essential enhancements were done:

- The circumferential strains depend now on the distance to the adjacent hinges.

- The effective crushing distance δ_{e} is introduced. It is obtained as $\delta_{\mathrm{e}} = 2h - 2x_{\mathrm{m}} - t$ (see Figure 2.13), where $x_{\mathrm{m}} \approx 0.28\,(h/2)$.

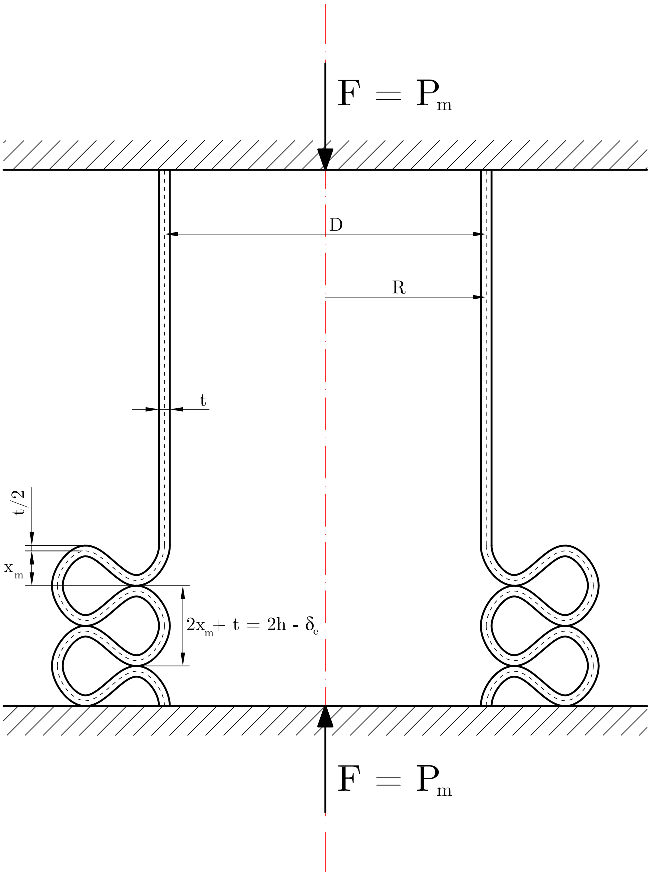

Figure 2.13: Abramowicz and Jones model.

Assuming the latter, Equation (2.26) and Equation (2.28) are rewritten as

$$h = 0.88\sqrt{Dt} \tag{2.30}$$

and

$$\frac{P_{\mathrm{m}}}{M_0} = \frac{20.79\sqrt{\dfrac{D}{t}} + 11.9}{0.86 - 0.568\sqrt{\dfrac{t}{D}}}. \tag{2.31}$$

An additional improvement was proposed in 1986 [34] to consider fold bending angles of $\theta > \pi$. The modifications led to the following expressions:

$$h = 0.893\sqrt{Dt} \tag{2.32}$$

and

$$\frac{P_{\mathrm{m}}}{M_0} = \frac{25.30\sqrt{\dfrac{D}{t}} + 14.7}{0.86 - 0.568\sqrt{\dfrac{t}{D}}}. \tag{2.33}$$

Even though Alexander's theory offers a good agreement with experimental data in general terms, it was reconsidered by Wierzbicki and Bhat [35] in 1986. These authors firstly described theoretically the movement of the plastic hinges along the shells, significantly improving the theoretical descriptions of the geometry of the folds. This enhancement led to the following expressions for the fold length and the mean load:

$$h = 1.335\sqrt{Dt} \tag{2.34}$$

and

$$\frac{P_{\mathrm{m}}}{M_0} = 30.5\sqrt{\frac{D}{t}}. \tag{2.35}$$

Wierzbicki et al. [36] proposed a last modification of the theory in 1992 with the introduction of what they called *super-folding elements*, which described the geometry of the folds with an improved degree of accuracy. This allows the folds to move inward and outward, offering values for the peak loads during the crushing. Even though this prediction is not very accurate, the introduction of the intermediate peaks is remarkably important. Final expressions are:

$$h = 1.31\sqrt{Dt} \tag{2.36}$$

and

$$\frac{P_{\mathrm{m}}}{M_0} = 31.74\sqrt{\frac{D}{t}}. \tag{2.37}$$

Many further extensions have been made by other authors [37–40], consisting of refinements of the theory to account for the periodical force-displacement responses, the hardening properties of the materials, the eccentricity of the folds, etc. What transpires for all of them[3] is the proportionality of the term P_m/M_0 to $\sqrt{D/t}$.

The dimensionless factors called *structural effectiveness* η_c and *solidity ratio* ϕ will be introduced here, which can help in the presentation and comparison of experimental data and theoretical predictions. These two ratios were proposed by Pugsley [42] in 1960. The former reads

$$\eta_\mathrm{c} = \frac{P_\mathrm{m}}{A\sigma_0}, \tag{2.38}$$

where A is the cross-sectional area of the thin-walled cross section. For a circular tube:

$$\eta_\mathrm{c} = \frac{P_\mathrm{m}}{2\pi R t \sigma_0}. \tag{2.39}$$

The solidity ratio is defined as

$$\phi = \frac{A}{\Omega}, \tag{2.40}$$

where Ω is the cross-sectional area enclosed by the middle line of the cross section. For a circular section,

$$\phi = \frac{2\pi R t}{\pi R^2} = \frac{2t}{R}, \tag{2.41}$$

given that $\Omega = \pi R^2$.

Using Equations (2.29) and (2.31), the structural effectiveness for concertina and diamond modes can be expressed as follows:

$$\eta_\mathrm{c}^\circ = \frac{P_\mathrm{m}}{2\pi R t \sigma_0} = \frac{3.36\,(1 + 0.29\sqrt{\phi})}{\dfrac{3.03}{\sqrt{\phi}} - 1} \tag{2.42}$$

and

$$\eta_\mathrm{c}^\star = 3.14\phi^{2/3}, \tag{2.43}$$

---

[3] A single exception was found in the experimental work by Guillow et al. [41], where the normalized mean force P_m/M_0 was stated to be proportional to $\sqrt[3]{D/t}$.

where η_c° and $\eta_c^\star$ are the structural effectiveness for concertina and diamond collapse modes, respectively. It is straightforward to check that $\eta_c^\star > \eta_c^\circ$ and thus, a diamond mode is more efficient in energy absorption than a concertina mode for the same ϕ, as will be seen in Figure 2.17.

Square tubes - theoretical models

Like circular tubes, the axial collapse mode of a square hollow section is determined by the ratio of the side width b to the wall thickness t. Three possible modes can be developed: an extensional mode (only for thick walls, $b/t < 7.5$), a symmetric mode (the most common, for $b/t > 40.8$), or an asymmetric mixed progressive buckling mode ($7.5 < b/t < 40.8$). The theoretical difference of the crushing forces of the latter two modes is so small that either one or another can be developed in a specimen with slight imperfections [24]. A representation of these collapse modes is provided in Figure 2.14.

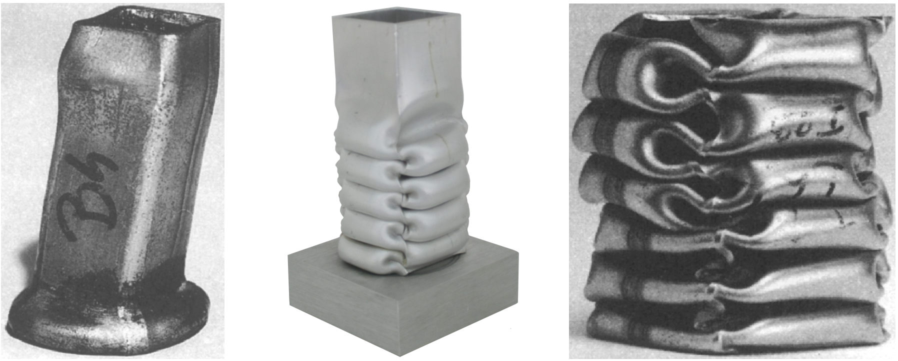
(a) Extensional mode. **(b)** Symmetric mode. **(c)** Asymmetric mixed mode.

Figure 2.14: Axial progressive collapse modes of thin-walled metal square tubes. Images (a) and (c) were taken from [24].

A theoretical procedure similar to the one presented for circular tubes can be followed for the analysis of thin-walled square tubes subjected to axial crushing. In 1983, Wierzbicki and Abramowicz [43] identified two basic collapse elements, namely types I and II (see Figure 2.15), whose combination can predict all the aforementioned mechanisms. Collapse element type I consists of adjacent inward and outward forming faces, so that the mid-line suffers no extension. Type II collapse elements consist of both faces moving outwards, and therefore the mid-line extends. It transpires that the necessary crushing force is greater for elements type II since larger deformations are present.

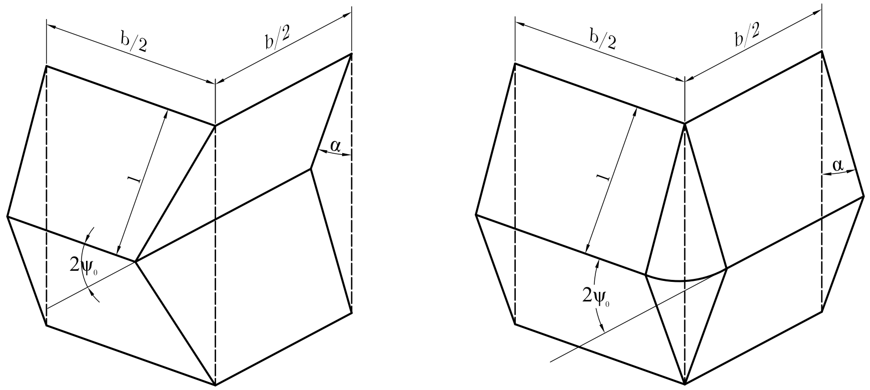

(a) Element type I (inextensional). **(b)** Element type II (extensional).

Figure 2.15: Basic collapse elements for thin-walled square sections [43].

The three collapse modes depicted in Figure 2.14 can be idealized with these basic collapse elements. This way, each lobe layer in the symmetrical mode is represented by four corner elements type I, while the extensional mode is modeled with four type II elements. Finally, the asymmetric mixed mode is represented by two adjacent layers of lobes made of seven type I elements and a single type II element. This is why the theoretical prediction of the mean crushing force for the latter mode is so similar to that predicted for the symmetrical mode. Given that the symmetrical mode is the most common, the theoretical development to obtain the mean crush force is only presented for this mode.

Like circular cross-sections, the mean crushing force is obtained by equating the internal energy needed to form a complete lobe with four type-I elements to the external work of the axial crushing force. This leads to

$$\frac{P_{\mathrm{m}}}{M_0} = 38.12\sqrt[3]{\frac{b}{t}}, \tag{2.44}$$

and, for the lobe length,

$$\frac{h}{t} = 0.99\left(\frac{b}{t}\right)^{2/3}. \tag{2.45}$$

Experimental work showed that the lobes do not close completely, so an effective crushing length L_{e} is introduced as

$$\frac{L_{\mathrm{e}}}{2h} = 0.73. \tag{2.46}$$

The mean crushing force can now be rewritten as

$$\frac{P_\mathrm{m}}{M_0} = 52.22\sqrt[3]{\frac{b}{t}}. \tag{2.47}$$

A word of caution has to be entered here: Wierzbicki and Abramowicz used the Tresca yield criterion for this development, thus $M_0 = \sigma_0 t^2/4$.

The structural effectiveness and the solidity ratio can be obtained as

$$\eta_\mathrm{s} = \phi^{2/3}, \tag{2.48}$$

where

$$\eta_\mathrm{s} = \frac{P_\mathrm{m}}{4bt\sigma_0} \tag{2.49}$$

and

$$\phi = \frac{A}{\Omega} = \frac{4t}{b}. \tag{2.50}$$

As a particular case of square sections, top and double-hat sections are frequently encountered in automotive body structural components. These sections consist of two cold-formed metal sheets usually assembled together by means of spot welds or rivets. They are easy to manufacture and very flexible in terms of dimensions and materials, advantages which usually overcome the inconvenience of a slightly lower specific energy absorption compared to regular square tubes [44, 45]. In 1988-1989, Mamalis et al. [46, 47] studied the inextensional collapse of thin plastic top-hat and double-hat structures. In 1999, White et al. [48] carried out a theoretical study supported by an extensive experimental campaign [44] to determine the mean crushing load P_m of top-hat and double-hat, spot-welded mild steel sections. The super-element theory was successfully applied here, leading to expressions of the same form than the previous ones. For the asymmetric collapse of top-hat sections, the authors proposed the following expression of the mean crushing load[4]:

$$\frac{P_\mathrm{m}}{M_0} = 32.89\left(\frac{S}{t}\right)^{1/3}, \tag{2.51}$$

---

[4] These expressions are valid only for perfectly rigid-plastic materials. For strain hardening materials, the reader is referred to [48].

where S is the total perimeter of the cross section, including flanges. For the lobe length, the authors proposed

$$\frac{h}{t} = 0.39 \left(\frac{S}{t}\right)^{2/3} . \tag{2.52}$$

For the asymmetric collapse of double-hat sections, the mean crushing force can be obtained as

$$\frac{P_{\mathrm{m}}}{M_0} = 52.20 \left(\frac{S}{t}\right)^{0.29} , \tag{2.53}$$

and the lobe length as

$$\frac{h}{t} = 0.247 \left(\frac{S}{t}\right)^{0.64} . \tag{2.54}$$

In [44], the authors also proposed an empirical expression for the structural effectiveness factor in terms of the solidity ratio valid for top and double-hat square sections, reading

$$\eta_{\mathrm{h}} = 0.57\phi^{0.63}. \tag{2.55}$$

Figure 2.16 [44] depicts the asymmetric collapse modes of top-hat and double-hat sections.

In 2006, Tarigopula et al. [45] conducted quasi-static and dynamic axial crushing tests on thin-walled high-strength steel square and top-hat sections. The authors proved that the theoretical expressions for the mean crushing force proposed by White et al. tend to over-predict the results produced in quasi-static and low-velocity impact tests. However, they are in good agreement with experiments conducted at high impact velocities.

Spot welding is the most usual bonding technique in the production of hat sections. The strength, location and number of spot welds has been proved to have a significant effect on the crashworthiness of top-hat and double-hat sections. Schneider and Jones [49] investigated the influence of the spot-weld failure on the crushing force of top-hat sections. Besides, the influence of the spacing between spot welds has been also studied in [45]. In this last work, the authors stated that if the spacing between the spot-welds was below a 10 % of the tube length, there was no additional improvement in the specific energy absorption. If the spacing was increased over 10 % of the tube length, separation of the material between the spot welds appeared and irregular folding patterns were developed.

(a) Asymmetric collapse of a top-hat profile.

(b) Asymmetric collapse of a double-hat profile.

Figure 2.16: Asymmetric collapse of top and double-hat profiles [44].

For comparative purposes, the structural effectiveness is plotted in Figure 2.17 for a circular section with both collapse modes, a square section collapsing under a symmetrical mode and a hat section collapsing under an asymmetrical mode. It can be concluded that $\eta_{\mathrm{c}}^{\star} > \eta_{\mathrm{c}}^{\circ} > \eta_{\mathrm{s}} > \eta_{\mathrm{h}}$.

Multi-cell tubes - theoretical models

The influence of the number of “corner elements” on the energy absorption of a tube has been proved in [43] and [50]. Therefore, a large number of authors investigated the crashworthiness of thin-walled sheet metal profiles with internal webs to increase their efficiency. These structural systems are referred to as «multi-cell tubes». A first experimental study dating back to 2000 [51] investigated the axial crushing of single and double-hat sections with internal flanges filled with aluminum foam and found an improvement of the specific energy absorption by about 20 %. In 2001, Chen and Wierzbicki [52] studied the axial crushing of empty and foam-filled multi-cell columns with single, double and triple inner cells. Once again, the super folding element theory was applied with a simple folding element consisting of three extensional triangular elements and three stationary hinge lines. For brevity, the reader is referred to [52] for a

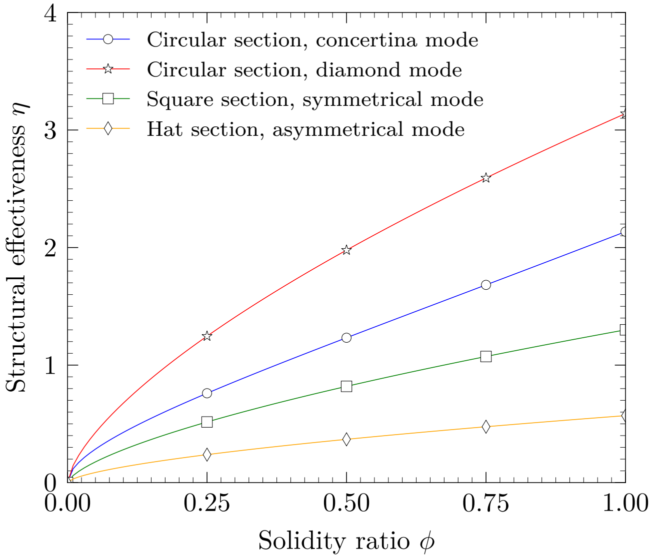

Figure 2.17: Comparison of the theoretical structural effectiveness of circular, square and hat tubes for $0 < \phi \leq 1$.

complete description of these elements and the collapse mechanism.

The expression provided for the mean axial crushing force of a multi-cell section with N contributing flanges, i.e., N half-lengths between corners in the cross section (14 for double-cell and 20 for triple-cell) reads

$$P_{\mathrm{m}} = \frac{2}{3}\sigma_0 t\sqrt{\pi N A}, \tag{2.56}$$

where A is the cross-sectional area. This expression accounts for an effective crush distance of 0.75 times the wavelength h, which can be obtained as

$$h = \sqrt{\frac{\pi S t}{N}}, \tag{2.57}$$

where S is the total length of the walls and internal webs of the cross section. For double-cell and a triple-cell sections, Equation (2.56) becomes

$$P_{\mathrm{m}}^{\mathrm{II}} = 9.89\sigma_0 b^{1/2} t^{3/2} \tag{2.58}$$

and

$$P_{\mathrm{m}}^{\mathrm{III}} = 12.94\sigma_0 b^{1/2} t^{3/2}, \tag{2.59}$$

respectively.

Regarding the specific energy absorption, the gain of the double and triple cell sections is about 15 % compared to the single cell, according to [52].

In 2002, this formulation was successfully applied to three new types of multi-cell designs [53], proving its reliability. In 2006, Zhang et al. [54] reviewed Chen's formulas and analyzed the contribution of the different parts of a multi-cell cross section to the energy absorption levels, this analysis being supported by finite element simulations. Multiple alternative designs were analyzed since the mid 2000s, including unequal cell sizes [55], cylindrical multi-cell sections [56], triangular multi-cell sections [57], or multi-cell sections filled with aluminum foam [58].

2.3.2 Composite materials

A considerable research effort has been shown in the use of fiber-reinforced plastics for crashworthiness applications due to their energy absorption characteristics, which are superior to those of metals. Nevertheless, a large number of variables determine the crushing behavior of these elements and, therefore, it is not a straightforward matter to understand and predict their crash performance. These variables include (and not limited to) the matrix and fiber materials, the stacking sequence and fiber orientation, the specimen geometry, the triggering mechanism and the loading conditions. The main issue here is that if some specific conditions regarding these variables are not fulfilled, the crash box will develop an unstable or even catastrophic failure mode resulting in very low energy absorption levels.

In 1982, Thornton and Edwards [59] compared the axial crushing behavior of cylindrical, square and rectangular section tubes fabricated using glass, graphite and aramid (Kevlar) prepregs. Graphite and glass tubes showed a progressive fracture of the material whereas aramid tubes collapsed in a more ductile way which recalled the collapse modes of metal tubes. A critical range of tube geometries was found over which stable collapses occurred, and thinner tubes tended to collapse in an unstable mode with lower energy absorption. Furthermore, the presence of aramid fibers in glass and carbon-epoxy tubes produced an unstable buckling of the tube. Farley [60] published a work in 1983 where the energy absorption of composite tubes made of materials similar to those in [59] was compared to aluminum tubes. The progressive folding mechanism associated with ductile aramid fibers was also reported. Farley also stated that the energy absorption of hybrid specimens (with different fiber materials together) were not significantly better than those of an equivalent single-fiber type. In 1986, Thornton [61] expanded this study putting the focus on the influence of the geometry, fiber orientation, triggering and section shape on the energy absorption of glass-fiber tubes. Also in 1986, Farley [62, 63] studied the influence of the material and geometrical properties of composite tubes, stating that the ultimate strains of the matrix material has a direct influence on the stability of the collapse mechanism, since higher ultimate strains avoid interlaminar cracking between layers and therefore improve the energy absorption. In 1987, Price and Hull [64] studied the axial crushing of fiberglass-polyester cones achieving high specific energy absorptions and concluding that no triggering was required to initiate stable collapse modes.

Hull [65] published a comprehensive work on the axial crushing of composite tubes, studying the influence of the aforementioned variables and classifying the developed collapse modes into three general ways: Euler buckling, shell buckling (progressive folding) and brittle fracture. The latter is the most common in carbon and glass reinforced thermosets, and offers very high levels of energy absorption if the correct trigger is used. Farley and Jones [66] agreed with Hull in reporting that tubes undergoing this brittle, progressive crushing mode exhibit a combination of two inner degradation mechanisms in the composite walls: the *splaying/lamina bending* and the *fragmentation/transverse shearing* crushing modes, as named in [65] and [66], respectively. The former, depicted in Figure 2.18a, consists of very long interlaminar, intralaminar and parallel-to-fiber cracks with a minimum or null fracture of axial laminar bundles. The energy is mainly dissipated by the crack growth. The latter, depicted in Figure 2.18b, exhibits a wedge-shaped end of the laminates, with short interlaminar and longitudinal cracks. The basic energy absorption mechanism here is the fracture of the lamina bundles. The represented laminates in Figure 2.18 consist of two outer layers of hoop-orientated fibers and an inner layer of axially orientated fibers (Figure 2.18a), and a glass cloth epoxy tube (Figure 2.18b).

It is generally accepted that the fragmentation mode usually results in higher energy absorptions. As an example, Table 2.2 [67] provides values of specific energy absorptions and failure modes for different carbon fiber reinforced epoxy tubes.

In 1992, Hamada et al. [68] compared the experimental energy absorption of carbon fiber tubes with different fiber orientations, achieving values up to 180 kJ/kg. In a later work [69], the authors put the focus on the description of the different stages during axial compression loading of carbon/PEEK (polyether ether ketone) tubes.

In the field of crashworthiness of composite structural systems, the works by Mamalis et al. include a large number of comprehensive studies on the crushing and energy absorption of glass and carbon fiber structures. These authors

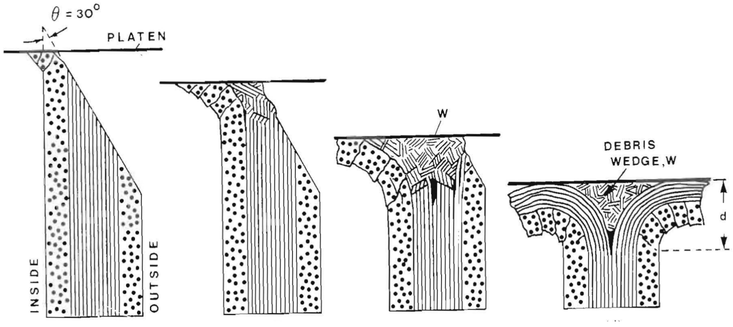

(a) Splaying.

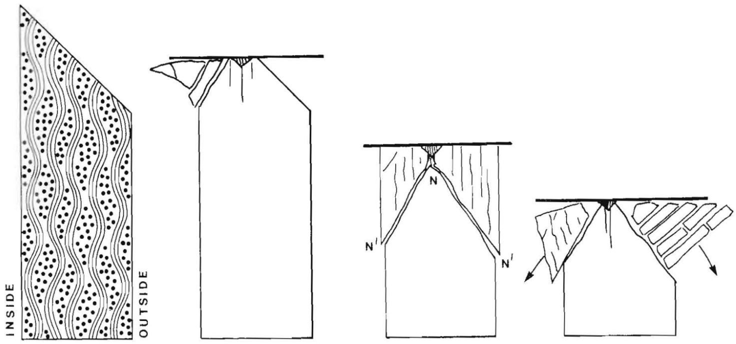

(b) Fragmentation.

Figure 2.18: Failure modes of composite laminates subjected to axial crushing [65].

Matrix failure strain	Lay-up	*SEA* [kJ/kg]	Failure mode
0.020	$[0/\pm15]_4$	125	Fragmentation
0.010	$[0/\pm15]_4$	94	Splaying
0.020	$[0/\pm45]_4$	85	Fragmentation
0.010	$[0/\pm45]_4$	69	Splaying
0.020	$[0/\pm75]_4$	74	Fragmentation
0.010	$[0/\pm75]_4$	54	Splaying

Table 2.2: Specific energy absorption and failure mode of different carbon fiber epoxy reinforced tubes, adapted from [67]. Lay-up angles quoted with respect to the longitudinal axis of the tube.

studied in 1992 the influence of the specimen geometry and crush speed on the specific energy absorption of glass fiber tubes with different matrix materials [70]. In 1994, Mamalis et al. [71] studied the axial crushing of glass fiber tubes at high strain rates focusing on the geometry, arrangement of fibers, material properties and stacking sequence. Stable and unstable failure modes were reported and expressions for the prediction of the mean crushing load are provided for cylindrical tubes and cones. The effect of strain rate was stated to be almost negligible. A design of a glass fiber automotive frame rail was proposed in 1996 [72], including a theoretical analysis. Also in 1996, these authors published two works [73, 74]. In the former, glass fiber square frusta are axially loaded at different strain rates in an experimental campaign. The conclusion of this study was that, if statically loaded, circular frusta are better for energy absorption. The second study proposed a theoretical model which accounts for the following four energy dissipation sources:

- Frictional resistance.
- Bending of the fronds.
- Internal cracking.
- Axial splitting between fronds.

The proposed equation consisted of the sum of the previous contributions, and some minor improvements were later provided in [74]. Mamalis and his coauthors published also remarkable works on the energy absorption of carbon fiber tubes, including an experimental campaign in 2004 focused on the quasi-static compression of square CFRP tubes [75], a comparison between static and dynamic crushing [76] and a finite element model for correlation in 2006 [77].

In the vein of early comparative studies, Jacob et al. [78] experimentally compared the crashworthiness of automotive structural systems made of chopped carbon fibers, graphite epoxy cross-ply laminates, a graphite/epoxy braided material system and a glass-reinforced continuous strand mat. The authors concluded that the chopped carbon fibers provided the best performance, but with a very high economical cost. In general, research works in the 2000's decade were also focused on the comparison of the collapse modes and energy absorption of carbon and glass fiber tubes, but usually including now a correlation of finite element models with experimental tests (see for example [79–83]). In general terms, carbon fiber tubes have been proved to exhibit higher levels of energy absorption than glass fiber structures.

2.3.3 Fiber-reinforced metal tubes

As described, fiber-resin composites usually have high strength to weight ratios compared to metals, but their crushing is typically dominated by brittle, unstable failure modes. A relatively recent advent of crashworthiness engineering is the design of externally-wrapped fiber-reinforced metal tubes. This way, the ductile metal crushing modes are combined with the high strength and brittle fracture of the fibers with no harm to the predictability or stability of the overall system. These designs have two main advantages compared to an only-metal structure [84]:

- Composite-metal structures are intended to reduce the weight of the structural member while keeping or improving the energy absorption and stiffness compared to metal structures.
- Extreme environmental conditions or minor shocks can cause some problems in metal structures. The composite wrapping acts as a coating and improves the durability of the system.

Even though composites are not considered, a research article from 1991 by Mamalis et al. [85] studied the axial crushing of bi-material tubes, not only to increase the force levels but also (and mainly) to provide a protective coating for the main metal member. PVC, aluminum cooper and high-strength steel were combined together in bi-material tubes, and the peak and mean crushing loads were analyzed. No statements concerning the specific energy absorption were made. The first theoretical study on the progressive axial crushing of externally reinforced fiber-metal tubes was published by Hanefi and Wierzbicki [86] in 1996, where the authors proposed a theoretical model based on Alexander's idealization for metal tubes [30]. The adopted crushing mechanism is depicted in Figure 2.19, and the reader is referred to [86] for the theoretical model itself.

Song et al. [87] carried out an experimental study on the axial crushing of composite-wrapped metal tubes and analyzed the influence of the composite thickness, ply orientation and metal properties on the crushing behavior. The theoretical model by Hanefi and Wierzbicki was improved to account for impact loadings. An important remark in this study was the fact that an unappropriated orientation of the composite materials led to brittle, unstable failure modes by delamination or fracture (see Figure 2.20). A further improvement of the model can be found in [88].

The axial crushing of GFRP externally-reinforced square aluminum sections was investigated by Shin et al. [89] in 2002. Further works by Bambach et al. studied the theoretical crushing of CFRP-wrapped square steel tubes [90],

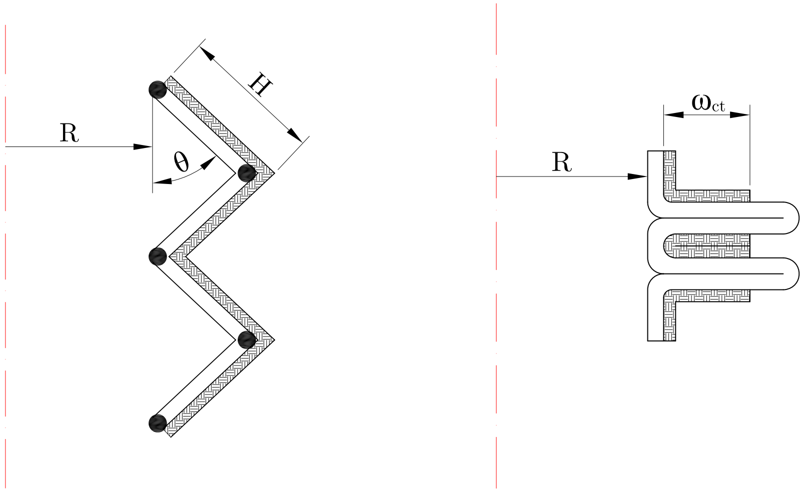

(a) **(b)**

Figure 2.19: Theoretical collapse mode of a composite-metal wall section of length 4H during collapse (a) and after collapse (b), according to [86].

provided some insightful experimental data for square hollow sections [91] and spot-welded [92] fiber-reinforced sections. The authors used here a digital image correlation (DIC) technique to analyze the deformation fields of the previous sections [93, 94] built in steel or aluminum. Lastly, aluminum-CFRP sections were recently investigated by Kim et al. [95].

The general conclusion is that both mean crushing load and specific energy absorption can be increased with this kind of external reinforcement, so that they are even higher than the sum of the two individual contributions of both materials acting separately.

2.3.4 Foam-filled sections

Foams used in energy absorption consist of a three-dimensional cellular structure which progressively collapses when crushed. They have been used extensively in the packaging industry due to their ability to be crushed with a constant force and their low weight. Two types of foam are predominant: metal and polymer foams. Although the former were not studied in the present work, their crucial importance makes it mandatory to include both in this literature review. Metal foams are made commonly by mixing organic beads into the liquid metal in an inert atmosphere. Then the metal cools down and solidifies, while the carbon burns off to leave a cellular matrix [6]. Polymer foams, on the other hand, are

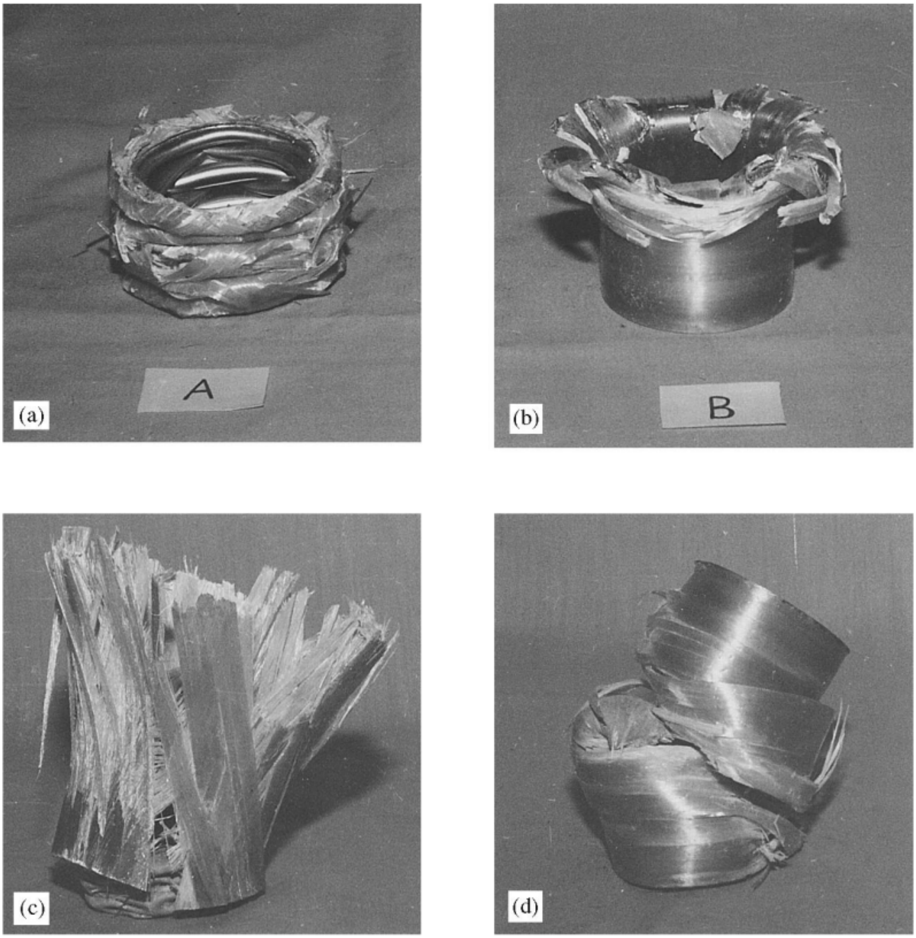

Figure 2.20: Typical collapse modes of compound tubes: (a) compound diamond, (b) compound fragmentation, (c) delamination and (d) catastrophic failure [87].

usually produced by blowing air bubbles into a hot polymer or a liquid monomer.

Foam-filled metal sections are a solution with potential use in structures dedicated to impact energy absorption. The foam substantially alters the crushing behavior of the outer thin-walled column compared to the empty extrusion, improving the energy absorption levels. This alteration is due to the fact that the foam filling acts as an “elastic” side constraint of the extrusion walls, reducing the buckling length and, therefore, allowing more lobes to be developed during the complete axial crushing. Figure 2.21, taken from [21], clearly depicts this phenomenon for empty and foam-filled square aluminum extrusions. Furthermore, the presence of the foam filling may also change the deformation mode in circular extrusions (see Figure 2.22).

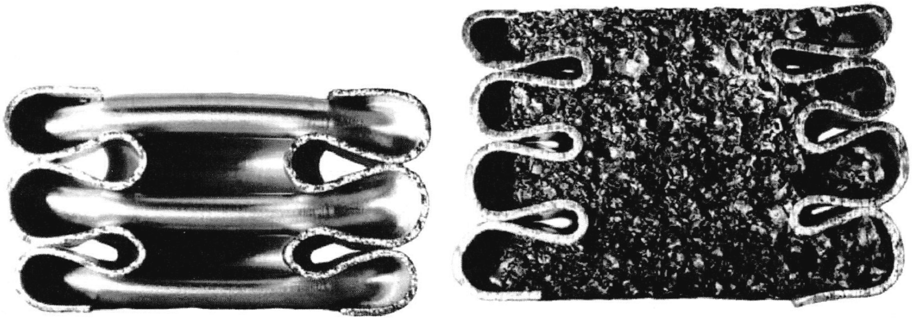

Figure 2.21: Non-filled vs. foam-filled square extrusion after quasi-static loading, taken from [21].

An early publication on this topic by Thornton [96] assumed that the mean collapse load of the foam-filled structure was determined simply from the separate contribution of the shell and foam, even though the author warned about its doubtful validity. The same assumption was made by Lampinen and Jeryan [97], leading to an underestimation of the average crush force. An enhancement of this approach was developed by Reid et al. [98] and Reid and Reddy [99] for straight and tapered mild steel tubes filled with polyurethane foam of different densities. Here, the authors modified the theoretical expressions for empty tubes by Wierzbicki and Abramowicz [43]. Another simplified theoretical formulation was published by Reddy and Wall [100] for foam-filled cylindrical shells. Abramowicz and Wierzbicki carried out a theoretical development also for foam-filled tubes with an arbitrary cross section [101], considering the coupling between the folding of tubes and the compression of foams. This theoretical approach was validated with the experimental results in [98]. First numerical simulations of the axial crushing of foam-filled extrusions arose in 1997 by Seitzberger et al. [102] with

Figure 2.22: Axial crushing of non-filled and foam-filled circular and square extrusions, quasi-static loading, taken from [21].

a good agreement with experimental results of the compression of steel tubes filled with aluminum foam. Singace and El-Sobky [103] investigated the crumpling of empty and foam-filled corrugated metal and PVC tubes. An increase of the mean load was produced, but no interaction was reported here between the foam and the profiles, given that the corrugation of the tubes pre-defined the collapse mode of the system.

In 1998, Langseth et al. [104] published the first extensive experimental campaign to assess the crash behavior of empty and foam-filled aluminum tubes with different tempers, thickness and foam densities, concluding that the specific energy absorption of the components increased with higher wall thicknesses and foam densities. Santosa and Wierzbicki [105] performed a numerical study on the crash behavior of box columns filled with aluminum foam or aluminum honeycomb, reporting a better performance of the latter but only for perfectly axially aligned loads.

To the author's knowledge, the most comprehensive studies on the quasi-static and dynamic axial crushing of foam-filled extrusions were published by Hanssen et al. from 1999 to 2001. Square aluminum extrusions filled with aluminum foam were investigated under quasi-static and dynamic loading in [26, 106], where the authors also provide a validated predictive formula for the mean crushing load accounting for the interaction effect:

$$F_{\mathrm{avg}} = F^0_{\mathrm{avg}} + \sigma_{\mathrm{f}} b_{\mathrm{i}}^2 + C_{\mathrm{avg}} \sigma_{\mathrm{f}}^{\alpha} \sigma_0^{(1-\alpha)} b_{\mathrm{m}}^{\beta} h^{(2-\beta)}, \tag{2.60}$$

where F_{avg} is the total average crushing force, F^0_{avg} is the average crushing force of the empty aluminum extrusion, σ_{f} is the yield stress of the aluminum foam, b_{i} is the inner diameter of the extrusion, σ_0 is the yield stress of the aluminum alloy, $b_{\mathrm{m}} = b - h$, and b and h are the outer diameter and wall thickness of the extrusion, respectively. Lastly, C_{avg}, α and β are parameters to be calibrated with experimental tests. Formulas for the peak force, crush force efficiency and stroke efficiency were also developed. Circular aluminum extrusions with aluminum foam filler were also investigated under the same conditions (statically and dynamically) in [107]. The interaction formulas were also validated here with simple modifications for the change in the geometry. An optimization of the square components was eventually published in 2001 [108], where the authors use a nonlinear algorithm on the theoretical formulas for quasi-static loading to improve the efficiency of the designs. They found that the optimal foam-filled designs displayed smaller cross-sections than the non-filled tubes, thus allowing reduction in mass, volume and length using aluminum foam.

In parallel, Santosa et al. [109] studied experimentally and numerically the previous designs and validated the interaction formulas. The experimental axial crushing of single and bi-tubal steel columns filled with aluminum foam was studied by Seitzberger et al. [110]. Bi-tubal foam-filled sections were proved to improve the specific energy absorption by up to 60 % compared to the mono-tubal profiles. A picture of some tested designs is presented in Figure 2.23. A similar investigation on empty and foam-filled multi-cell tubes was published by Chen and Wierzbicki [111].

Oblique impact on circular and square foam-filled sections was investigated by Børvik et al. [112] and Reyes et al. [113], respectively. The use of PVC [114] and polystyrene foams [115] as a filler for thin-walled aluminum tubes was studied using numerical and experimental analysis. Changes in the collapse modes of circular extrusions were reported as well. Lastly, foam-filled conical tubes were studied experimentally and numerically by Ahmad and Thambiratnam [116].

In the last 10 years, efforts were mainly focused on the optimization of foam-filled sections. Zarei and Kröger [117] optimized the crashworthiness of square hollow sections filled with aluminum foam or honeycomb using finite element simulations and surrogate models. A similar work was published in 2009 by Hou et al. [118]. Multi-tubular foam-filled structures were optimized by Bi et al. [119] and a series of research articles were published from 2011 to 2014 on the optimization of sections filled with graded foams [120], foam-filled conical

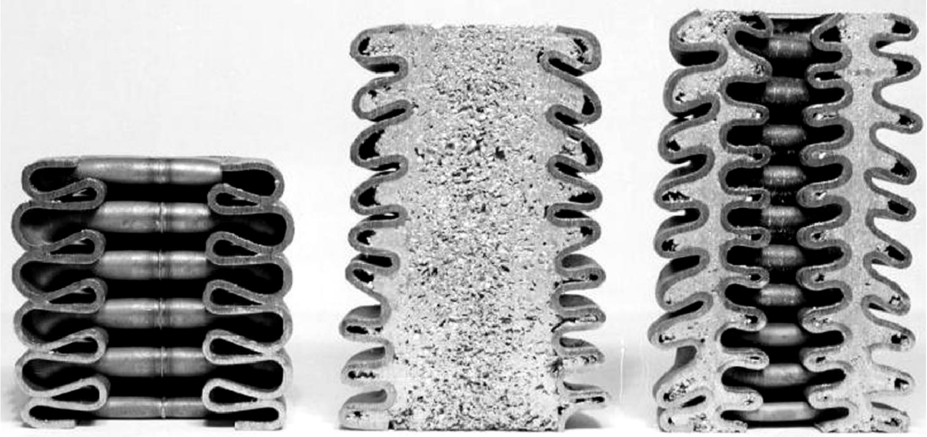

Figure 2.23: Comparison of the axial collapse of empty mono-tubal, foam-filled mono-tubal and foam-filled bi-tubal sections [110].

tubes [121], bi-tubal structures [122], tapered square tubes [123], and single and bi-tubal polygonal geometries [124].

Lastly, a paper by Lin et al. [125] was recently published where the authors combine a conical metal tube, a fiber reinforcement and a foam filler. This combination of materials is in line with the specimens studied in this thesis.

On the topic of energy absorption with cellular materials, some recent investigations have studied the possibility of filling the metal extrusions with natural or agglomerated cork [126]. This renewable material can dissipate the impact energy the same way foam does, with the drawback that a certain amount of energy is elastically stored and eventually released (spring-back effect). Cork-wall interactions and changes in deformation modes of the metal tube typical for foam-filled extrusions were also reported for cork-filled aluminum tubes by Gameiro and Cirne [127]. A cork-epoxy composite (see Figure 2.24) was also studied as a filler by Alcântara et al. with promising results [128].

Cork has also been applied to side-impact door protections, being studied in [129] and [130]. Of particular importance is the correct characterization of this complex material to be included in finite element simulations [131–133].

2.3.5 Honeycombs

The honeycomb structure, which can be seen as an extension of multi-cell tubes, is arguably one of the most extensively used energy absorbing structures in industry. They are placed inside automobile bumper bars, at the front of high-speed

Figure 2.24: Specimens of epoxy-cork composite, taken from [128].

trains locomotives or in a large number of aircraft structures. They are usually made of metals (being aluminum and steel the most common), but also thermoplastics, elastomers or molded polyolefin. The preferred shape is hexagonal, but a variety of geometries have been (and are being) investigated.

Honeycomb structures have been studied theoretically also by Wierzbicki [134], achieving a good agreement with experimental data. The behavior of honeycombs subjected to compressive loading resembles that of foams: an elastic loading followed by a stress plateau and a final densification phase. The plateau phase is produced by the progressive plastic collapse of the cells (metal honeycombs) or by the brittle fracture of the thin walls (rigid, brittle materials like some thermoplastics). The energy absorbing capability of honeycombs is ruled by the cell wall thickness, length, width and height.

The dynamic behavior of honeycomb sandwich panel was investigated by Yasui [135]. Zhao and Gary [136] used a Split-Hopkinson pressure bar (SHPB) with viscoelastic bars to study the dynamic response of aluminum honeycombs. They concluded that the strain rate effects were only remarkable in out-of-plane loading. The reader is referred to [137] for further details on the properties of honeycombs and cellular materials.

2.4 Computational analysis of energy absorbers

In the previous section, analytical models of the axial crushing of relatively simple structures have been described. However, these models have evident limitations, among others:

- Force oscillations during axial crushing are not reproduced fairly.
- Cross-sectional geometries are limited to simple, symmetric shapes.

- Analytical models cannot predict the highly complex collapse models undergone by most absorbers.
- Analytical models are unable to reproduce failure of structural bonding systems (spot welds, adhesives, etc.) which occurs in the real life.
- Oblique impact is difficult to reproduce in an analytical model.
- Inertial effects are extremely difficult to account for.
- The mechanical behavior of materials is much more complex than what is generally assumed for analytical models.

This section includes some considerations and guidelines arisen from the experience of many authors regarding the use of high-end finite element packages for the design and analysis of energy absorbers. Some advice by the author are provided as well, based on the experience with numerical models gathered with this thesis. Part of the following information can be found in the ABAQUS documentation [138].

Prior to the use of dynamic finite element codes, designers usually turn to specialized software based on analytical models. As an example, the code CRASH CAD (developed by Abramowicz [139]) provides a tool to predict the behavior of user-defined thin-walled metal cross sections under axial crushing and bending. In a second stage, the design can be run in a finite element code to obtain more detailed results. In this work, due to the complexity of the involved designs, the finite element simulations were run directly.

Finite element codes use either an implicit or explicit solution scheme, but only the latter can provide reliable and relatively fast results for problems involving extreme deformations, inertial effects and complex contact interactions. Implicit methods use time increments determined from accuracy and convergence criteria, without any size limitation. They take much larger time increments than explicit methods to solve a simulation, but the cost per increment is much higher since a complete set of equations must be solved in each increment. Because of that, very few authors have published on the energy absorption of structures using an implicit integration scheme. Karagiozova et al. [140] used ABAQUS/Standard in its 5.7 version for the numerical axisymmetric simulation of the crumpling of aluminum tubes. The assumption of axisymmetric collapse allowed here to analyze only a slice of the tube, thus easing the convergence of the model. Recently, Kazanc and Bathe [141] achieved good quality results using implicit time integration analyses in 3D crushing analysis, but this approach seems to work only with special 3D elements which can develop very large deformations.

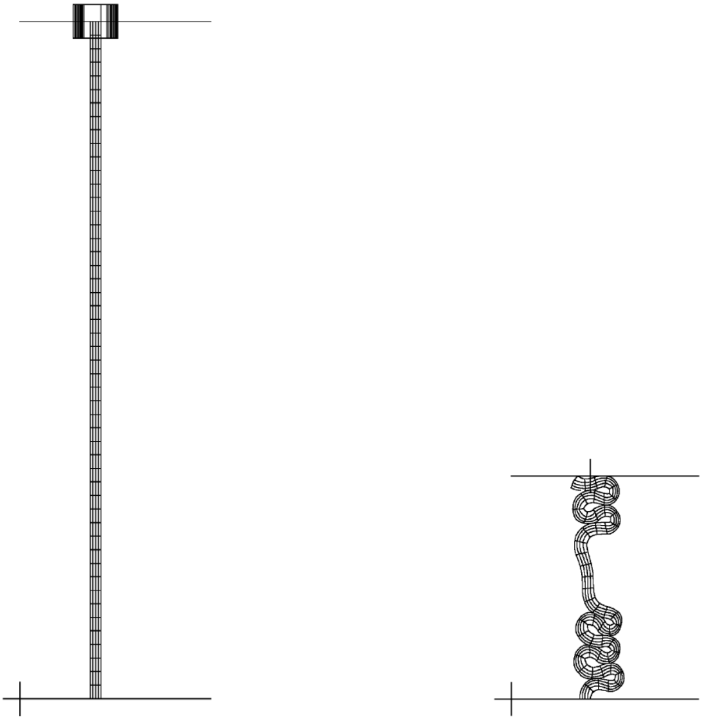

(a) Initial state **(b)** Final state

Figure 2.25: Axisymmetric implicit finite element model for the crush analysis of aluminum tubes [140].

On the other hand, explicit methods demand very small time increments whose size depends on the size and density of the elements but the cost of each increment is relatively small. In this thesis, ABAQUS/Explicit was used in its 6.12, 6.13 and 6.14 versions[5]. This code is specially suited for simulations involving inertia-dominated high-speed dynamic events, and problems with sudden stiffness changes or complex contacts. Therefore, it is specially useful to be used in the impact analysis of crash boxes.

The explicit method is based on the integration of the equations of motion, which at time increment n are given by

$$\mathbf{M}\mathbf{a}^n = \mathbf{f}^{\text{ext}}\left(\mathbf{u}^n, t^n\right) - \mathbf{f}^{\text{int}}\left(\mathbf{u}^n, t^n\right) = \mathbf{f}^n \tag{2.61}$$

---

[5] The ABAQUS version used by the author for this work has been upgraded every time a new release was issued. The consistency of the results was conveniently checked with each upgrade.

subject to

$$g_{\mathrm{I}}\left(\mathbf{u}^{n}\right)=0, \quad I=1,\dots,n_{\mathrm{c}}, \tag{2.62}$$

where $\mathbf{M}$ is the mass matrix, $\mathbf{a}$ are the nodal accelerations, $\mathbf{f}^{\mathrm{ext}}$ are the external nodal forces and $\mathbf{f}^{\mathrm{int}}$ are the internal nodal forces. Internal nodal forces arise from the resistance of the solid to deformation, i.e., they correspond to the stresses inside the material. On the other hand, external forces correspond to the externally applied loads. Both external and internal nodal forces are a function of nodal displacements $\mathbf{u}$ and time t. In Equation (2.62), g_{I} are the n_{c} boundary conditions and other constraints on the model. For a Lagrangian mesh, the mass matrix is constant and has to be built only once. Nodal accelerations are obtained at each time increment t^{n} from Equation (2.61) by doing

$$\mathbf{a}^{n}=\mathbf{M}^{-1}\mathbf{f}^{n}. \tag{2.63}$$

For the nodal accelerations to be obtained without solving any equation, the mass matrix $\mathbf{M}$ must be diagonal. A diagonal mass matrix M_{ij}^{D} can be easily obtained from a consistent mass matrix M_{ij}^{C} by, for example, the row-sum technique:

$$M_{ii}^{\mathrm{D}}=\sum_{j} M_{ij}^{\mathrm{C}}. \tag{2.64}$$

Diagonal mass matrix are often called *lumped mass matrix*. Given that the total momentum of the body with the diagonal mass is equal to that of the consistent mass, the former can be safely used to solve Equation (2.61).

ABAQUS/Explicit uses then a central difference integration scheme to obtain the nodal velocities and displacements from the nodal accelerations. This scheme is described next.

In the explicit method, the size of each time increment is variable in general in order to adapt the algorithm to mesh deformations and changes in the speed of the stress waves. Since a central difference integration method is employed here, it is useful to define the time increments considering their values at the half-increments too. For a simulation time $0 \leq t \leq t_{\mathrm{E}}$, where t_{E} is the total time of the simulation, subdivided in time increments Δt^{n}, $n=1,2,\dots,n_{\mathrm{T}I}$ with $n_{\mathrm{T}I}$ being the total number of increments, the time increments can be defined by

$$\Delta t^{n+1/2}=t^{n+1}-t^{n}, \tag{2.65a}$$

$$t^{n+1}=\frac{1}{2}\left(t^{n+1}+t^{n}\right), \tag{2.65b}$$

$$\Delta t^{n}=t^{n+1/2}-t^{n-1/2}. \tag{2.65c}$$

The central difference method implies that, once the dynamic equilibrium equations are satisfied at the beginning of the increment t^n, the accelerations obtained at t^n by Equation (2.63) are used to advance the velocity solution to time $t^{n+1/2}$ and the displacement solution to time t^{n+1}. In particular,

$$\mathbf{a}^n = \frac{\mathbf{v}^{n+1/2} - \mathbf{v}^{n-1/2}}{t^{n+1/2} - t^{n-1/2}} \implies \mathbf{v}^{n+1/2} = \mathbf{v}^{n-1/2} + \Delta t^n \mathbf{a}^n \tag{2.66}$$

and

$$\mathbf{v}^{n+1/2} = \frac{\mathbf{u}^{n+1} - \mathbf{u}^n}{t^{n+1} - t^n} \implies \mathbf{u}^{n+1} = \mathbf{u}^n + \Delta t^{n+1/2} \mathbf{v}^{n+1/2}. \tag{2.67}$$

It is important to remark that no iterations or tangent stiffness matrix are required in the explicit procedure, given that the internal forces vector $\mathbf{f}^{\text{int}}$ is assembled from contributions from the individual elements such that a global stiffness matrix need not to be formed. The use of a lumped mass matrix avoids simultaneous equations to be solved and reduces the required calculations to a minimum, where the nodal accelerations at a certain increment are obtained only using the nodal mass and the net acting forces. Then, velocities and displacements are obtained explicitly through time, i.e., the values at the end of an increment are computed using only the values at the start of the increment. These are the salient characteristics of an explicit method: the time integration of the discrete momentum equations does not require the solution of any system of equations at all. This is also why smaller time increments are required for a reliable solution.

The pseudo-code for an explicit time integration adapted from [142] is shown on pages 56 and 57. Here, damping is introduced by means of a viscous force $\mathbf{f}^{\text{damp}} = \mathbf{C}^{\text{damp}}\mathbf{v}$, so that the total force in Equation (2.63) is $\mathbf{f} - \mathbf{C}^{\text{damp}}\mathbf{v}$. Furthermore, the energy balance must be checked at integer time increments, so the velocity update is broken here into two sub-increments by

$$\mathbf{v}^n = \mathbf{v}^{n-1/2} + \left(t^n - t^{n-1/2}\right)\mathbf{a}^n, \quad \mathbf{v}^{n+1/2} = \mathbf{v}^n + \left(t^{n+1/2} - t^n\right)\mathbf{a}^n. \tag{2.68}$$

As can be seen from the aforementioned. code, an explicit method is easily implemented. Moreover, explicit time integration is very robust and the algorithms seldom abort due to failure of the numerical procedure. However, these advantages are paid with the conditional stability of the method: if the time increment exceeds a critical value Δt^{crit}, the solution will be unboundedly wrong. The stability limit for the central-difference operator is given by

$$\Delta t \leq \alpha \Delta t^{\text{crit}}, \quad \Delta t^{\text{crit}} = \frac{2}{\omega_{\max}}, \tag{2.69}$$

Pseudo-code for explicit time integration (adapted from [142])

```
1. Initial conditions and initialization:
      set $\mathbf{v}^0$, $\boldsymbol{\sigma}^0$, and initial values of other material state variables;
      $\mathbf{u}^0 = \mathbf{0}$, $n = 0$, $t = 0$; compute $\mathbf{M}$
2. Call getforce
3. Compute accelerations $\mathbf{a}^n = \mathbf{M}^{-1}\left(\mathbf{f}^n - \mathbf{C}^{\text{damp}}\mathbf{v}^{n-1/2}\right)$
4. Time update: $t^{n+1} = t^n + \Delta t^{n+1/2}$, $t^{n+1/2} = \frac{1}{2}\left(t^n + t^{n+1}\right)$
5. First partial update of nodal velocities:
      $\mathbf{v}^{n+1/2} = \mathbf{v}^n + \left(t^{n+1/2} - t^n\right)\mathbf{a}^n$
6. Enforce velocity boundary conditions:
      if node $I$ on $\Gamma_{v_i}$: $v_{iI}^{n+1/2} = \bar{v}_i\left(\mathbf{x}_I, t^{n+1/2}\right)$
7. Update nodal displacements: $\mathbf{u}^{n+1} = \mathbf{u}^n + \Delta t^{n+1/2}\mathbf{v}^{n+1/2}$
8. Call getforce
9. Compute $\mathbf{a}^{n+1}$
10. Second partial update of nodal velocities:
      $\mathbf{v}^{n+1} = \mathbf{v}^{n+1/2} + \left(t^{n+1} - t^{n+1/2}\right)\mathbf{a}^{n+1}$
11. Check energy balance at time increment $n+1$
12. Update counter: $n \longleftarrow n+1$
13. Output: if the simulation is not complete, go to 4.
```

Subroutine *getforce*

```
0. Initialization: $\mathbf{f}^n = \mathbf{0}$, $\Delta t_{\mathrm{crit}} = \infty$
1. Compute global external forces $\mathbf{f}^{\mathrm{ext},n}$
2. Loop over elements $e$
    i. Gather element nodal displacements and variables
    ii. $\mathbf{f}^{\mathrm{int},n} = \mathbf{0}$
    iii. Loop over integration points $\boldsymbol{\xi}_Q$
        1. If $n = 0$, go to 4
        2. Compute measures of deformation: $\mathbf{D}^{n-1/2}\left(\boldsymbol{\xi}_Q\right)$, $\mathbf{F}^n\left(\boldsymbol{\xi}_Q\right)$, $\mathbf{E}^n\left(\boldsymbol{\xi}_Q\right)$
        3. Compute stress $\boldsymbol{\sigma}^n$ by constitutive equation
        4. Compute $\mathbf{f}^{\mathrm{int},n}$ by relevant equation
    iv. Compute $\mathbf{f}^{\mathrm{ext},n}$
    v. $\mathbf{f}_e^n = {\mathbf{f}^{\mathrm{ext},\ n}}_e - {\mathbf{f}^{\mathrm{int},n}}_e$
    vi. Compute ${\Delta t^{\mathrm{crit}}}_e$, if ${\Delta t^{\mathrm{crit}}}_e < \Delta t^{\mathrm{crit}}$ then $\Delta t^{\mathrm{crit}} = {\Delta t^{\mathrm{crit}}}_e$
    vii. Scatter $\mathbf{f}_e^n$ to global $\mathbf{f}^n$
3. $\Delta t = \alpha \Delta t^{\mathrm{crit}}$
```

where ω_{max} is the highest natural frequency of the undamped system and α is a reduction factor, called the Courant number [143], that accounts for the destabilizing effects of nonlinearities and is usually in the range $0.8 \leq \alpha \leq 0.98$ An approximation to the stability limit can be written as the smallest transit time of a stress wave across the smallest element in the mesh, i.e.

$$\Delta t^{\mathrm{crit}} \approx \frac{L_{\mathrm{min}}}{c_{\mathrm{d}}}, \tag{2.70}$$

where L_{min} is the smallest element dimension in the model and c_{d} is the stress wave speed. This speed is obtained as

$$c_{\mathrm{d}} = \sqrt{\frac{\widehat{\lambda} + 2\widehat{\mu}}{\rho}}, \tag{2.71}$$

where ρ is the material density and $\hat{\lambda}$ and $\hat{\mu}$ are the effective Lamé's constants (see [138]). For an isotropic, elastic material the effective Lamé's constants can be defined in terms of Young's modulus E, and Poisson's ratio ν by

$$\hat{\lambda} = \lambda_0 = \frac{E\nu}{(1+\nu)(1-2\nu)} \tag{2.72}$$

and

$$\hat{\mu} = \mu_0 = \frac{E}{2(1+\nu)}. \tag{2.73}$$

Putting everything together, it can be seen that the stable time increment, without damping, can be estimated by

$$\Delta t \leq \min\left\{ L_{\mathrm{e}} \sqrt{\frac{\rho}{\hat{\lambda} + 2\hat{\mu}}} \right\}, \tag{2.74}$$

where L_{e} is the characteristic element length.

An energy balance can be performed to detect instabilities caused by an excessively large time increment. This balance consists of a simple check of the energy conservation, which requires that the external energy W_{ext} equals the internal energy W_{int} plus the kinetic (inertial) energy W_{kin} or, in a more numerically oriented way,

$$|W_{\mathrm{kin}} + W_{\mathrm{int}} - W_{\mathrm{ext}}| \leq \varepsilon_{\mathrm{tol}} \max\left(W_{\mathrm{ext}}, W_{\mathrm{int}}, W_{\mathrm{kin}}\right), \tag{2.75}$$

where $\varepsilon_{\mathrm{tol}}$ is a small tolerance, on the order of 10^{-2} [142]. The internal and external energies are integrated by a simple trapezoidal rule:

$$\begin{aligned} {W_{\mathrm{int}}}^{n+1} &= {W_{\mathrm{int}}}^{n} + \frac{\Delta t^{n+1/2}}{2} \left(\mathbf{v}^{n+1/2}\right)^{\mathrm{T}} \left(\mathbf{f}^{\mathrm{int},n} + \mathbf{f}^{\mathrm{int},n+1}\right) \\ &= {W_{\mathrm{int}}}^{n} + \frac{1}{2}\Delta\mathbf{u}^{\mathrm{T}} \left(\mathbf{f}^{\mathrm{int},n} + \mathbf{f}^{\mathrm{int},n+1}\right) \end{aligned} \tag{2.76}$$

and

$$\begin{aligned} {W_{\mathrm{ext}}}^{n+1} &= {W_{\mathrm{ext}}}^{n} + \frac{\Delta t^{n+1/2}}{2} \left(\mathbf{v}^{n+1/2}\right)^{\mathrm{T}} \left(\mathbf{f}^{\mathrm{ext},n} + \mathbf{f}^{\mathrm{ext},n+1}\right) \\ &= {W_{\mathrm{ext}}}^{n} + \frac{1}{2}\Delta\mathbf{u}^{\mathrm{T}} \left(\mathbf{f}^{\mathrm{ext},n} + \mathbf{f}^{\mathrm{ext},n+1}\right), \end{aligned} \tag{2.77}$$

where $\Delta\mathbf{u}^{\mathrm{T}} = \mathbf{u}^{n+1} - \mathbf{u}^{n}$. The kinetic energy is given by

$${W_{\mathrm{kin}}}^{n} = \frac{1}{2}(\mathbf{v}^{n})^{\mathrm{T}}\mathbf{M}\mathbf{v}^{n}, \tag{2.78}$$

being obtained at an integer time increment. This is the reason why the velocity update was broken into two sub-increments in Equation (2.68).

ABAQUS Explicit can automatically update the stable time increment along an analysis, in a similar way to the end statement of the subroutine *getforce*, on page 57. In the following example, a finite element model simulated the axial crushing of an AA6063-T5 circular aluminum extrusion at 10 m/s, whose deformed configuration is depicted in Figure 2.26. Values of the internal, external and kinetic energies during the analysis are plotted in Figure 2.27, and the evolution of the stable time increment is provided in Figure 2.28. The stable time increment decreases as more severe mesh deformations take place. In this case, the maximum error in the energy balance expressed in Equation (2.75) was 1.1 %.

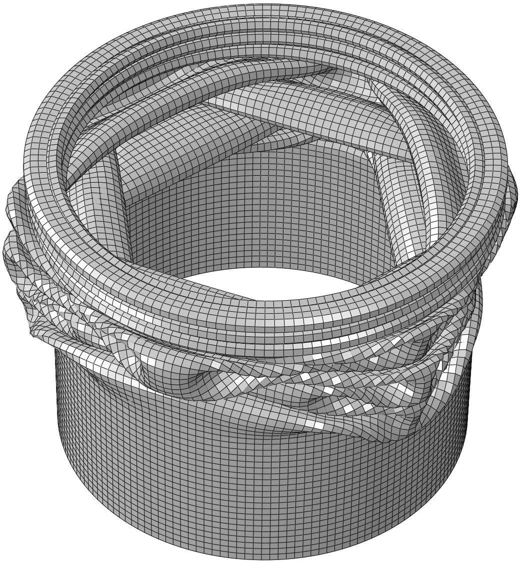

Figure 2.26: Finite element model of an axially crushed AA6063-T5 aluminum circular column.

The explicit method is computationally attractive for problems where the total dynamic response time that must be analyzed is only a few orders of magnitude longer than the stability limit. This limit, for the problems concerned in the present work, is usually between 10^{-8} and 10^{-6} seconds. The dynamic axial crushing of a crash box at 10 m/s can take around 30 milliseconds. However, quasi-static responses have to be analyzed as well, and real experimental

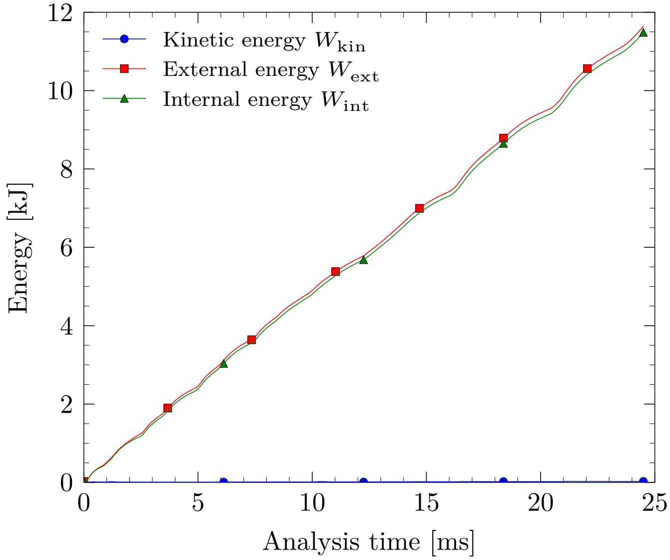

Figure 2.27: Evolution of the internal, external and kinetic energies during the impact simulation of an axially-crushed cylinder.

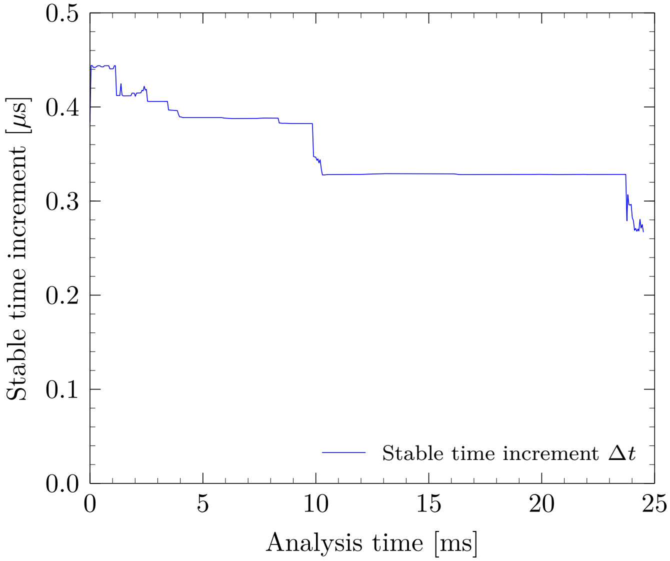

Figure 2.28: Evolution of the stable time increment during the simulation of the axial crushing of a cylinder under impact conditions.

tests can take several minutes. This would lead to an extremely large number of increments and therefore, the resultant error would be too high. Furthermore, the simulation could take too long (for the models developed in this thesis, two or three months could be required). Two techniques can be applied in order to reduce the computational cost of these analyses and improve their accuracy: time scaling and mass scaling.

Time scaling consists of increasing the loading rate of the analysis. This reduces the time scale of the process so that fewer increments are necessary (e.g. a quasi-static compression test can be simulated in $0.5\,\mathrm{s}$). Special care must be taken with strain-rate sensitive materials, since their corresponding strain-rate parameters must be scaled by the same factor. Time scaling can be done up to a limit where inertial effects come into play. This limit will be recalled later.

Mass scaling has a similar effect, but obtained by increasing the material densities. This way, the stable increment increases (see Equations (2.70) and (2.71)) and a reduced number of increments is required to complete the simulation. Mass scaling allows processes to be modeled in their natural time scale when considering rate-sensitive materials. Artificially increasing the material density by a factor of f increases the stable time increment by a factor of $\sqrt{f}$. This can be done up to a certain limit, as well.

The aforementioned scaling limits are usually given by experience or convergence tests, but some simple rules (particularized here for the quasi-static analysis of energy absorbers) can be followed to obtain reliable results. A first rule related to the loading rate consists of ramping up the load velocity smoothly from zero over part of the analysis step. If the crash box is compressed by a rigid plate, for example, a constant speed of the plate from the beginning of the test can result in a sudden impact load onto the deformable body of the crash box. This induces the propagation of a stress wave through the model and produces undesired results, since inertial effects cause increased resistance to initial deformation producing a steep initial slope in the force-displacement curve. Besides, localized buckling near the applied load (typical in dynamic analysis) can be developed. By ramping up the speed, e.g, during the first half of the analysis, the initial contact between the loading plate and the component is soft enough to avoid stress waves to be propagated.

Mass scaling has the same influence on inertia effects as artificially increasing the loading rates, thus, excessive mass scaling can lead to erroneous solutions. Again, a convergence test is recommended in which increasing mass scaling factors are applied to the model until results start to differ significantly. The undesired effects are the same as those produced by an excessive time scaling factor. An additional word of caution has to be entered here regarding multi-material crash boxes, like the ones studied in this thesis. Different mass scaling factors can be applied to different materials, which means that higher factors can be applied to the stiffest or lightest parts. If we think, for example, of the quasi-static analysis of a metal tube internally reinforced with GFRP plates, the composite part will determine the stable time increment of the overall model due to its lightness and stiffness, under the assumption that the element sizes are similar for both materials. One could think about scaling the mass of the GFRP parts so that the simulation speeds up. However, if this is done an inconvenience will arise, as GFRP is a fragile material, which implies sudden fractures releasing an important part of previously stored elastic energy. When fracture starts to occur, dislodged GFRP fragments will be propelled in random directions, some of them hitting the outer tube, the action-reaction plates or other GFRP parts. If a mass scaling factor was applied, these fragments will acquire a high kinetic energy and damage the impacted parts, producing severe deformations in the tube or GFRP parts or erroneous records of reaction force if they impact the reaction plate. This is even more dangerous in designs like the one studied in Chapters 5 and 6, where the GFRP is surrounded by foam. Dislodged fragments can generate extreme distortions in the foam part which will become a challenge for the overall convergence of the model. Therefore, mass scaling must be applied carefully when fragile parts are present in the model.

A common rule to estimate the maximum time or mass scaling a model can assume consists of checking the energy balance. It is generally assumed that if the kinetic energy of the model remains under the 5 % of the total energy, then the analysis can be considered to be quasi-static. However, this does not exclude the necessity of checking the simulation for undesired effects, like the ones previously described in this section.

Regarding the global accuracy, the central difference method is second order in time, which means that the truncation error is of the order Δt^2 in displacements. This is almost equivalent to state that this error is of the order h^2 for linear elements, where h is the element size (see [142] for details). Special care must be taken for simulations requiring a very large number of increments since cumulative errors could be large. Even though simulations for this thesis do not usually exceed the recommended limit of 2 000 000 increments, all analyses were run in double precision to avoid inaccuracies due to this fact.

All the present work has been done using finite element models with linear solid and shell elements, which are the only available in ABAQUS Explicit up to date. One of the reasons why higher order elements are still not available for explicit analysis in most commercial finite element codes is linked to the requirement of a diagonal matrix. When the lumped matrix for high-order elements is built, most of the mass is lumped at the center node(s), which causes rather strange behavior when high-order modes are excited. Therefore, linear elements are usually preferred.

References

[5] J. De Kanter. “Energy absorption of monolithic and fibre reinforced aluminium cylinders”. PhD thesis. Faculty of Aerospace Engineering - Delft University of Technology, 2006.

[6] G. Nagel. “Impact and energy absorption of straight and tapered rectangular tubes”. PhD thesis. School of Civil Engineering, Queensland University of Technology, 2005.

[21] M. Langseth. *Lecture notes on impact dynamics.* Structural impact laboratory, NTNU, Trondheim (Norway), 2005.

[22] H. W. Henn. “Crash tests and the head injury criterion”. *Teaching mathematics and its applications* 17.4 (1998), pp. 162–170.

[23] G. Lu and T. X. Yu. *Energy absorption of structures and materials.* Woodhead Publishing, Cambridge (UK), 2003.

[24] N. Jones. *Structural Impact.* Second edition. Cambridge University Press, Cambridge (UK), 2011.

[25] K.-H. Lin and G. T. Mase. “An assessment of add-on energy absorbing devices for vehicle crashworthiness”. *Journal of Engineering Materials and Technology, Transactions ASME* 112.4 (1990), pp. 406–411.

[26] A. Hanssen, M. Langseth, and O. Hopperstad. “Static and dynamic crushing of circular aluminum extrusions with aluminum foam filler”. *International Journal of Impact Engineering* 24.5 (2000), pp. 475–507.

[27] N. Jones. “Energy-absorbing effectiveness factor”. *International Journal of Impact Engineering* 37.6 (2010), pp. 754–765.

[28] A. Mallock. “Note on the instability of tubes subjected to end pressure, and on the folds in a flexible material”. *Proceedings of the Royal Society of London. Series A, Containing Papers of a Mathematical and Physical Character* 81.549 (1908), pp. 388–393.

[29] A. Pugsley. “The large-scale crumpling of cylindrical columns”. *The Quarterly Journal of Mechanics and Applied Mathematics* 13.1 (1958), pp. 1–9.

[30] J. M. Alexander. “An approximate analysis of the collapse of thin cylindrical shells under axial loading”. *Quarterly Journal of Mechanics and Applied Mathematics* 13.1 (1960), pp. 10–15.

[31] A. Pugsley. “On the crumpling of thin tubular struts”. *The Quarterly Journal of Mechanics and Applied Mathematics* 32.1 (1979), pp. 1–7.

[32] T. Wierzbicki. *Optimum design of integrated front panel against crash.* Tech. rep. Report for Ford Motor Company, Vehicle Dept., 1983.

[33] W. Abramowicz and N. Jones. “Dynamic axial crushing of circular tubes”. *International Journal of Impact Engineering* 2.3 (1984), pp. 263–281.

[34] W. Abramowicz and N. Jones. “Dynamic progressive buckling of circular and square tubes”. *International Journal of Impact Engineering* 4.4 (1986), pp. 243–270.

[35] T. Wierzbicki and U. Bhat. “A moving hinge solution for axysimmetric crushing of tubes”. *International Journal of Mechanical Sciences* 83.3 (1986), pp. 135–151.

[36] T. Wierzbicki, U. Bhat, and W. Abramowicz. “Alexander revisited - A two folding elements model of progressive crushing of tubes”. *International Journal of Solids and Structures* 29.24 (1992), pp. 1269–1288.

[37] R. Grzebieta. “An alternative method for determining the behaviour of round stocky tubes subjected to an axial crush load”. *Thin-Walled Structures* 9.1-4 (1990), pp. 61–89.

[38] A. Singace, H. Elsobky, and T. Reddy. “On the eccentricity factor in the progressive crushing of tubes”. *International Journal of Solids and Structures* 32.24 (1995), pp. 3589–3602.

[39] A. Singace and H. Elsobky. “Further experimental investigation on the eccentricity factor in the progressive crushing of tubes”. *International Journal of Solids and Structures* 33.24 (1996), pp. 3517–3538.

[40] N. Gupta and R. Velmurugan. “An analysis of axi-symmetric axial collapse of round tubes”. *Thin-Walled Structures* 22.4 (1995), pp. 261–274.

[41] S. Guillow, G. Lu, and R. Grzebieta. “Quasi-static axial compression of thin-walled circular aluminium tubes”. *International Journal of Mechanical Sciences* 43.9 (2001), pp. 2103–2123.

[42] A. Pugsley. “The crumpling of tubular structures under impact conditions”. *Proceedings of the Symposium on the use of aluminium in railway rolling stock* (1960), pp. 33–41.

[43] T. Wierzbicki and W. Abramowicz. “On the crushing mechanics of thin-walled structures”. *Journal of Applied Mechanics* 50.4a (1983), pp. 727–734.

[44] M. White and N. Jones. “Experimental quasi-static axial crushing of top-hat and double-hat thin-walled sections”. *International Journal of Mechanical Sciences* 41.2 (1999), pp. 179–208.

[45] V. Tarigopula, M. Langseth, O. Hopperstad, and A. Clausen. “Axial crushing of thin-walled high-strength steel sections”. *International Journal of Impact Engineering* 32.5 (2006), pp. 847–882.

[46] A. Mamalis, D. Manolakos, G. Vieghlan, and W. Johnson. “On the crumpling of thin plastic closed top-hat sections by compressive loadings”. *International Journal of Vehicle Design* 9.6 (1988), pp. 675–685.

[47] A. Mamalis, D. Manolakos, G. Vieghlan, and S. Minarecioglou. “The inextensional axial collapse of thin plastic double top-hat sections”. *International Journal of Vehicle Design* 10.3 (1989), pp. 269–279.

[48] M. White, N. Jones, and W. Abramowicz. “A theoretical analysis for the quasi-static axial crushing of top-hat and double-hat thin-walled sections”. *International Journal of Mechanical Sciences* 41.2 (1999), pp. 209–233.

[49] F. Schneider and N. Jones. “Influence of spot-weld failure on crushing of thin-walled structural sections”. *International Journal of Mechanical Sciences* 45.12 (2003), pp. 2061–2081.

[50] W. Abramowicz and T. Wierzbicki. “Axial crushing of multicorner sheet metal columns”. *Journal of Applied Mechanics, Transactions ASME* 56.1 (1989), pp. 113–120.

[51] W. Chen and D. Nardini. “Experimental study of crush behaviour of sheet aluminium foam-filled sections”. *International Journal of Crashworthiness* 5.4 (2000), pp. 447–468.

[52] W. Chen and T. Wierzbicki. “Relative merits of single-cell, multi-cell and foam-filled thin-walled structures in energy absorption”. *Thin-Walled Structures* 39.4 (2001), pp. 287–306.

[53] H.-S. Kim. “New extruded multi-cell aluminum profile for maximum crash energy absorption and weight efficiency”. *Thin-Walled Structures* 40.4 (2002), pp. 311–327.

[54] X. Zhang, G. Cheng, and H. Zhang. “Theoretical prediction and numerical simulation of multi-cell square thin-walled structures”. *Thin-Walled Structures* 44.11 (2006), pp. 1185–1191.

[55] A. Alavi Nia and M. Parsapour. “An investigation on the energy absorption characteristics of multi-cell square tubes”. *Thin-Walled Structures* 68 (2013), pp. 26–34.

[56] Z. Tang, S. Liu, and Z. Zhang. “Analysis of energy absorption characteristics of cylindrical multi-cell columns”. *Thin-Walled Structures* 62 (2013), pp. 75–84.

[57] T. Tran, S. Hou, X. Han, W. Tan, and N. Nguyen. “Theoretical prediction and crashworthiness optimization of multi-cell triangular tubes”. *Thin-Walled Structures* 82 (2014), pp. 183–195.

[58] H. Yin, G. Wen, Z. Liu, and Q. Qing. “Crashworthiness optimization design for foam-filled multi-cell thin-walled structures”. *Thin-Walled Structures* 75 (2014), pp. 8–17.

[59] P. Thornton and P. Edwards. “Energy absorption in composite tubes”. *Journal of Composite Materials* 16.6 (1982), pp. 521–545.

[60] G. L. Farley. “Energy absorption of composite materials”. *Journal of Composite Materials* 17.3 (1983), pp. 267–279.

[61] P. Thornton. “The crush behavior of glass fiber reinforced plastic sections”. *Composites Science and technology* 27 (1986), pp. 199–223.

[62] G. L. Farley. “Effect of fiber and matrix maximum strain on the energy absorption of composite materials”. *Journal of Composite Materials* 20.4 (1986), pp. 322–334.

[63] G. L. Farley. “Effect of specimen geometry on the energy absorption capability of composite materials”. *Journal of Composite Materials* 20.4 (1986), pp. 390–400.

[64] J. Price and D. Hull. “Axial crushing of glass fibre-polyester composite cones”. *Composites Science and technology* 28 (1987), pp. 211–230.

[65] D. Hull. “A unified approach to progressive crushing of fibre-reinforced composite tubes”. *Composites Science and Technology* 40.4 (1991), pp. 377–421.

[66] G. L. Farley and R. M. Jones. “Crushing characteristics of continuous fiber-reinforced composite tubes”. *Journal of Composite Materials* 26.1 (1992), pp. 37–50.

[67] G. L. Farley. “The effect of fiber and matrix maximum strain on the energy absorption of composite materials”. *Journal of Composite Materials* 20 (1986), pp. 322–334.

[68] H. Hamada, J. Coppola, D. Hull, Z. Maekawa, and H. Sato. “Comparison of energy absorption of carbon/epoxy and carbon/PEEK composite tubes”. *Composites* 23.4 (1992), pp. 245–252.

[69] H. Hamada, S. Ramakrishna, and H. Satoh. “Crushing mechanism of carbon fibre/PEEK composite tubes”. *Composites* 26.11 (1995), pp. 749–755.

[70] A. Mamalis, Y. Yuan, and G. Viegelahn. “Collapse of thin-wall composite sections subjected to high speed axial loading”. *International Journal of Vehicle Design* 13.5-6 (1992), pp. 564–579.

[71] A. Mamalis, D. Manolakos, G. Demosthenous, and M. Ioannidis. “Axial collapse of thin-walled fibreglass composite tubular components at elevated strain rates”. *Composites Engineering* 4.6 (1994), pp. 653–677.

[72] A. Mamalis, D. Manolakos, G. Demosthenous, and M. Ioannidis. “The static and dynamic axial collapse of fibreglass composite automotive frame rails”. *Composite Structures* 34.1 (1996), pp. 77–90.

[73] A. Mamalis, D. Manolakos, G. Demosthenous, and M. Ioannidis. “Energy absorption capability of fibreglass composite square frusta subjected to static and dynamic axial collapse”. *Thin-Walled Structures* 25.4 (1996), pp. 269–295.

[74] A. Mamalis, D. Manolakos, G. Demosthenous, and M. Ioannidis. “Analytical modelling of the static and dynamic axial collapse of thin-walled fibreglass composite conical shells”. *International Journal of Impact Engineering* 19.5–6 (1997), pp. 477–492.

[75] A. Mamalis, D. Manolakos, M. Ioannidis, and D. Papapostolou. “Crashworthy characteristics of axially statically compressed thin-walled square CFRP composite tubes: Experimental”. *Composite Structures* 63.3-4 (2004), pp. 347–360.

[76] A. Mamalis, D. Manolakos, M. Ioannidis, and D. Papapostolou. “On the response of thin-walled CFRP composite tubular components subjected to static and dynamic axial compressive loading: experimental”. *Composite Structures* 69.4 (2005), pp. 407–420.

[77] A. Mamalis, D. Manolakos, M. Ioannidis, and D. Papapostolou. “The static and dynamic axial collapse of CFRP square tubes: Finite element modelling”. *Composite Structures* 74.2 (2006), pp. 213–225.

[78] G. Jacob, J. Fellers, J. Starbuck, and S. Simunovic. “Crashworthiness of automotive composite material systems”. *Journal of Applied Polymer Science* 92.5 (2004), pp. 3218–3225.

[79] C. Bisagni, G. Di Pietro, L. Fraschini, and D. Terletti. “Progressive crushing of fiber-reinforced composite structural components of a formula one racing car”. *Composite Structures* 68.4 (2005), pp. 491–503.

[80] H. Ghasemnejad, B. Blackman, H. Hadavinia, and B. Sudall. “Experimental studies on fracture characterisation and energy absorption of GFRP composite box structures”. *Composite Structures* 88.2 (2009), pp. 253–261.

[81] H. Hadavinia and H. Ghasemnejad. “Effects of mode-I and mode-II interlaminar fracture toughness on the energy absorption of CFRP twill/weave composite box sections”. *Composite Structures* 89.2 (2009), pp. 303–314.

[82] S. Ochelski and P. Gotowicki. “Experimental assessment of energy absorption capability of carbon-epoxy and glass-epoxy composites”. *Composite Structures* 87.3 (2009), pp. 215–224.

[83] H. Ghasemnejad and A. Hadavinia H.and Aboutorabi. “Effect of delamination failure in crashworthiness analysis of hybrid composite box structures”. *Materials & Design* 31.3 (2010), pp. 1105–1116.

[84] J. Bouchet, E. Jacquelin, and P. Hamelin. “Static and dynamic behavior of combined composite aluminium tube for automotive applications”. *Composites Science and Technology* 60 (2000), pp. 1891–1900.

[85] A. Mamalis, D. Manolakos, G. Demosthenous, and W. Johnson. “Axial plastic collapse of thin bi-material tubes as energy dissipating systems”. *International Journal of Impact Engineering* 11.2 (1991), pp. 185–196.

[86] E. Hanefi and T. Wierzbicki. “Axial resistance and energy absorption of externally reinforced metal tubes”. *Composites Part B: Engineering* 27.5 (1996), pp. 387–394.

[87] H.-W. Song, Z.-M. Wan, Z.-M. Xie, and X.-W. Du. “Axial impact behavior and energy absorption efficiency of composite wrapped metal tubes”. *International Journal of Impact Engineering* 24.4 (2000), pp. 385–401.

[88] X. Wang and G. Lu. “Axial crushing force of externally fibre-reinforced metal tubes”. *Proceedings of the Institution of Mechanical Engineers, Part C: Journal of Mechanical Engineering Science* 216.9 (2002), pp. 863–874.

[89] K. Shin, J. Lee, K. Kim, M. Song, and J. Huh. “Axial crush and bending collapse of an aluminum/GFRP hybrid square tube and its energy absorption capability”. *Composite Structures* 57.1-4 (2002), pp. 279–287.

[90] M. Bambach and M. Elchalakani. “Plastic mechanism analysis of steel SHS strengthened with CFRP under large axial deformation”. *Thin-Walled Structures* 45.2 (2007), pp. 159–170.

[91] M. Bambach, M. Elchalakani, and X. Zhao. “Composite steel–CFRP SHS tubes under axial impact”. *Composite Structures* 87.3 (2009), pp. 282–292.

[92] M. Bambach, H. Jama, and M. Elchalakani. “Static and dynamic axial crushing of spot-welded thin-walled composite steel–CFRP square tubes”. *International Journal of Impact Engineering* 36.9 (2009), pp. 1083–1094.

[93] M. Bambach. “Axial capacity and crushing of thin-walled metal, fibre–epoxy and composite metal–fibre tubes”. *Thin-Walled Structures* 48.6 (2010), pp. 440–452.

[94] M. Bambach. “Axial capacity and crushing behavior of metal–fiber square tubes – Steel, stainless steel and aluminum with CFRP”. *Composites Part B: Engineering* 41.7 (2010), pp. 550–559.

[95] H. Kim, D. Shin, J. Lee, and J. Kwon. “Crashworthiness of aluminum/CFRP square hollow section beam under axial impact loading for crash box application”. *Composite Structures* 112.1 (2014), pp. 1–10.

[96] P. H. Thornton. “Energy absorption by foam filled structures”. *SAE Technical Paper 800081* (1980).

[97] B. Lampinen and R. Jeryan. “Effectiveness of polyurethane foam in energy absorbing structures”. *SAE Technical Paper 820494* (1983).

[98] S. Reid, T. Reddy, and M. Gray. “Static and dynamic axial crushing of foam-filled sheet metal tubes”. *International Journal of Mechanical Sciences* 28.5 (1986), pp. 295–322.

[99] S. Reid and T. Reddy. “Axial crushing of foam-filled tapered sheet metal tubes”. *International Journal of Mechanical Sciences* 28.10 (1986), pp. 643–656.

[100] T. Reddy and R. Wall. “Axial compression of foam-filled thin-walled circular tubes”. *International Journal of Impact Engineering* 7.2 (1988), pp. 151–166.

[101] W. Abramowicz and T. Wierzbicki. “Axial crushing of foam-filled columns”. *International Journal of Mechanical Sciences* 30.3-4 (1988), pp. 263–271.

[102] M. Seitzberger, F. Rammerstorfer, H. Degischer, and R. Gradinger. “Crushing of axially compressed steel tubes filled with aluminium foam”. *Acta Mechanica* 125.1-4 (1997), pp. 93–105.

[103] A. Singace and H. El-Sobky. “Behaviour of axially crushed corrugated tubes”. *International Journal of Mechanical Sciences* 39.3 (1997), pp. 249–268.

[104] M. Langseth, O. Hopperstad, and A. Hanssen. “Crash behaviour of thin-walled aluminium members”. *Thin-Walled Structures* 32.1-3 (1998), pp. 127–150.

[105] S. Santosa and T. Wierzbicki. “Crash behavior of box columns filled with aluminum honeycomb or foam”. *Computers and Structures* 68.4 (1998), pp. 343–367.

[106] A. Hanssen, M. Langseth, and O. Hopperstad. “Static and dynamic crushing of square aluminum extrusions with aluminum foam filler”. *International Journal of Impact Engineering* 24.4 (2000), pp. 347–383.

[107] A. Hanssen, M. Langseth, and O. Hopperstad. “Static and dynamic crushing of circular aluminium extrusions with aluminium foam filler”. *International Journal of Mechanical Sciences* 24.4 (2000), pp. 475–570.

[108] A. Hanssen, M. Langseth, and O. Hopperstad. “Optimum design for energy absorption of square aluminum columns with aluminum foam filler”. *International Journal of Mechanical Sciences* 43.1 (2001), pp. 153–176.

[109] S. Santosa, T. Wierzbicki, A. Hanssen, and M. Langseth. “Experimental and numerical studies of foam-filled sections”. *International Journal of Impact Engineering* 24.5 (2000), pp. 509–534.

[110] M. Seitzberger, F. Rammerstorfer, R. Gradinger, H. Degischer, M. Blaimschein, and C. Walch. “Experimental studies on the quasi-static axial crushing of steel columns filled with aluminium foam”. *International Journal of Solids and Structures* 37.30 (2000), pp. 4125–4147.

[111] W. Chen and T. Wierzbicki. “Relative merits of single-cell, multi-cell and foam-filled thin-walled structures in energy absorption”. *Thin-Walled Structures* 39.4 (2001), pp. 287–306.

[112] T. Børvik, O. Hopperstad, A. Reyes, M. Langseth, G. Solomos, and T. Dyngeland. “Empty and foam-filled circular aluminium tubes subjected to axial and oblique quasi-static loading”. *International Journal of Crashworthiness* 8.5 (2003), pp. 481–494.

[113] A. Reyes, O. Hopperstad, and M. Langseth. “Aluminum foam-filled extrusions Subjected to oblique loading: experimental and numerical study”. *International Journal of Solids and Structures* 41.5-6 (2004), pp. 1645–1675.

[114] S. Meguid, M. Attia, and A. Monfort. “On the crush behaviour of ultralight foam-filled structures”. *Materials and Design* 25.3 (2004), pp. 183–189.

[115] L. Aktay, A. Toksoy, and M. Güden. “Quasi-static axial crushing of extruded polystyrene foam-filled thin-walled aluminum tubes: Experimental and numerical analysis”. *Materials and Design* 27.7 (2006), pp. 556–565.

[116] Z. Ahmad and D. Thambiratnam. “Crushing response of foam-filled conical tubes under quasi-static axial loading”. *Materials and Design* 30.7 (2009), pp. 2393–2403.

[117] H. Zarei and M. Kröger. “Crashworthiness optimization of empty and filled aluminum crash boxes”. *International Journal of Crashworthiness* 12.3 (2007), pp. 255–264.

[118] S. Hou, Q. Li, S. Long, X. Yang, and W. Li. “Crashworthiness design for foam filled thin-wall structures”. *Materials and Design* 30.6 (2009), pp. 2024–2032.

[119] J. Bi, H. Fang, Q. Wang, and X. Ren. “Modeling and optimization of foam-filled thin-walled columns for crashworthiness designs”. *Finite Elements in Analysis and Design* 46.9 (2010), pp. 698–709.

[120] G. Sun, G. Li, S. Hou, S. Zhou, W. Li, and Q. Li. “Crashworthiness design for functionally graded foam-filled thin-walled structures”. *Materials Science and Engineering A* 527.7-8 (2010), pp. 1911–1919.

[121] S. Hou, X. Han, G. Sun, S. Long, W. Li, X. Yang, and Q. Li. “Multiobjective optimization for tapered circular tubes”. *Thin-Walled Structures* 49.7 (2011), pp. 855–863.

[122] Y. Zhang, G. Sun, Z. Li G.and Luo, and Q. Li. “Optimization of foam-filled bitubal structures for crashworthiness criteria”. *Materials and Design* 38 (2012), pp. 99–109.

[123] X. Song, G. Sun, G. Li, W. Gao, and Q. Li. “Crashworthiness optimization of foam-filled tapered thin-walled structure using multiple surrogate models”. *Structural and Multidisciplinary Optimization* 47.2 (2013), pp. 221–231.

[124] G. Zheng, S. Wu, G. Sun, G. Li, and Q. Li. “Crushing analysis of foam-filled single and bitubal polygonal thin-walled tubes”. *International Journal of Mechanical Sciences* 87 (2014), pp. 226–240.

[125] J. Lin, X. Wang, C. Fang, and X. Huang. “Collapse loading and energy absorption of fiber-reinforced conical shells”. *Composites Part B: Engineering* 74 (2015), pp. 178–189.

[126] S. P. Silva, M. A. Sabino, E. M. Fernandes, V. M. Correlo, L. F. Boesel, and R. L. Reis. “Cork: properties, capabilities and applications”. *International Materials Reviews* 50.6 (2005), pp. 345–365.

[127] C. Gameiro and J. Cirne. “Dynamic axial crushing of short to long circular aluminium tubes with agglomerate cork filler”. *International Journal of Mechanical Sciences* 49.9 (2007), pp. 1029–1037.

[128] I. Alcántara, F. Teixeira-Dias, and M. Paulino. “Cork composites for the absorption of impact energy”. *Composite Structures* 95 (2013), pp. 16–27.

[129] M. Paulino and F. Teixeira-Dias. “An energy absorption performance index for cellular materials - Development of a side-impact cork padding”. *International Journal of Crashworthiness* 16.2 (2011), pp. 135–153.

[130] Y. Tay, C. Lim, and H. Lankarani. “A finite element analysis of high-energy absorption cellular materials in enhancing passive safety of road vehicles in side-impact accidents”. *International Journal of Crashworthiness* 19.3 (2014), pp. 288–300.

[131] F. Fernandes, R. Pascoal, and R. Alves de Sousa. “Modelling impact response of agglomerated cork”. *Materials and Design* 58 (2014), pp. 499–507.

[132] R. Jardin, F. Fernandes, A. Pereira, and R. Alves de Sousa. “Static and dynamic mechanical response of different cork agglomerates”. *Materials and Design* 68 (2015), pp. 121–126.

[133] S. Sánchez-Sáez, S. García-Castillo, E. Barbero, and J. Cirne. “Dynamic crushing behaviour of agglomerated cork”. *Materials and Design* 65 (2015), pp. 743–748.

[134] T. Wierzbicki. “Crushing analysis of metal honeycombs”. *International Journal of Impact Engineering* 1.2 (1983), pp. 157–174.

[135] Y. Yasui. “Dynamic axial crushing of multi-layer honeycomb panels and impact tensile behavior of the component members”. *International Journal of Impact Engineering* 24.6 (2000), pp. 659–671.

[136] H. Zhao and G. Gary. “Crushing behaviour of aluminium honeycombs under impact loading”. *International Journal of Impact Engineering* 21.10 (1998), pp. 827–836.

[137] L. J. Gibson and M. F. Ashby. *Cellular solids, structure and properties.* Second edition. Cambridge University Press, Cambridge (UK), 1997.

[138] *ABAQUS 6.14 Documentation.* Dassault Systèmes. Providence Road, Rhode Island. 2014.

[139] W. Abramowicz. “Thin-walled structures as impact energy absorbers”. *Thin-Walled Structures* 41.2-3 (2003), pp. 91–107.

[140] D. Karagiozova, M. Alves, and N. Jones. “Inertia effects in axisymmetrically deformed cylindrical shells under axial impact”. *International Journal of Impact Engineering* 24.10 (2000), pp. 1083–1115.

[141] Z. Kazanc and K.-J. Bathe. “Crushing and crashing of tubes with implicit time integration”. *International Journal of Impact Engineering* 42 (2012), pp. 80–88.

[142] T. Belytschko, W. K. Liu, B. Moran, and K. I. Elkhodary. *Nonlinear finite elements for continua and structures.* Second edition. John Wiley & Sons, Hoboken (New Jersey, USA), 2014.

[143] R. Courant, K. Friedrichs, and H. Lewy. “Über die partiellen differenzengleichungen der mathematischen physik”. *Mathematische Annalen* 100.1 (1928), pp. 32–74.

3

Experimental and numerical crashworthiness of bi-material crash boxes

This chapter deals with the experimental and numerical assessment of the axial crushing behavior of bi-material (or hybrid) components made of carbon-fiber reinforced polymers, glass-fiber reinforced polyamide, polyethylene terephthalate foam, or cork conglomerates, in combination with cold-formed steel polygonal tubes using quasi-static and dynamic numerical simulation verified with experimental results. Non-linear effects, contacts, strain rate dependent effects, geometrical imperfections and residual stresses were taken into account to achieve realistic results. The hybrid components showed a remarkable improvement in terms of energy absorption in most cases, and a good agreement of the numerical results with experimental data was achieved. A combination of a glass-fiber reinforced polyamide padding and a steel box provided the best results, and a detailed study of the sensitivity of its specific energy absorption with respect to the thickness of the components was carried out as well. Lastly, a brief study on the influence of the welding pattern on the crash response is presented.

3.1 Introduction

The objective of the work presented in this chapter was to improve the energy absorption of a conventional hollow crash box (see Figure 3.1) by filling it with a core made of different lightweight materials. The performance of the different combinations was evaluated by means of experimental tests and numerical simulations carried out in the framework of the research project *Hybrid Body*, funded by the regional government of Galicia (Xunta de Galicia) under the plan *Plan Galego de Investigación, Desenvolvemento e Innovación Tecnolóxica*, project reference 10DPI025CT. This investigation was done in collaboration with partner CTAG (Centro Tecnolóxico da Automoción de Galicia), where the experimental part was carried out. The contents of this chapter have been published in the International Journal of Impact Engineering [10], and presented in the SAE 2013 World Congress & Exhibition [144] and in the 16th International Conference on Computational Methods and Experimental Measurements (2013) [145]. Furthermore, national Spanish patent number ES-2.386.269.B1, co-invented by the author, was derived from the material presented in this chapter. This patent is included as Appendix D.

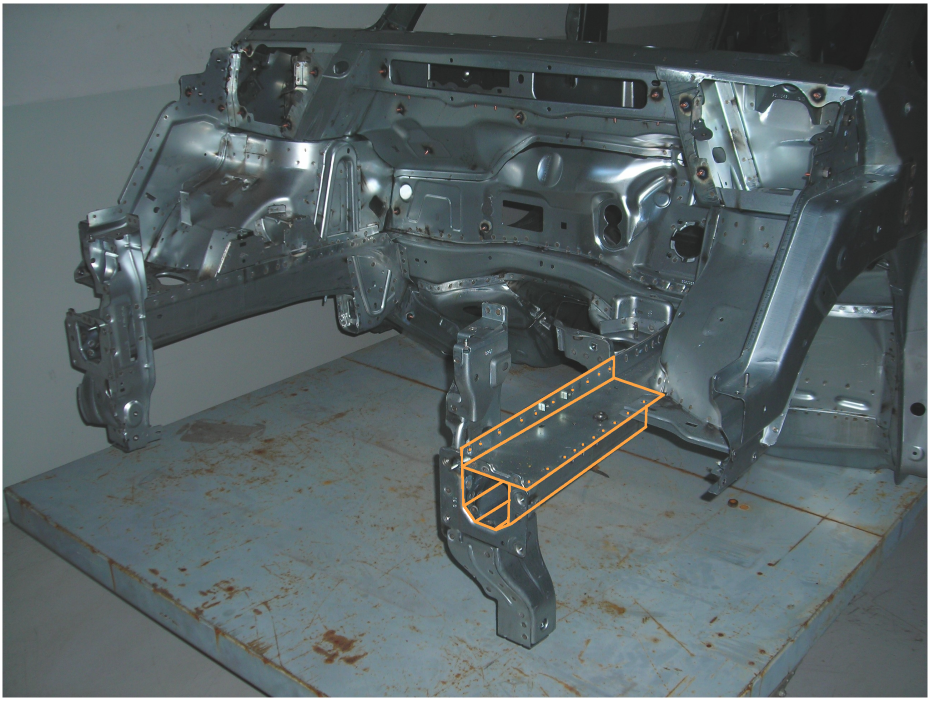

Figure 3.1: Location of the frontal energy absorption devices in a car structure (adapted from a photograph provided by CTAG).

3.2 Components description and methodology

Five components consisting of a combination of a steel casing and a core made of one of the selected materials were developed. All the five different types were 220 mm long, and their different material configurations are described next. Simulations were carried out using the ABAQUS Explicit FEA package in its version 6.11 [146].

3.2.1 Component 0

Component 0 consisted of an empty steel tube made from two curved cold-formed steel sheets which were 1 mm thick. These two sheets were joined with tungsten inert gas (TIG) spot welds, as shown in Figure 3.2. The longitudinal distance between spot welds was 30 mm. These test pieces represented the conventional crash boxes widely used nowadays, and were considered the baseline which the bi-material alternatives were compared to.

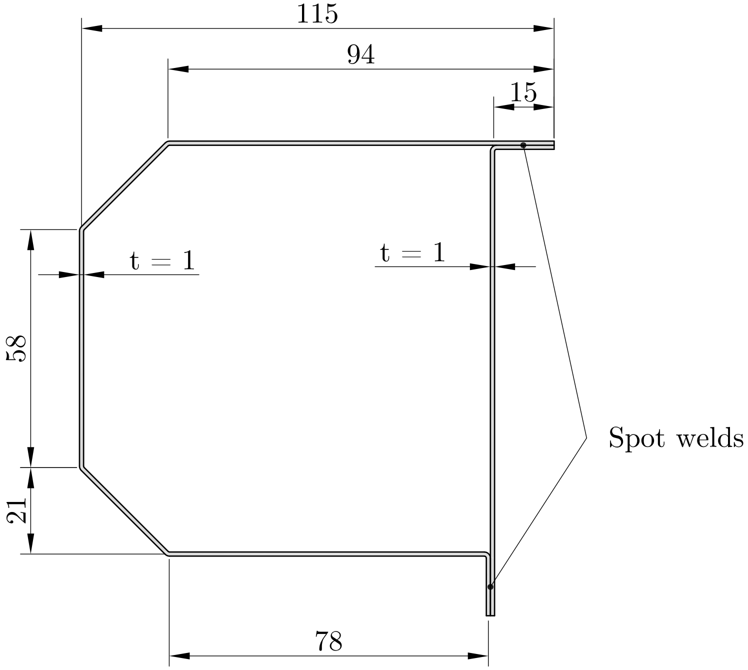

Figure 3.2: Dimensions of the steel box cross-section, in millimeters.

The selected steel for these tubes was a standard S-275 J0H steel with an initial yield strength of $\sigma_{\mathrm{y}}^{0} = 275\,\mathrm{MPa}$, Poisson's ratio $\nu = 0.3$ and density $\rho = 7.85\,\mathrm{t/m^3}$, which conferred a mass of 750 g to this component.

Regarding the constitutive plasticity model for the numerical simulations, a Johnson-Cook isotropic hypoelastic-viscoplastic material model was adopted in order to account for large plastic deformations and strain rate sensitivity. In particular, an additive decomposition of the strain rate tensor **D** was assumed:

$$\mathbf{D} = \mathbf{D}^{\mathrm{e}} + \mathbf{D}^{\mathrm{p}}, \tag{3.1}$$

$\mathbf{D}^{\mathrm{e}}$ and $\mathbf{D}^{\mathrm{p}}$ being the elastic and plastic parts, respectively. We can consider that the elastic deformations are relatively small, thus we can express the (hypo)elastic part of the strain rate tensor in terms of the Green-Naghdi stress rate:

$$\mathbf{D}^{\mathrm{e}} = \frac{1+\nu}{E}\boldsymbol{\sigma}^{\nabla \mathrm{G}} - \frac{\nu}{E}\mathrm{trace}\left(\boldsymbol{\sigma}^{\nabla \mathrm{G}}\right)\mathbf{I}, \tag{3.2}$$

where E is the Young's modulus, ν is the elastic Poisson's ratio, $\boldsymbol{\sigma}^{\nabla \mathrm{G}}$ is the Green-Naghdi rate[1] of the Cauchy stress tensor $\boldsymbol{\sigma}$ and $\mathbf{I}$ is the identity tensor.

If we assume now an associated flow rule, we can write the plastic part of the strain rate tensor as

$$\mathbf{D}^{\mathrm{p}} = \dot{\lambda}\frac{\partial f}{\partial \boldsymbol{\sigma}}, \tag{3.3}$$

where $\dot{\lambda}$ is the plastic multiplier and f is the yield criterion. As is customary, a J_2-based pressure-independent flow rule has been adopted for this metal model. In particular, the von Mises flow rule was chosen, so the equivalent stress is the von Mises stress:

$$\sigma_{\mathrm{eq}} = \sqrt{\frac{3}{2}\boldsymbol{\sigma}' : \boldsymbol{\sigma}'}, \tag{3.4}$$

where $\boldsymbol{\sigma}'$ is the deviatoric stress tensor, obtained as

$$\boldsymbol{\sigma}' = \boldsymbol{\sigma} - \frac{1}{3}\mathrm{trace}\left(\boldsymbol{\sigma}\right)\mathbf{I}. \tag{3.5}$$

The Johnson-Cook yield condition f can be written as

$$f\left(\boldsymbol{\sigma}, p\right) = \sigma_{\mathrm{eq}}\left(\boldsymbol{\sigma}\right) - \left(A + Bp^{n}\right), \tag{3.6}$$

where p is the equivalent plastic strain, A is the initial yield strength and B, n are material constants which control the isotropic hardening. Note that the viscosity term is not written here, since it is included in the expression of the equivalent plastic strain rate $\dot{p}$, described below. For von Mises plasticity, the plastic multiplier $\dot{\lambda}$ in Equation (3.3) equals the equivalent plastic strain rate $\dot{p}$. If we combine this with Equations (3.3) and (3.4) we get the following expression for $\mathbf{D}^{\mathrm{p}}$:

$$\mathbf{D}^{\mathrm{p}} = \frac{3}{2}\dot{p}\frac{\boldsymbol{\sigma}'}{\sigma_{\mathrm{eq}}}. \tag{3.7}$$

---

[1] N.B. $\boldsymbol{\sigma}^{\nabla \mathrm{G}} = \dot{\boldsymbol{\sigma}} - \boldsymbol{\Omega}\boldsymbol{\sigma} - \boldsymbol{\sigma}\boldsymbol{\Omega}^{\mathrm{T}}$, with $\boldsymbol{\Omega} = \dot{\mathbf{R}}\mathbf{R}^{\mathrm{T}}$, where $\mathbf{R}$ is the rotation tensor.

In order to account for the strain rate sensitivity, the equivalent plastic strain rate $\dot{p}$ is defined as a function of the equivalent stress, the isotropic hardening function $R = Bp^n$ and the reference equivalent plastic strain rate $\dot{p}_0$:

$$\dot{p} = \begin{cases} 0 & \text{if } f \leq 0 \\ \dot{p}_0 \exp\left[\dfrac{1}{C}\left(\dfrac{\sigma_{\mathrm{eq}}(\boldsymbol{\sigma})}{A + Bp^n} - 1\right)\right] & \text{if } f > 0. \end{cases} \tag{3.8}$$

The Johnson-Cook constitutive equation in the viscoplastic domain ($f > 0$) can now be written out as follows:

$$\sigma_{\mathrm{eq}} = [A + Bp^n]\left[1 + C \ln \frac{\dot{p}}{\dot{p}_0}\right]. \tag{3.9}$$

In this chapter, values of $A = 275\,\mathrm{MPa}$, $B = 50\,\mathrm{MPa}$, $C = 0.03$, $n = 0.4$ and $\dot{p}_0 = 0.0001\,\mathrm{s}^{-1}$ were adopted. Since no specific experimental studies were found for this steel, these parameters were obtained by taking the values for a similar ASTM A36 steel [147] and adjusting them with our own experimental data for component 0. Figure 3.3 shows the behavior of the modeled material at different strain rates.

In addition to this plasticity model, a ductile failure model was included with the purpose of removing from the numerical analyses those elements reaching their energy dissipation limits and becoming severely distorted. Since no cracks or failures were observed in the steel parts after the experimental tests, this failure model was only included to avoid a very few heavily distorted elements to become an obstacle for the analysis convergence. A value of $p_{\mathrm{D}} = 0.35$ has been taken as the ultimate plastic strain, applying a total stiffness loss to those elements whose effective strain overpasses this value. The criterion to start the damage is met when the following condition is satisfied:

$$\int \frac{\mathrm{d}p}{p_{\mathrm{D}}} = 1. \tag{3.10}$$

Only 1 % of the elements on the steel tube were deleted by the failure model.

Regarding the finite element model itself, a general scheme is shown in Figure 3.4b. Four node shell elements with 3 integration points through their thickness and reduced integration were chosen for the steel part. A view of the hardware component is provided in Figure 3.4a.

Mesh size is a crucial parameter when simulating metal folding processes since its value should allow the mesh to adapt itself to the curvatures of the wall.

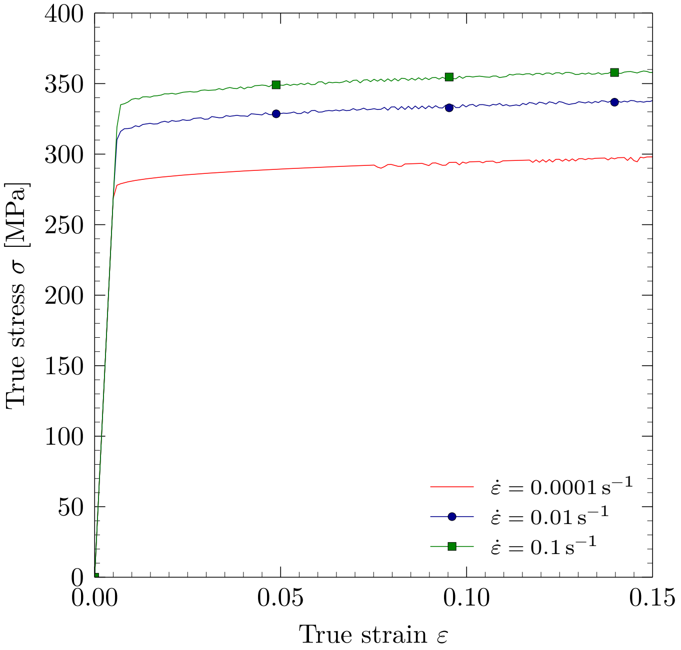

Figure 3.3: Stress-strain curves of the modeled S275 steel at different strain rates. Minor oscillations are due to the error arising from using a single, linear solid element to obtain the curves.

After some benchmarking, consisting of mesh convergence analyses, a 2 mm mesh was adopted for the analyses, which accurately emulated the steel folding process in the casing. This benchmarking consisted of a convergence test by which the finite element model of the empty tube was crushed at 10 m/s with different mesh sizes. The results of this test are provided in Figure 3.5, justifying the selection of the 2 mm mesh.

Geometrical imperfections are usually included in this kind of studies. The development of a certain collapse mode can be triggered by applying a deformation pattern based on buckling modes [5], on the shapes obtained from real experiments or introducing mesh indentations [148]. In this case, imperfections were based on the deformed shapes obtained from the experimental tests and were introduced on the steel part only. These imperfections were applied at the top of the components to guarantee that its collapse begins there. This is important since during the calibration process, alterations in some variables could lead to a change in the collapsing mode. Even though the amount of absorbed energy

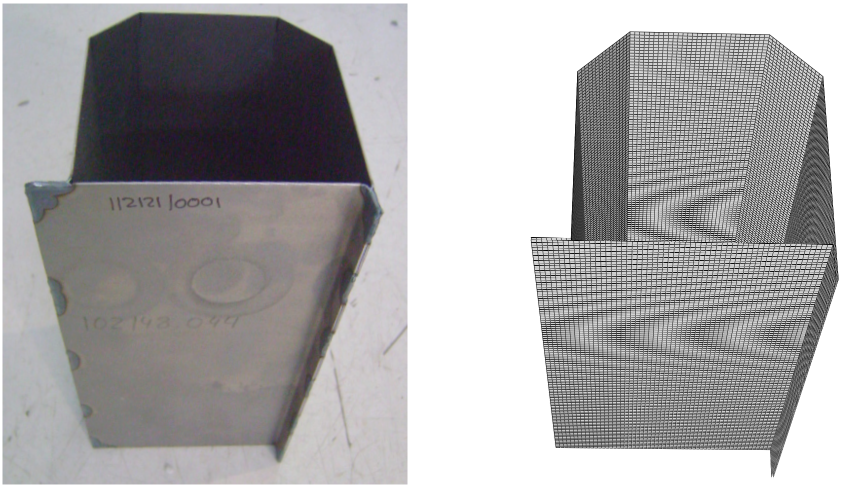

(a) Hardware component 0. **(b)** Mesh of the finite element model.

Figure 3.4: Type 0 specimen: hardware test piece and finite element model.

is almost constant regardless of the developed collapse mode when crushing the entire piece, its value can suffer alterations if that mode is changing when only a part of the piece is crushed. Also, experimental results show that one of the specimen's ends is hosting the crushing initiation more often than the other one. The free end is usually initiating the collapse, since the experiment setup fixes one end while the other one receives the load from an articulated piston. In addition to this, geometrical imperfections allowed also to obtain a reliable peak load, since the collapse was started before reaching the theoretical yielding force. In particular, experimental results show a peak force of around 50 kN for specimen 0, whereas a non-triggered model produced a peak load of around 120 kN, close to the product of the yield stress and the cross-sectional area.

The pattern depicted in Figure 3.6 was obtained from some analyses which resulted on the same collapse mode than the hardware specimen. The maximum displacement of 0.95 millimeters was obtained through a calibration process in order to obtain peak loads matching the ones obtained from experimental data, as previously described.

Since both steel sheets require a cold forming process prior to their assembly, residual plastic strains were applied to the corners of both plates through an initial load step and right before applying the displacements field leading to geometrical imperfections. The initial stresses were applied together with temporary boundary conditions which confined them in the corners. These boundary con-

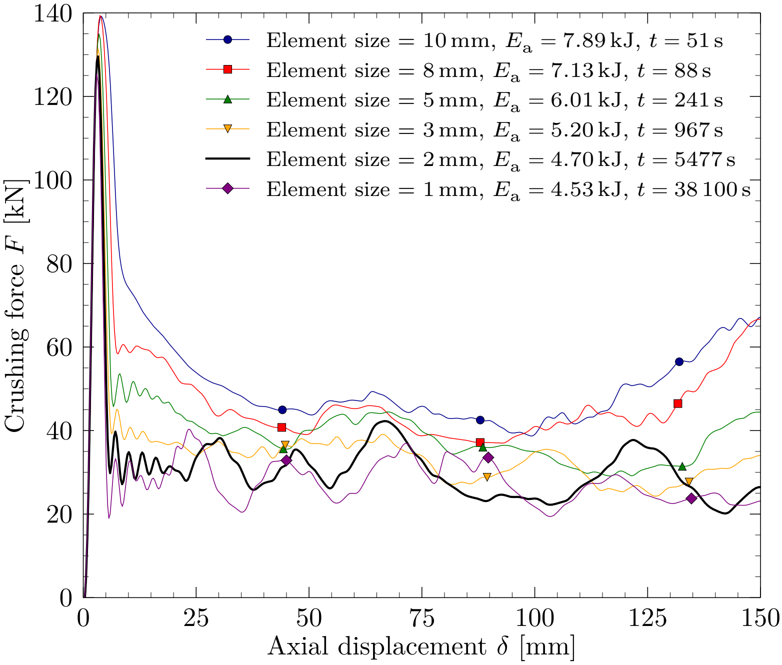

Figure 3.5: Convergence test to determinate the mesh size of shell elements for the steel profile. Barely any progressive folding is observed for mesh sizes over 5 mm since no force oscillations appear. The model stiffness increases with the mesh size. Values of absorbed energy E_a and total simulation time including triggering t (in a high-end workstation) are provided as well. Here, a triggering pattern softer than the one explained for the steel tube was used.

ditions consisted of constraining both displacements and rotations at the nodes surrounding the affected region at an approximate distance of 5 mm away from the corners. Once this step is finished, boundary conditions are released, releasing the stresses too since the specimen is not constrained; but plastic strains resulting from this step remained along the crushing analysis. The region size and the value of the pre-stresses were obtained from a previous cold-forming FE analysis of a steel sheet with the same properties as the metal tube. Their values and their effect on the load-displacement curves are shown in Figure 3.7. This almost neglectable effect consists of a reduction of the peak load and a slight variation of the absorbed energy, around 1-2 %.

The amplitude of all these imperfections and the material parameters described at the beginning were obtained from a calibration process which led to a quality agreement between experimental and numerical results. Figure 3.8

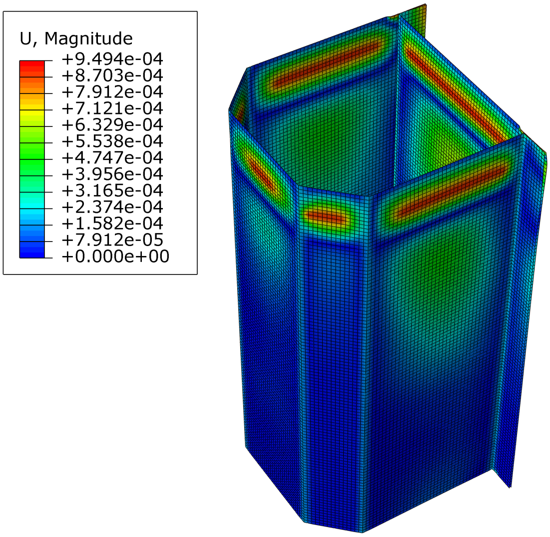

Figure 3.6: Imperfections pattern on the impacted end of the steel tube. The contoured plot corresponds to the absolute displacements.

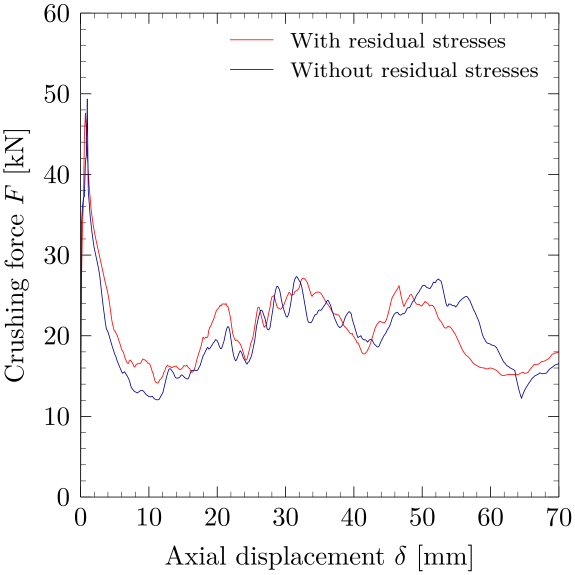

Figure 3.7: Effect of the residual plastic strains in the steel part.

represents the force-displacement and energy-displacement curves obtained from simulations and experimental tests for component 0, including imperfections and residual strains.

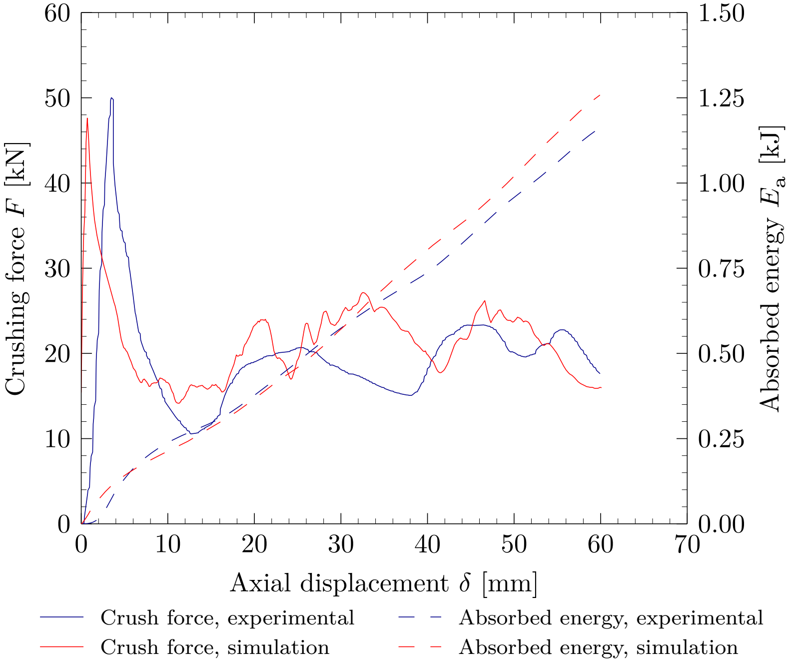

Figure 3.8: Correlation between experimental and simulation results for specimen 0.

Welds were modeled as a rigid *bushing* connection in Abaqus software, which offered quality results in other investigations [149]. This connection consists of a rigid joint between both sheets at the locations of the spot welds.

3.2.2 Component A

These components consisted of the previous steel box filled with an inner core made of 2.5 millimeter-thick GFRP laminates. The core material's commercial name is Ultramid A3WG10 BK00564, produced by BASF. This material was selected for its relatively low economical cost compared to carbon fiber prepregs and its high resistance-to-weight ratio. For the work described in this chapter, its relevant mechanical properties were obtained from the manufacturer's data sheets [150] and included in the finite element model. Values are provided in Table 3.1.

E	ν	ρ	σ_u	ε_u
10.16 GPa	0.4	1.55 t/m^3	254 MPa	2.6 %

Table 3.1: Mechanical properties of Ultramid A3WG10 BK00564.

A linear elastic model with fragile failure was selected as constitutive model for this material. Isotropic properties were assumed since the selected GFRP consisted of chopped short glass fibers following random orientations. Material failure was modeled through a strain-based failure initiation criterion with no damage evolution to produce a brittle failure according to Equation (3.10). Since this criterion is based on plastic deformations, a very small plastic region was added to the model at the end of the elastic loading curve, allowing the damage model to proceed. The ultimate plastic strain was set to $p_\mathrm{D} = 0.0001$.

Cores for components A were meshed with element lengths between 3 and 3.5 mm. Given that the fracture was simulated through an element-deletion technique, the mesh size had to be small enough to reproduce fracture with a certain degree of accuracy. The selected mesh size provided good results (see for instance Figure 3.27). The GFRP structure was to be eventually mass-produced through an injection process. However, for the laboratory tests, a handcrafting process was employed: crosses were built by cutting two rectangular pieces and making a fissure in both of them, so they could be fitted together orthogonally. This produced pieces which were less stiff than the final ones, and although the FE model was built in the same way, the hardware parts were slightly curved, making the loading plate crush them with a certain attack angle and, thus, decreasing the resulting forces and the energy absorption parameters. A view of a real A specimen and a detail of the mesh in the core is provided in Figure 4.4. The mass of these specimens was 1190 g.

3.2.3 Component B

In this case, the steel tube was filled with four CFRP laminates. The laminates were undulated, which concentrated the material failures in the tops and bottoms of the waves. Each of these laminates was made from eight uni-directional prepregs MTM57/T700S (24K)–35 % RN with an individual thickness of 0.301 mm, arranged in a stacking sequence [0/90/+45/0/-45/+45/90/0]. According to [151, 152], the elastic properties of this material are those shown in Table 3.2.

A damage model specifically applicable to fiber-reinforced composite materials based on Hashin's theory [153, 154] was adopted. The onset of degradation starting this damage model can be reached through four different initiation mech-

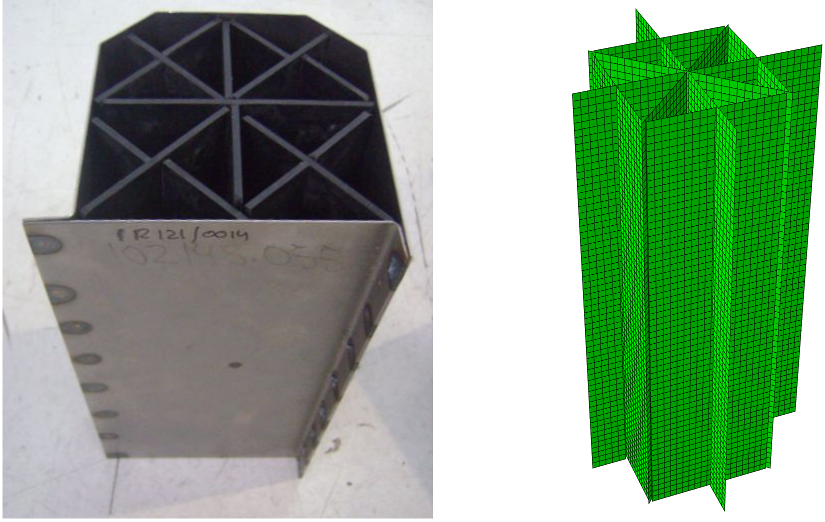

(a) Hardware specimen A.

(b) Core mesh.

Figure 3.9: Specimen A: hardware test piece and FE model of the core.

E_1	E_2	G_{12}	ν_{12}
150.67 GPa	9.32 GPa	2.54 GPa	0.3

Table 3.2: Elastic properties for MTM57/T700S (24K)–35 % RN CFRP pre-pregs.

anisms: fiber tension/compression and matrix tension/compression. The specific criteria for each type of damage initiation are provided in Equations (3.11) to (3.14):

$$F_{\mathrm{f}}^{\mathrm{t}} = \left(\frac{\hat{\sigma}_{11}}{X^{\mathrm{T}}}\right)^2 + \alpha \left(\frac{\hat{\tau}_{12}}{S^{\mathrm{L}}}\right)^2, \tag{3.11}$$

$$F_{\mathrm{f}}^{\mathrm{c}} = \left(\frac{\hat{\sigma}_{11}}{X^{\mathrm{C}}}\right)^2, \tag{3.12}$$

$$F_{\mathrm{m}}^{\mathrm{t}} = \left(\frac{\hat{\sigma}_{22}}{Y^{\mathrm{T}}}\right)^2 + \left(\frac{\hat{\tau}_{12}}{S^{\mathrm{L}}}\right)^2, \tag{3.13}$$

$$F_{\mathrm{m}}^{\mathrm{c}} = \left(\frac{\hat{\sigma}_{22}}{2S^{\mathrm{T}}}\right)^2 + \left[\left(\frac{Y^{\mathrm{C}}}{2S^{\mathrm{T}}}\right)^2 - 1\right] \frac{\hat{\sigma}_{22}}{Y^{\mathrm{C}}} + \left(\frac{\hat{\tau}_{12}}{S^{\mathrm{L}}}\right)^2. \tag{3.14}$$

In the previous equations, $F_{\mathrm{f/m}}^{\mathrm{t/c}}$ denotes the damage criterion indicators for fiber / matrix, tension / compression failure, being met when $F_{\mathrm{f/m}}^{\mathrm{t/c}}$ reaches a value of 1 or greater. X denotes the longitudinal tensile (T) or compressive (C) strengths, Y denotes the transverse tensile (T) or compressive (C) strengths, S denotes the longitudinal (L) or transverse (T) shear strengths, α balances the contribution of the shear stress to the fiber tensile initiation criterion and $\hat{\sigma}_{11}$, $\hat{\sigma}_{22}$ and $\hat{\tau}_{12}$ are the effective stresses (components of the effective stress tensor), product of the true stresses by a damage operator. Further information on this model can be found in [146, 153, 154].

Values for the ultimate stresses were taken from the literature [151, 152], and are presented in Table 3.3. Damage evolution was included by setting the fracture energy for modes I and II. The values of the fracture energy were taken from an investigation on a similar composite material [155], and are equal to 16 kJ/m^2 for mode I and 1 kJ/m^2 for mode II. A detailed explanation of the energy-based damage evolution model can be found in [146]. An element size of about 4 × 4 mm was adopted with good results. The core mesh and a picture of the real specimen are shown in Figure 3.10. Components B had a mass of 951 g.

X^{T}	X^{C}	Y^{T}	S^{L}
2481 MPa	1296 MPa	52.9 MPa	115 MPa

Table 3.3: Failure properties for MTM57/T700S (24K) CFRP pre-pregs.

3.2.4 Component C

Component C consisted of a steel casing filled with a PET foam or cork conglomerate padding, producing Cf or Cc components, respectively. This core was set up by stacking 18 slices of cork or foam with an individual thickness of 12 mm.

The selected PET foam for components Cf was ArmaFORM W/AC135, manufactured by ARMACELL, which was modeled through a *crushable foam* constitutive model [146]. This consists of an elastic-plastic model with volumetric hardening [156]. Given the nature of the material, the yield surface f includes pressure dependency in addition to deviatoric stresses, i.e., $f = f\left(I_{\sigma}, J_2\right)$ where I_{σ} and J_2 are the first and second stress invariants, respectively. We have adopted an expression for f consisting of an ellipse in the σ_{H}–σ_{eq} plane, which evolves in hardening (see Figure 3.11). This evolution is governed by the volumetric compacting plastic strain experienced by the material. The expression

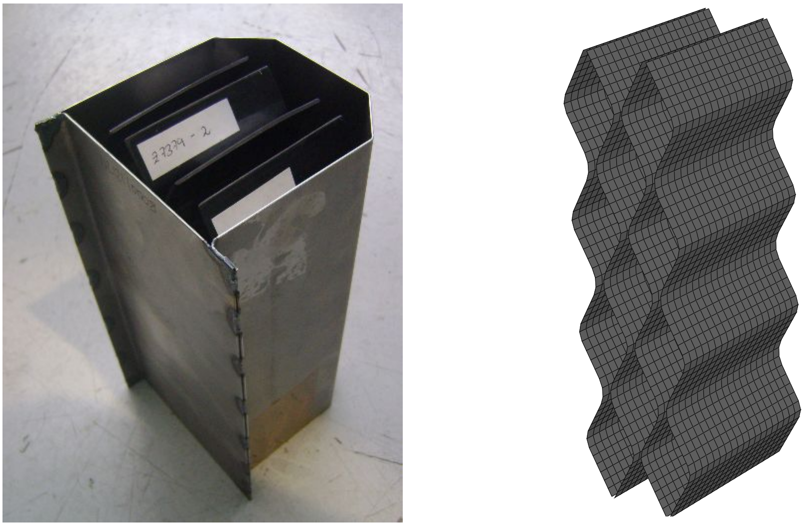

(a) Hardware specimen B. **(b)** Core mesh.

Figure 3.10: Specimen B: hardware test piece and FE model of the core.

for the yield surface f reads:

$$f = \sqrt{{\sigma_{\mathrm{eq}}}^2 + \alpha^2 \sigma_{\mathrm{H}} - {\sigma_{\mathrm{H}}^{0}}^2} - B = 0, \tag{3.15}$$

where $\sigma_{\mathrm{eq}} = \sqrt{3J_2}$ is the von Mises equivalent stress and $\sigma_{\mathrm{H}} = I_\sigma/3$ is the hydrostatic stress. B is the size of the vertical semi-axis of the yield ellipse, which is obtained from the size of the horizontal axis A as

$$B = \alpha A = \alpha \frac{\sigma_{\mathrm{H}}^{\mathrm{C}} + \sigma_{\mathrm{H}}^{\mathrm{T}}}{2}, \tag{3.16}$$

where $\sigma_{\mathrm{H}}^{\mathrm{C}}$ and $\sigma_{\mathrm{H}}^{\mathrm{T}}$ are the yield strengths in hydrostatic compression and tension, respectively. The value of the parameter α is obtained from the initial yield stresses in uniaxial compression σ_{C}^{0}, hydrostatic compression $\sigma_{\mathrm{H,C}}^{0}$ and hydrostatic tension $\sigma_{\mathrm{H,T}}$ as

$$\alpha = \frac{3k}{\sqrt{(3k_{\mathrm{t}} + k)\,(3 - k)}}, \tag{3.17}$$

with

$$k = \frac{\sigma_{\mathrm{C}}^{0}}{\sigma_{\mathrm{H,C}}^{0}} \tag{3.18}$$

and

$$k_\mathrm{t} = \frac{\sigma_\mathrm{H}^\mathrm{T}}{\sigma_\mathrm{H,C}^0}. \tag{3.19}$$

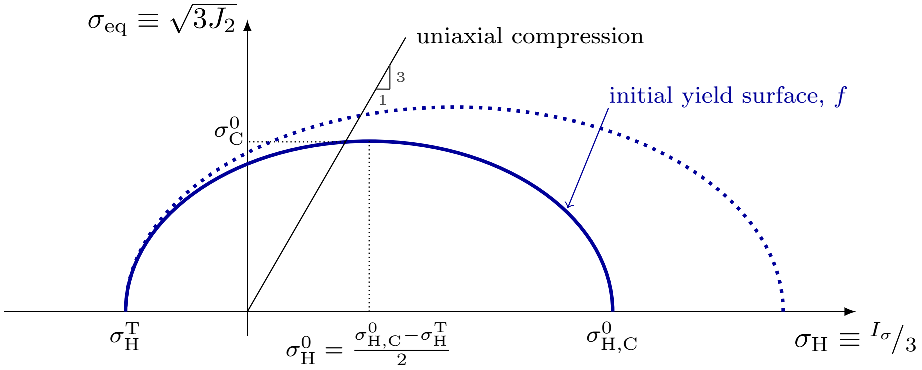

Figure 3.11: Generic representation of the yield surface of the constitutive model for the polymeric foam on the σ_H–σ_eq plane.

In Equation (3.15), σ_H^0 is the center of the initial yield ellipse on the σ_H axis, i.e.,

$$\sigma_\mathrm{H}^0 = \frac{\sigma_\mathrm{H,C}^0 - \sigma_\mathrm{H}^\mathrm{T}}{2}. \tag{3.20}$$

Based on the manufacturer's data sheet and some investigations [157, 158], mechanical input data are shown in Table 3.4.

E	ν	ρ	k	k_t	σ_y
90 MPa	0.1	0.135 t/m^3	1.5	1	2.5 MPa

Table 3.4: Material properties for ArmaFORM W/AC135, taken from the manufacturer's specifications.

Even though the model is flexible to account for hardening, this was not considered at this stage since the manufacturer reported no remarkable hardening in the plateau stress region of the material. Furthermore, in this chapter, strain rate effects on foam [157] are not taken into account since this component was only subjected to low-speed crushing, not being selected to be included in the impact tests. The reader is referred to Chapter 6 for a more comprehensive modeling of this material.

The Cc variant of C components incorporated cork instead of foam as a filler. In this case, the selected agglomerate was Corecork NL25, by Amorim. Cork is a renewable natural material which is much more affordable than the other reinforcements in this work, and has a good energy-absorption response [127, 129, 159–161]. This material shows a strong strain-rate dependent behavior [129, 162] and, thereby, these effects must be regarded and included in the material model. A visco-hyperelastic model denominated *low density foam* in ABAQUS was selected for the cork core, consisting of a numerical construction of the strain energy potential from experimental data. As long as no experimental results for this material can be found in the literature, compression stress-strain curves were obtained from laboratory experimental tests (see Figure 3.12) and used as input data for the constitutive model. Details are provided in Appendix A.

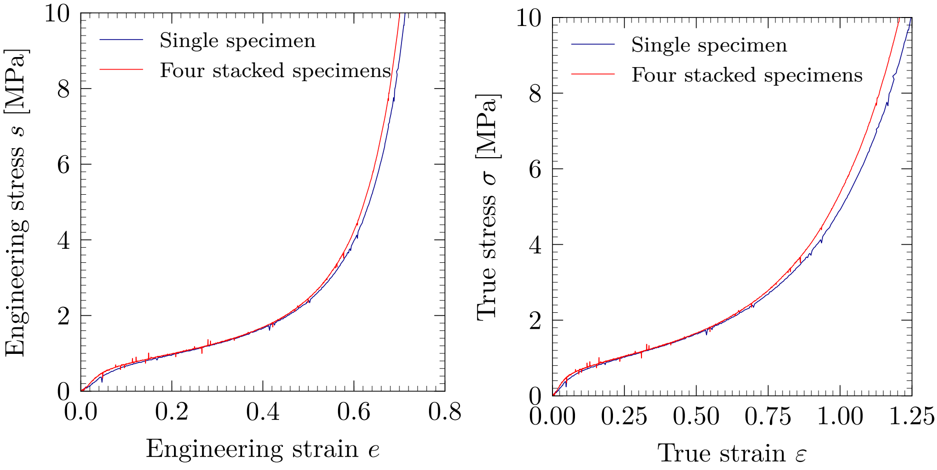

(a) Engineering values.

(b) True values.

Figure 3.12: Experimental compressive stress-strain curves of Corecork NL25.

The mesh of these two cores was made of 3D solid elements with lengths about five millimeters, balancing the quality of the results and the time required to complete the analyses. Figure 3.13 shows photographs of the real pieces and the core mesh.

Foam-filled and cork-filled components C had a mass of 983 g and 1050 g, respectively.

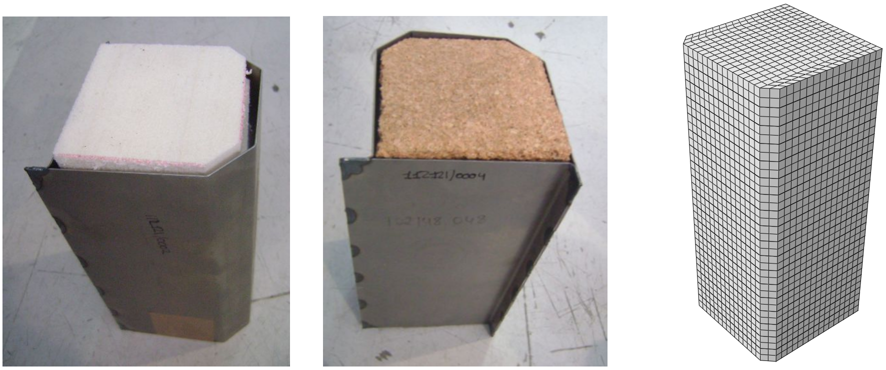

(a) Foam-filled tube. **(b)** Cork-filled tube. **(c)** Core mesh.

Figure 3.13: Specimen C: real test pieces and FEM model of the core.

3.2.5 Methodology of the simulations and experimental tests

Quasi-static analyses were run for all components, consisting of a low speed crushing (about 1 mm/s) of the first 7 cm of the pieces. Additionally, three of the components were subjected to a dynamic drop tower test: specimen 0 for comparative purposes, specimen A for providing the best results in the quasi-static tests (see results section) and specimen C-cork, since fewer investigations on its behavior have been carried out. In these tests, a mass of 350 kg was dropped from a height of 2.5 m, impacting the components at an approximated speed of 6.7 m/s. A scheme and a photograph of the test device at CTAG facilities are provided in Figure 3.14.

Standard crashworthiness parameters were calculated for each one of the force-displacement curves obtained from quasi-static and dynamic tests results in order to assess their crash performance and facilitate their direct comparison. These indicators were: absorbed energy (E_{a}), specific energy absorption (SEA), mean crushing load (P_{m}), peak crushing load (P_{peak}) and load ratio (LR), described in Chapter 2.

Experimental tests were conducted at a constant crushing velocity of 1 mm/s, but simulations were sped up by running them at a mean rate of 12 mm/s. Therefore, a time scaling factor of 12 was applied to the quasi-static explicit simulations and the value of the reference strain rate was accordingly modified by the same factor. Moreover, a mass-scaling factor of 10 has been applied to the steel parts in our quasi-static simulations in order to obtain shorter computation times without affecting the quality of the results. This value was obtained by comparing the force-displacement curves for the same specimen with mass scaling factors

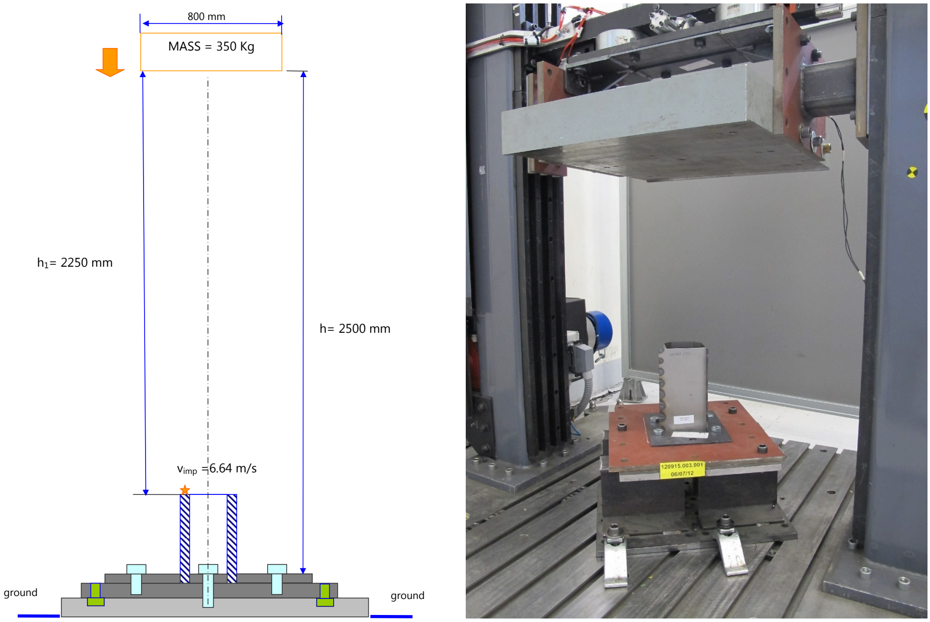

(a) Scheme of the drop tower rig. **(b)** Drop test device with component.

Figure 3.14: General scheme of the drop tower test set-up (CTAG).

of 1, 10, 100 and 1000. A factor of 10 produced a negligible error compared to the curve produced with no scaling. Applying any mass scaling to the cores, specially to A and B specimens, could lead to inaccurate results as a sudden failure of the laminae dislodges some fragments at a relatively high speed which usually hit other parts of the piece. If their mass is increased, these inertial effects could produce some distortion or noise in the results. Furthermore, according to the recommendations outlined in Chapter 2, the crushing load in the quasi-static analysis was smoothly ramped so that the kinetic energy was kept under a 5 % of the total energy. This energy check is provided in Figure 3.15 for the quasi-static analysis of a non-triggered component 0 with no residual stresses.

Eight processors in parallel were used for each analysis, each one computing one of the eight domains which the problem was divided into. 3000 megabytes of RAM were assigned to each processor. This 8-p 8-d configuration was proved to be the best for this problem, after testing other different configurations (up to 32 processors and many possible numbers of domains, always an even multiple of the number of processors, according to the recommendations by the software developers [146]). Double precision mode was activated in all the analyses due to

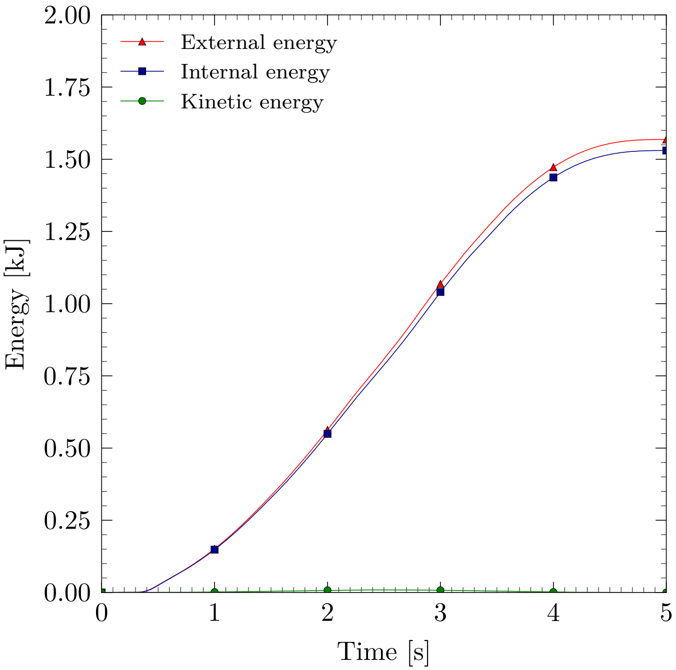

Figure 3.15: External, internal and kinetic energies during the quasi-static crushing simulation of a non-triggered component 0 without residual stresses. The smoothly ramped load can be glimpsed through the shapes of the three functions.

the extreme number of iterations, since results from single and double precision analyses differed in 5-10 % in this case. Computation was carried out in a high performance computing (HPC) cluster with a theoretical peak performance of 5.1 TFLOPS[2].

3.3 Tests and simulations results

3.3.1 Quasi-static crushing tests

Crushed steel boxes are depicted in Figure 3.16, showing a similar geometrical crushing pattern in the finite element model and in the experimental test. Pictures of the hybrid components after the experimental crushing test are shown in Figure 3.17. Some spot welds failed during the test, so lower forces could be expected in the experimental force-displacement curves compared to the numerical ones. Apart from that, the developed crushing modes and the behavior

---

[2] At the final stages of this thesis, the peak performance was increased up to 10.6 TFLOPS.

of the different inner reinforcements were very similar in both results. After the experimental test, cork and CFRP cores recovered almost its initial length due to their elastic properties, whereas simulations do not show this behavior because the tests ended when the loading plate was in the position of maximum displacement, i.e., spring-back was not simulated.

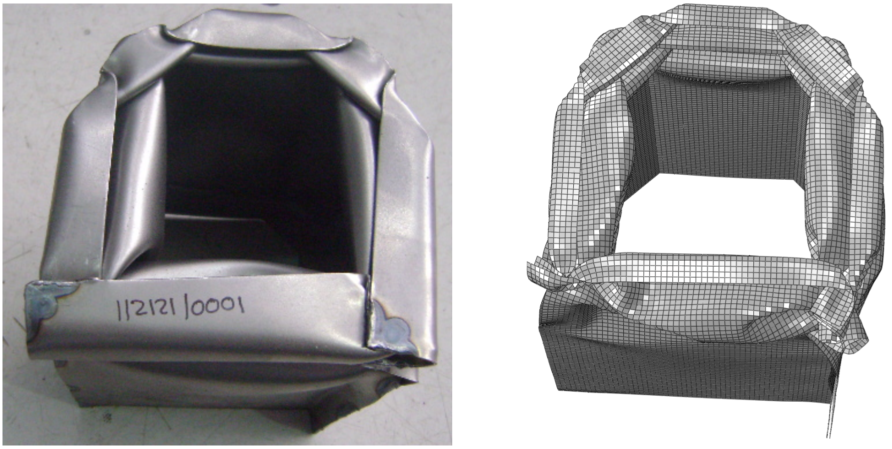

(a) Hardware component 0.

(b) Finite element model.

Figure 3.16: Steel box after axial crushing: hardware component and finite element model. The geometry of the folds was captured adequately.

Figures 3.19 and 3.20 show the force-displacement curves for the quasi-static crushing simulations and experimental test of all components, and the comparison parameters obtained from them are presented in Tables 3.5 and 3.6. Steel parts were 220 mm long, whereas cores A and B had a length of 200-210 mm with the aim of distributing the peak load, avoiding a higher peak at the beginning of the test. Thereby, the effects of crushing the core were perceptible only after the first 10–20 mm of crushing.

A remarkable fact is that in all the hybrid components, load ratios were softer than specimen 0. This factor has a notable influence on the severity of the injuries suffered by car occupants, since lower values indicate more constant loading and acceleration conditions. The idea of the offset for specimen A resulted in a distribution of their initial peak load in two lower peaks, which also reduced this factor. In fact, components A showed the best behavior in terms of load ratio.

GFRP and CFRP inserts were not perfectly aligned in the experiments. This resulted in a reduction of the peak force when the GFRP reinforcement started

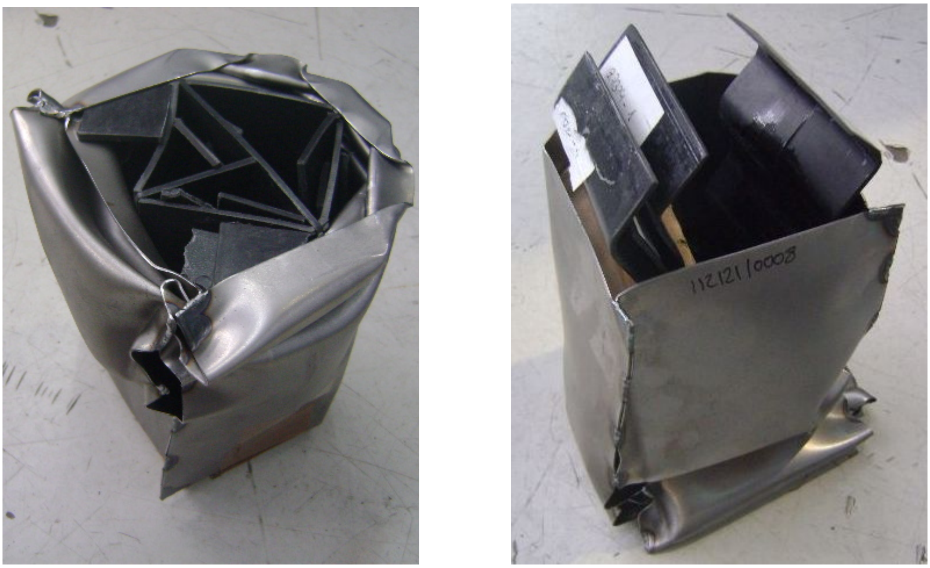

(a) Component A (GFRP). **(b)** Component B (CFRP).

(c) Component Cc (cork). **(d)** Component Cf (PET foam).

Figure 3.17: Components after experimental crushing test.

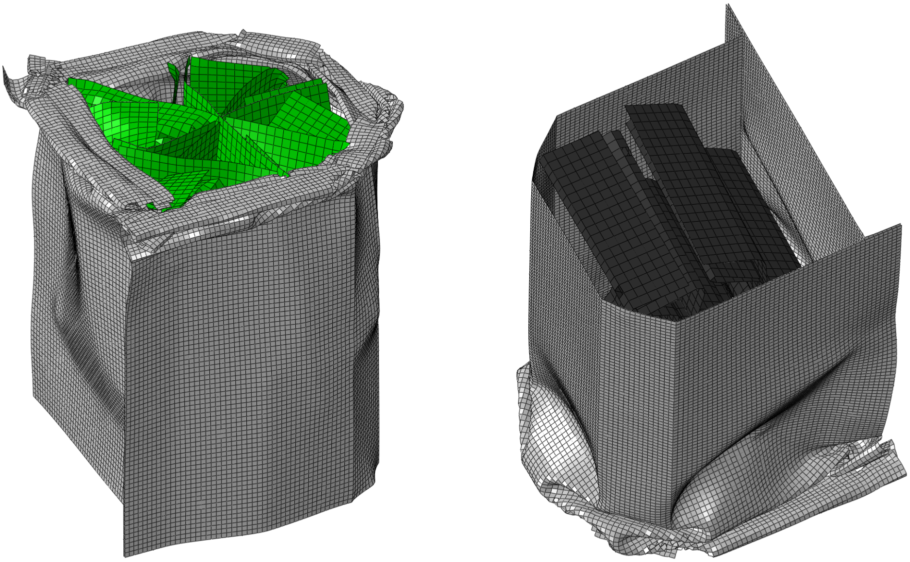

(a) Component A (GFRP). **(b)** Component B (CFRP).

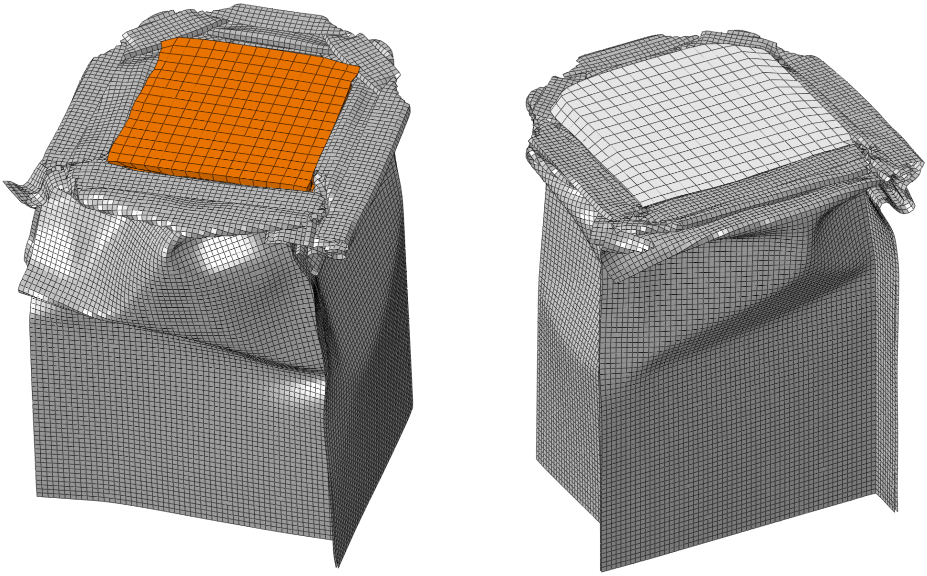

(c) Component Cc (cork). **(d)** Component Cf (PET foam).

Figure 3.18: Components after simulations of the crushing test.

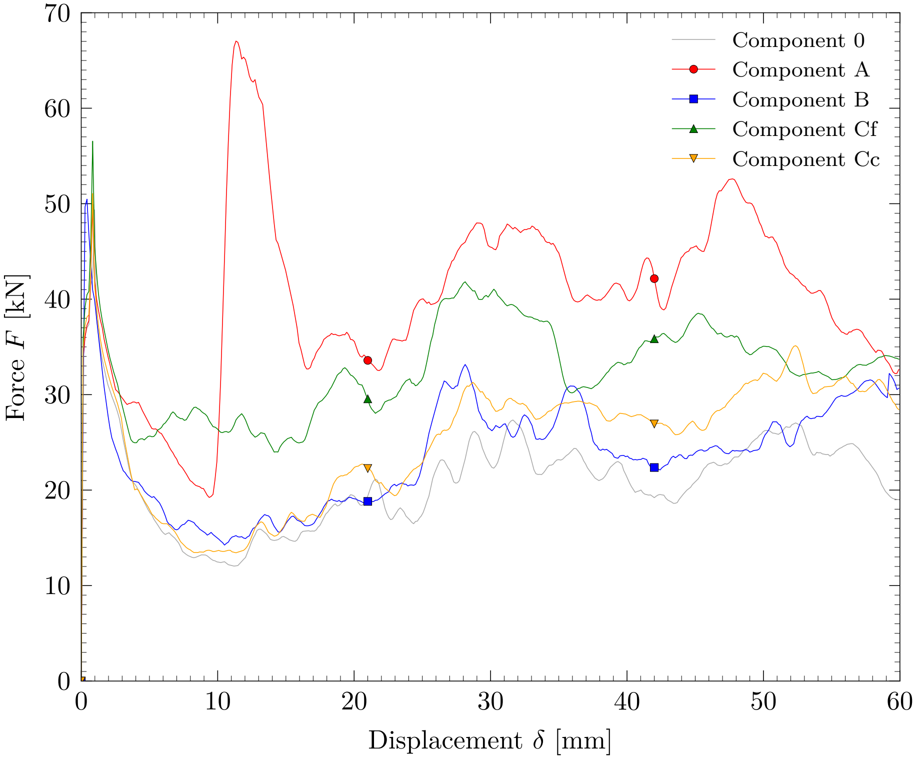

Figure 3.19: Force-displacement curves obtained in quasi-static simulations.

to be crushed due to the variation of the effective stiffness of the part. This effect did not appear in the CFRP core, since the laminates slid to the top corners of the specimen, even if they were perfectly aligned. To illustrate and measure this effect, a finite element analysis was run for different imposed initial displacements at the top end of the GFRP structure. The effect on the peak force of the complete crushing is shown in Figure 3.21. This effect did not appear in the dynamic tests due to the fact that the initial stroke of the mass on the top of the steel tube made the insert sway and misalign itself.

3.3.2 Impact tests

Force-displacement curves obtained in simulations and drop tower are provided in Figure 3.22, showing a good agreement between experimental and numerical results. A standard SAE-180 filter was applied to both results in order to remove high-frequency vibration noise. This filter consists of a two-pass, zero phase shift,

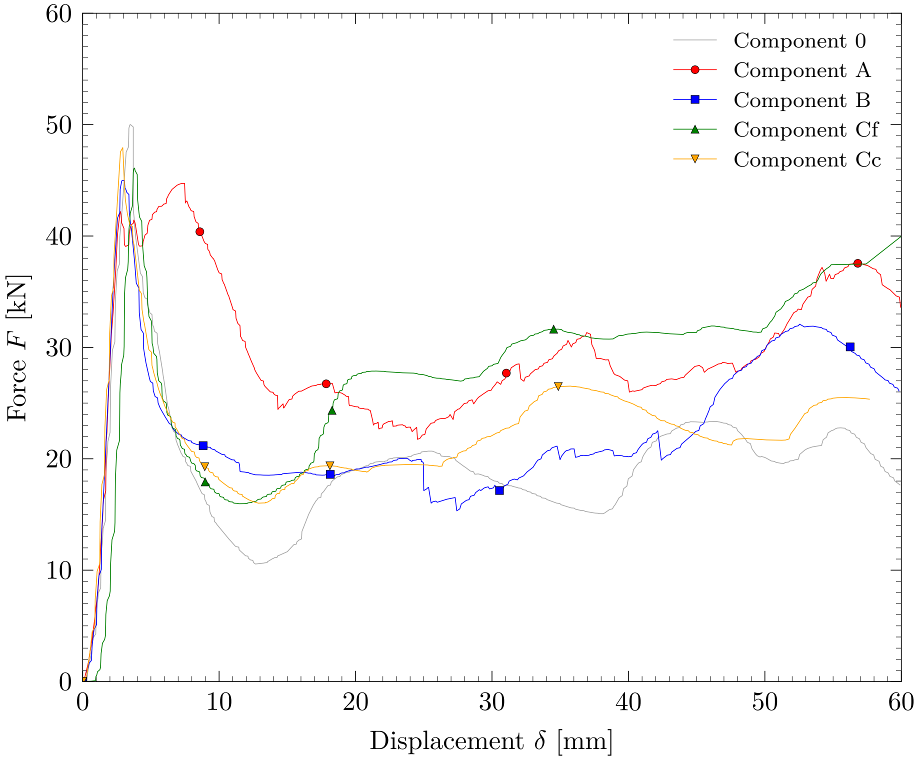

Figure 3.20: Force-displacement curves obtained in experimental quasi-static tests.

second-order Butterworth filter. The deformed configuration of the components (experimental and numerical) is presented in Figure 3.23.

Crashworthiness indicators obtained from these impact tests are provided in Table 3.7. It must be indicated that the cork-filled specimen sprang back after the test (this effect can be observed in the pictures and in the curve obtained from simulation only, since the experimental curve has been cropped). Therefore, it can be concluded that the studied cork agglomerate is not the best option for energy absorption applications, since a part of the stored energy was sprung back after crushing. In particular, the cork padding inside the tube recovered its length up to 160 mm of an original length of 220 mm.

Component label	E_a [kJ]	SEA [kJ/kg]	P_m [kN]	P_peak [kN]	LR
0	1.25	6.11	20.83	49.35	2.37
A	2.40	7.39	40.00	*67.04	1.68
B	1.50	5.78	25.00	50.01	2.00
C - cork	1.51	5.27	25.17	51.07	2.03
C - foam	1.96	7.31	32.67	56.55	1.73

Table 3.5: Energy absorption parameters obtained from simulations. An asterisk indicates that the maximum load value was not produced at the beginning of the test (see curves in Figures 3.19 and 3.20).

Component label	E_a [kJ]	SEA [kJ/kg]	P_m [kN]	P_peak [kN]	LR
0	1.17	5.72	19.50	50.01	2.56
A	1.78	5.48	29.67	*44.73	1.51
B	1.35	5.21	22.50	45.01	2.00
C - cork	1.28	4.47	21.33	47.94	2.25
C - foam	1.60	5.97	26.67	46.01	2.25

Table 3.6: Energy absorption parameters obtained from experimental tests. An asterisk indicates that the maximum load value was not produced at the beginning of the test (see curves in Figures 3.19 and 3.20).

3.4 Discussion of results

3.4.1 General discussion

In the light of the obtained results, it can be concluded that an acceptable correlation between experimental and computational data was achieved. The most remarkable differences appeared comparing the results for GFRP-filled components, although in both cases (experimental and numerical) they showed a very good behavior, being the best in experimental tests. This difference and the reason why components A were not as good as Cf (foam-filled) in real tests was due to the handcrafting process to build specimens A in the laboratory. As can be slightly appreciated in Figure 4.4, the cross-shaped core elements were built by fixing two separated pieces, thus the resulting hardware pieces were not totally straight. The crushing forces were therefore softer for real components than for the perfectly-aligned FE model. In the final prototype, the thermoplastic core would be built by injection, which would produce much stiffer results. Although in this investigation the paddings were not glued to the steel outer part, final prototypes might require an adhesive joint between them, to produce optimal

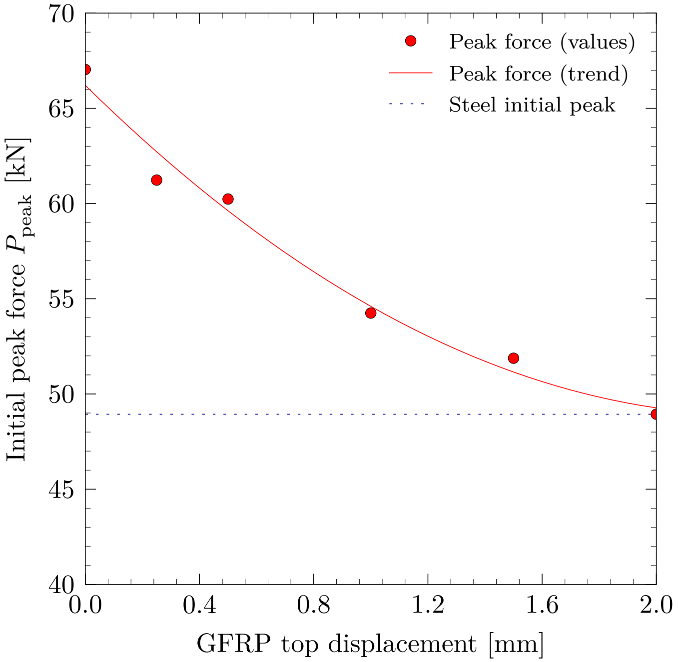

Figure 3.21: Effect of an initial misalignment of the GFRP plates on the initial peak crushing force of component A (FE simulation).

results and to avoid noise and vibration problems.

Furthermore, curves produced by experimental testing showed lower load values than the ones produced in simulations. This difference is due to the failure and opening of some spot welds, specially in the quasi-static analyses, producing a softening of the crushing process. This effect can be simulated with the finite element software, but we preferred to keep results without failures since the final prototype would be more accurately welded and no failure was expected.

In addition, although *SEA* results were quite close between components A and Cf (foam), we must remark the fact that, for longer crushing distances, the load-displacement curves for A increased due to a progressive compacting of the core elements and dislodged fragments, while curves for foam-filled tubes remained in similar values due to the progressive collapse of inner cells in the foam. To sum up, specimens A showed the best behavior in terms of absorbed energy and specific energy absorption.

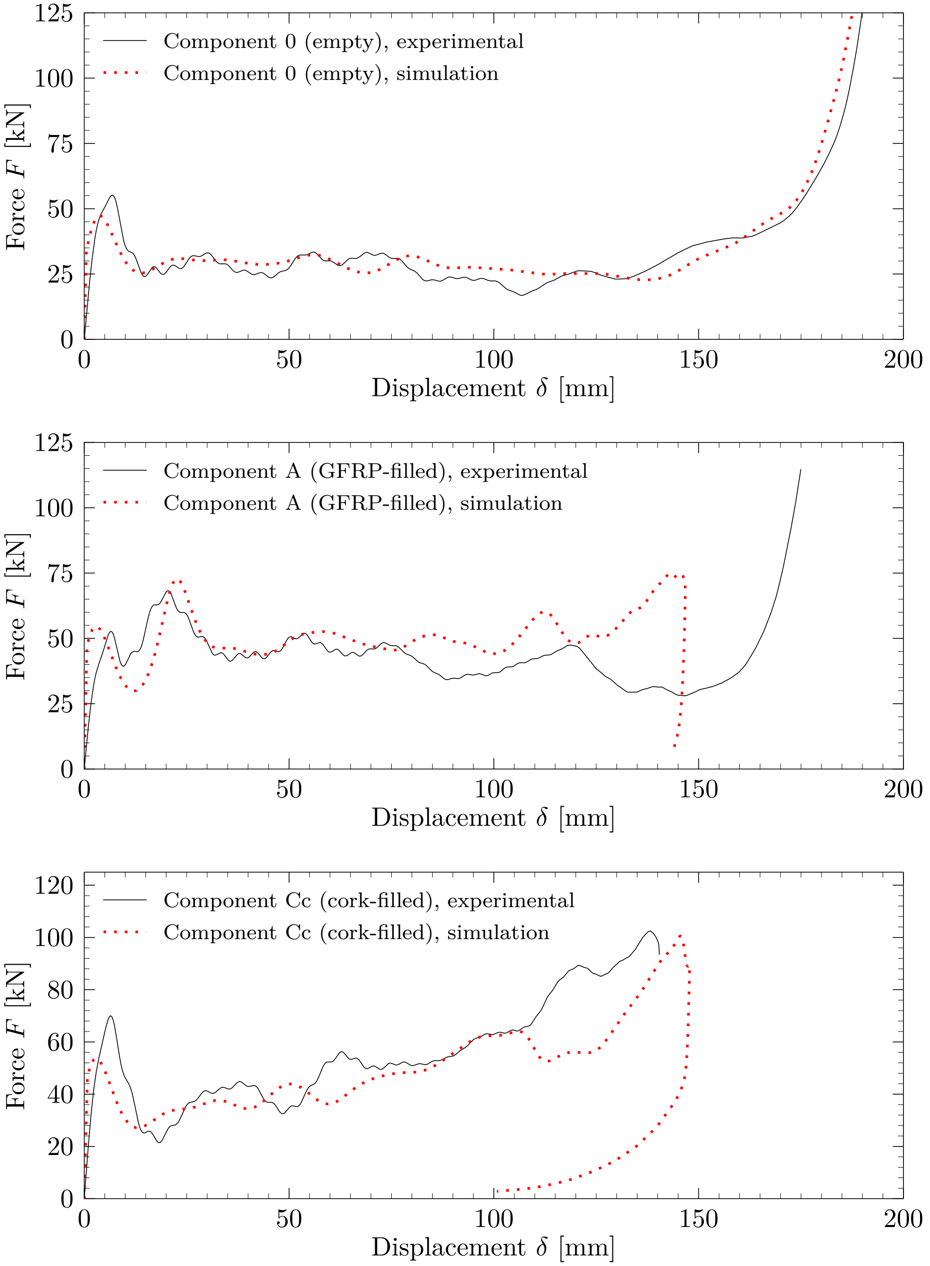

Figure 3.22: Force-displacement curves obtained in the impact tests. Experimental and numerical results for specimens 0, A and Cc.

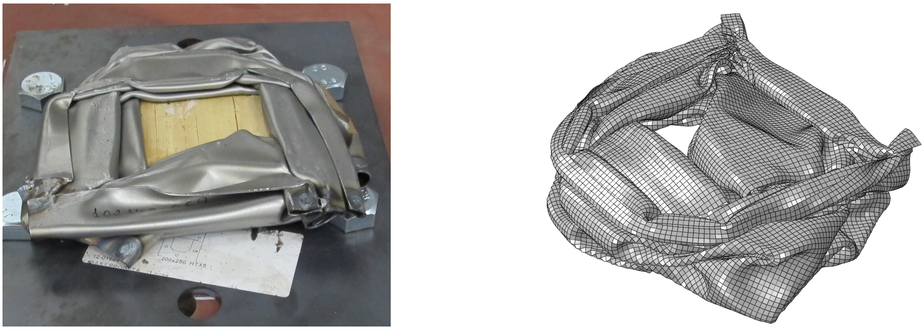

(a) Specimen 0 - Experimental. **(b)** Specimen 0 - Simulation.

(c) Specimen A - Experimental. **(d)** Specimen A - Simulation.

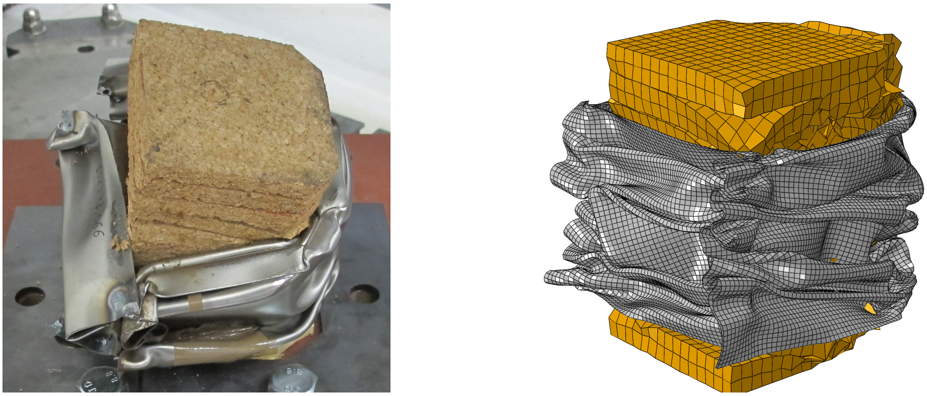

(e) Specimen Cc - Experimental. **(f)** Specimen Cc - Simulation.

Figure 3.23: Final state of the components after experimental impact tests and simulations.

Test	δ_{max} [cm]	S_{E} [%]	$E_{\text{a}}\,(\delta_{\text{max}})$ [kJ]	*SEA* [kJ/kg]	P_{m} [kN]	P_{peak} [kN]	*LR*
0 exp.	16	72.73	4.55	6.07	28.44	55.20	1.94
0 sim.	16	72.73	4.69	6.25	29.29	47.32	1.62
A exp.	16	72.73	6.96	5.82	41.81	*68.24	1.63
A sim.**	>14.67	>66.68	>7.83	>6.81	53.36	*72.95	1.37
Cc exp.	12.70	57.73	5.72	5.45	45.03	70.03	1.56
Cc sim.	12.50	76.82	5.80	5.52	46.33	53.69	1.16

Table 3.7: Energy absorption parameters obtained from experimental and simulation impact tests. An asterisk indicates that the maximum load value was not produced at the beginning of the test. Two asterisks indicate that the specimen did not reach its maximum crushing distance (no 'bottoming-out' was observed), hence, the absorbed energy was equal to the total launched energy.

Some improvements in specimen B could be achieved by changing the orientation of the laminates, making the curved boundaries to contact with the loading and reaction plates. This set-up has been proved to be very efficient in recent investigations like [163], and could even reach better results than components A since their crushing process is very similar.

Components A showed the best energy absorption characteristics. The mechanism behind this behavior consists of a regular folding of the steel part according to the typical folding mechanism for angled elements. In particular, an approximate scheme of this folding pattern for the steel part is idealized in Figure 3.24.

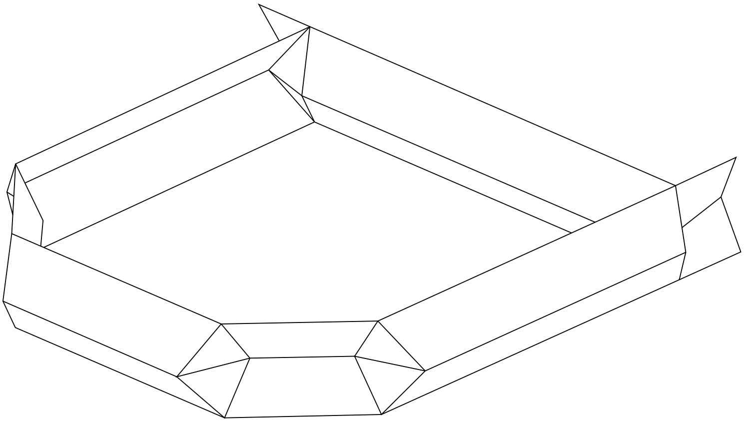

Figure 3.24: Folding scheme of the steel part.

The cork padding placed into components Cc presented the same behavior in the experimental tests and the finite element prediction. The core sprang back after impact, as depicted in Figure 3.25a, recovering almost its initial position (16 of 21.6 centimeters). No external damage or fracture was observed in the cork slices after the test, but internal collapsing of the material cells was present, leading to a reduction of the height of the slices. A close view of two slices after the test is offered in Figure 3.25b.

(a) Spring-back of the cork slices. **(b)** Close view of two slices.

Figure 3.25: Close view of the cork spring-back effect and two slices after impact.

A detailed observation of the steel tubes after tests showed that no fracture was present on the specimen, apart from the opening of a few spot welds. In the finite element model, the selected ductile failure model removed from the analysis only very few elements in the folding of the corners at 90 °. A close view of the steel tube is shown in Figure 3.26, where the opening of the first spot weld on the right side can be observed.

Thermoplastic inserts of specimen A collapsed by fragile fracture producing residual fragments which were between 2 and 4 centimeters long (see Figure 3.23c). A close view of the debris is offered in Figure 3.27a, showing the failure of both matrix and short chopped glass fibers. For comparative purposes, a view of the damaged finite element model is shown in Figure 3.27b, in which a similar fracture behavior can be observed. According to this kind of fracture, the thickness of these parts should have a direct effect on the final quantity of absorbed energy. In order to study this influence, a parametric study was carried out, which is offered in the next section.

Figure 3.26: Specimen 0 after impact. Plasticity phenomena without fracture.

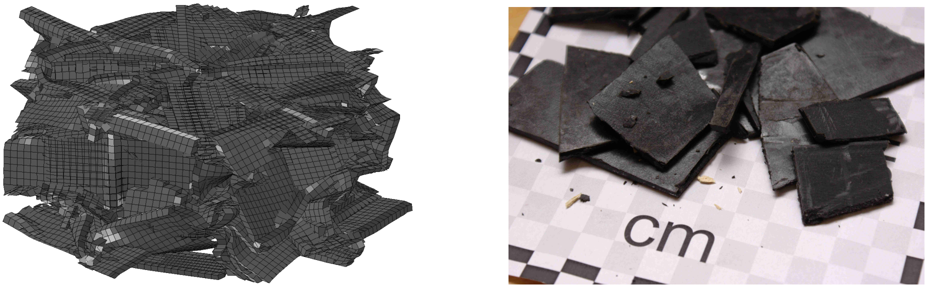

(a) GFRP debris (FE model).

(b) GFRP debris (real).

Figure 3.27: Comparative image of the GFRP residual and the numerical prediction.

3.4.2 Parametric analysis of component A

With the aim of understanding the influence of the wall and reinforcement thicknesses on the energy absorption characteristics of component A, a parametric study was conducted. Two different cases were considered: a first case where all the inner parts have the same thickness and a second one where two different thicknesses are considered; one for the large central cross and a different one for the external smaller crosses. Thicknesses ranged between 2 and 4 millimeters for the GFRP parts and between 0.87 and 2.44 mm for the steel walls. The analyses run for this sensitivity study slightly differed from the previous dynamic analysis, since using the same configuration had resulted in different crushing lengths for the different specimens. In this case, components were crushed up to a crushing distance δ of 12 centimeters at a constant speed of 6.7 m/s. From the simulations, the specific energy absorption of each design was computed and plotted in a contour graph to understand its dependency on the thickness of the different parts. It is worth mentioning that the specific energy absorptions were obtained by dividing the absorbed energy by the fraction of the part's mass corresponding to the 12 crushed centimeters.

For the first case, a uniform thickness was assigned to the thermoplastic reinforcements and a different one for the steel part, in order to show the influence of each part on the final specific energy absorption. The result of this analysis is provided in Figure 3.28, showing a higher sensitivity to the steel thickness than to the reinforcement thickness. This indicates that the increase in the steel thickness, and therefore in the mass of the specimen, is worthy thanks to the gain in the absorbed energy.

For the second case, the thickness of the steel part was kept constant and equal to 1.74 mm and two variable values were assigned to the thickness of the two GFRP parts. Results are provided in Figure 3.29. A stronger influence of the secondary cross thickness was observed, which indicated a higher contribution to the specific energy absorption compared to the main cross.

3.5 Influence of the number and distribution of the spot welds

In this section, the effect of welded joints on the crashworthiness response of the previously studied components is presented. Results showed that variations in the number or the geometric distribution of the spot welds have a direct and noticeable effect on the final amount of energy that the part can dissipate. This is due to the crushing mechanism of the metallic column which is highly sensitive to the way that cold-formed sections are joined. From these results, several design

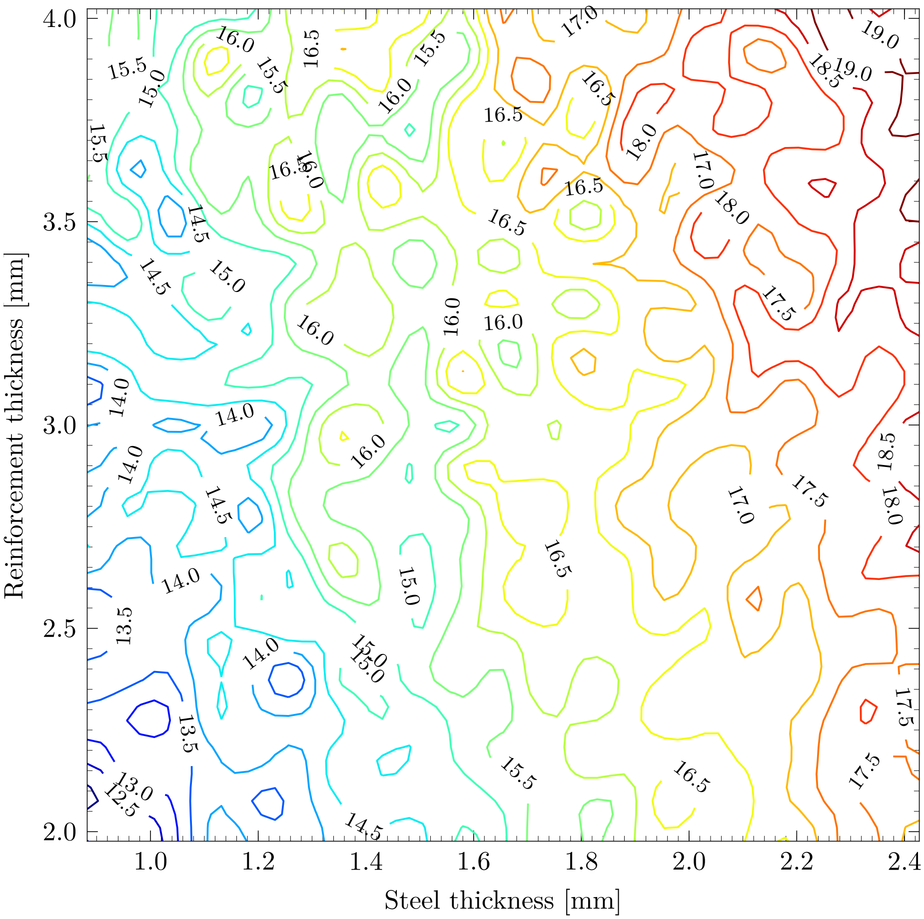

Figure 3.28: Specific energy absorption for different steel and GFRP thickness.

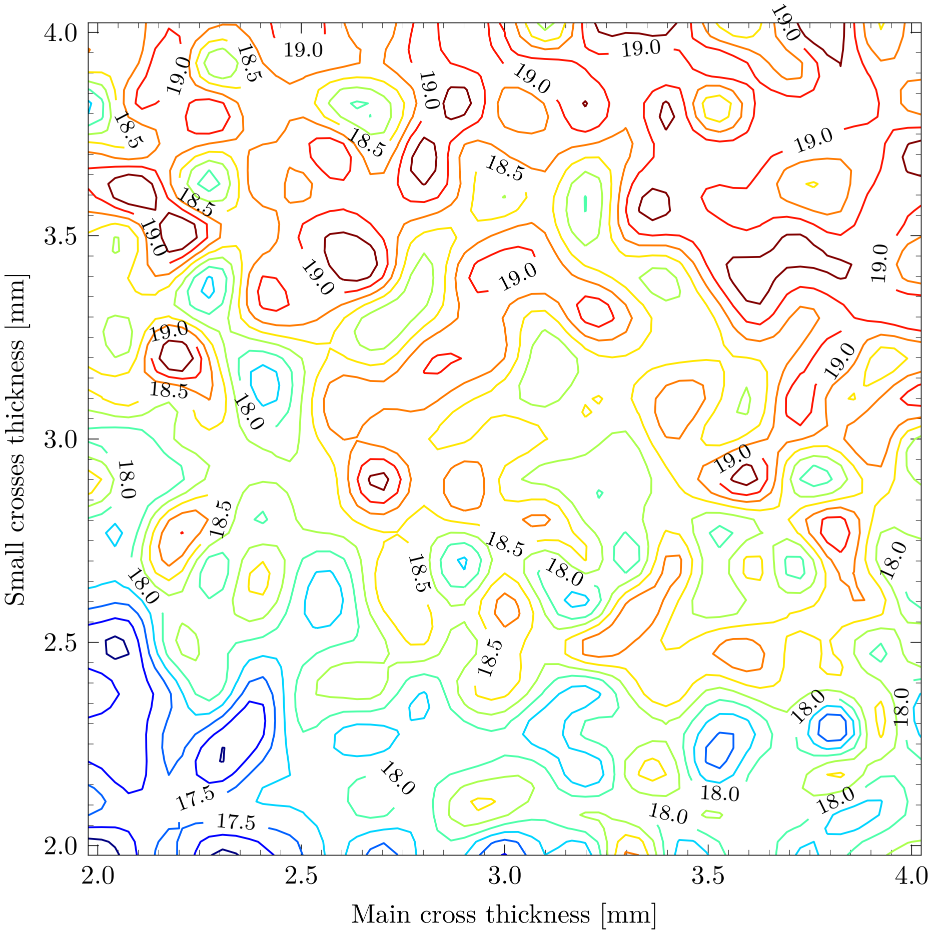

Figure 3.29: Specific energy absorption for different values of reinforcement thickness.

recommendations can be proposed for the design of hybrid elements with welded joints, depending on the geometrical and material properties of the system.

Previous research about this topic includes the works by Nex and Smith [164] in 1998, who mentioned an influence of the spacing between spot welds on the crushing modes of a steel hat section. In 2003, Schneider and Jones [165] studied the failure of spot welds in steel columns subjected to axial crushing, and its influence on their crashworthiness properties. Peroni et al. [166] compared the crashworthiness of steel columns joined by different procedures (spot welds or continuous welding by laser or adhesives), stating some advantages of the continuous welds over the spot welds. Xiang et al. [149] published in 2006 an investigation on the optimal design of spot-welded hat sections, where they do a brief analysis with a variable number of spot welds, which is in line with the results obtained in this section.

Therefore, the main goal in this section is to find out to what extent the welding pattern affects the energy absorption of these devices. In that regard, a study was carried out to obtain values of absorbed energy from a dynamic impact numerical analysis of components with different welding configurations.

Spot welds were placed according to three different distributions (see Figure 3.30). Distribution 1 consisted in a uniform and evenly-spaced pattern. Distributions 2 and 3 were set according to a geometric (quadratic) series with spot welds concentrated towards the impact or reaction areas of the specimen, respectively. The number of spot welds ranged between 2 and 14, both included. In all the possible combinations of number of spot welds and distributions, two of the spot welds were always placed at the ends of the specimen with an offset of 5 mm between them and the edge of the piece. Thus, the spot welds were distributed in a total length of 210 mm and placed along the middle line of the flanges.

A dynamic impact simulation was run for each specimen. These tests consisted of dropping a mass of 700 kg on the components from a height of 2.5 m. The resulting force-displacement curves allowed the study of the crashworthiness characteristics of each specimen. Only the data of the first 13 cm of crushing was considered, since bottoming-out of some components started at a crushing distance of 140-170 mm (depending also on the collapse mode of the specimen, which was influenced by the welding patterns). A mass of 700 kg guaranteed that even the strongest specimen was crushed until 130 mm.

Force-displacement curves were obtained for each specimen, varying the number of spot welds and their distribution. Figure 3.31 shows the results obtained for evenly-spaced spot welds for all components.

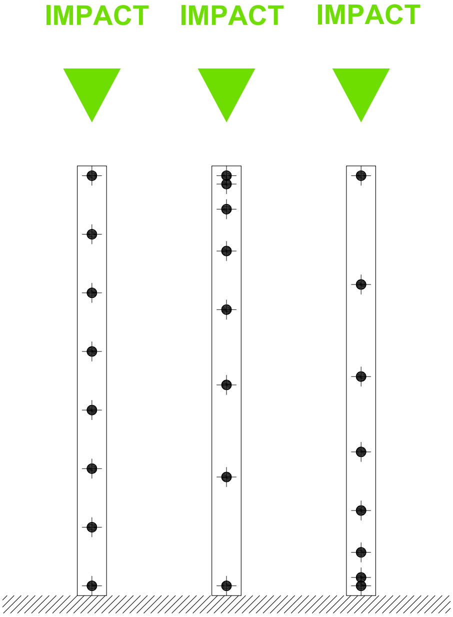

Figure 3.30: Spots distributions 1, 2 and 3 (eight spot welds).

In Figure 3.31, it can be observed that the GFRP-filled tubes (component A) showed, undoubtedly, the best results for any number of spot welds regarding the absorbed energy. Even with two spot welds, the resulting piece absorbed more energy than the second better (foam-filled) with the maximum number of spot welds. In line with what was described in previous sections, components B showed the lowest absorbed energies of all the hybrid parts, foam-filled profiles (Cf) showed very good absorptions, close to those obtained for component A; and cork-filled tubes (Cc) showed a good energy absorption too. Even though cork showed a good result, the performance of the foam-filled sections was slightly better for any distribution of spot welds. Additionally, foam actually absorbed the kinetic energy of the impact while cork worked as an accumulator – a remarkable part of the energy is sent back to the mass after the collision.

Regarding the number of spot welds, a remarkable fact is that the foam-filled tube seemed to be less sensitive to variations in the number of spot welds than the others. This was mainly due to the fact that the foam core itself can regulate in a certain way the crushing mechanism of steel, since the tube was completely filled by the core and the contact between both materials constrains the tube walls making their collapse more stable, even for a low number of spot welds. In the

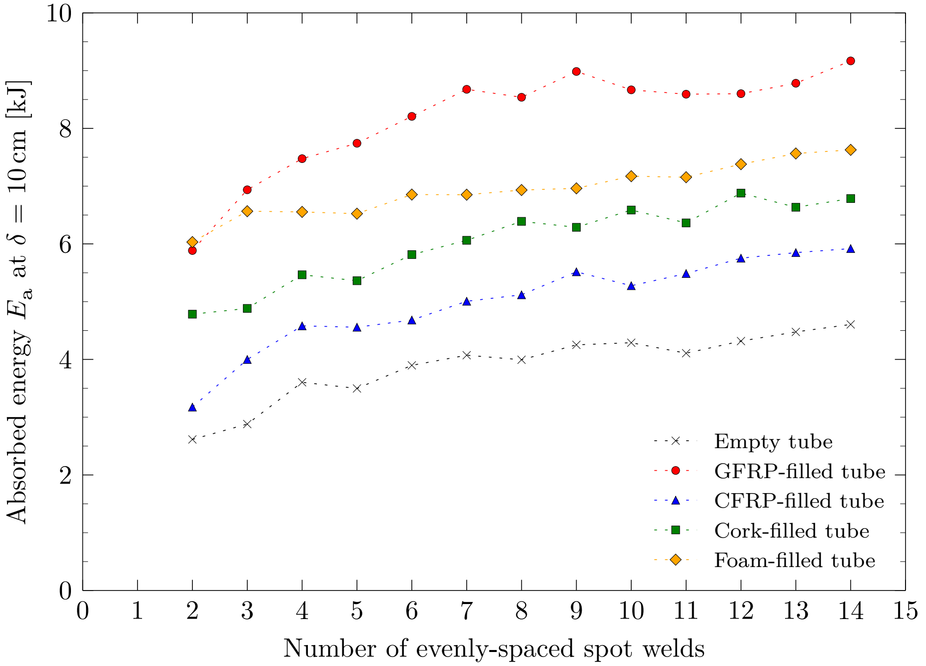

Figure 3.31: Energy absorption for all specimens with a uniform distribution of the spot welds.

light of Figure 3.31, components A showed a remarkable sensitivity to variations in the number of spot welds. Therefore, the production of these pieces should take into account this last fact. Regarding the differences in the energy absorbed by the three possible configurations of the spot welds (Figure 3.32), distribution 1 (evenly spaced spot welds) seemed to show a better response than the others (spot welds concentrated at one end of the part), but nothing can be clearly stated about the existence of any significant difference between distributions 2 and 3. Hence, a concentration of the spot welds in one of the specimen's ends was not useful in terms of crashworthiness.

Some pictures of specimen 0 with evenly spaced spot welds are provided in Figure 3.33 in order to compare the evolution of the crushing modes when the number of spot welds is changed. Two parts of the specimen with a different behavior could be observed. The crushing mode of the L-shaped part was strongly dependent on the number of spot welds: the more spot welds, the more folds were developed. The curved plate showed the typical collapse mode for angled elements at the beginning, but the differences in the lobe lengths between this

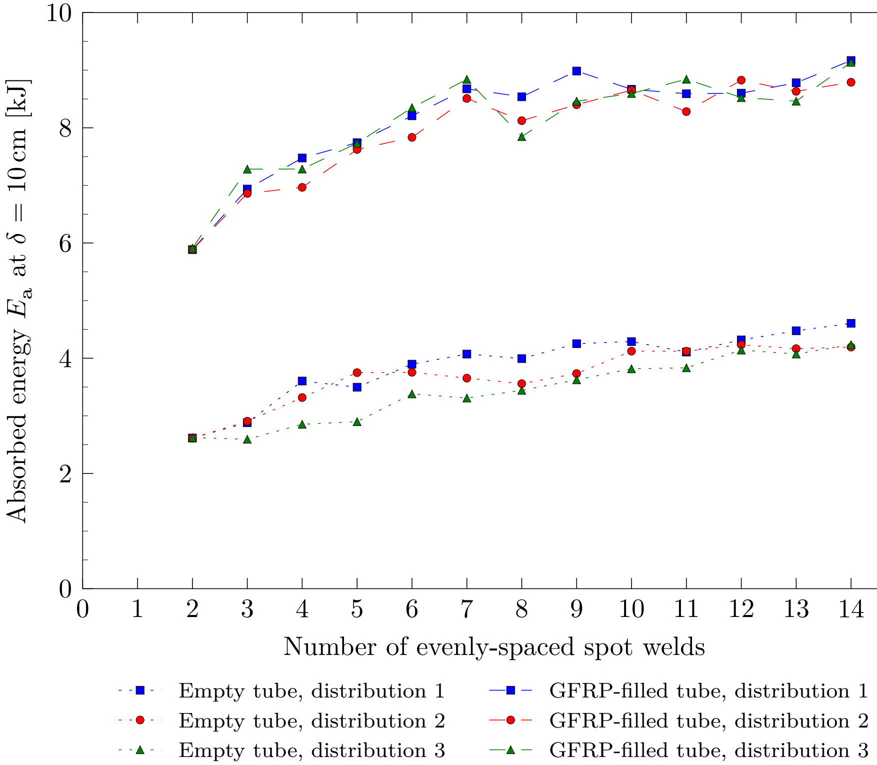

Figure 3.32: Energy absorption for specimen 0 (empty) and specimen A (GFRP-filled) with different distributions of the spot welds.

part and the L-shaped one made that, at a certain point, an angled fold in the curved part triggered a non-stable collapse mode. Thus, it can be seen that the disposition of the spot welds was mainly affecting the crushing mode of the L-shaped sheet.

In the light of these results, a remarkable influence of the disposition and number of spot welds on the crashworthiness of hybrid elements was observed. Those patterns with evenly spaced spot welds along the flanges showed, in general terms, the best behavior. The main reason was the absence of long distances without spot welds which promoted the formation of larger folds, leading to untapped areas.

The number of spot welds showed also a direct effect on the quantity of absorbed energy for all the components configurations. In general, less than six spot welds per row (with a separation between consecutive spots of a 16.7 % of

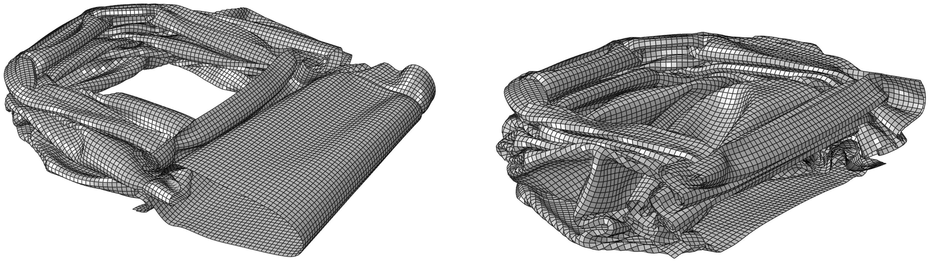

(a) 2 spot welds. **(b)** 6 spot welds.

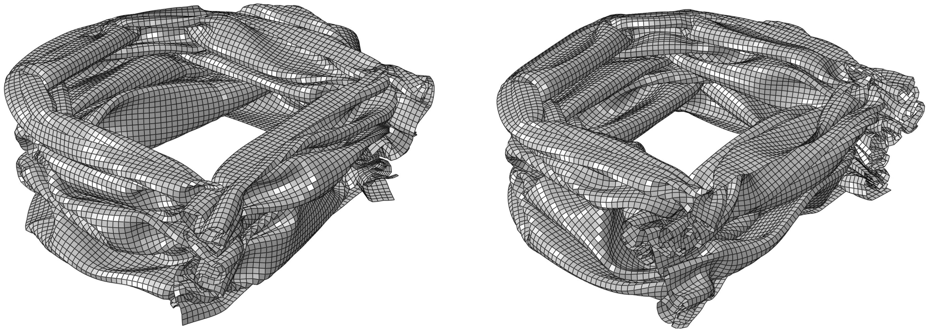

(c) 10 spot welds. **(d)** 14 spot welds.

Figure 3.33: Evolution of the crushing modes when the number of spot welds is changed.

the total length) should be disregarded as large sections of the steel part were not progressively folded (it can be recalled here that Jones indicated a 10 % as the minimum distance for empty tubes, see Chapter 2). For more than six spot welds, the amount of absorbed energy increased at a slow rate, and the optimum design should be a decision taken by the manufacturer depending on economic reasons and the configuration of the production line.

3.6 Conclusions

Five different configurations of a car crash absorber were analyzed in experimental tests and numerical simulations with a good agreement between them. Results showed a general improvement in terms of energy absorption of all the filled components in comparison with the original empty crash box. However, if the specific energy absorption is regarded, the tube with corrugated CFRP inserts (component B) and the cork-filled tube (component Cc) should be re-designed or discarded, since the results of the simulations showed that the gain in absorbed energy did not compensate for the increase in mass.

The tube with GFRP inserts (Specimen A) exhibited the best results, and the influence of its components on its total specific energy absorption was studied.

When it comes to cost reduction, PET foam-filled tubes (Cf) are an option to take into consideration, as materials and production costs should be much more affordable than GFRP (component A). Even though results for longer crushing distances showed a decrease in efficiency when comparing to the solution with GFRP inserts, PET foam was undoubtedly a very good filler.

Cork-filled tubes showed the lowest *SEA* results in both experimental and numerical results, and presented a more elastic behavior, although its economical cost was the most competitive among all cores.

The effect of different distributions of spot welds on the crashworthiness properties of several multi-material components has been analyzed, showing a strong influence of the welding pattern on the final performance of the part. As a general rule, if the ratio of the number of spot welds over the length of the part's crushing distance is less than 0.27, the crash box is not fully utilized to absorb energy. In this case, at least 6 spot welds must be applied to obtain acceptable results. About the pattern of these spot welds, its concentration in the impact or reaction ends of the piece did not show better results than an evenly-spaced pattern along the length of the flange, so a uniform configuration is recommended.

Regarding the methodology, explicit analyses were an excellent tool for solving problems in which high nonlinearities are involved in an affordable time, even if these problems consisted of slow loading or low inertial effects, as long as some requirements were fulfilled.

References

[5] J. De Kanter. "Energy absorption of monolithic and fibre reinforced aluminium cylinders". PhD thesis. Faculty of Aerospace Engineering - Delft University of Technology, 2006.

[10] M. Costas, J. Díaz, L. Romera, S. Hernández, and A. Tielas. "Static and dynamic axial crushing analysis of car frontal impact hybrid absorbers". *International Journal of Impact Engineering* 62 (2013), pp. 166–181.

[127] C. Gameiro and J. Cirne. "Dynamic axial crushing of short to long circular aluminium tubes with agglomerate cork filler". *International Journal of Mechanical Sciences* 49.9 (2007), pp. 1029–1037.

[129] M. Paulino and F. Teixeira-Dias. “An energy absorption performance index for cellular materials - Development of a side-impact cork padding”. *International Journal of Crashworthiness* 16.2 (2011), pp. 135–153.

[144] M. Costas, J. Díaz, L. Romera, S. Hernández, and R. Ledo. “Influence of welded joints on the crashworthiness response of hybrid structural elements”. *SAE Technical Papers* 2 (2013).

[145] M. Costas, L. E. Romera, J. Díaz, S. Hernández, and A. Tielas. “Computational and experimental analysis of a hybrid car impact absorber”. *Computational Methods and Experimental Measurements XVI* 55 (2013).

[146] *ABAQUS 6.11 Documentation.* Dassault Systèmes. Providence Road, Rhode Island. 2011.

[147] J. Seidt. “EOD material characterization, supplemental reports: constitutive and fracture models for ASTM A36 hot rolled steel”. *Battelle Technical report prepared for the Naval Explosive Ordenance Disposal Technology Division, Columbus, Ohio* (2005).

[148] X. Zhang and H. Zhang. “Experimental and numerical investigation on crush resistance of polygonal columns and angle elements”. *Thin-Walled Structures* 57 (2012), pp. 25–36.

[149] Y. Xiang, Q. Wang, Z. Fan, and H. Fang. “Optimal crashworthiness design of a spot-welded thin-walled hat section”. *Finite Elements in Analysis and Design* 42 (2006), pp. 846–855.

[150] BASF. *Ultramid (R) A3WG10 BK00564 Polyamide 66. Product information sheet.* 2012.

[151] E. Totry, J. Molina-Aldareguía, C. González, and J. Llorca. “Effect of fiber, matrix and interface properties on the in-plane shear deformation of carbon-fiber reinforced composites”. *Composites Science and Technology* 70.6 (2010), pp. 970–980.

[152] F. Garattoni. “Crashworthiness and composite materials: development of an experimental test method for the energy absorption determination and implementation of the relative numerical model”. PhD thesis. Universitá di Bologna, 2011.

[153] Z. Haszin. “Failure criteria for unidirectional fiber composites”. *Journal of Applied Mechanics, Transactions ASME* 47.2 (1980), pp. 329–334.

[154] Z. Hashin. “Fatigue failure criteria for unidirectional fiber composites”. *Journal of Applied Mechanics, Transactions ASME* 48.4 (1981), pp. 846–852.

[155] S. Jose, K. Kuma, M. Jana, and G. Rao. “Interlaminar fracture toughness of a cross-ply laminate and its constituent sub-laminates”. *Composites Science and Technology* 61.8 (2001), pp. 1115–1122.

[156] V. Deshpande and N. Fleck. “Isotropic constitutive models for metallic foams”. *Journal of the Mechanics and Physics of Solids* 48.6–7 (2000), pp. 1253–1283.

[157] J. Zhang, N. Kikuchi, V. Li, A. Yee, and G. Nusholtz. “Constitutive modeling of polymeric foam material subjected to dynamic crash loading”. *International Journal of Impact Engineering* 21.5 (1998), pp. 369–386.

[158] A. Micuzzi and G. Elvira. “Caracterización computacional de placas de espuma de poliestireno expandido bajo cargas dinámicas de impacto”. In: *IBEROMET XI, X CONAMET/SAM*. 2010.

[159] M. Paulino, F. Teixeira-Dias, C. Gameiro, and J. Cirne. “Hyperelastic and dynamical behaviour of cork and its performance in energy absorption devices and crashworthiness applications”. *International Journal of Materials Engineering Innovation* 1.2 (2009), pp. 197–234.

[160] C. Gameiro, J. Cirne, and G. Gary. “Experimental study of the quasi-static and dynamic behaviour of cork under compressive loading”. *Journal of Materials Science* 42.12 (2007), pp. 4316–4324.

[161] S. P. Silva, M. A. Sabino, E. M. Fernandes, V. M. Correlo, L. F. Boesel, and R. L. Reis. “Cork: properties, capabilities and applications”. *International Materials Reviews* 50.6 (2005), pp. 345–365.

[162] C. Gameiro, J. Cirne, V. Miranda, J. Pinho-Da-Cruz, and F. Teixeira-Dias. “Dynamic behaviour of cork and cork-filled aluminium tubes: Numerical simulation and innovative applications”. *Holzforschung* 61.4 (2007), pp. 400–405.

[163] V. Sokolinsky, K. Indermuehle, and J. Hurtado. “Numerical simulation of the crushing process of a corrugated composite plate”. *Composites Part A: Applied Science and Manufacturing* 42.9 (2011), pp. 1119–1126.

[164] C. Nex and R. Smith. “Impact performance of model spot welded stainless steel structures”. *Experimental Mechanics* (1998).

[165] F. Schneider and N. Jones. “Influence of spot-weld failure on crushing of thin-walled structural sections”. *International Journal of Mechanical Sciences* 45 (2003), pp. 2061–2081.

[166] L. Peroni, M. Avalle, and G. Belingardi. “Comparison of the energy absorption capability of crash boxes assembled by spot-weld and continuous joining techniques”. *International Journal of Impact Engineering* 36 (2009), pp. 498–511.

4

Optimization of metal tubes internally reinforced with GFRP structures

This chapter deals with the optimization of component A (i.e., steel tubes internally reinforced with a GFRP skeleton) based on the results of Chapter 3. Two different optimization approaches were studied here and compared: a multi-objective optimization using adaptive surrogate models and a Fletcher-Reeves conjugate-gradient method, and the same optimization using fixed surrogate models and a multi-objective genetic algorithm. A part of the work presented here was published by the author in a peer-reviewed article [11] and in an international conference [19]. Furthermore, the author co-authored three additional peer-reviewed articles on the multi-objective crashworthiness optimization of an aluminum extrusion filled with a GFRP honeycomb for automotive [167] and aeronautical [15] applications, and the reliability-based, constrained multi-objective optimization of components type A using hybrid approximations [168]. These last three works were not a part of the present thesis, so they were not included in this document.

In the field of surrogate-based crashworthiness optimization, the first attempts date from late 1990s, when K. Yamazaki [169] used an approximate response surface to maximize the crushing energy of square and circular tubes, with the aim of using the minimum number of finite element structural analyses. Later in 2001, P.O. Marklund and L. Nilsson [170] applied linear and quadratic approximations to minimize the mass of a car B-pillar, which was reduced by 25 % maintaining the safety requirements. In the same year, J. Sobieszczanski-Sobieski et al. [171] carried out a size optimization of a full car body finite element model under constraints of noise, vibration and harshness (NVH) and crash using different approximations, and reducing the mass of the car body. In 2003, T. Jansson et al. [172] successfully applied surrogate models and response surfaces to engineering problems of sheet metal forming and crashworthiness design with a limited number of design variables. Fast improvements in computation capabilities allowed a rapid increase of the problem size and the solution accuracy. In 2007, S. Hou et al. [173] carried out an optimization of hexagonal metal tubes taking as objective functions the specific energy absorption and the peak crushing load by means of a surrogate approach built up from a full-factorial sampling strategy of finite element models. The same authors attempted and optimization of a hybrid foam-filled thin-walled metal structure via surrogate-based meta-modeling in 2009 [118]. Since then, similar investigations on single-material and foam-filled crashworthy parts can be found in the literature, including indentations or grooves on the metal part [174], or based on different tube geometries like circular [121] or square [123] tapered metal tubes, with or without a foam filling. In 2013, the performance of different surrogate models, including robustness or reliability criteria, was evaluated in [175], and vibrations design criteria were also recently taken into consideration [176]. The presence of the specific energy absorption as objective function is common in most of the investigations on this topic. Occupant's safety is also taken into consideration by means of the peak force or the load ratio, which was preferred for this section.

4.1 Multi-objective optimization using a conjugate-gradient method

4.1.1 Optimization problem and methodology

The goal of this section was to improve the crash performance of component A. To that end, a set of optimum designs addressing two objective functions was obtained. These functions were the specific energy absorption (SEA) of the crash absorber and its load ratio (LR). Both parameters were obtained from the force-displacement curves produced by finite element simulations. Prior to the calculation of these indicators, a standard SAE 600 filter [177] was applied to the raw force-displacement curves resulting from the simulations, which removed high-frequency noise from the curves by a 1000 Hz cutoff frequency. This filter is recommended for vehicle component analysis in the specialized literature [178].

The selection of these two functions for the multi-objective optimization problem was not arbitrary. While specific energy absorption can be increased with higher thickness values (up to a certain point), this increment of the thickness makes the initial peak force much higher, increasing the load ratio and the severity of the injuries suffered by the car occupants. In addition to this, the offset of the GFRP reinforcement with respect to the front of the component plays also a very important role in the value of both indicators. Setting these offsets to 0 (reinforcement starts at the same level than the steel tube) increases the total amount of absorbed energy and the *SEA*, but the initial peak grows since the peaks of all materials happen at the same time. Shifting the reinforcement leads to a distribution and reduction of the peak forces, but *SEA* is affected in a negative way.

Crashworthiness optimization is usually affected by two well-known problems. The first issue is the large computational cost of this kind of analysis, involving severe plasticity, failure, friction and contact phenomena. Each of these requires a specific formulation which makes the analyses slower, advising against optimization methods which require many sequential evaluations of the objective functions. This makes gradient-based optimization procedures almost unaffordable, even if parallelization is used. The second big problem of these analyses are the noisy results, which lead to coarsely non-linear objective functions in which a gradient-based optimization cannot run properly. This computational noise stems from the schemes used to set up computational models, involving iterative approaches in which the solutions are not completely independent of the number of iterations or the discretization. As an example, Figure 4.1 shows the evolution of the specific energy absorption of an empty steel tube like the one used in this research when the corner diagonal projection varies from 0 (orthogonal corner) to 50 mm (sheet bends at half the side length). This variable was one of the selected variables for the optimization study, and it happened to be the most noisy and the one with a minor influence on the results.

At a first stage, an optimization was run with a gradient-based method directly on the finite element model, which required numerous evaluations, each of which took several hours to complete. Furthermore, the strong nonlinearities of the objective functions caused that the algorithm got stuck no matter which initial point was selected.

Fortunately, there is a solution which overcame both issues: the use of surrogate-based optimization methods. These are based on the construction of a cheap-to-evaluate function $\hat{f}$ which approaches the original objective function f. Optimization is then run on $\hat{f}$, which is usually a n-th order polynomial or a set of basis functions (splines, Gauss functions, etc). This optimization can be now carried out using any gradient-based or meta-heuristic strategy, given the softness of $\hat{f}$. Obviously, the goodness of the results will depend to a large extent on the quality of the approach. This approximation of the objective function is called a metamodel or surrogate model.

The construction of this surrogate model begins with the design of a sampling plan. The aim of this stage is to intelligently place the sampling points in the design space to generate then a quality surrogate model. Since one objective

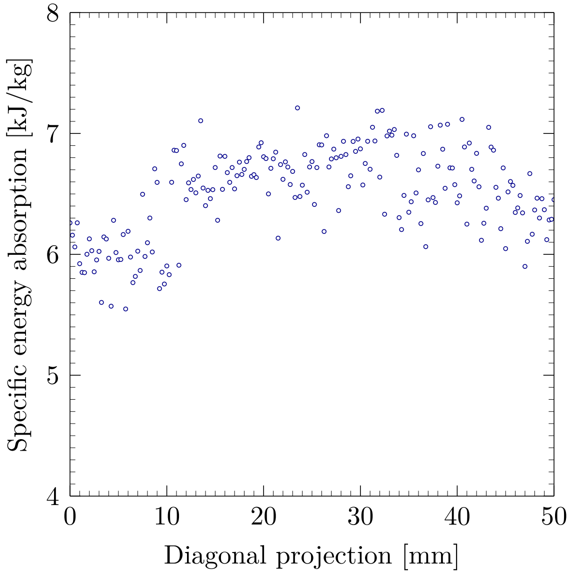

Figure 4.1: Specific energy absorption of component 0 for different values of the diagonal projection length. This variable produced particularly noisy results.

is to avoid unnecessary simulation runs, a full factorial sampling (based on a sampling by means of a rectangular grid of points) is discarded. Instead of that, a Latin Hypercube Sampling (LHS) strategy has been selected. This technique was first described by Eglājs and Audze [179] in 1977, even though McKay et al. [180] are usually regarded as the original authors. Further elaboration was presented in 1981 by Iman and Campbell [181]. This stratified method allows getting a set of random data points whose projections onto the variable axes are uniform, given the fact that each dimension of the design space is divided into a number of segments equal to the number of sampling points. This implies that a square grid containing sample positions is a Latin square if and only if there is a single sample in each row and each column (i.e. in each segment). One of the advantages of this method is that the sampling scheme does not require more samples for more variables. The maximum number of different LH samples for a domain with M divisions and N variables is given by

$$\prod_{n=0}^{M-1} (M-n)^{N-1} = (M!\,)^{N-1}\,. \tag{4.1}$$

As a simple example, Figure 4.2 shows a LH sampling with 10 samples distributed on a square domain with a uniform probability distribution. It can be observed that all the rows and columns are seeded with a sample point, so that no rows or columns have more than one point and all of them are sampled. In this chapter, samples of 40, 100 and 200 data points were used for the approximations, being the differences explained in the Results section.

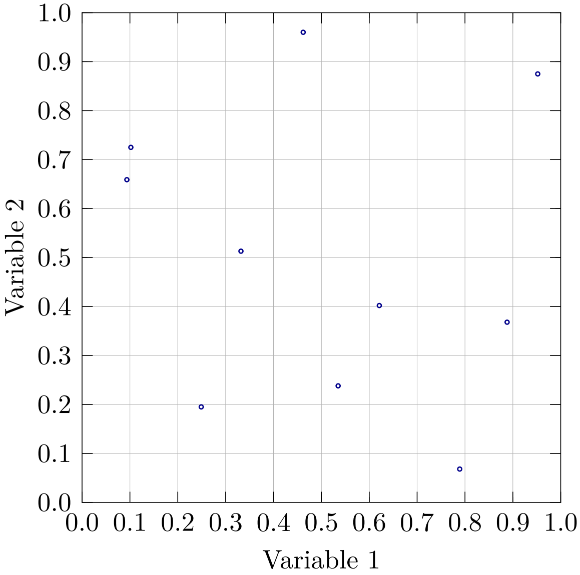

Figure 4.2: Example of a 10-points latin hypercube sampling applied to a 2-D square domain. Sample points are distributed so that all projection sub-domains (rows and columns) are seeded with one point.

After the sampling is performed, a surrogate model has to be adjusted to the sample points. In this research, four different models have been considered and evaluated. These models were:

Quadratic polynomial A quadratic polynomial with 28 coefficients (according to (4.3)), with general form

$$\hat{f}(\mathbf{x}) = c_0 + \sum_{i=1}^{n} c_i x_i + \sum_{i=1}^{n} \sum_{j \geq i}^{n} c_{ij} x_i x_j, \tag{4.2}$$

$$n_{\mathrm{c,quadratic}} = \frac{(n+1)(n+2)}{2}, \tag{4.3}$$

$\mathbf{x}$ being the variables vector, n is the number of variables, $x_{i,j}$ are the components of $\mathbf{x}$ and the terms c_0, c_i and c_{ij} are the polynomial coefficients.

$n_{\mathrm{c,quadratic}}$ is the number of coefficients needed for the quadratic response approach.

Cubic polynomial Similar to the previous one, with 182 coefficients (from (4.5)) and with a general form

$$\hat{f}(\mathbf{x}) = c_0 + \sum_{i=1}^{n} c_i x_i + \sum_{i=1}^{n} \sum_{j \geq i}^{n} c_{ij} x_i x_j + \sum_{i=1}^{n} \sum_{j \geq i}^{n} \sum_{k \geq j}^{n} c_{ijk} x_i x_j x_k, \quad (4.4)$$

$$n_{\mathrm{c,cubic}} = \frac{\left(n^3 + 6n^2 + 11n + 6\right)}{6}. \quad (4.5)$$

Gaussian process (Kriging) It is one of the most common models in surrogate-based optimization. The approximation follows the structure

$$\hat{f}(\mathbf{x}) = \mathbf{g}(\mathbf{x})^{\mathrm{T}} \boldsymbol{\beta} + \varepsilon(\mathbf{x}) \quad (4.6)$$

where $\mathbf{x}$ is the current point, $\mathbf{g}(\mathbf{x})$ is the vector of basis functions at $\mathbf{x}$ and $\boldsymbol{\beta}$ is a vector containing the least squares estimates of the basis function coefficients. In this research, quadratic polynomials were used as the trend basis functions. The last term, $\varepsilon(\mathbf{x})$, is the stationary Gaussian process error model, and it is used to correct the trend functions $\mathbf{g}(\mathbf{x})$. The stationary Gaussian process error model, with a mean equal to 0 and a constant variance σ^2, contains a stationary autocorrelation function $r(\mathbf{x}, \mathbf{x}')$ so its autocovariance function is of the form

$$\sigma_{\hat{f}(\mathbf{x})\hat{f}(\mathbf{x}')} = \sigma_{\hat{\varepsilon}(\mathbf{x})\hat{\varepsilon}(\mathbf{x}')} = \sigma^2 r(\mathbf{x}, \mathbf{x}'). \quad (4.7)$$

This error $\varepsilon(\mathbf{x})$ adjusts the trend function guaranteeing that at the given sampling points the overall error is zero. An anisotropic generalized exponential model (4.8) was used for the $r(\mathbf{x}, \mathbf{x}')$ function:

$$r(\mathbf{x}, \mathbf{x}') = \exp\left(-\sum_{k=1}^{\Omega} \theta_k \left|x_k - x_k{}'\right|^{\gamma}\right), \quad (4.8)$$

where Ω is the number of input dimensions, $0 < \gamma < 2$ and $0 < \theta_k$. For the Gaussian correlation function $\gamma = 2$, which is infinitely differentiable, the correlation parameters $\boldsymbol{\theta}$ are related to the correlation lengths L_k by

$$\theta_k = \frac{1}{2L_k^2}. \quad (4.9)$$

The correlation lengths are analogous to the standard deviation in the normal distribution.

Multivariate adaptive regression splines (MARS) This model approaches the objective function by means of a continuous surface of splines. MARS consists of a non-parametric regression technique first described by H. Friedman in 1991 [182]. The approximation is of the form

$$\hat{f}(\mathbf{x}) = \sum_{m=1}^{M_\mathrm{b}} a_m B_m(\mathbf{x}), \tag{4.10}$$

where a_m are the coefficient of the power basis functions B_m and M_b is the number of functions. The model consists of a weighted sum of M_b basis functions $B_m(\mathbf{x})$. These basis functions take the form of hinge functions, described in detail in [182]. The design space is split into sub-regions, in each of which regression methods are applied to fit a local approximation. Then, these approximations are joined together to produce a global, smooth surrogate model. In this case, the basis functions were cubic splines.

In particular, the process begins with a first data fit by means of a first single spline $B_1(\mathbf{x})$. Next, the design space is partitioned into 2 sub-regions at a split point called knot, whose location is automatically selected to produce the best fit. A second spline is introduced using this knot and fitting its sub-region. The process is continued by adding an additional spline and its sub-region in each iteration, whose location is optimized as well. This process constitutes the first phase of the MARS algorithm, a forward pass, ending when the maximum number of bases allowed by the user M_b is reached. At the end of this first step, a model with M_b splines is obtained. A second phase consisting of a backward pass is then performed. Each iteration of this second phase removes one basis function, which is chosen so that its deletion either improves the fit the most or degrades it the least. All bases can be removed except $B_1(\mathbf{x})$, to avoid holes to appear in the model. At the end of this second phase, a set of $M_\mathrm{b} - 1$ models is obtained, and the algorithm finally chooses the best among them. Cubic base functions were used, so the obtained model had a C^2 continuity.

The accuracy of the different approaches was judged by means of the correlation coefficient R^2 (4.11). This indicator is obtained as

$$\begin{aligned} R^2 &= \left(\frac{\sigma_{\mathbf{f}\hat{\mathbf{f}}}}{\sqrt{\sigma_{\mathbf{f}}^2 \sigma_{\hat{\mathbf{f}}}^2}} \right)^2 \\ &= \left(\frac{N_\mathrm{p} \sum_{i=0}^{N_\mathrm{p}} f_i \hat{f}_i - \sum_{i=0}^{N_\mathrm{p}} f_i \sum_{i=0}^{N_\mathrm{p}} \hat{f}_i}{\sqrt{\left[N_\mathrm{p} \sum_{i=0}^{N_\mathrm{p}} f_i^2 - \left(\sum_{i=0}^{N_\mathrm{p}} f_i \right)^2 \right] \left[N_\mathrm{p} \sum_{i=0}^{N_\mathrm{p}} \hat{f}_i^2 - \left(\sum_{i=0}^{N_\mathrm{p}} \hat{f}_i \right)^2 \right]}} \right)^2 , \end{aligned} \tag{4.11}$$

where $\mathbf{f} \equiv f_i$ are the values obtained from the FEA model, $\hat{\mathbf{f}} \equiv \hat{f}_i$ are the values of the obtained approximated function and N_p is the size of the data set.

Once the surrogate models for the specific energy absorption and the load ratio were completed, they were subjected to Pareto weighted objective method optimization strategy which optimized the surrogate models using the Fletcher-Reeves conjugate gradient method, devised by Fletcher and Reeves [183] in 1964. This method was proposed as an improvement of the classic steepest descent method (see, for instance [184]), in which the search direction of the algorithm at iteration k, $\mathbf{s}^k$, is the negative of the gradient of the objective function, i.e.

$$\mathbf{s}^k = -\nabla f\left(\mathbf{x}^k\right), \tag{4.12}$$

where $f\left(\mathbf{x}^k\right)$ is the value of the objective function at the current point $\mathbf{x}^k$. At the k-th iteration of the steepest descent method, the transition from the current point $\mathbf{x}^k$ to the new point $\mathbf{x}^{k+1}$ is given by

$$\mathbf{x}^{k+1} = \mathbf{x}^k + \Delta\mathbf{x}^k = \mathbf{x}^k + \alpha^k \mathbf{s}^k = \mathbf{x}^k - \alpha^k \nabla f\left(\mathbf{x}^k\right), \tag{4.13}$$

where $\Delta\mathbf{x}^k$ is the vector from $\mathbf{x}^k$ to $\mathbf{x}^{k+1}$, and α^k is an scalar which determines the step length in direction $\mathbf{s}^k$, obtained by a line search. Once at the minimum, the value of the components of the gradient vector vanishes.

The difficulty with the steepest descent method is its sensitivity to the scaling of the objective function $f\left(\mathbf{x}\right)$. A typical example of this issue happens when the algorithm has to descent a narrow valley or a ridge, doing a zigzagging movement which slows down the convergence. For these reasons, the steepest descent is not an effective optimization technique. Conjugate gradient methods are much faster and more accurate.

Fletcher-Reeves method computes the search direction by a linear combination of the current gradient and the previous search direction. This can be applied to very large problems provided that only a small amount of memory is required at each evaluation (only the previous search direction has to be temporary stored). The steps of the method are provided in the following chart:

Fletcher-Reeves conjugate gradient method [183, 184]

1. At the initial point $\mathbf{x}^0$, compute $f\left(\mathbf{x}^0\right)$. Let $\mathbf{s}^0 = -\nabla f\left(\mathbf{x}^0\right)$.
2. Save $\nabla f\left(\mathbf{x}^0\right)$ and compute $\mathbf{x}^1 = \mathbf{x}^0 + \alpha^0 \mathbf{s}^0$ by minimizing $f\left(\mathbf{x}\right)$ with respect to α in the search direction $\mathbf{s}^0$ (unidimensional search for α^0).
3. Calculate $f\left(\mathbf{x}^1\right)$ and $\nabla f\left(\mathbf{x}^1\right)$. The new search direction is a linear combination of $\mathbf{s}^0$ and $\nabla f\left(\mathbf{x}^1\right)$:

   $$\mathbf{s}^1 = -\nabla f\left(\mathbf{x}^1\right) + \mathbf{s}^0 \frac{\nabla^{\mathrm{T}} f\left(\mathbf{x}^1\right) \nabla f\left(\mathbf{x}^1\right)}{\nabla^{\mathrm{T}} f\left(\mathbf{x}^0\right) \nabla f\left(\mathbf{x}^0\right)}.$$

   For the k-th iteration the relation is

   $$\mathbf{s}^{k+1} = -\nabla f\left(\mathbf{x}^{k+1}\right) + \mathbf{s}^k \frac{\nabla^{\mathrm{T}} f\left(\mathbf{x}^{k+1}\right) \nabla f\left(\mathbf{x}^{k+1}\right)}{\nabla^{\mathrm{T}} f\left(\mathbf{x}^k\right) \nabla f\left(\mathbf{x}^k\right)}. \tag{4.14}$$

4. Test for convergence to the minimum of $f\left(\mathbf{x}\right)$. If negative, go to 3.
5. Terminate the algorithm when $\left\|\nabla f\left(\mathbf{x}^k\right)\right\|$ is less than the prescribed tolerance.

The algorithm terminates if the norm of the gradient $\left\|\nabla f\left(\mathbf{x}^k\right)\right\|$ is less than a predefined tolerance. This is related to the theoretical conditions for the existence of an optimum formulated by Karush [185] in 1939, and later by Kuhn and Tucker [186] in 1951, known as Karush–Kuhn–Tucker conditions. These necessary conditions include that the gradient of the objective function vanishes at a local minimum as long as it is not located on a boundary of the design space, in an unconstrained problem like the studied here.

Fletcher and Reeves proved that Equation (4.14) gives conjugate directions and quadratic convergence. A difficulty of this method is the linear dependence of search directions (e.g. when the ratio of the inner products of the gradients from iteration $k+1$ relative to iteration k is very small, the conjugate gradients methods behaves similarly to the steepest direction). This is overcome by periodically restarting the conjugate gradient method with the steepest descent search (step 1 in the previous chart). Additional details on the conjugate gradient method can be found in [187–189].

In this section, the multi-objective Pareto sets were obtained by optimizing a single objective function built from a weighted sum of the surrogate models of the specific energy absorption and the load ratio. Therefore, the multi-objective problem of $\widehat{SEA}(\mathbf{x})$ and $\widehat{LR}(\mathbf{x})$ (the surrogate models) is converted into a mono-objective optimization of a function $f'(\mathbf{x})$ so that

$$\hat{f}'(\mathbf{x}) = -w_1 \widehat{SEA}(\mathbf{x}) + w_2 \widehat{LR}(\mathbf{x}), \tag{4.15}$$

where w_1 and w_2 are the sum weights satisfying $w_1 + w_2 = 1$ and $w_1 \geq 0$, $w_2 \geq 0$. It is clear that if $w_1 = 1$ and $w_2 = 0$, the problem is reduced to maximize the specific energy absorption, and $w_1 = 0$ and $w_2 = 1$ minimizes the load ratio.

The accuracy of the obtained optimum values wanted to be improved using an iterative process. This strategy consisted of obtaining the optimum design of the function $\hat{f}'$ and re-calculating this design with the finite element code. This new point is added to the sample set, replacing any possible coincident point, and the surrogate model is re-adjusted including the new sample. This process was iterated until convergence. The full algorithm is known as surrogate-based global optimization (SBGO) [190], whose general process is shown in Figure 4.3. The SBGO procedure was implemented via DAKOTA framework in its version 5.3.1 [190].

4.1.2 Application to specimen A: design variables

A view of the cross-section of specimen A is presented in Figure 4.4a, in which four of the six design variables are marked. A render view of the model is provided in Figure 4.4b, in which the offsets of the two reinforcement elements (large and smalls crosses) are annotated. These two offsets were the two remaining design variables for the optimization problem.

Therefore, the considered design variables were the thickness of the steel tube (T1), the thickness of the main GFRP reinforcement (large cross, T2), the thickness of the secondary reinforcements (small crosses, T3), the length of the projection of the steel chamfer on one of the sides (DIAG) and the offsets of the

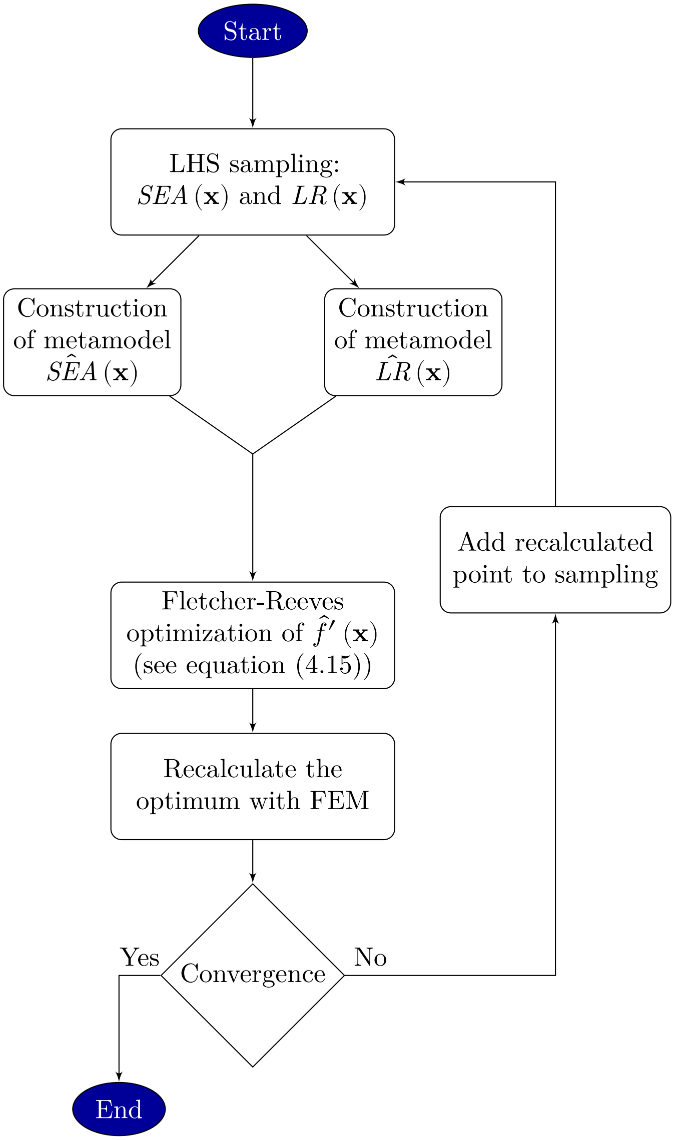

Figure 4.3: Flowchart of the multi-objective optimization algorithm including surrogate-based global optimization.

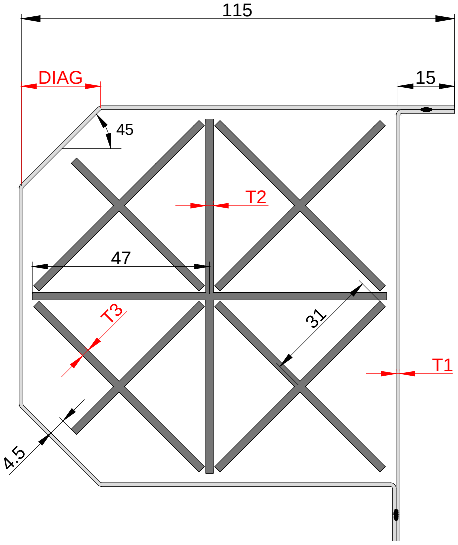

(a) Cross-section, dimensions in millimeters. The four design variables of the cross section are annotated in red.

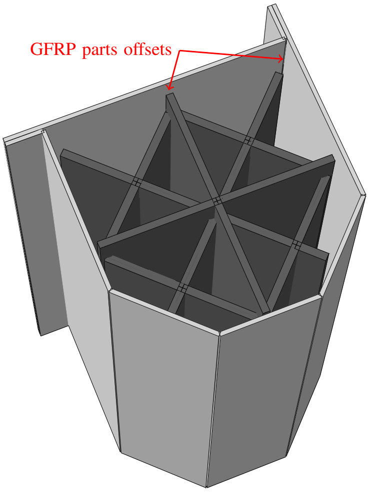

(b) Render view of the crash box. The offsets of the GFRP reinforcements are two design variables (labeled in red).

Figure 4.4: Geometry of the crash box, with the design variables annotated in red.

main and secondary reinforcements (MRO and SRO, respectively). The upper and lower bounds of the six design variables are provided in Table 5.1.

Design variable	Units	Bounds		Initial design
		Lower	Upper	(Chapter 3)
T1	mm	0.87	2.44	1.00
T2	mm	2.00	4.00	2.50
T3	mm	2.00	4.00	2.50
DIAG	mm	1.00	40.00	21.00
MRO	mm	1.00	30.00	20.00
SRO	mm	1.00	30.00	20.00

Table 4.1: Ranges of the six design variables and values at the initial design (from Chapter 3).

4.1.3 Analysis settings

The simulations consisted of the impact of a rigid plate against one of the ends of the crash absorber, being the other end in contact with an immobile rigid plate. The loading plate crushes the absorber at a constant speed of 64 km/h (17.78 m/s), matching Euro NCAP standards for frontal impact tests [3], up to a crushing length δ of 150 mm. The reason to stop the crushing at this point was to avoid the bottom-out effect, which occurred at δ = 170-180 mm. A scheme of the analysis is provided in Figure 4.5.

All the simulations were run using the Explicit module of Abaqus 6.12 FEA package [191]. Four parallel processors were used for each analysis, each one computing one of the 4 domains which the problem was divided into. Some influence of the number of computation sub-domains on the final results was observed, which is also reported in the FEA package documentation [191]. The selection of four domains and four processors was the result of a previous analysis in which the same case was run in a single domain (undivided problem) and one processor, and compared with the results for 2d-2p, 4d-4p, 8d-8p, 16d-16p, 32d-32p and 64d-64p, checking the resulting values of specific energy absorption and the computation times. The results of this previous study can be observed in Figure 4.6. It can be stated that a problem decomposition into four domains did not alter the *SEA* results significantly and offered reasonable computation times. The 8d-8p option was the fastest, but the results were a bit further from the ones obtained in the undivided analysis. From 8d-8p on, the increase in the communication times between cores was larger than the improvements obtained

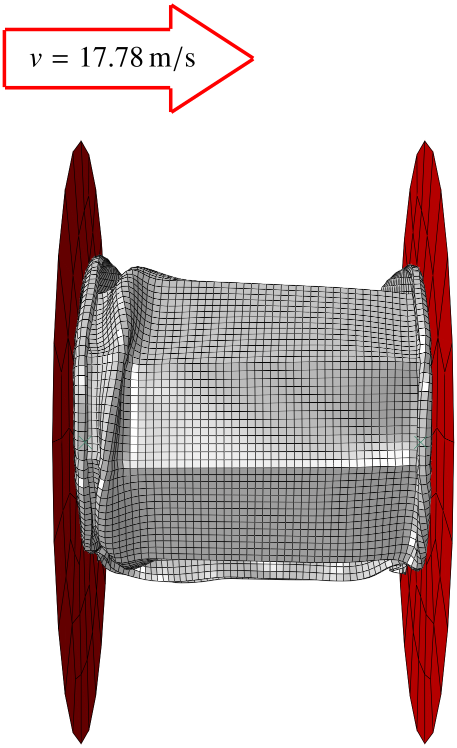

Figure 4.5: Scheme of the finite element analysis.

by working with multiple processors, making the overall computation time grow. Given these facts, all FEA evaluations were run with a 4d-4p configuration. 3000 megabytes of RAM were assigned to each processor. Computation was carried out in a High Performance Computing (HPC) cluster with a theoretical peak performance of 5.1 TFLOPS.

4.1.4 Results and discussion

Results of the initial design

The results of the initial design subjected to the dynamic simulation are provided in the first place, in Table 4.2.

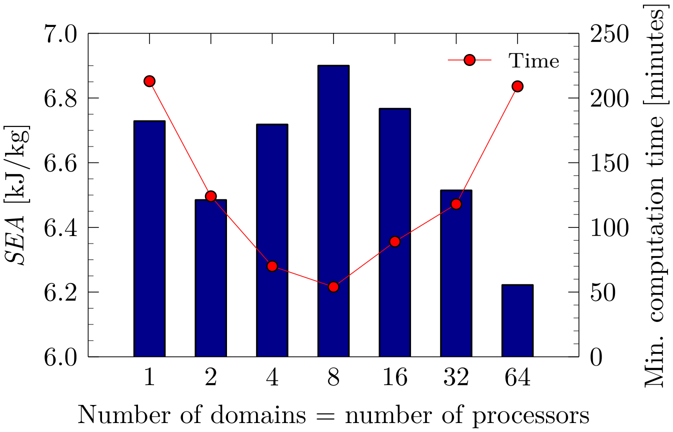

Figure 4.6: Influence of the number of domains or processors in the results and computation times.

Parameter	Units	Type	Value
T1	mm	Design variable	1.00
T2	mm	Design variable	2.50
T3	mm	Design variable	2.50
DIAG	mm	Design variable	21.00
MRO	mm	Design variable	20.00
SRO	mm	Design variable	20.00
SEA	kJ/kg	Objective function	8.71
LR	-	Objective function	3.11

Table 4.2: Properties and results of the initial design, taken from Chapter 3.

Comparison of surrogate meta-models

Four different surrogate models have been evaluated, which were judged taking into consideration not only the R^2 coefficient, but also the accuracy of the global optimum for each objective function compared with a final FE evaluation of the same design. The specific energy absorption was easily approximated by all models (only polynomials and Kriging are shown), but severe problems were found to accurately approach the *LR* function because it had very different shapes in different areas. For instance, when trying to approximate it by means of a quadratic polynomial with only the MRO and SRO variables active (2-D domain), there was a region in which the response is flat. This happened because, from a certain point on, an increase in the offsets of the reinforcements does not reduce the peak load, which is then determined by the initial peak of the steel tube, making the *LR* function independent of these two variables in this area. These slopes discontinuities were the reason why only the MARS and GP model could accurately represent the *LR* function. Of particular interest were all the different approaches to emulate the *LR* function, which are all shown in Table 4.3.

Model	Function	Samples	R^2	% error (iterations)
Polynomial quadratic	*SEA*	100	0.95	0.31 (3)
	LR	100	0.66	10.70 (5)
Polynomial cubic	*LR*	100	0.60	0.48 (3)
Gaussian Process	*SEA*	100	1.00	0.00 (2)
	LR	100	1.00	0.00 (2)
	SEA	40	1.00	0.00 (2)
	LR	40	1.00	0.00 (2)
	SEA	30	1.00	2.46 (2)
	LR	30	1.00	22.54 (2)
MARS, 36 base functions	*SEA*	40	0.96	2.27 (2)
	LR	40	0.61	1.64 (2)
	SEA	100	0.97	0.22 (2)
	LR	100	0.85	3.88 (2)
	SEA	200	0.94	2.34 (2)
	LR	200	0.83	1.43 (2)

Table 4.3: Evaluation of the fitting quality of different meta-models. The last column indicates the relative error after the number of SBGO iterations required for convergence.

At the sight of these results, it could look like Kriging model is the best-fitting approach for these problems, but it is not. Due to its definition, Kriging model is guaranteed to pass through all the response data values that are used to construct the model, which would be a positive property. However, due to this fact, both approximations for *SEA* and *LR* made from 100 data points have captured part of the noise in the original response, obstructing the future optimization process on the surrogate models. A reduction to 40 points was taken into consideration, but the noise was still present and the final Pareto results were not consistent. This was the reason why a MARS approach was eventually chosen, which was able to accurately emulate the slope discontinuities and filter almost all the numerical noise. However, a brief study was carried out to determine the maximum number of basis functions employed in the construction of the surrogate model M_b, since this affected the quality of the approximation and the amount of noise to be filtered out. Samples of 40, 100 and 200 data points were evaluated, and the maximum number of basis functions ranged between 1 and 36. The results are provided in Figure 4.7.

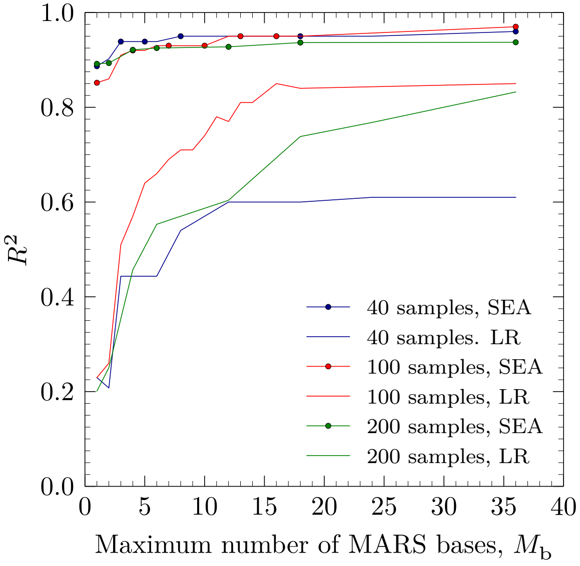

Figure 4.7: Influence of the sample size and the maximum number of MARS basis functions on the R^2 goodness indicator.

It can be appreciated a very good fit of the *SEA* functions in all configurations, and a more difficult approximation of the *LR* function. The maximum number of bases required to stabilize the R^2 indicator increased with the sample size. Taking into consideration the R^2 indicator and computational cost criteria, a sample size of 100 data points was selected. The model was fit to this sample with 12, 18 and 36 basis functions, being the best results those provided by the last choice. Thus, the number of basis functions was large enough to offer a quality fit and not large enough to capture the numerical noise. This was the chosen configuration to obtain the Pareto optimum set.

Pareto optimum set

Once the MARS model is chosen, the Pareto weighted objective strategy was run on the models and the optimum design pairs were obtained. These values for different weights are provided in Table 4.4 and plotted in Figure 4.8.

Pareto weights		Objective functions		Design variables [mm]					
w_{SEA}	w_{LR}	*SEA* [kJ/kg]	*LR*	*T1*	*T2*	*T3*	*DIAG*	*MRO*	*SRO*
1.00	0.00	13.31	1.86	2.4*	3.46	3.38	34.26	20.00	22.53
0.90	0.10	13.30	1.86	2.4*	2.80	3.49	36.68	19.40	21.99
0.80	0.20	13.30	1.85	2.4*	2.53	3.47	40.00**	18.49	23.51
0.70	0.30	13.29	1.83	2.4*	3.27	3.42	40.00**	17.45	23.42
0.60	0.40	13.28	1.82	2.4*	3.94	3.51	40.00**	16.24	23.93
0.50	0.50	13.25	1.80	2.4*	3.21	3.45	34.33	15.54	22.53
0.45	0.55	13.23	1.79	2.4*	3.21	3.43	33.87	14.77	22.66
0.40	0.60	13.27	1.68	2.4*	2.80	3.21	40.00**	7.85	22.57
0.35	0.65	13.24	1.58	2.4*	2.91	3.15	40.00**	1.00*	23.09
0.30	0.70	13.22	1.57	2.4*	2.90	3.14	40.00**	1.00*	23.69
0.25	0.75	13.13	1.54	2.4*	3.02	3.04	40.00**	1.00*	25.04
0.23	0.77	13.06	1.52	2.4*	2.97	3.17	38.32	1.00*	24.75
0.20	0.80	12.61	1.39	2.4*	3.05	2.03	40.00**	1.00*	27.37
0.15	0.85	12.37	1.35	2.4*	2.98	2.08	37.35	1.00*	30.00**
0.10	0.90	12.37	1.35	2.4*	2.98	2.00*	37.29	1.00*	30.00**
0.00	1.00	11.91	1.33	2.4*	3.01	2.00*	33.84	1.00*	30.00**

Table 4.4: Pareto solutions for selected weights. One asterisk indicates lower bound, two asterisks indicate upper bound.

A good balance between the functions was found when a 35 % of the weight was applied to the specific energy absorption and a 65 % to the load ratio. *SEA* was increased by 52 % with respect to the original design, whereas *LR* was reduced by 49 %. The force-displacement curves of the original and the best-balanced optimum design are provided in Figure 4.9. The mass of the final design was 2.30 kg.

At the sight of the Pareto results table, several conclusions can be pointed out. All along the frontier, the results of *SEA* and *LR* were much better than the ones produced with the original design. From the beginning of the table, the *LR* was gradually reduced thanks to a reduction of the main reinforcement offset, which separated this from the secondary reinforcement parts. Once the main reinforcement got to the top of the part, *LR* could still be reduced by separating the secondary reinforcement down to its lower bound of 30 mm. Once the separation between these two parts reached its allowed maximum, the *LR*

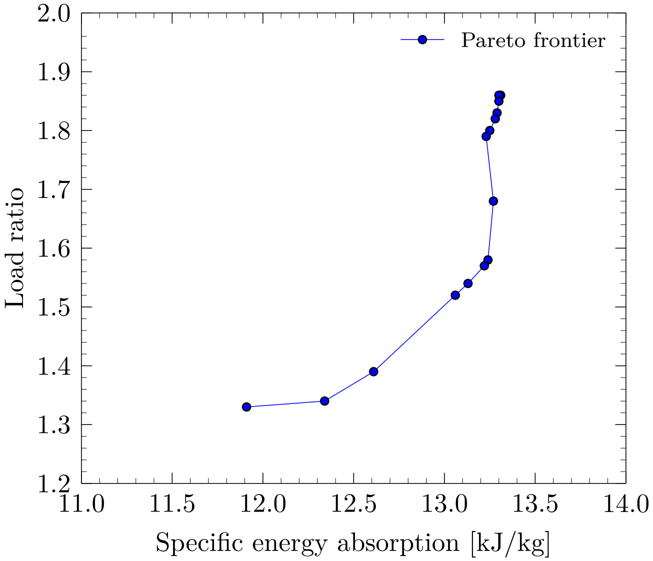

Figure 4.8: Representation of the Pareto frontier obtained with the Fletcher-Reeves conjugate gradient method.

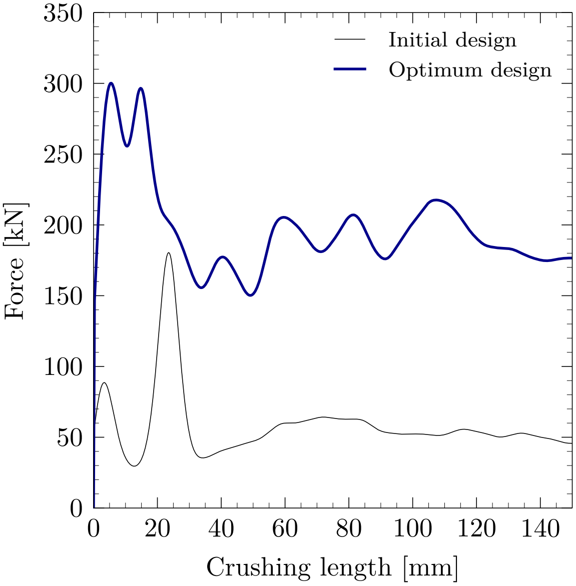

Figure 4.9: Force-displacement curves for the initial and final designs.

could not be reduced anymore. The thickness of the steel part can be increased up to its limit, always increasing the specific energy absorption. In fact, this was its value in all the designs placed along the Pareto frontier. A value between 35 and 40 mm for the diagonal projection should be adopted.

4.2 Multi-objective optimization using a genetic algorithm

In this section, the same specimen was optimized using an evolutionary multi-objective algorithm run on the same MARS surrogate model built on the previous pages. Genetic algorithms, comprehensively explained in [192–194], have become a popular and useful application in the past 15 years, using a population-based approach instead of a sequential search guided by the gradients of the objective functions. This allows them to be applied to a wide variety of optimization problems. Furthermore, evolutionary algorithms use more than one solution at each iteration, which provides them with a parallel processing power achieving a computationally quick overall search.

The process begins with a population randomly distributed in the design region, whose fitness is evaluated according to a certain rule. The algorithm enters then into the operation of creating a new population by the use of four mechanisms: selection, crossover, mutation and elite-preservation. Selection consists of choosing the best solutions at each iteration for a mating pool. Several stochastic selection methods have been proposed in the literature, the simplest being the called *tournament* selection, which consists of picking two random solutions from the population and selecting the fittest one for reproduction. With the aim of ranging all the design space, variations are forced to occur during the iterative evolutionary process. These are achieved by means of two basic mechanisms: crossover and mutation. Crossover is applied to a certain percentage of each population, and consists of picking two individuals (solutions) from the mating pool and exchanging information among them to generate one or more additional solutions. Each child solution resulting from the crossover operation is then perturbed by a mutation process which alters the values of its design variables, with the aim of searching locally on a solution independently on the location (design variables) of the remaining solutions. Finally, the elitism operator keeps the best individuals among the parent and child population, which guarantees a monotonically non-degrading performance of the algorithm. The process is iteratively repeated until a termination criterion is satisfied. A flowchart with the complete process is provided in Figure 4.10.

When it comes to evolutionary multi-objective optimization algorithms, the weighted sum method for obtaining the Pareto front is usually avoided due to

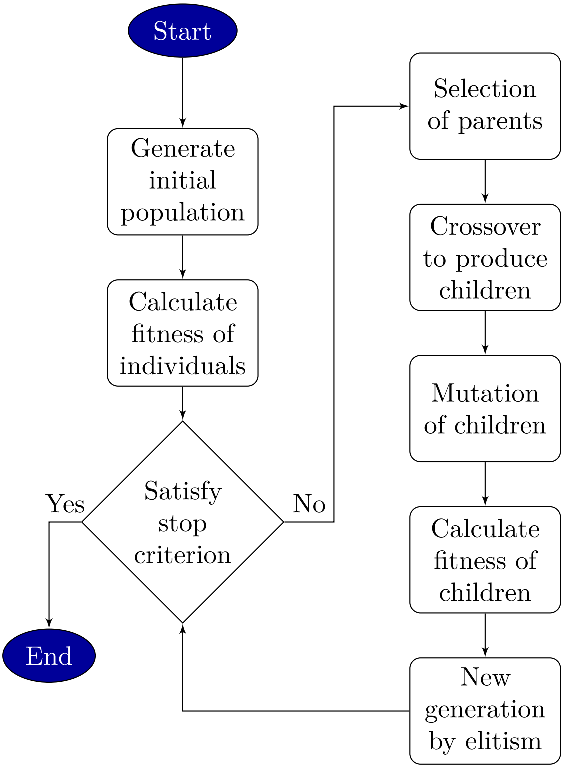

Figure 4.10: Flowchart of an evolutionary optimization algorithm.

its poor performance. Common pitfalls of the weighted sum method include the inability to generate a uniform sampling of the frontier [195, 196], the inability to generate points in non-convex portions of the front [197, 198], a non-intuitive relationship between weights and performances, and a general poor efficiency (requiring an excessive number of functions evaluations). In general, genetic algorithms generate Pareto fronts by means of an evaluation of the designs' fitness based on their dominance over other designs. In this case, the multi-objective method devised by Eddy and Lewis [199] in 2001 was used, implemented in DAKOTA framework [190] through the JEGA package. Given that an unconstrained optimization was performed, the fitness function simply ranks each member by the number of members that dominate it. The parameters for the optimization algorithm are provided in Table 4.5.

Regarding the termination criterion, a limit of 50 000 function evaluations was imposed to the algorithm, which implied that the number of generations

Parameter	Value
Population size	500
Offset normal mutation rate	0.1
Two-point crossover probability	0.8
Elitism	50
Maximum allowed individuals	10^6

Table 4.5: Configuration parameters for the evolutionary optimization algorithm.

was about 15 000-20 000.

It is very important to remark that most genetic algorithms (like the one used here) terminate when a maximum number of iterations is completed. This means that the obtained designs are not proved to be optimum designs from a theoretical point of view, provided that Karush–Kuhn–Tucker conditions are not checked. As an exception, a recent simulation study [200] employed a particular evolutionary algorithm which progressed towards theoretical Karush–Kuhn–Tucker points.

The Pareto front obtained using this methodology is presented in Figure 4.11, together with the front previously obtained using the Fletcher-Reeves method, for comparison.

At the sight of Figure 4.11, it can be observed that both algorithms converged to the same region of the model in the central area of the fronts. This guarantees that the genetic algorithm converged adequately to the theoretically-proved optimums. For higher optimized specific energy absorptions, the evolutionary algorithm was able to find a region in the surrogate model unexplored by the conjugate gradient method, where some optimum pairs were located. Regarding the left part of the front, more sample points would be required to model the flat zone of the front properly. This justified that more extensive samplings were run in Chapter 6.

4.2.1 Conclusions

- A multi-objective structural optimization of the crashworthiness of a glass-fiber - steel impact absorber was carried out. The specific energy absorption and load ratio were chosen as objective functions due to their contrasting nature. A multi-adaptive regression splines surrogate model was chosen between other alternatives to accurately simulate the responses of the expensive-to-evaluate and noisy objective functions. Optimum pairs

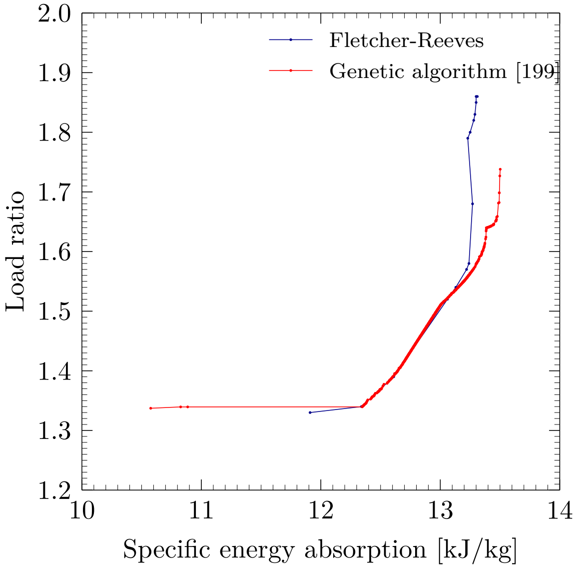

Figure 4.11: Representation of the Pareto frontiers obtained using the Fletcher-Reeves conjugate gradient method and using the genetic algorithm. In the central region, both methods converge to the same results. The genetic algorithm provided a longer front.

have been obtained after a Pareto optimization strategy using a conjugate gradient method and an evolutionary algorithm. The final results improve the initial design by near 50 % for both objective functions.

- Multi-adaptive regression splines and kriging models have been able to capture the complex shapes of the *LR* function, despite its strong slopes discontinuities. None of the other models offered a quality result for this function. *SEA* can be successfully emulated by even the simplest quadratic polynomial models.

- The iterative improvement of the original surrogate models has allowed that the comparison of the predicted optimum points with an eventual FE evaluation was successful. Usually, 2-3 iterations were enough to get a quality approach.

- The kriging model captured the noise in the functions once a minimum sample size was satisfied to match the goodness criteria. This made the optimization difficult to run, and a multi-adaptive regression splines approach was preferred at the end.

- Regarding the two algorithms employed in the optimization, it can be stated that both of them converged to the same optimums to a large extent, which indicates a good performance of the meta-heuristic method, able to converge to the theoretical optimums. Some optimums were only found by the genetic algorithm, specially in the regions of the curve were the slope was close to a vertical or horizontal line. This is also explained by the fact that the Fletcher-Reeves multi-objective strategy used here was based on the weighted sum of the objective functions to obtain the Pareto front, which led to some troubles when flat or non-convex areas of the front have to be obtained.
- Given that the evolutionary algorithm performed properly, and its independence from the weight factors required by the alternative method, in Chapter 6 this meta-heuristic multi-objective algorithm was preferred to optimize a new design considering other objective functions smoother than the load ratio.

References

[3] *Frontal Impact Testing Protocol, Version 6.0.* European New Car Assessment Programme (Euro NCAP), 2012.

[11] M. Costas, J. Díaz, L. Romera, and S. Hernández. “A multi-objective surrogate-based optimization of the crashworthiness of a hybrid impact absorber”. *International Journal of Mechanical Sciences* 88 (2014), pp. 46–54.

[15] J. Paz, J. Díaz, L. Romera, and M. Costas. “Size and shape optimization of aluminum tubes with GFRP honeycomb reinforcements for crashworthy aircraft structures”. *Composite Structures* 133 (2015), pp. 499–507.

[19] J. Díaz, M. Costas, L. Romera, J. Paz, and S. Hernández. “Surrogate-based multi-objective optimization of glass-fiber - steel crash absorbers”. In: *35th FISITA World Automotive Congress, Maastrich (Netherlands).* 2014.

[118] S. Hou, Q. Li, S. Long, X. Yang, and W. Li. “Crashworthiness design for foam filled thin-wall structures”. *Materials and Design* 30.6 (2009), pp. 2024–2032.

[121] S. Hou, X. Han, G. Sun, S. Long, W. Li, X. Yang, and Q. Li. “Multiobjective optimization for tapered circular tubes”. *Thin-Walled Structures* 49.7 (2011), pp. 855–863.

[123] X. Song, G. Sun, G. Li, W. Gao, and Q. Li. “Crashworthiness optimization of foam-filled tapered thin-walled structure using multiple surrogate models”. *Structural and Multidisciplinary Optimization* 47.2 (2013), pp. 221–231.

[167] J. Paz, J. Díaz, L. Romera, and M. Costas. “Crushing analysis and multiobjective crashworthiness optimization of GFRP honeycomb-filled energy absorption devices”. *Finite Elements in Analysis and Design* 91 (2014), pp. 30–39.

[168] M. Cid Montoya, M. Costas, J. Díaz, L. Romera, and S. Hernández. “A multi-objective reliability-based optimization of the crashworthiness of a metallic-GFRP impact absorber using hybrid approximations”. *Structural and Multidisciplinary Optimization* 52.4 (2015), pp. 827–843.

[169] K. Yamazaki and J. Han. “Maximization of the crushing energy absorption of tubes”. *Structural Optimization* 16.1 (1998), pp. 37–46.

[170] P. Marklund and L. Nilsson. “Optimization of a car body component subjected to side impact”. *Structural and Multidisciplinary Optimization* 21.5 (2001), pp. 383–392.

[171] J. Sobieszczanski-Sobieski, S. Kodiyalam, and R. Yang. “Optimization of car body under constraints of noise, vibration, and harshness (NVH), and crash”. *Structural and Multidisciplinary Optimization* 22.4 (2001), pp. 295–306.

[172] T. Jansson, L. Nilsson, and M. Redhe. “Using surrogate models and response surfaces in structural optimization - With application to crashworthiness design and sheet metal forming”. *Structural and Multidisciplinary Optimization* 25.2 (2003), pp. 129–140.

[173] S. Hou, Q. Li, S. Long, X. Yang, and W. Li. “Design optimization of regular hexagonal thin-walled columns with crashworthiness criteria”. *Finite Elements in Analysis and Design* 43.6-7 (2007), pp. 555–565.

[174] E. Acar, M. Guler, B. Gereker, M. Cerit, and B. Bayram. “Multi-objective crashworthiness optimization of tapered thin-walled tubes with axisymmetric indentations”. *Thin-Walled Structures* 49.1 (2011), pp. 94–105.

[175] X. Gu, G. Sun, G. Li, L. Mao, and Q. Li. “A Comparative study on multiobjective reliable and robust optimization for crashworthiness design of vehicle structure”. *Structural and Multidisciplinary Optimization* (2013), pp. 1–16.

[176] M. Kiani, I. Gandikota, A. Parrish, K. Motoyama, and M. Rais-Rohani. “Surrogate-based optimisation of automotive structures under multiple crash and vibration design criteria”. *International Journal of Crashworthiness* (2013).

[177] *SAE Standard J211: Instrumentation for Impact Test.* Society of Automotive Engineers.

[178] M. Huang. *Vehicle Crash Mechanics.* CRC Press, Boca Raton, USA, 2002.

[179] V. Eglājs and P. Audze. “New approach to the design of multifactor experiments”. *Problems of Dynamics and Strengths* (in Russian) (1977), pp. 104–107.

[180] M. McKay, R. Beckman, and W. Conover. “A comparison of three methods for selecting values of input variables in the analysis of output from a computer code”. *Technometrics* 21.2 (1979), pp. 239–245.

[181] J. Iman R.L.; Helton and J. Campbell. “An approach to sensitivity analysis of computer models, Part 1. Introduction, input variable selection and preliminary variable assessment”. *Journal of Quality Technology* 13.3 (1981), pp. 174–183.

[182] J. H. Friedman. “Multivariate adaptive regression splines”. *Annals of Statistics* 19 (1991), pp. 1–141.

[183] R. Fletcher and C. M. Reeves. “Function minimization by conjugate gradients”. *The Computer Journal* 7.2 (1964), pp. 149–154.

[184] R. Haftka and Z. Gürdal. *Elements of Structural Optimization.* Third edition. Springer Netherlands, 1991.

[185] W. Karush. “Minima of Functions of Several Variables with Inequalities as Side Constraints”. MA thesis. Dept. of Mathematics, Univ. of Chicago, Chicago, Illinois., 1939.

[186] H. Kuhn and A. Tucker. “Nonlinear programming”. *Proceedings of 2nd Berkeley Symposium* (1951), pp. 481–492.

[187] R. Fletcher. *Unconstrained Optimization. Practical Methods of Optimization.* John Wiley & Sons, Chichester, 1981.

[188] P. Gill. *Practical Optimization.* Academic Press, London, 1982.

[189] I. Griva, S. Nash, and A. Sofer. *Linear and Nonlinear Optimization.* Second edition. Society for Industrial Mathematics, Philadelphia, 2008.

[190] B. Adams, L. Bauman, W. Bohnhoff, K. Dalbey, M. Ebeida, J. Eddy, M. Eldred, P. Hough, K. Hu, J. Jakeman, L. Swiler, and V. D. *DAKOTA, A Multilevel Parallel Object-Oriented Framework for Design Optimization, Parameter Estimation, Uncertainty Quantification, and Sensitivity Analysis: Version 5.3.1 User's Manual.* Sandia National Laboratories. December 2009. Updated April 2013.

[191] *ABAQUS 6.12 Documentation.* Dassault Systèmes. Providence Road, Rhode Island. 2012.

[192] J. Holland. *Adaptation in natural and artificial systems.* University of Michigan Press, Michigan, USA, 1975.

[193] D. Goldberg. *Genetic algorithms in search, optimization and machine learning.* Addison-Wesley Longman Publishing, Boston, USA, 1989.

[194] M. Mitchell. *An introduction to genetic algorithms.* MIT Press, Cambridge, USA, 1998.

[195] W. Chen, M. Wiecek, and J. Zhang. "Quality utility: a compromise programming approach to robust designs". *ASME journal of mechanical design* 121 (1999), pp. 179–187.

[196] I. Das and J. Dennis. "A closer look at drawbacks of minimizing weighted sums of objectives for Pareto set generation in multicriteria optimization problems". *Structural optimization* 14 (1997), pp. 63–69.

[197] A. Messac, J. Sundararaj, R. Tappeta, and J. Renaud. "The ability of objective functions to generate points on non-convex Pareto frontiers". *AIAA journal* 38 (2000), pp. 1084–1091.

[198] A. Messac, E. Melachrinoudis, and C. Sukam. "Aggregate objective functions and Pareto frontiers: required relationships and practical implications". *Optimization and engineering* 1 (2000), pp. 171–188.

[199] J. E. Eddy and K. Lewis. "Effective Generation of Pareto Sets using Genetic Programming". *Proceedings of ASME Design Engineering Technical Conference* (2001).

[200] K. Deb, R. Tiwary, M. Dixit, and J. Dutta. "Finding trade-off solutions close to KKT points using evolutionary multi-objective optimization". *Proceedings of the congress on evolutionary computation* (2007), pp. 2109–2116.

5

Crashworthiness of metal tubes filled with PET foam and GFRP. Part I: experimental tests

This chapter presents an investigation on the axial crushing behavior of a combination of three different materials in the same design. This idea was motivated by the good performance of the GFRP plates and the PET foam in Chapters 3 and 4, studied separately. It was observed that the performance of the GFRP-filled crash box could be improved adding some kind of confinement system which prevented the GFRP plates to fall apart after their incipient fracture. To that end, circular aluminum extrusion in alloy AA6063-T5 filled with a GFRP skeleton confined with PET foam were looked into. The components were tested under quasi-static and impact loading conditions supported by a material testing campaign. A previous design of an hexagonal double-hat was tested as well and discarded for weaknesses in the weldings.

Absorbed energy, crush force efficiency and specific energy absorption were obtained from the experimental tests in order to assess the performance of a design proposal. Besides, the interaction effects between the different materials has been analyzed in depth and compared to the results for aluminum foam filled extrusions available in the literature. The confinement effect of the foam on the glass fiber plates has been found to have a very remarkable contribution to the energy absorption levels of the component, whereas a negligible foam-extrusion interaction was observed due to the gaps in the initial geometry of the specimen.

The investigated components show an overall good performance of the design, specially in terms of crush force efficiency. The investigated component showed an overall good performance: the absorbed energy increased by almost 100 % compared to an empty extrusion, the specific energy absorption was reduced by approximately 15 % and the crush force efficiency was increased from 0.41 to 0.83.

The work presented in this chapter was carried out in close collaboration with the Structural Impact Laboratory (SIMlab) at the Norwegian University of Science and Technology (NTNU) during a research stay of six months funded by Fundación Barrié and the Clúster de Empresas de Automoción de Galicia (CEAGA). A part of this chapter has been published in Thin-Walled Structures [12].

5.1 Introduction and design proposals

In the present chapter an enhanced absorber design is proposed motivated by the improvements outlined in Chapters 3 and 4 where a metal tube was internally reinforced either with a structure of a glass-fiber reinforced polyamide (GFRP) or with a polymeric foam to improve the energy absorption and crashworthiness of the whole crash box. These improvements were mainly due to the contribution of the reinforcement itself to the energy absorption and the well-known interaction between the foam and metal parts. However, it was observed that the efficiency of the design with an inner GFRP structural reinforcement could be significantly enhanced with some kind of constraining or confinement system which prevented the GFRP parts to fall apart after the first brittle cracks. In this chapter, a foam filling was considered as a confinement for this structure. Therefore, a combination of the three materials is proposed: an outer metal tube made of aluminum internally reinforced with a structure made of GFRP plates and filled with a polyethylene terephtalate (PET) foam. The reason to choose an aluminum hollow section was its lower density and stable collapse mechanisms. The role of the aluminum profile was to confine the filler materials and also to contribute to the energy absorption levels. This proposal does not require the use of any structural bonding since the parts fit perfectly, which also avoids noises and vibrations. The goal was not only to evaluate the crashworthiness of a combination of these three materials but also to observe and quantify the possible interactions between the different materials involved.

At a first stage, some preliminary work was done in order to define the geometrical design of the element in which single and double-hat square and hexagonal sections were taken into consideration. These preliminary tests, based on finite element simulations, showed that a double-hat hexagonal section should be used in order to guarantee the best performance in terms of specific energy absorption and stability of the collapse modes. At this stage, an AA5754-H111 aluminum alloy was chosen for its commercial availability and adequate behavior, with an elastic modulus of 51 GPa, an initial yield stress of 139 MPa and hardening with a tangent modulus of 389 MPa. The alloy was modeled by a simple bi-linear stress-strain diagram based on the previous mechanical properties. Tensile tests were carried out on plane specimens extracted from the aluminum sheets used to build the casings. For brevity, the results of these tests are provided in Appendix A.

Three different alternatives were analyzed for the outer tube: a single-hat square section, a double-hat square section and a double-hat hexagonal section. Dimensions and details of the three alternatives are summarized in Figure 5.1.

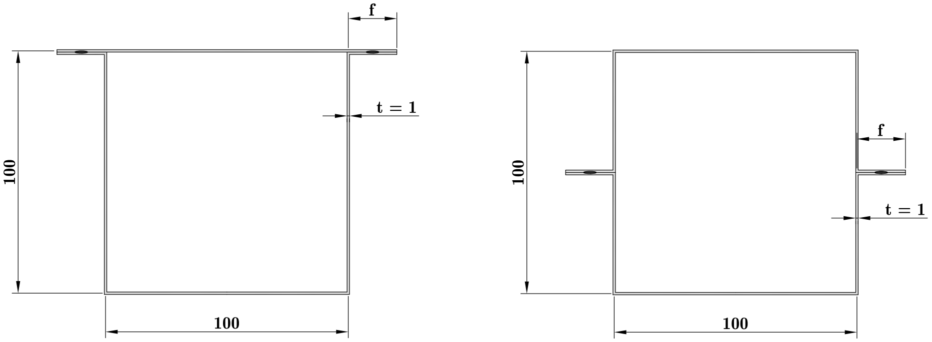

(a) Single-hat square section.

(b) Double-hat square section.

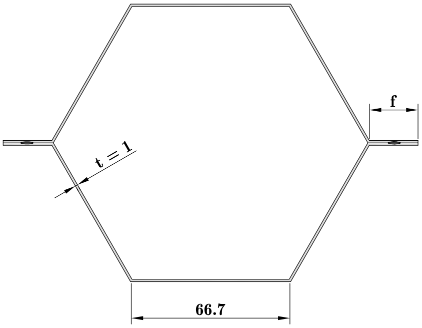

(c) Double-hat hexagonal section.

Figure 5.1: Different cross-sections considered for the outer cold-formed tube of the crash box. Spot welds are indicated in the flanges. Dimensions in millimeters.

The side lengths have been selected so that the three tubes have the same perimeter, and therefore the same weight, according to the relationship

$$l_{\text{hexagon}} = \frac{2}{3} l_{\text{square}}. \tag{5.1}$$

The tubes have been analyzed for flange widths f of 10 and 20 mm.

The crushing simulations carried out on hollow single and double-hat sections showed that non-regular modes were developed in all specimens, assuming no failure in the welds. The collapse of single-hat sections is unstable from the very beginning, whereas double-hat sections start their collapse following a symmetric scheme that turns into antisymmetric with the ongoing crushing. The length of the flanges housing the weldings has a certain influence on the point where the symmetric collapse turns into antisymmetric [201].

Some views of the finite element models during the crushing are offered in Figure 5.2. Unstable collapses are observed in all configurations.

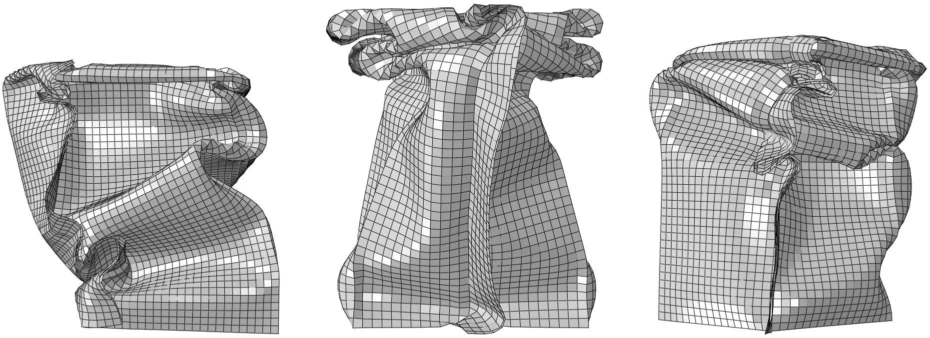

(a) Single-hat square section, $\delta = 0.5\delta_{\text{max}}$.

(b) Double-hat square section, $\delta = 0.5\delta_{\text{max}}$.

(c) Double-hat hexagonal section, $\delta = 0.5\delta_{\text{max}}$.

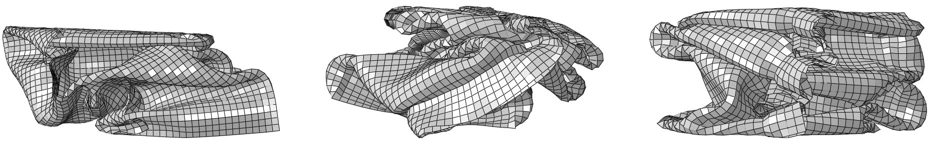

(d) Single-hat square section, $\delta = \delta_{\text{max}}$.

(e) Double-hat square section, $\delta = \delta_{\text{max}}$.

(f) Double-hat hexagonal section, $\delta = \delta_{\text{max}}$.

Figure 5.2: Axial collapse of squared single-hat, squared double-hat and hexagonal double-hat empty aluminum tubes with a flange width of 20 mm. All three designs developed non-symmetrical, unstable collapse modes. See dimensions in Figure 5.1.

Given that unstable collapse modes were present for the three designs for any flange wisth, the analyses were repeated adding a PET-foam core, which would be present in the final design as well. The aim was to stabilize the collapse modes for a better performance of the metal part. Besides, the foam should increase the crushing force levels and therefore the absorbed energy. The results obtained for the designs with a foam padding showed that stable collapse modes were actually achieved for all configurations and flange widths (see, for instance, the crushing mode of the hexagonal profile in Figure 5.3). Results are summarized in Table 5.1. Double-hat hexagonal profile exhibited the highest specific energy absorption.

Section	f [mm]	SEA [kJ/kg]	Collapse mode
Single hat, square	10	15.64	Regular, stable
	20	15.43	Regular, stable
Double hat, square	10	15.46	Symm. → asymm.
	20	16.72	Symmetric
Double hat, hexagonal	10	17.07	Symmetric
	20	17.10	Symmetric

Table 5.1: Specific energy absorption and collapse modes of the analyzed sections filled with foam.

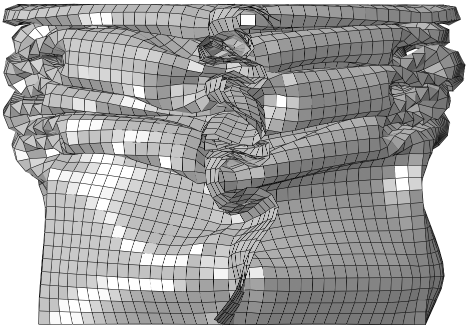

Figure 5.3: Regular, progressive axial collapse of a foam-filled double-hat hexagonal profile, in contrast to Figure 5.2f.

The hexagonal cross section was selected for the new components for its higher specific energy absorption. A series of empty specimens with different bonding techniques were produced to undergo experimental axial crushing tests and select the strongest welding for the filled components. These techniques included spot welds and single or double-bead laser welding. Spot welds opened with the quasi-static axial crushing in all the tested tubes and the single-bead laser welding was too weak too, whereas components joined by double-bead laser weldings passed the preliminary quasi-static axial crushing tests. Therefore, this technique was selected for the GFRP–foam filled components.

Experimental quasi-static crushing tests on laser-welded hexagonal profiles filled with PET foam and GFRP were conducted. However, despite the promising results of the simulations, these tests showed that the heat-affected zone near the weldings, which also presented some root humping [202], was too week to withstand the crushing of the filled component. This derived in a catastrophic failure when the filler pushed outwards during compression, depicted in Figure 5.4.

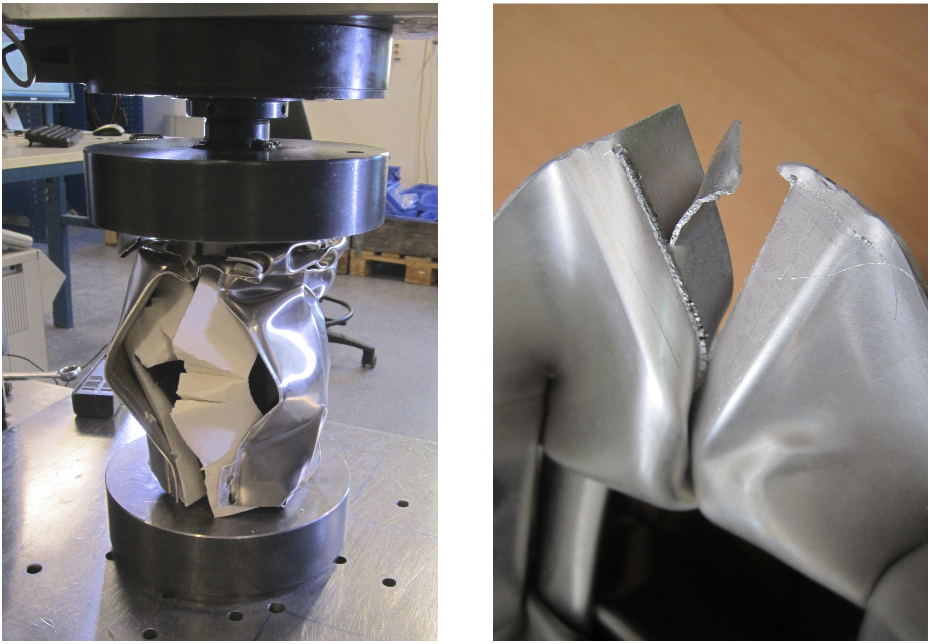

(a) Component failure. **(b)** Weld failure (heat-afected zone).

Figure 5.4: Catastrophic failure of a laser-welded hexagonal aluminum box filled with PET foam and GFRP.

Given the difficulties found in the structural bonding of the double-hat sections, an extruded profile was considered to be used for the outer tube. However, no commercial hexagonal extruded profiles were available in Europe in the studied range of dimensions and the price of a custom die was not affordable. As an alternative, the crash box shown in Figure 5.5a was studied, which consisted of an AA6063-T5 aluminum circular extrusion internally reinforced with a structure made of three plates of a glass-fiber reinforced polyamide and polymeric foam. The aluminum thickness was increased to 1.9 mm to obtain a more progressive crushing (see irregular folds in Figure 5.4a, due to an insufficient thickness). The gaps between aluminum and GFRP parts are now partially filled with the polymeric foam prisms. The total length of the component is 350 mm and its mass is equal to 1736 g. The length of the foam prisms is equal to the total length of the component, and the length of the GFRP plates is reduced in 2 mm to avoid an overlapping of the initial peak forces.

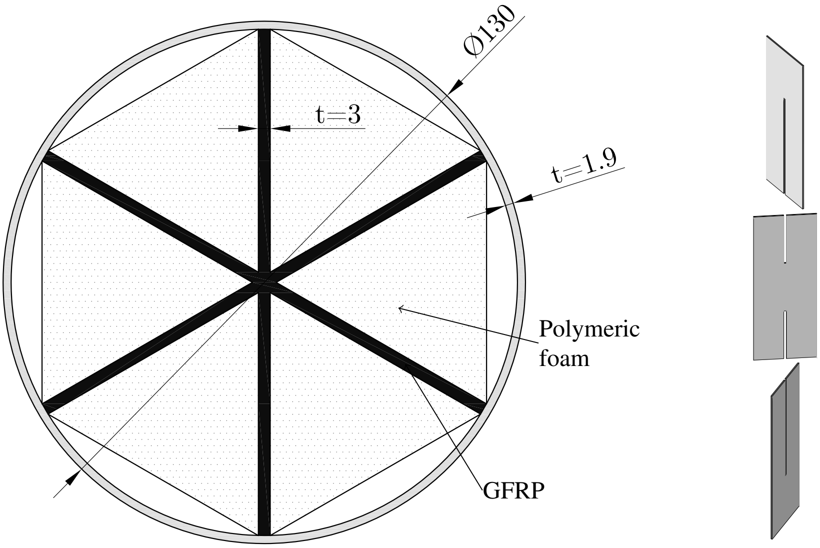

(a) Cross-section of the crash box. **(b)** GFRP assembly.

Figure 5.5: Cross-section of the proposed crash box made of aluminum (gray), polymeric foam (dotted) and GFRP plates (black) and assembly scheme. Dimensions in millimeters.

5.2 Material behavior

In order to help to understand the performance of the proposed design, a test campaign was planned to obtain the mechanical properties of the selected materials. These tests and their results are described next.

5.2.1 AA6063-T5 aluminum alloy extrusion

Since the material properties of metals have a strong dependency on the industrial production process, material specimens extracted from the same extruded circular hollow aluminum sections employed for the crash boxes were tested. These extractions were made so that their longitudinal axis was aligned with the extrusion direction of the tubes, which inevitably leads to a certain curvature of the specimens. The detailed geometry of the tensile specimens is offered in Figure 5.6.

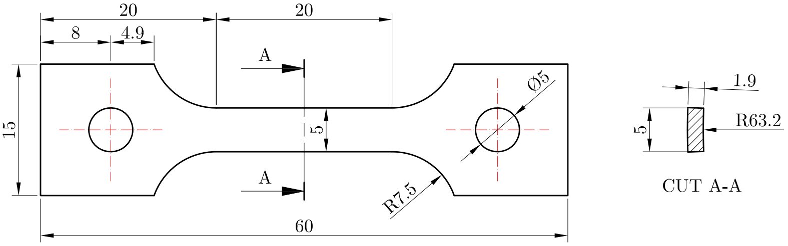

Figure 5.6: Dimensions of the AA6063-T5 tensile specimens extracted from the tubes in their longitudinal direction, in millimeters.

The stress-strain response of these specimens was compared to the results obtained from regular cylindrical tensile specimens of the same alloy, extracted from a extruded block. This was done in order to check the influence of the extrusion process on the material behavior.

Tensile tests have been performed on three extracted specimens and two cylindrical specimens at a constant rate of 1 mm/min and true stress-strain curves were obtained, shown in Figure 6.1. Strain values were measured with an extensometer, so they are valid up to diffuse necking only.

Different properties between the alloy in the tubes and the regular specimens were clearly observed: the former had a higher initial yield strength and reduced hardening compared to the latter. These high yield strength and reduced hardening, shown in Figure 6.1, are common for tempers T5 and T6 in the 6xxx series. Some useful mechanical properties have been obtained from these tests and included in Table 6.1 from the extracted specimens. Negligible strain rate sensitivity was expected, as usually happens with 6xxx alloys [203, 204].

5.2.2 Glass-fiber reinforced polyamide

The first reinforcement part was made of Ultramid A3WG10 BK00564 (BASF). The parts were built by injecting 3-millimeter thick plates, cutting them and

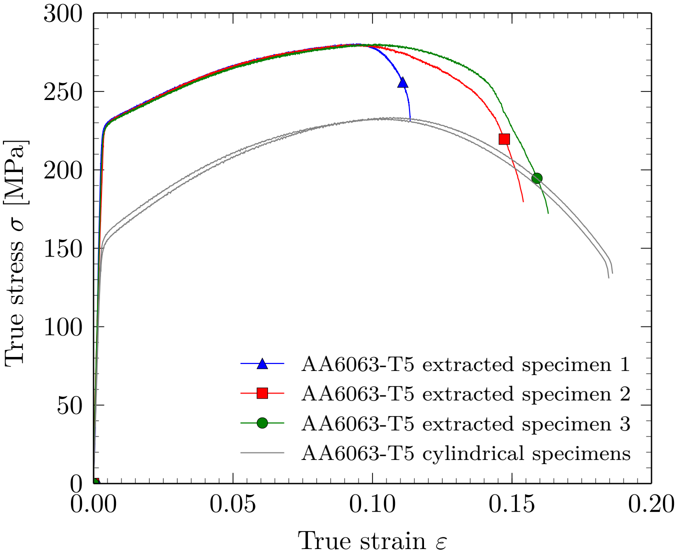

Figure 5.7: AA6063-T5 extrusion true stress-strain curves obtained from experimental tensile tests on plane specimens extracted from circular hollow extrusion and cylindrical specimens from a block extrusion.

Property	Value
Density [t/m^3]	2.56
Young's modulus [GPa]	53.85
Poisson ratio	0.33
Initial yield stress [MPa]	225.00

Table 5.2: Material properties of aluminum alloy AA6063-T5 in circular hollow extrusion.

assembling the three elements required for each tube in the way shown in Figure 5.5b. Some tensile tests on plane specimens at different strain rates were conducted to get some information about its behavior, even though higher strain rates were reached in the component impact tests. The dimensions of the plane specimens are plotted in Figure 5.8.

The material was tested in tension up to failure at strain rates of $3.25 \times 10^{-5}\,\mathrm{s}^{-1}$, $3.25 \times 10^{-4}\,\mathrm{s}^{-1}$ and $8.12 \times 10^{-3}\,\mathrm{s}^{-1}$, which correspond to test speeds of 0.2, 2 and 50 mm/min, respectively. Three repetitions were made for each speed, and representative curves are plotted in Figure 6.4.

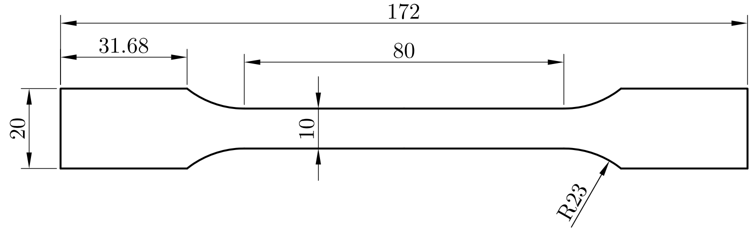

Figure 5.8: Dimensions of the GFRP plane tensile specimens, in millimeters.

In view of the curves, the material exhibits a certain degree of strain rate sensitivity for the $\dot{\varepsilon}$ levels tested. A value of 15.48 GPa is obtained for the Young's modulus, which indicates a relatively stiff thermoplastic material. Its density ($1.55\,\mathrm{t/m^3}$) and Poisson's ratio (0.40) are available in [205], together with the theoretical elastic modulus and other mechanical properties.

It can also be observed that the failure strain tends to rise with higher strain rates: 2.14 % at $3.25 \times 10^{-5}\,\mathrm{s^{-1}}$, 2.38 % at $3.25 \times 10^{-4}\,\mathrm{s^{-1}}$ and 2.54 % at $8.12 \times 10^{-3}\,\mathrm{s^{-1}}$.

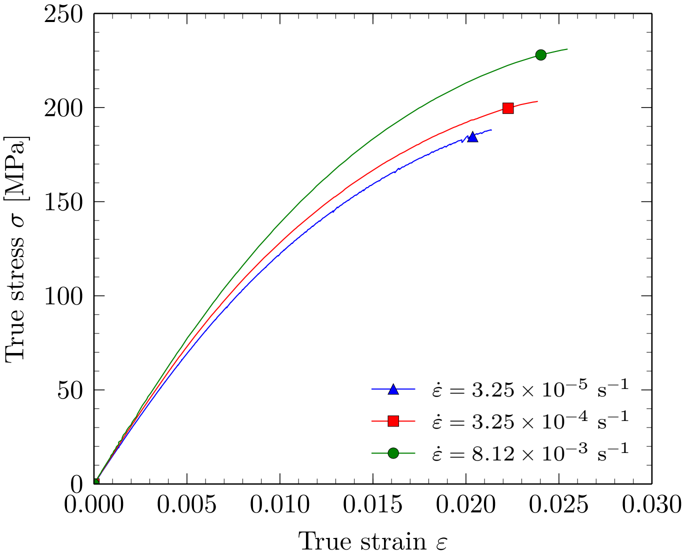

Figure 5.9: True stress-strain curves obtained from experimental uniaxial tests at different strain rates from smooth tensile specimens of Ultramid A3WG10 BK00564.

5.2.3 PET-based polymeric foam

The second element of the reinforcement consisted of six prisms of the PET-based foam ArmaFORM PET/W AC 135. Six triangular prisms were inserted between the glass fiber plates and the extruded tube, as shown in Figure 5.5a.

Given that this material is manufactured through an extrusion process, some anisotropy in the mechanical properties can be expected. Therefore, the material parameters were obtained in the load direction of the crash box, which is orthogonal to the direction in which the foam was extruded during its manufacture process. Meeting the requirements of ISO 844:2014 [206], specimens of 50 × 50 × 30 mm were extracted and loaded in uniaxial compression at different rates along the 30 mm direction, which is orthogonal to the extrusion orientation. Additionally, this material was tested at an elevated strain rate using a drop tower in which a mass of 8 kg was dropped at 6.78 m/s on specimens with dimensions 50 × 50 × 40 mm, cut in the same direction as the ones for the quasi-static compression tests.

True stress-strain curves were computed taking into consideration the compressibility of the material, as follows:

$$\sigma = s \exp\left(-2\nu^{\mathrm{p}}\varepsilon_1\right), \tag{5.2}$$

where σ is the true stress, s is the engineering stress, ν^{p} is the plastic Poisson ratio and ε_1 are the axial true strains. An additional assumption was made when it comes to obtaining the plastic Poisson's ratio, originally defined for isotropic materials as the ratio of the transverse plastic strains to the plastic strain in the load direction:

$$\nu^{\mathrm{p}} = \frac{\varepsilon^{\mathrm{p}}_{2,3}}{\varepsilon^{\mathrm{p}}_1}. \tag{5.3}$$

Considering the anisotropy of the material ($\varepsilon^{\mathrm{p}}_2 \neq \varepsilon^{\mathrm{p}}_3$) the mean value of both transverse directions was used to obtain the transverse plastic strain. According to this, a value of $\nu^{\mathrm{p}} = 0.089$ is derived from the uniaxial compression tests.

Table 6.5 contains a summary of the mechanical properties of the PET foam in the orientation orthogonal to the extrusion direction, and the stress-strain curves for three different loading rates are plotted in Figure 6.6. The continuous line for 6.78 m/s is an average of the original signal (dashed line) so that the noise arising from stress waves traveling along the load cell can be removed. Some strain rate sensitivity was observed.

Property	Value at 6 mm/min
Density [t/m^3]	0.135
Young's modulus [MPa]	20.41
Elastic Poisson ratio	0.10
Initial yield stress [kPa]	770.00
Plastic Poisson's ratio	0.09

Table 5.3: Material properties and model parameters of ArmaFORM PET/W AC 135 PET-based foam in the direction orthogonal to extrusion.

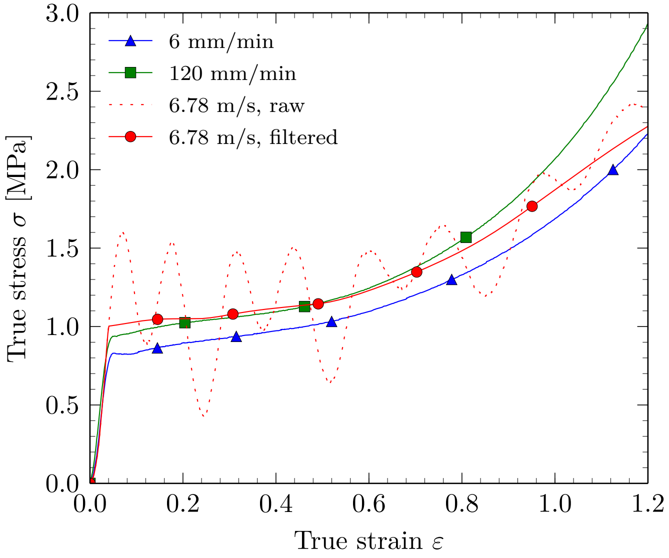

Figure 5.10: True stress-strain curves from uniaxial compression tests at different loading rates for Armaform PET/W AC 135 PET-based foam in the direction orthogonal to the extrusion direction.

5.3 Component testing program

5.3.1 Quasi-static compression tests

Low-speed compression tests were carried out on the components to assess their quasi-static behavior. An INSTRON 1332 universal test machine was employed for this task. Components were axially compressed at a constant velocity of 50 mm/min until bottoming out of the part, i.e. approximately 200-250 mm. Three parallel component tests were carried out and named C1, C2 and C3. Additionally, for comparative purposes, an empty circular extrusion (C0), a glass-fiber reinforced extrusion (CG) and a foam-filled extrusion (CF) were tested as well. Table 5.4 contains a summary of the tested components in the quasi-static campaign.

All specimens were triggered at their impacted ends by bending inwards the generatrix edge of the aluminum extrusion about 2 mm, forcing the progressive collapse to start with a stable concertina mode. For all components except C0, triggering was only possible in those regions which are not in initial contact with the glass-fiber structure or the foam (see Figure 5.5a). For the sake of consistency, the same triggering pattern in specimen C0 was used even though its entire edge could be bent inwards. Minor geometrical imperfections were also detected in the cross-section of the extrusion consisting of a deformation about 1 mm in the circular geometry, and the triggering helped also to avoid undesired collapse modes caused by this fact.

5.3.2 Dynamic impact tests

Crash boxes should behave in a similar, predictable way, independently of the impact speed. In order to verify this point, dynamic impact tests were carried out on the chosen design. Components were tested at a high rate using a large pendulum accelerator, Figure 5.11. The reader is referred to [207] for a detailed description of the pendulum accelerator at SIMLab, but a brief description is provided next.

The test rig consists of a hydraulically-actuated rotational arm which accelerates a trolley with a mass of 1500 kg to a certain velocity. The trolley was equipped with a 500 kN load cell in order to obtain forces, displacements, velocities and accelerations. Displacement measurements were also checked with a high-speed camera which recorded the impact behavior at a frame rate of 16 000 frames per second. The differences between both measurements were negligible. Initial impact velocities were checked with a photocell, which provided an estimated error of a 1.3% on the preset speed of 10 m/s. The last 50 mm of the specimens were clamped and screwed to a massive concrete reaction wall

(150 000 t), which gives a free deformation length of 300 mm.

For safety reasons, two buffers had to be placed at both sides of the specimen to stop the trolley safely and to avoid extreme force values in the load cell due to the bottoming-out of the specimens. This caused that the obtained force-displacement curves were only valid before the contact between the trolley and the buffers, which in this case occurred after 185 mm of axial crushing. A photograph of the clamped component and the two safety buffers is provided in Figure 5.12. Two components were tested at 10 m/s under the described impact conditions, labeled D1 and D2 (see test matrix in Table 5.4).

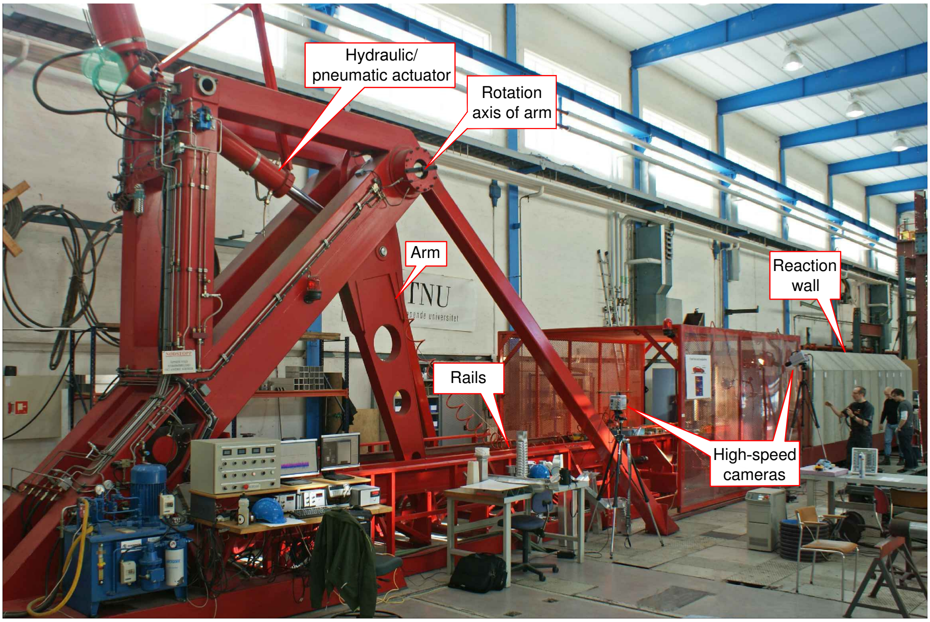

Figure 5.11: The «kicking machine» or pendulum accelerator at SIMLab facilities. Image taken from [208].

5.4 Results and discussion

5.4.1 Quasi-static compression tests

The force-displacement curves obtained from the quasi-static axial crushing tests are shown in Figure 5.13a for an empty tube and for tubes with reinforcement.

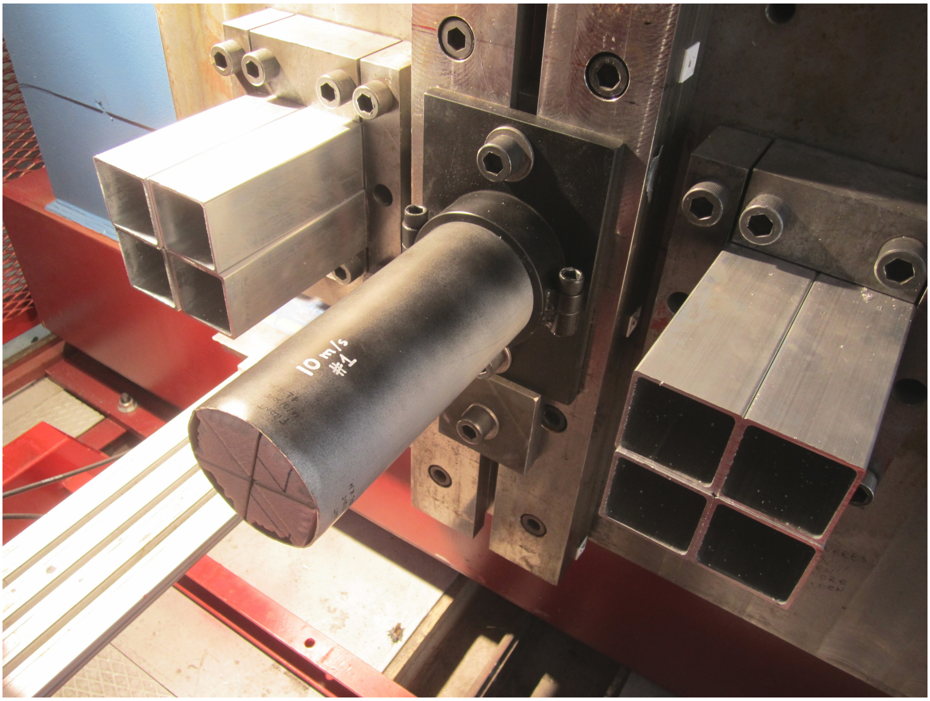

Figure 5.12: Impact test set-up: component (center) and safety buffers (sides). The component is airbrushed with black paint to avoid reflections in the images captured by the top camera.

The current average crushing force is also provided in Figure 5.13b, obtained as

$$F_{\text{avg}} = \frac{1}{\delta} \int F \mathrm{d}\delta. \tag{5.4}$$

As additional information, Figure 5.14 contains some sequential pictures of the tests where the different collapse modes can be observed.

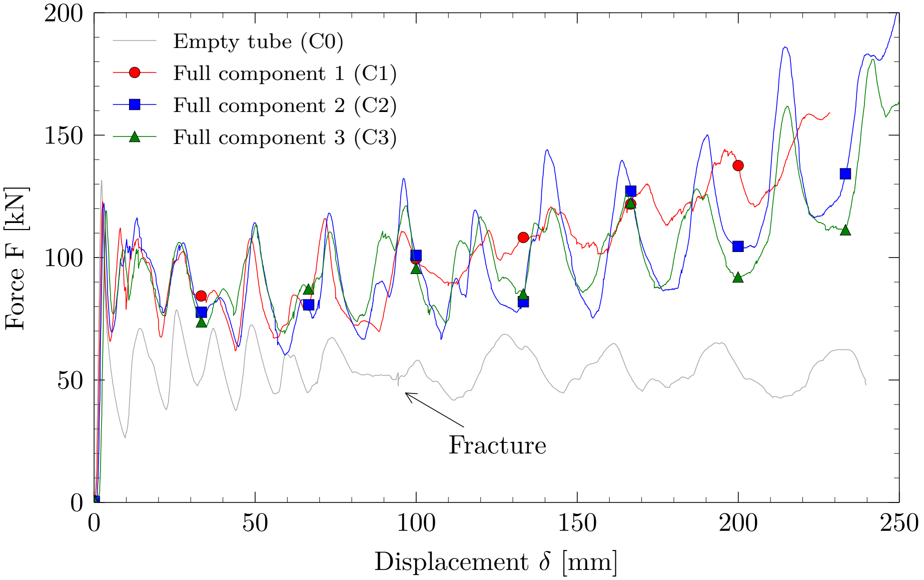

(a) Force-displacement curves.

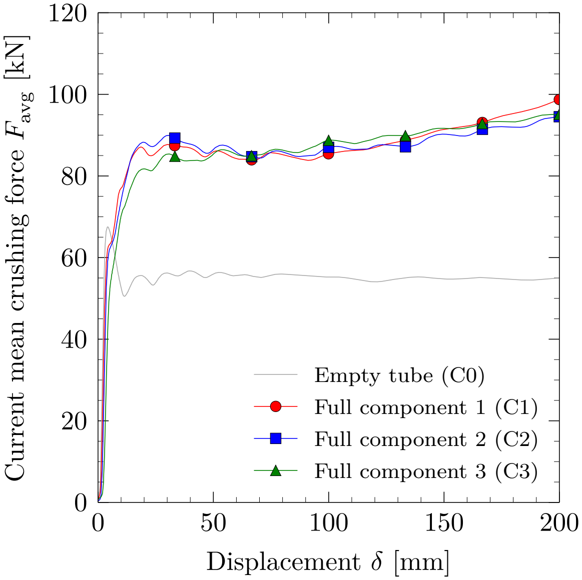

(b) Average force-displacement curves.

Figure 5.13: Instantaneous and average force-displacement curves obtained from the quasi-static crushing tests of components C1, C2 C3 and an empty tube (C0).

(a) $\delta = 4.7\,\mathrm{mm}$ **(b)** $\delta = 137.1\,\mathrm{mm}$ **(c)** $\delta = 239.0\,\mathrm{mm}$

(d) $\delta = 5.0\,\mathrm{mm}$ **(e)** $\delta = 137.4\,\mathrm{mm}$ **(f)** $\delta = 228.0\,\mathrm{mm}$

Figure 5.14: Quasi-static compression tests: progressive collapse of specimen C0 (*a* to *c*), and components C1 (*d* to *f*) and C2 (*g* to *i*). The collapse mode of the component C3, omitted here for brevity, was identical to C2. Continues on next page.

Component label	Characteristics	Test speed
C0	AA6063-T5 extrusion	Quasi-static
CG	AA6063-T5 extrusion + GFRP structure	Quasi-static
CF	AA6063-T5 extrusion + PET-foam prisms	Quasi-static
C1, C2 and C3 (repetitions)	Full component	Quasi-static
D1 and D2 (repetition)	Full component	Impact at 10 m/s

Table 5.4: Summary of the testing campaign: labels and descriptions of the tested designs.

(g) $\delta = 5.0\,\mathrm{mm}$ **(h)** $\delta = 137.4\,\mathrm{mm}$ **(i)** $\delta = 255.7\,\mathrm{mm}$

Figure 5.14: (Continues from previous page) Quasi-static compression tests: progressive collapse of specimen C0 (*a* to *c*), and components C1 (*d* to *f*) and C2 (*g* to *i*). The collapse mode of the component C3, omitted here for brevity, was identical to C2.

It is interesting to point out the different modes developed by the component depending on its inner reinforcement. The empty tube (C0) developed a concertina-like collapse at the beginning (due to triggering) which evolved into a three-lobe diamond mode. Although the latter is theoretically more efficient for energy absorption purposes, it is also true that larger strains are reached in the vertices and therefore fracture can be present. This is specially threatening in aluminum alloys with temper T5 or T6, which are less ductile than, for example, T4. It was indeed observed some incipient fracture in this specimen in the diamond lobes. In fact, a first fracture can be easily observed in the transition between the two modes in the force-displacement curves, at a crushing distance of 90 mm approximately (Figure 5.13a). Besides, the lobe wavelengths for the diamond mode are larger than the ones for the concertina mode, thus a minor number of lobes can be developed with a diamond-like collapse. This specimen showed six concertina lobes (three inwards and three outwards) and four alternate triangles up to a crushing length of 250 mm. This relatively high number of lobes is due to the reduced hardening shown by the T5 temper (Figure 6.1), which concentrates the yielded regions and therefore the lobe lengths are reduced. A picture of the axially crushed specimen C0 is presented in Figure 5.15a.

Specimen CG exhibited the same pattern as C0: six concertina folds (three inwards, three outwards) and a series of diamond lobes. These are slightly more irregular due to the presence of the glass fiber plates inside the structure. Relatively large fragments of the plates were found after the test, so the energy absorption of this design is not exploited at its best. The force-displacement curve for this specimen is analyzed in Section 5.4.4 (Figure 5.19a), and a picture of the crushed specimen is offered in Figure 5.15b.

Specimen CF developed a transition mode very similar to the one observed in specimen C0, with four concertina lobes (two inwards, two outwards) followed by a series of diamond-like lobes. Also, only very minor fracture initiations were observed in some corners of the diamond lobes. The similarities between C0 and CF are explained by the presence of gaps between the foam prisms and the outer extrusion in the undeformed configuration, which prevents any interaction of the foam with the extrusion. The reader is referred to Figure 5.19a for the force-displacement curve of CF and Figure 5.15c for a picture of the crushed specimen.

Regarding the full components, component C1 showed also a combined collapse mode (concertina to three-lobe diamond) with some crack initiations in the triangular lobes, which are perceptible in Figures 5.14e and 5.14f. However, components C2 and C3 developed a very stable concertina collapse mode with 19 folds developed at a crushing distance of 225 mm, and the differences between these two were minimum. Crushed component C3 is depicted in Figure 5.15d. Nevertheless, even though C1 collapsed in a mixed mode, the average force levels for the three full components were very similar (Figure 5.13a).

(a) Specimen C0. **(b)** Specimen CG.

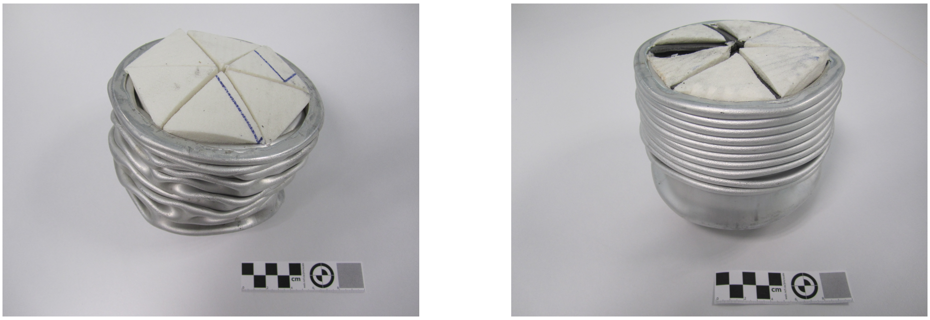

(c) Specimen CF. **(d)** Component C3.

Figure 5.15: Specimens C0, CG, CF and component C3 after quasi-static axial crushing (continues on next page).

5.4.2 Crashworthiness assessment

The absorbed energy, specific energy absorption, mean crushing load and crush force efficiency were obtained for a crushing length of 228 mm (65 %) for the proposed design and the empty extrusion. A very remarkable increase in the absorbed energy is achieved, even though the specific energy absorption of the design is slightly reduced compared to the aluminum extrusion alone. Besides, the crush force efficiency is strongly enhanced as well, since there is almost no difference between the initial peak load and the mean load. The differences in the initial peak loads for identical components (C1, C2, C3) lie in the minor differences when triggering the components manually. These results can probably

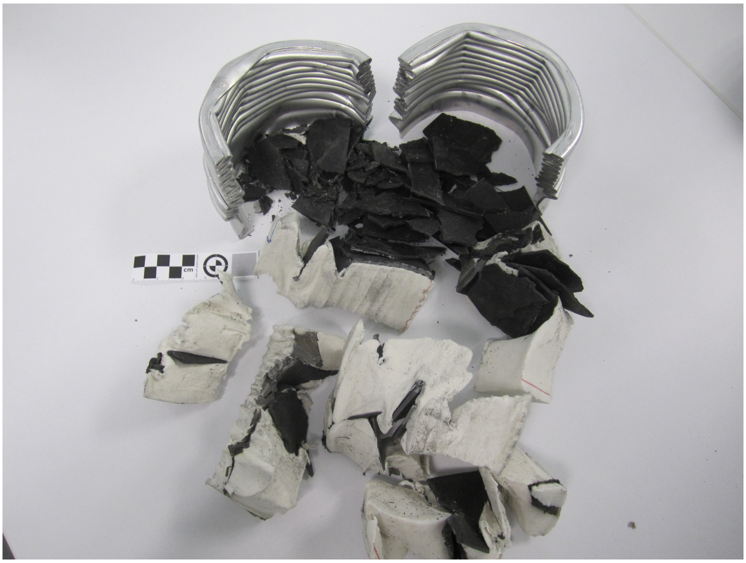

(e) Component C2 cut and unassembled for analysis.

Figure 5.15: (Cont.) Specimens C0, CG, CF and component C3 after quasi-static axial crushing.

be improved with a larger crushing distance since no clear bottoming-up was reached. All results are listed in Table 5.5, including the developed collapse modes: C (concertina) and D3 (three-lobe diamond).

	Collapse mode	Mass [g]	P_{peak} [kN]	P_{m} [kN]	*CFE*	E_{a} [kJ]	*SEA* [kJ/kg]
Specimen C0	C→D3	738	131.56	53.84	0.41	12.30	16.66
Component C1	C→D3	1737	122.92	103.19	0.84	23.57	13.57
Component C2	C	1737	122.12	98.70	0.81	22.54	12.98
Component C3	C	1737	119.17	97.30	0.82	22.25	12.80

Table 5.5: Crashworthiness parameters for an AA6063-T5 circular extrusion and for the proposed design obtained from quasi-static compression tests (both triggered) for a crushing distance of 228 mm. Collapse modes: C (concertina), D3 (three-lobe diamond).

According to Chapter 2, the mean crushing load of the empty extrusion can be estimated by Equation (2.37) for a concertina collapse mode and by Equation (2.29) for a diamond collapse mode. If these equations are applied, mean crushing loads of 49.16 kN and 65.38 kN are obtained for concertina and diamond modes, respectively. The experimental value fits into this range, provided that a mixed mode was observed.

5.4.3 Dynamic impact tests

The force-displacement curves obtained from the dynamic tests in the pendulum accelerator are shown in Figure 5.16a, where the corresponding quasi-static curves are presented as well for comparative purposes. These dynamic curves have been filtered using a moving-average filter to remove part of the high-frequency signals caused by the stress waves traveling along the load cell. Note that, as explained in Section 5.3.2, these results are only valid up to a crushing distance of 185 mm, due to the presence of two safety buffers.

Folding lengths were increased in the dynamic tests, as can be appreciated in Figure 5.16a, where the distance between consecutive folding peaks is shorter in the quasi-static curve than in the dynamic curves. Average force-displacement curves are also provided in Figure 5.16b, where it can be seen that larger folding lengths in the dynamic tests led to a certain reduction of the mean force and, thus, the absorbed energy.

Identical concertina collapse modes have been observed in both specimens, matching those obtained for specimens C2 and C3. The force levels are almost identical to the ones obtained in quasi-static tests and the folding lengths are also similar. Eighteen folds were developed for a crushing distance of 225 mm, i.e., one less fold than the quasi-static specimens. A sequential view of one of the tests is offered in Figure 5.17, and a view of components D1 and D2 after impact is provided in Figure 5.18.

The absorbed energy up to 185 mm of components D1, D2 and C3 is provided in Table 5.6. The slight decrease in energy absorption compared to the quasi-static tests was due to the reduction of the folding length observed in the dynamic components.

Component label	Absorbed energy up to 185 mm [kJ]
D1 (10 m/s)	15.92
D2 (10 m/s)	16.84
C3 (quasi-static)	17.31

Table 5.6: Energy absorbed up to an axial crushing of 185 mm by components D1 and D2 (impact) and C3 (quasi-static).

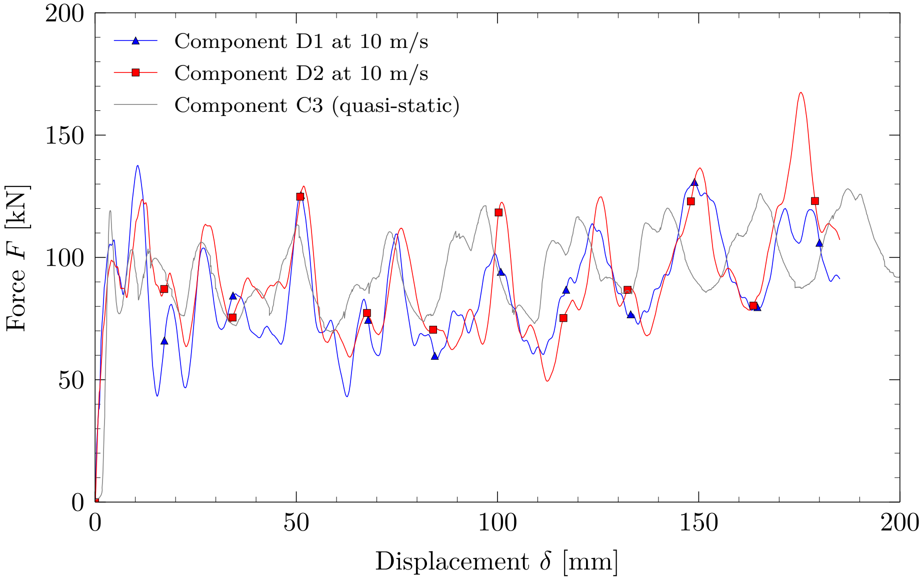

(a) Force-displacement curves.

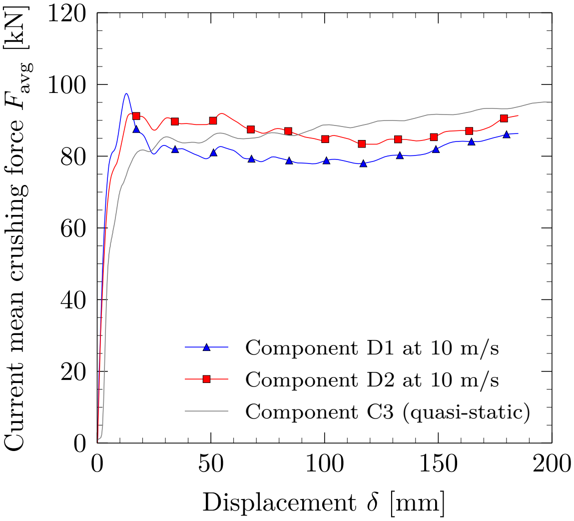

(b) Average force-displacement curves.

Figure 5.16: Instantaneous and average force-displacement curves obtained from the dynamic impact tests on components D1 and D2 at 10 m/s. A slight reduction of the folding lengths can be observed in the dynamic curves compared to the quasi-static values.

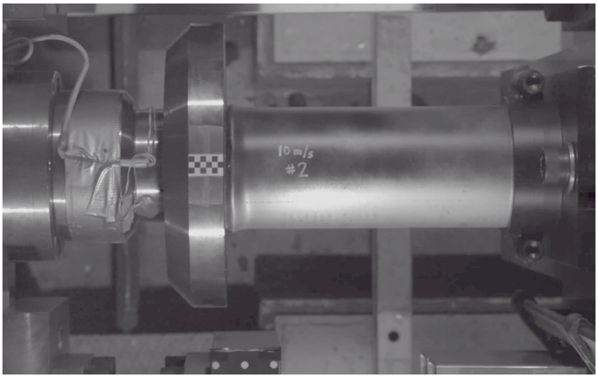

(a) $\delta = 5\,\mathrm{mm}$, t = 0.51 ms.

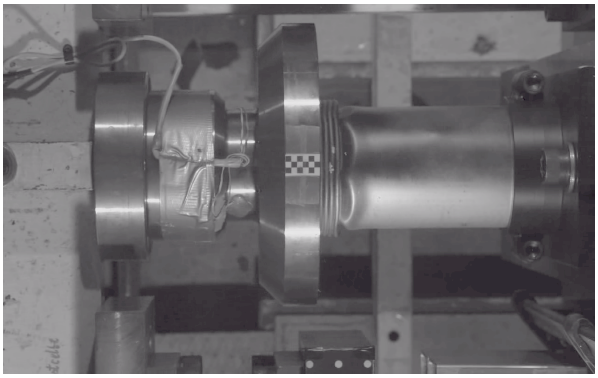

(b) $\delta = 5\,\mathrm{mm}$, t = 9.66 ms.

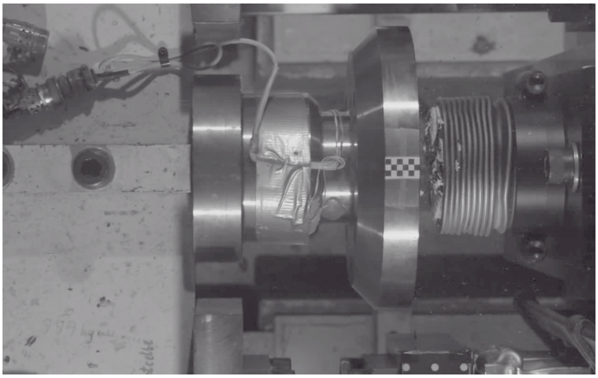

(c) Component after spring-back.

Figure 5.17: Sequential images from the 10 m/s impact test of component D2 in the kicking machine (top view).

Figure 5.18: Components D1 (left) and D2 (right) after impact test at 10 m/s. The clamped length of 50 mm is clearly appreciable.

5.4.4 Assessment of the interaction effect of the polymeric foam

When foam-filled metal columns are subjected to a crushing process, it is usual to observe that the total force-displacement curve is higher than the sum of the curves corresponding to each part separately. This is due to the interaction of the foam with the metal walls: the foam acts as a constraint which reduces the buckling length and, therefore, increases the number of lobes to be developed. In the proposed design, this phenomena could appear between the foam and the extrusion and also between the foam and the glass-fiber plates, since the former acts as a confinement which could contribute to a more efficient, progressive failure of the latter.

Hanssen et al. [26, 106] investigated the interaction between aluminum foam fillings and aluminum extrusions. In particular, they developed an additive design formula to obtain the average crushing force of circular aluminum extrusions with aluminum foam filler accounting for the interaction effect. This formula reads as

$$F_{\mathrm{avg}} = F_{\mathrm{avg}}^{0} + A_{\mathrm{f}}\sigma_{\mathrm{f}} + C_{\mathrm{avg}}\sigma_{\mathrm{f}}^{\alpha}\sigma_{0}^{(1-\alpha)}b_{\mathrm{m}}^{\beta}h^{(2-\beta)}, \tag{5.5}$$

where F_{avg} is the total average crushing force, F_{avg}^{0} is the average crushing force of the empty aluminum extrusion, σ_{f} is the yield stress of the aluminum foam,

A_f is the cross-sectional area of the foam, σ_0 is the yield stress of the aluminum alloy, $b_\mathrm{m} = b - h$, and b and h are the outer diameter and wall thickness of the extrusion, respectively. Lastly, C_avg, α and β are parameters to be calibrated.

Since this design contains three different materials, it was necessary to evaluate each material separately in order to analyze how far the total response of the crash box was better than the sum of the three materials separately. However, neither the foam prisms nor the glass-fiber structure can be crushed alone: the foam columns buckle outwards and the GFRP plates fall apart after incipient fracture. Therefore, both materials were analyzed inside the aluminum extrusion and denoted CG (GFRP) and CF (foam), Table 5.4.

The force-displacement curves for CG and CF specimens are plotted in Figure 5.19, together with the curves obtained for the aluminum extrusion alone (C0) and the complete component C1. Specimen C1 was chosen because its mixed collapse mode is more similar to the ones obtained for specimens C0, CF and CG. It is clearly seen in Figure 5.19a that the individual contribution of the foam and the glass fiber plates was very small, which is an indicator of the presence of some kind of additional contribution generated by the interaction between the materials.

It was analyzed if this phenomenon could be explained with the well-known interaction effect between the foam and the aluminum extrusion, even though the contacts between these parts are not closed before crushing. To this end, and following Hanssen's procedure [26, 106], the curves for the empty extrusion (C0), the foam-filled extrusion (CF), an estimation of the response of the foam prisms in uniaxial compression and the sum of this estimation and the empty extrusion were plotted together (see Figure 5.20). The estimation was made because of the infeasibility of obtaining the crushing response of the foam prisms alone without buckling. In view of the curves, it can be seen that the sum of C0 and foam is approximately equal to the response of specimen CF (see curves in Figure 5.20 and absorbed energies in Table 5.7), and therefore it can be stated that the interaction effect between foam and extrusion is negligible. However, an improvement of the interaction levels was observed as the crushing length increased, which was due to the fact that the space between foam and extrusion closed with the axial compression. Hence, closing the space between materials when designing a multi-material component for energy absorption is important.

Once the interaction between foam and extrusion was found to be of minor importance, the force-displacement curves of component C1 were compared to the sum of specimen CG and the estimated response of the foam (see Figure 5.21). A major difference between these curves was now observed and gray-shaded. Given

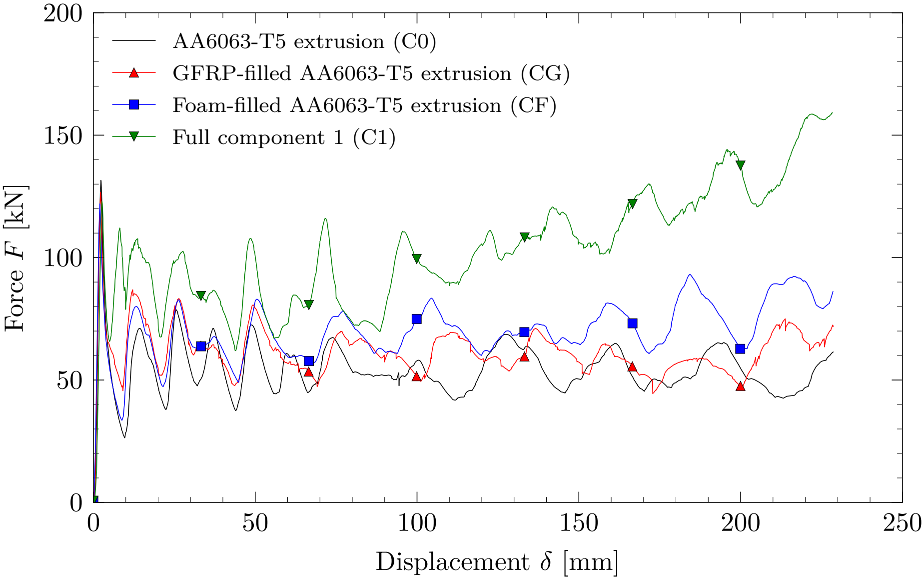

(a) Force-displacement curves.

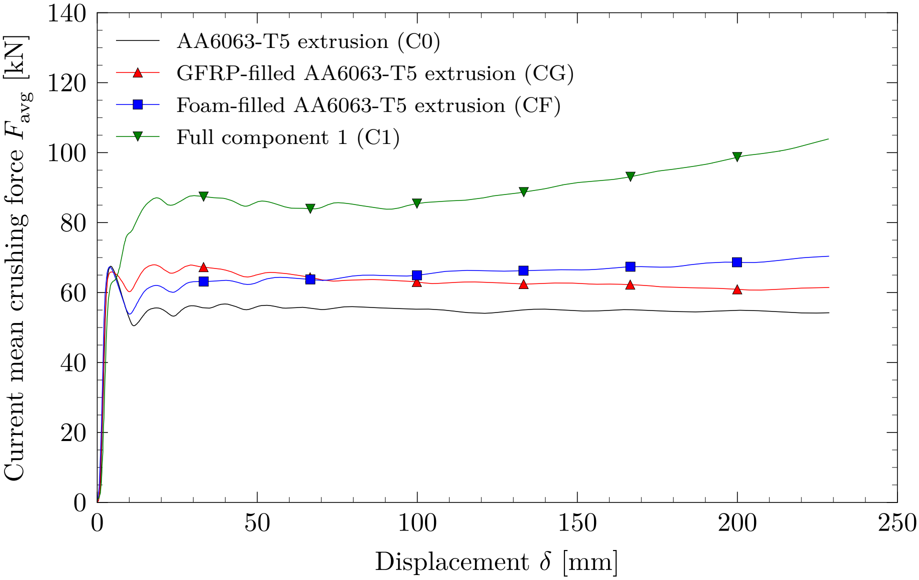

(b) Average force-displacement curves.

Figure 5.19: Force-displacement curves of different material combinations for the evaluation of the interaction effects in the proposed design.

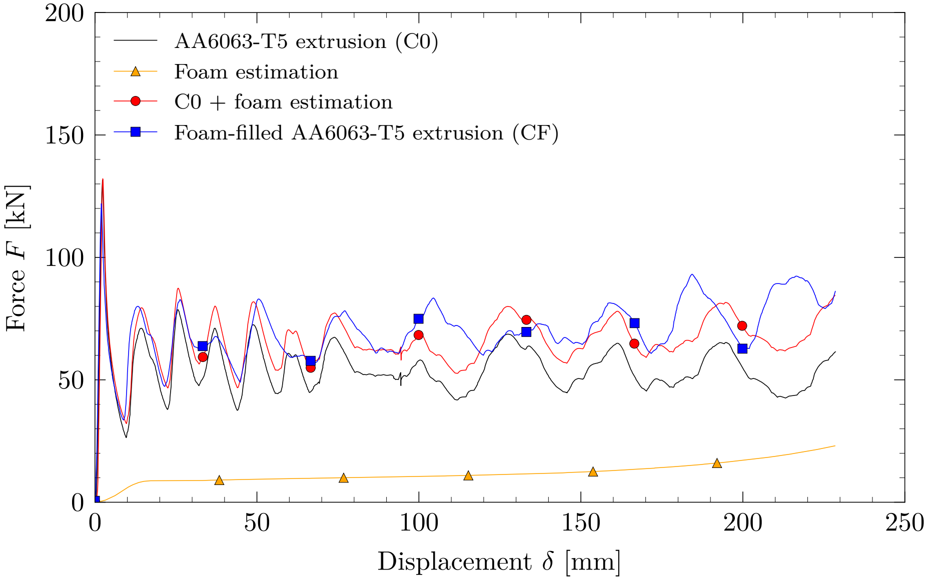

(a) Force-displacement curves.

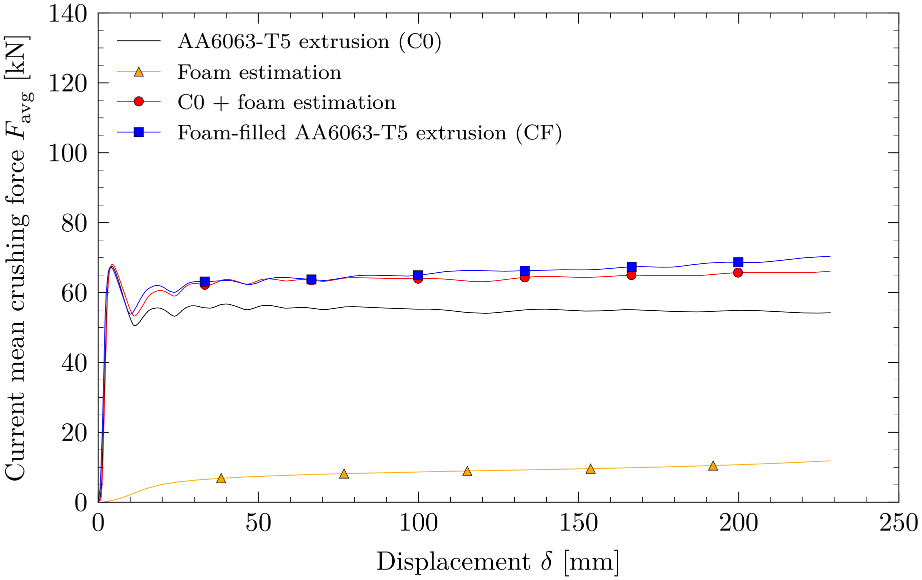

(b) Average force-displacement curves.

Figure 5.20: Force-displacement curves of different material combinations for the evaluation of the interaction effects in the proposed design.

that the foam is negligibly interacting with the extrusion, this improvement can only be due to the interaction (or confinement) of the foam and the glass-fiber plates. Indeed, the foam constrains the plates so that they do not fell apart after their first brittle fractures and keeps them in position for further degradation. In order to quantify this effect, the absorbed energies of component C1, CG and the sum of CG and foam are provided also in Table 5.7. A major difference (from 16.76 kJ to 23.57 kJ) arises as a consequence of the interaction effect.

	C0	CG	CF	Foam (est.)	C0 + foam	CG + foam	C1
E_a at $\delta = 228\,\mathrm{mm}$ [kJ]	12.30	14.04	16.08	2.72	15.02	16.76	23.57

Table 5.7: Energy absorbed by the compared specimens up to 228 mm.

With the aim of verifying this last statement, component C3 was cut (see Figure 5.15e) and compared the extracted GFRP debris with the spare GFRP fragments resulting from specimen CG. A comparison of the sizes of the fragments showed that the GFRP was more severely damaged when confined by the foam, Figure 5.22, and thus an increased contribution to the global energy absorption was achieved.

In order to quantify this interaction, and based on [106], α and β are taken equal to 0.5 and 1, respectively, for Equation (5.5). Here, σ_f was taken equal to $\sigma_{0.3} = 933.27\,\mathrm{kPa}$ and $A_\mathrm{f} = 9475.37\,\mathrm{mm}^2$, with $\sigma_{0.3}$ being the compression true stress corresponding to a true strain of 0.3 at a rate of 6 mm/min. This value has been taken as representative for the stress plateau in the stress-strain response of the foam. Due to the presence of mixed collapse modes, the average crushing force of the empty aluminum extrusion is obtained from the experiments, with a value of 53.84 kN. Furthermore, the last term of Hanssen's original equation was modified in order to account for the mechanical properties of the GFRP. To that end, the ultimate tensile strength $\sigma_\mathrm{u} = 200\,\mathrm{MPa}$ has been included. The exponents of this last term were changed to 1/3 to keep the dimensional consistency of the formula. To sum up, the expression proposed for our design reads as

$$F_\mathrm{avg} = F^0_\mathrm{avg} + \sigma_\mathrm{f} A_\mathrm{f} + C_\mathrm{avg} \sqrt[3]{\sigma_\mathrm{f}\sigma_0\sigma_\mathrm{u}}\, b_\mathrm{m} h. \tag{5.6}$$

The GFRP sheets cannot be crushed without a confinement because they buckle and fall apart. Therefore, their contribution is linked to the interaction effect. For this reason, the first addend (F^0_avg) refers to the average crushing force of the aluminum tube, i.e., the full component without any filling. This is related to the term in Hanssen's equation for the empty extrusion F^0_avg, which

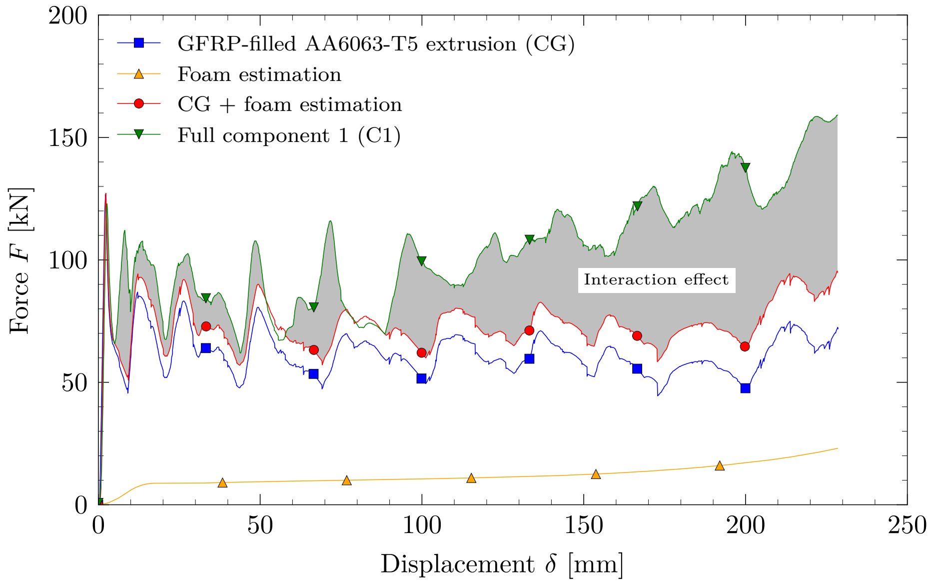

(a) Force-displacement curves.

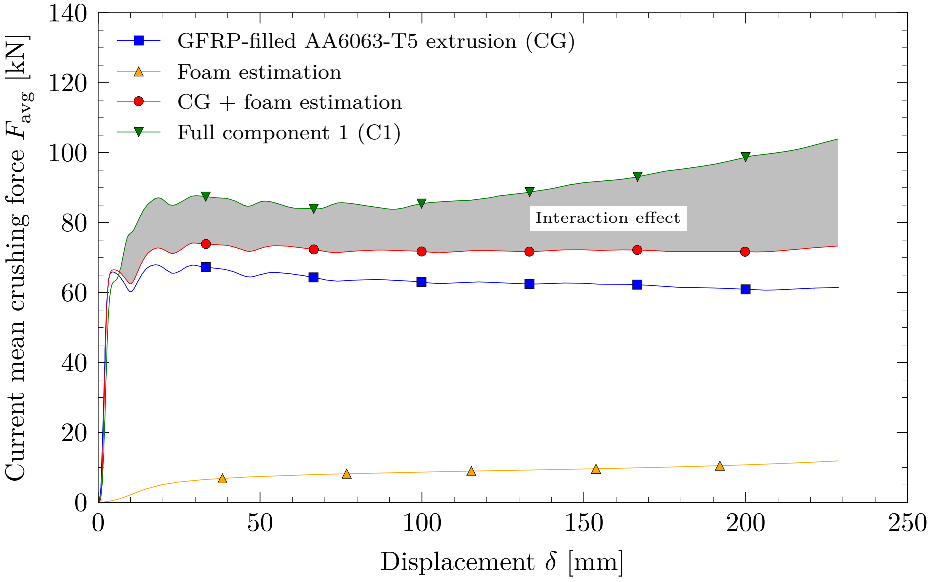

(b) Average force-displacement curves.

Figure 5.21: Force-displacement curves of different material combinations for the evaluation of the interaction effects in the proposed design.

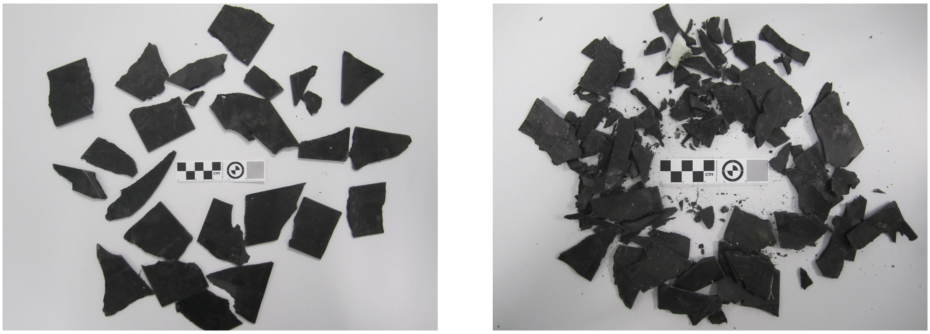

(a) GFRP debris after crushing specimen CG.

(b) GFRP debris after crushing component C3.

Figure 5.22: Comparison of the fragments of GFRP after crushing of specimen CG and component C3. A more severe degradation is observed for the latter.

also corresponds to the full component minus the foam part. The values of C_{avg} were obtained for different crushing lengths and they were compared to Hanssen's. These values are presented in Table 5.8.

Crushing length (%)	20	30	40	50	60
C_{avg} (Hanssen) [26]	1.08	2.07	2.45	2.74	2.90
C_{avg} (present)	2.46	2.65	3.09	3.67	4.29

Table 5.8: C_{avg} parameters for circular extrusions filled with aluminum foam (Hanssen, [26]) and circular extrusions filled with PET foam and GFRP (present).

In view of Table 5.8, it can be stated that the interaction effect for the proposed design was larger than for Hanssen's design, but in the same order of magnitude. This increment was due to the strong interaction between foam and GFRP and also to the fact that the contribution of the GFRP alone was negligible, i.e. its contribution arose only from its interaction with surrounding materials.

5.5 Conclusions

An experimental study on the crashworthiness of a three-material crash box has been carried out, including a material testing campaign. The components were analyzed quasi-statically and under impact and the following conclusions can be drawn:

- A double-hat hexagonal section had to be discarded at a first stage provided that none of the tested structural bondings - spot welds and single or double-bead laser welding - was able to resist the complete axial crushing of the components. Double-bead laser weld did keep both parts together during the axial crushing of the empty tube, but it did not resist the compression of the filled tube.

- It was observed that aluminum alloy AA6063 in temper T5 exhibits a very good performance in energy absorption by axial crushing, due to its high yield stresses and sufficient ductility. Only minor fracture initiations were found.

- The energy absorption of the aluminum tube reinforced with PET foam and GFRP increased by almost 100 % when compared to an empty extrusion, in exchange for a 16 % reduction of the specific energy absorption. Besides, the crush force efficiency was increased from 0.41 to 0.83. The components behaved in a very similar way at quasi-static and dynamic loading conditions.

- The separate contributions of the three different materials to the force response of the complete component were analyzed and quantified, as well as the interaction and confinement effects. A strong contribution was found in the interaction between the glass fiber and the foam, since the latter confined the former enhancing its performance. Moreover, a negligible interaction was observed between the foam and the extrusion. This is due to the fact that both parts are not in closed contact in the undeformed configuration. Finally, the interaction effects in the proposed design arising from the foam-GFRP interface have been quantitatively compared to the ones observed for aluminum foam filled extrusions.

- The quantification of the interaction effect was carried out using a modification of Hanssen's formula for foam-filled sections. This modification consisted of including the ultimate tensile strength of the glass fiber in the interaction term, with the correspondent change of exponents for dimensional consistency.

- The absorbed energy of the aluminum extrusions reinforced only with PET foam or only with GFRP was not significantly higher than the absorbed energy of the empty extrusion, given the excellent characteristics of the alloy; but a very remarkable enhancement was indeed produced when all the three materials were combined in a single design. This is explained by the fact that the foam confines the glass fiber plates, improving their performance.

References

[12] M. Costas, D. Morin, M. Langseth, L. Romera, and J. Díaz. “Axial crushing of aluminum extrusions filled with PET foam and GFRP. An experimental investigation”. *Thin-Walled Structures* 99 (2016), pp. 45–57.

[26] A. Hanssen, M. Langseth, and O. Hopperstad. “Static and dynamic crushing of circular aluminum extrusions with aluminum foam filler”. *International Journal of Impact Engineering* 24.5 (2000), pp. 475–507.

[106] A. Hanssen, M. Langseth, and O. Hopperstad. “Static and dynamic crushing of square aluminum extrusions with aluminum foam filler”. *International Journal of Impact Engineering* 24.4 (2000), pp. 347–383.

[201] F. Wang, Y. Mo, J. Lv, F. Huang, and Q. He. “Numerical studies on STFD-HAT sections under axial dynamic impact”. *Thin-Walled Structures* 82 (2014), pp. 105–114.

[202] A. Castro and C. Prado. “Study of the root droplets in high thickness hybrid welding”. MA thesis. Dept. of Engineering Sciences and Mathematics, Luleå University of Technology, Sweeden, 2011.

[203] H. Zhu, L. Zhu, and J. Chen. “Damage and fracture mechanism of 6063 aluminum alloy under three kinds of stress states”. *Rare Metals* 27.1 (2008), pp. 64–69.

[204] V. Vilamosa. “Behaviour and Modelling of AA6xxx Aluminum Alloys Under a Wide Range of Temperatures and Strain Rates”. PhD thesis. SIMLab (Structural Impact Laboratory), NTNU, 2015.

[205] BASF. *Ultramid (R) A3WG10 BK00564 Polyamide 66. Product information sheet.* 2015.

[206] ISO. *Rigid cellular plastics – Determination of compression properties.* ISO 844:2014. International Organization for Standardization, 2014.

[207] A. Hanssen, T. Auestad, T. Tryland, and M. Langseth. “The kicking machine: A device for impact testing of structural components”. *International Journal of Crashworthiness* 8 (2003), pp. 385–392.

[208] M. Kristoffersen. “Impact against X65 offshore pipelines”. PhD thesis. SIMLab (Structural Impact Laboratory), NTNU, 2014.

6

Crashworthiness of metal tubes filled with PET foam and GFRP. Part II: computational simulation and multi-objective optimization

This chapter constitutes the continuation of the study of metal extrusions filled with PET foam and a GFRP skeleton, whose experimental part was presented in Chapter 5. Herein, a finite element model was calibrated with the results obtained in the material testing campaign described in Chapter 5 and Appendix A, using appropriate constitutive equations. These models have been improved compared to the models previously presented in Chapter 3. Three relevant design variables were selected: the thickness of the cylinder, the thickness of the GFRP plates and the density of the PET foam, the latter being related to its crushing strength. These design variables were used to formulate a design optimization problem to improve the component's crashworthiness. Given the high computational cost of each evaluation, metamodels were built on a large-scale sampling.

Derived from the conclusions about the effectiveness of different surrogate models presented in Chapter 4, MARS metamodels were conveniently fit to the data, and the multi-objective genetic optimization algorithm tested in Chapter 4 was employed to obtain the optimum sets of four different objective functions: the specific energy absorption, the initial peak load, the component's mass and the absorbed energy. Results allowed a deeper understanding of the contribution of each material to the overall response of the component and an improvement of the crash performance in terms o specific energy absorption and peak loads. Besides, the obtained Pareto fronts allow the selection of different optimum designs depending on the crashworthiness requirements.

6.1 Material constitutive models

This section presents the fit of selected material constitutive models to the obtained experimental results. Each model takes into account the most relevant characteristics of each material.

6.1.1 AA6063-T5 aluminum alloy

In order to account for large plastic deformations and strain rate sensitivity, an isotropic hypoelastic-viscoplastic material model consisting of a two-term Voce law [209] was adopted, multiplied by a viscosity term. The additive decomposition of the strain rate tensor **D** and the derivation of the flow rule presented on page 76 was applied, and a yield condition with isotropic hardening was also employed:

$$f\left(\boldsymbol{\sigma}, p\right) = \sigma_{\text{eq}}\left(\boldsymbol{\sigma}\right) - \left(\sigma_0 + R\left(p\right)\right), \tag{6.1}$$

where p is the equivalent plastic strain, σ_0 is the initial yield strength and the term $R\left(p\right)$ controls the isotropic hardening, which is now expressed as

$$R\left(p\right) = \sum_{j=1}^{2} Q_j \left[\left(1 - \exp\left(-b_j p\right)\right]. \tag{6.2}$$

In this equation, Q_j and b_j are material parameters to be calibrated through tensile tests.

In the same vein of what was derived in Chapter 3, the equivalent plastic strain rate $\dot{p}$ was defined as a function of the equivalent stress, the isotropic hardening function R and the reference equivalent plastic strain rate $\dot{p}_0$:

$$\dot{p} = \begin{cases} 0 & \text{if } f \leq 0 \\ \dot{p}_0 \left[\left(\dfrac{\sigma_{\text{eq}}\left(\boldsymbol{\sigma}\right)}{\sigma_0 + R\left(p\right)} \right)^{\dfrac{1}{C}} - 1 \right] & \text{if } f > 0. \end{cases} \tag{6.3}$$

Thus, the constitutive equation in the viscoplastic domain ($f > 0$) reads as follows:

$$\begin{aligned}\sigma_{\mathrm{eq}} &= \left[\sigma_0 + R\left(p\right)\right]\left[1 + \frac{\dot{p}}{\dot{p}_0}\right]^C \\ &= \left[\sigma_0 + \sum_{j=1}^{2} Q_j\left[1 - \exp\left(-b_j p\right)\right]\right]\left[1 + \frac{\dot{p}}{\dot{p}_0}\right]^C .\end{aligned} \tag{6.4}$$

The viscosity term is identical to the one proposed by Børvik et al. [210] for a modified Johnson-Cook model.

The values for the model parameters obtained from the tensile tests described in Section 5.2.1 with a least-squares fit are provided in Table 6.1. The value of the viscosity exponent C was taken from [203], where a value of $C = 0.0036$ was reported. This value indicates a low strain rate sensitivity, in line with most alloys of the 6xxx series [204]. Stress-strain curves from tensile experiments and simulations are provided in Figure 6.1 and show an excellent correlation between numerical and experimental data. Since an extensometer was used for strain measurements, experimental values are useful only up to the necking onset, marked in Figure 6.1.

Property or parameter	Value
Density, ρ [t/m^3]	2.56
Young's modulus, E [GPa]	53.8408
Poisson ratio, ν	0.33
σ_0 [MPa]	204.9386
Q_1 [MPa]	60.2799
b_1	19.2412
Q_2 [MPa]	3.9459
b_2	3078.8553
C	0.0036

Table 6.1: Material properties and model parameters of aluminum alloy AA6063-T5 in circular extrusion.

6.1.2 DDQ steel

For comparative purposes, the optimization algorithm was also run on a design consisting of a steel tube with identical dimensions and filling. A conventional deep drawing quality (DDQ) steel with a reported yield strength of 211.6 MPa

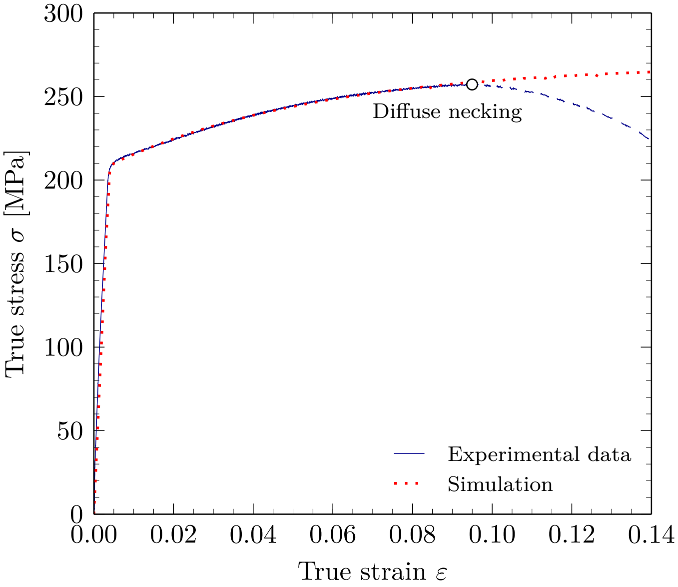

Figure 6.1: AA6063-T5 true stress-strain curves obtained from experimental tensile test and numerical simulation.

was considered, which was modeled through a Johnson-Cook constitutive equation identical to what was developed in Chapter 3. This material has a similar initial yield stress than that of the aluminum alloy[1] but larger hardening. In particular, saturation hardening for AA6063-T5 is about 65 MPa and the B parameter of the DDQ model, corresponding to the hardening at an equivalent plastic strain of 1, is about 500 MPa. A comparison of the stress-strain curves of both materials is provided in Figure 6.2, where it can be seen that the initial yield stress of the steel identified in [211] is arguable. The parameters for the steel model, presented in Table 6.2, have been taken from [211].

6.1.3 Glass-fiber reinforced polyamide

An isotropic hypoelastic-viscoplastic constitutive model with a failure criterion governed by the equivalent plastic strain, dependent on the strain rate and the stress triaxiality, was used to model the GFRP parts. This followed the same formulation than the aluminum model, with a minor modification related to the

---

[1] Since there is no agreement on the identification of the initial yield stress, Abedrabbo et al. [211] reported an arguable value of 211.6 MPa, which in the author's opinion falls short. Therefore, the difference between the initial yield stresses of the aluminum alloy and the steel is more relevant than what is stated.

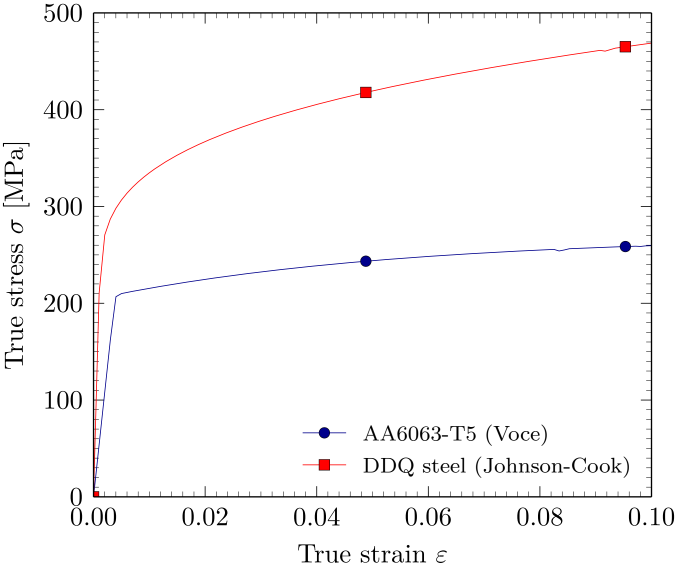

Figure 6.2: Comparison of the true stress-strain curves of AA6063-T5 extruded aluminum alloy and DDQ steel, both used in this chapter for the outer casing of the crash boxes. The curves correspond to a simulation of a single, linear solid 3D element loaded in tension.

Property or parameter	Value
Density, ρ [t/m^3]	7.85
Young's modulus, E [GPa]	210
Poisson ratio, ν	0.3
A [MPa]	211.6
B [MPa]	516.7
n	0.300
C	0.0346
$\dot{\varepsilon}_0$ [s^{-1}]	0.003

Table 6.2: Material properties and model parameters for DDQ steel, taken from [211].

strain rate sensitivity. Given the high stiffness of the material, it was considered that strains are elastic up to the value corresponding to a true stress of 25 MPa. A von Mises yield criterion was set at this point, and a Voce law with two terms was calibrated to fit the experimental hardening curves, as it was done for the aluminum model. The equation governing the hardening reads, therefore:

$$R(p) = \sigma_0 + \sum_{j=1}^{N_V} Q_j \left[1 - \exp\left(-b_j p\right)\right], \tag{6.5}$$

where σ_0 is the initial yield stress, set to 25 MPa, p is the equivalent plastic strain, N_V is the number of terms, set to two, and Q_j, b_j are the parameters to be calibrated, which were four in this case. The equivalent plastic strains were obtained from the uniaxial experimental tests as

$$p \approx \varepsilon^p = \varepsilon - \frac{\sigma}{E}, \tag{6.6}$$

where ε^p, ε and σ are the true plastic strain, the true total strain and the true stress, respectively.

The model accounts for strain-rate sensitivity through a definition of the equivalent plastic strain rate similar to Equation (6.3). However, since the value of the initial yield stress wanted to be fixed independently of the strain rate, this term had to be excluded from the multiplication by the viscosity term, thus

$$\dot{p} = \begin{cases} 0 & \text{if } f \leq 0 \\ \dot{p}_0 \left[\left(\dfrac{\sigma_{\text{eq}}(\boldsymbol{\sigma}) - \sigma_0}{R(p)}\right)^{\dfrac{1}{C}} - 1\right] & \text{if } f > 0. \end{cases} \tag{6.7}$$

This leads indeed to an expression for the equivalent stresses in the viscoplastic domain in which the initial yield strength is not affected by the viscosity term:

$$\begin{aligned} \sigma_{\text{eq}} &= \sigma_0 + R(p)\left[1 + \frac{\dot{p}}{\dot{p}_0}\right]^{\text{C}} \\ &= \sigma_0 + \left[\sum_{j=1}^{2} Q_j \left[1 - \exp\left(-b_j p\right)\right]\right]\left[1 + \frac{\dot{p}}{\dot{p}_0}\right]^{C}. \end{aligned} \tag{6.8}$$

The value of $\dot{p}$ was taken from the slowest tensile test, meaning that $\dot{p}_0 = 3.25 \times 10^{-5}\,\text{s}^{-1}$. Again, the viscosity term is of the form proposed by Børvik et al. [210]. This plasticity model was included in the finite element model through a user subroutine for Abaqus Explicit.

In addition, brittle fracture needed to be included in the model. To that end, a model based on Kolmogorov and Hooputra formulations [212, 213] was chosen, in which the equivalent plastic strain at the onset of damage p_{D} depends on the stress triaxiality and the equivalent plastic strain rate. The value of p_{D} is then simply interpolated by the model, using the input data from the experiments, which is of the form

$$p_{\mathrm{D}}\left(\sigma^{*}, \dot{p}\right). \tag{6.9}$$

The stress dimensionless triaxiality ratio σ^{*} is defined as the ratio of the hydrostatic stress σ_{H} to the equivalent stress σ_{eq}. If the von Mises equivalent stress is adopted, the triaxiality ratio reads as follows:

$$\sigma^{*}=\frac{\sigma_{\mathrm{H}}}{\sigma_{\mathrm{eq}}}=\frac{\frac{1}{3}\left(\sigma_{1}+\sigma_{2}+\sigma_{3}\right)}{\frac{1}{\sqrt{2}}\sqrt{\left(\sigma_{1}-\sigma_{2}\right)^{2}+\left(\sigma_{2}-\sigma_{3}\right)^{2}+\left(\sigma_{3}-\sigma_{1}\right)^{2}}}. \tag{6.10}$$

In (6.10), σ_1, σ_2 and σ_3 are the principal stresses. For a pure uniaxial stress state $\sigma_2, \sigma_3 = 0$ and therefore $\sigma^{*}=\frac{1}{3}$.

The finite element code will activate the damage in an element if its accumulated plastic strain reaches p_{D}, so this condition can be expressed as

$$\int \frac{\mathrm{d}p}{p_{\mathrm{D}}\left(\sigma^{*}, \dot{p}\right)}=1. \tag{6.11}$$

The value of the integral, which is discretized for each increment in the finite element code, increases monotonically with each increment of the plastic strain. The reader is referred to [212–214] for details.

The fact that the stress triaxiality ratio has a severe influence on the fracture behavior of many – specially ductile – materials is widely accepted. With the aim of obtaining the fracture strains for different triaxiality ratios, some notched specimens were produced. It is interesting to point out that, since shell elements were used for the GFRP parts, the triaxiality ratio was not allowed to take values greater than $\frac{2}{3}$, this value matching the stress state in which $\sigma_1 = \sigma_2 \neq 0$ and $\sigma_3 = 0$. Therefore, only notched tensile specimens undergoing triaxiality ratios up to $\frac{2}{3}$ were required. In particular, tensile tests with triaxiality ratios of 0.333, 0.500 and 0.600 were conducted. The geometries of the notches were obtained using a detailed solid finite element model of the specimen with a mesh size of 0.5×0.5×0.5 mm assuming elastic isotropic conditions (see Appendix A for details). Figure 6.3 shows two detailed views of the notches.

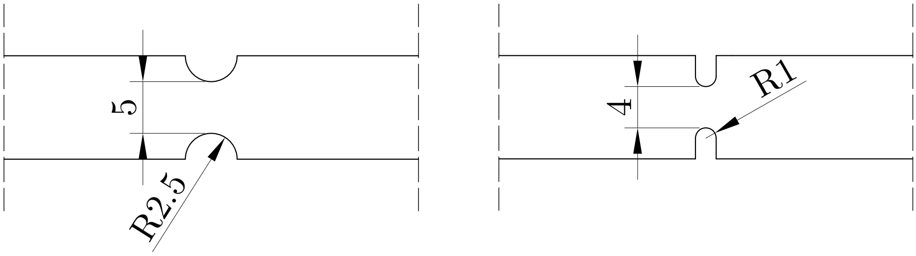

Figure 6.3: Details of the notches machined on the notched GFRP tensile specimens for σ^*=0.5 (left) and σ^*=0.6 (right), dimensions in millimeters.

These detailed FE models were also employed to determinate the load rate at which the tensile experiments on the notched specimens had to be run, so that the strain rate matched the highest value used with the smooth specimens ($8.12 \times 10^{-3}\,\mathrm{s}^{-1}$). This resulted in load rates of 20.3 mm/min for $\sigma^* = 0.5$ and 15.7 mm/min for $\sigma^* = 0.6$. Once the tensile tests were run, the FE model was used again to determinate the values of the ultimate total and plastic strains in the failure surface, since the failure was too sudden to use a digital image correlation technique without unacceptable noise levels. The process is explained in Appendix A. A word of caution has to be entered here since the point in the cross-section of the notch with maximum strain rate does not correspond with the point with the maximum triaxiality ratio, so these results must be treated carefully.

Tables 6.3 and 6.4 summarize the material properties and the model parameters of the glass-fiber reinforced polymer Ultramid A3WG10 BK00564. The values of p_{D} were obtained from Equation (6.6) for the uniaxial tensile test and from the finite element code for triaxiality ratios of 0.5 and 0.6. Stress-strain curves obtained from the uniaxial experimental tests and simulations for strain rates of 3.25×10^{-5} , 3.25×10^{-4} and $8.12 \times 10^{-3}\,\mathrm{s}^{-1}$, which correspond to test speeds of 0.2, 2 and 50 mm/min respectively for a triaxiality ratio of $\sigma^* = 0.333$, are compared in Figure 6.4.

6.1.4 PET-based polymeric foam

The polymeric foam ArmaFORM PET/W AC 135 was modeled through an elastic-plastic model with isotropic hardening originally developed for metallic foams by Deshpande and Fleck [215]. Given the collapsible nature of the material, the yield surface f had to include pressure dependency in addition to deviatoric stresses i.e. $f = f\left(I_\sigma, J_2\right)$, where I_σ and J_2 are the first and second

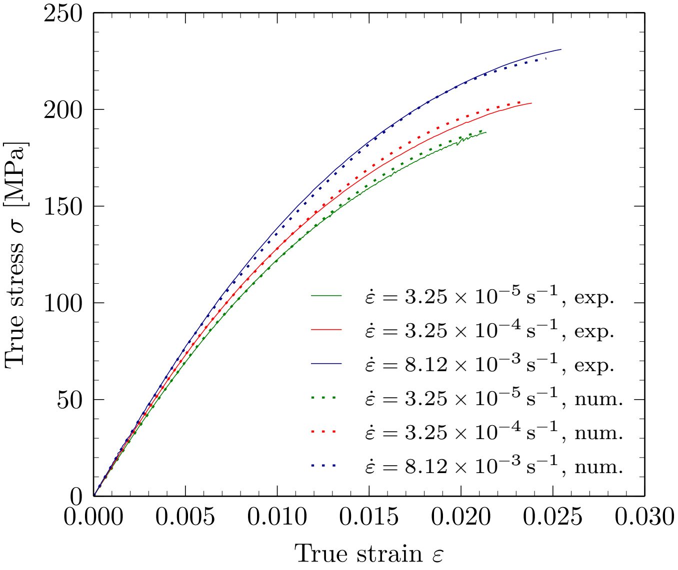

Figure 6.4: True stress-strain curves obtained from experimental uniaxial tests and numerical simulations at different strain rates for the material Ultramid A3WG10 BK00564 with $\sigma^* = 0.333$.

Property or parameter	Value
Density, ρ [t/m^3]	1.55 [150]
Mean Young's modulus, E [GPa]	15.4826
Poisson ratio, ν	0.4 [150]
σ_0 [MPa]	25.0
Q_1 [MPa]	124.87
b_1	315.90
Q_2 [MPa]	44.46
b_2	5748.46
C	0.0363

Table 6.3: Material properties and model parameters of Ultramid A3WG10 BK00564.

$\dot{\varepsilon}$ [s^{-1}]	σ^*	True ultimate strain ε_D	p_D
3.25×10^{-5}	0.333	2.1360×10^{-2}	0.8544×10^{-2}
3.25×10^{-4}	0.333	2.3836×10^{-2}	1.0682×10^{-2}
8.12×10^{-3}	0.333	2.5439×10^{-2}	1.1019×10^{-2}
8.12×10^{-3}	0.500	2.3280×10^{-2}	1.0092×10^{-2}
8.12×10^{-3}	0.600	2.0137×10^{-2}	0.8461×10^{-2}

Table 6.4: Ultimate plastic strains of Ultramid A3WG10 BK00564 for different stress triaxiality ratios and strain rates.

stress invariants, respectively[2]. In particular, the expression for f is an origin-centered ellipse in the σ_H-σ_eq plane which evolves proportionally in hardening (see Figure 6.5). This evolution is governed by the equivalent plastic strain p. The expression for this yield surface f reads

$$f = \sqrt{{\sigma_\mathrm{eq}}^2 + \alpha^2 {\sigma_\mathrm{H}}^2} - B = 0, \tag{6.12}$$

where $\sigma_\mathrm{eq} = \sqrt{3J_2}$ is the von Mises equivalent stress and $\sigma_\mathrm{H} = I_\sigma/3$ is the hydrostatic stress. The factor α defines the shape of the ellipse according to

$$\alpha = \frac{3\dfrac{\sigma_\mathrm{C}^0}{\sigma_\mathrm{H}^0}}{\sqrt{9 - \left(\dfrac{\sigma_\mathrm{C}^0}{\sigma_\mathrm{H}^0}\right)^2}}, \tag{6.13}$$

where σ_C^0 is the initial yield strength in uniaxial compression and σ_H^0 is the initial yield strength in hydrostatic compression. In Equation (6.12), B is defined as

$$B = \alpha \sigma_\mathrm{H}^\mathrm{y} = \sigma_\mathrm{C}^\mathrm{y} \sqrt{1 + \left(\frac{\alpha}{3}\right)^2}, \tag{6.14}$$

where $\sigma_\mathrm{H}^\mathrm{y}$ and $\sigma_\mathrm{C}^\mathrm{y}$ are the current yield stresses in hydrostatic and uniaxial compression, respectively. Therefore, B is the current size of the vertical axis of the yield ellipse.

Since no plastic properties can be found in the literature for this material, a flow potential g was adopted, reading

$$g = \sqrt{{\sigma_\mathrm{eq}}^2 + \beta^2 {\sigma_\mathrm{H}}^2} = 0, \tag{6.15}$$

---

[2] N. B. $I_\sigma = \sigma_{kk} = \mathrm{tr}\,(\boldsymbol{\sigma})$, $J_2 = \frac{1}{2}\left(\sigma_{ii}\sigma_{jj} - \sigma_{ij}\sigma_{ij}\right)$ and $J_3 = \epsilon_{ijk}\sigma_{i1}\sigma_{j2}\sigma_{k3} = \det\,(\boldsymbol{\sigma})$.

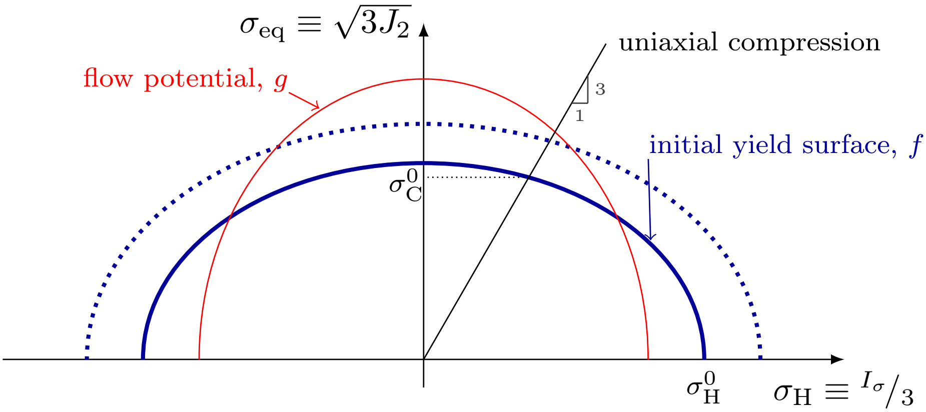

Figure 6.5: Representation of the yield surface and flow potential of the constitutive model for the polymeric foam in the σ_{H}-σ_{eq} plane.

so that the model was flexible enough to represent non-associated flow. This equation is in the same form as f, but with a different shape parameter (see Figure 6.5), meaning that if $\beta = \alpha$ then $\frac{\partial g}{\partial \boldsymbol{\sigma}} = \frac{\partial f}{\partial \boldsymbol{\sigma}}$, and the flow is associated. According to [214, 215], the factor β can be expressed in terms of the plastic Poisson's ratio ν^{p} as follows:

$$\beta = \frac{3}{\sqrt{2}} \sqrt{\frac{1 - 2\nu^{\text{p}}}{1 + \nu^{\text{p}}}}. \tag{6.16}$$

This allowed to obtain β from a simple uniaxial compression test in which the transverse plastic strains were measured. If this value is compared to α, it can be eventually stated if the plastic flow is associated or non-associated.

Given that this polymeric foam is manufactured through an extrusion process, some anisotropy in the material properties can be expected. Meeting the requirements of ISO 844:2014 [206], foam specimens were extracted and subjected to uniaxial compression along the directions parallel and orthogonal to the extrusion direction in the production line (see details in Appendix A). An assumption (particularized in Chapter 5) was made when it came to obtaining the plastic Poisson's ratio ν^{p}, customarily defined for isotropic materials as the ratio of the transverse plastic strains to the plastic strain in the load direction:

$$\nu^{\text{p}} = \frac{\varepsilon^{\text{p}}_{j,k}}{\varepsilon^{\text{p}}_{i}}, \text{ for } i \neq j \neq k. \tag{6.17}$$

Considering the anisotropy of the material ($\varepsilon^{\text{p}}_j \neq \varepsilon^{\text{p}}_k$), the mean value of both transverse directions was used to obtain the transverse plastic strain. According to this, the values of ν^{p} and β for both directions are provided in Table 6.5.

Regarding the parameter α, triaxial compression tests were carried out on foam samples with the extrusion direction orthogonal to the vertical loading axis. The description of these tests is included in Appendix A, leading to

$$k_{\mathrm{c}} = \frac{\sigma_{0.3}^{\mathrm{C}}}{\sigma_{0.3}^{\mathrm{H}}} = 0.708 \implies \alpha = 0.729. \tag{6.18}$$

This is clearly different from β, so the plastic flow of the material is non-associated.

The hardening curve has been included in the finite element model through a direct input of the yield stress–uniaxial plastic strain pairs obtained from the uniaxial compression tests, using Equation (6.6) with the singularity that the true stresses were computed taking into consideration the compressibility of the material, as described in Equation (A.1).

Strain-rate sensitivity is included in this model through a Cowper-Symonds overstress power law [216],

$$\dot{p} = D\,(R-1)^{n}\,, \tag{6.19}$$

where R is the ratio of the uniaxial yield compression strength at the current rate to the uniaxial yield compression strength at the initial rate. Again, the yield stresses corresponding to a true strain of 0.3 were used to obtain the value of R. D and n are material parameters calibrated according to [214] from experimental data at different strain rates (see Figure 6.6). This calibration led to $D = 1.0345\,\mathrm{s}^{-1}$ and $n = 0.01722$.

Table 6.5 contains a summary of the mechanical properties of the PET foam in weak and strong directions, and the experimental and numerical stress-strain curves for low-speed loading are plotted in Figure 6.6.

6.2 Finite element model

A detailed finite element model of the crash box has been constructed using the Abaqus Explicit package. This model was verified against the experimental results obtained in Chapter 5.

The metal tube was modeled using a fine mesh of 1.5 mm, 4-node linear shell elements with five integration points along their thickness and a reduced integration scheme [214], which allowed the tube to develop the correct folding pattern while keeping a good thickness/length ratio. The contact algorithm

Property or parameter	Orthogonal to extrusion	Parallel to extrusion
Density, ρ [t/m^3]	0.135	0.135
Young's modulus, E [MPa]	20.41	59.01
Elastic Poisson ratio, ν	0.1	0.1
$\sigma^{\mathrm{C}}_{0.3}$ [kPa]	982.98	2300.00
$\sigma^{\mathrm{H}}_{0.3}$ [kPa]	1383.30	*3236.67
α	0.729	*0.729
Plastic Poisson's ratio ν^{p}	0.089	0.067
β	1.8430	1.7217

Table 6.5: Material properties and model parameters of ArmaFORM PET/W AC 135 PET-based foam for different loading directions. An asterisk indicates that the value was obtained assuming the same α coefficient obtained for the weak direction of the foam.

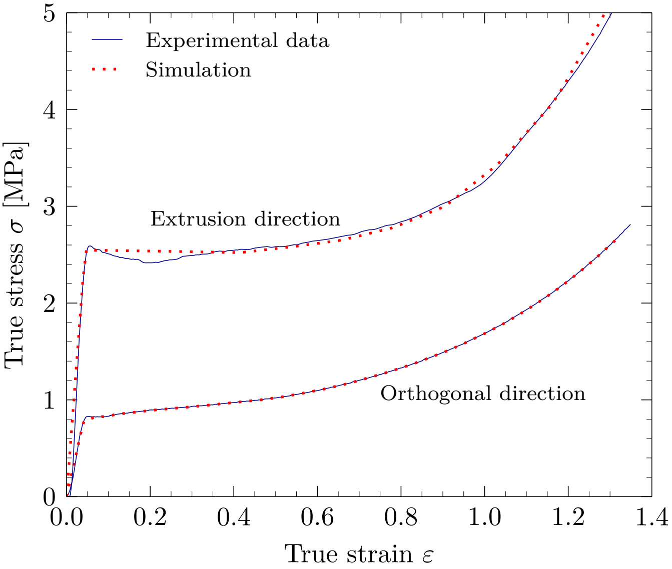

Figure 6.6: True stress-strain compressive curves from uniaxial tests and simulations for Armaform PET/W AC 135 PET-based foam in different directions.

accounted for the element thickness to avoid any undesired shifting of the force-displacement curves due to self-contact during folding. The end of the tube in contact with the loading plate is triggered according to the pattern applied to the experimental specimens (see Chapter 5), to ensure that the same collapse mode is initiated. These triggers were formed at a previous step by imposing a radial displacement of 1.5 mm directed inwards at the tube's edge. The elastic part of this displacement is recovered, resulting in a deformation of about 1.2 mm. Furthermore, the last 50 mm of the metal tube were clamped, as was done in the experimental tests in the pendulum accelerator.

GFRP sheets were modeled using the same 4-node linear shell elements with an element size of 3 mm. Given that we are using a fracture algorithm based on element deletion, the size of these elements must be small enough to accurately represent fracture in the GFRP parts. The GFRP structure is modeled respecting the mechanization process in which three independent sheets are assembled together without any adhesive, as was depicted in Figure 5.5b.

Finally, the foam prisms were modeled with 8-node, linear solid elements. The critical aspect governing the element size of these parts is the fact that the foam should be able to be captured inside the folds during crushing. This was also a challenge for the convergence of the analysis, since some elements captured into the folds experienced extreme distortions which decreased the stable time increment and compromised the overall convergence. To avoid or minimize this problem, a distortion control for the foam parts was included, which locked those elements undergoing deformations larger than 95 %. It was observed that only a few elements had to be locked in order to guarantee the convergence of the simulations.

Two additional parts were included in the model: a fixed reaction plate and a moving loading plate. These were modeled through rigid elements and a *rigid body* constraint. Even though in Chapter 5 the components were impacted by a mass of 1500 kg at 10 m/s, at this stage it was more convenient to load the specimens at a constant speed of 10 m/s, meaning that no decelerations were produced at the impactor. This was done to ensure that even those designs with a high energy absorption were crushed to the same distance (245 mm, equating a 70 % of the total length), and thus all designs could be objectively compared. Analyses were run in parallel with two cores dedicated to each simulation. Despite being considerably slower, loop parallelization was preferred to a faster domain-based strategy, due to the fact that the latter produces differences in the results depending on the number of domains (see Chapter 4).

A view of the finite element model is shown in Figure 6.7. Action and reaction plates are removed for a better view.

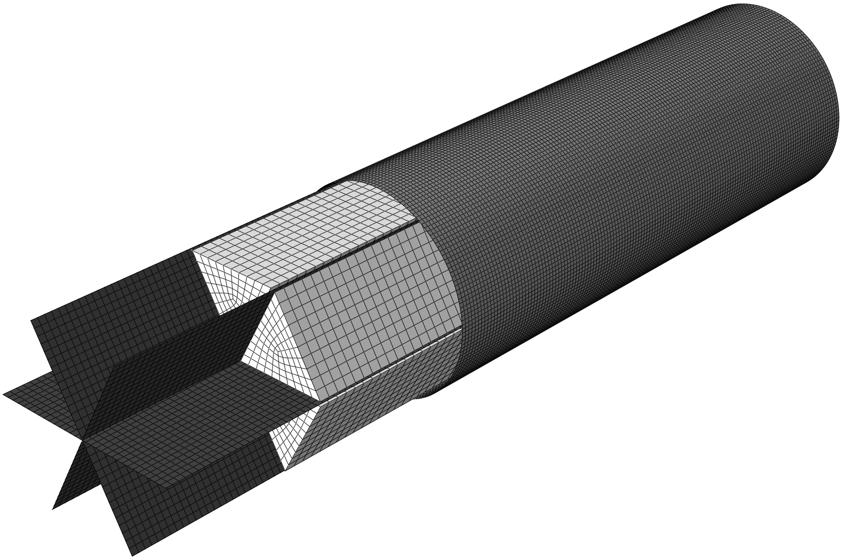

Figure 6.7: Finite element model of the crash box. The different parts have been partially disassembled for a better view.

This model was validated against the experimental impact tests performed in Chapter 5 at 10 m/s. Figure 6.8 shows that a good agreement was obtained, with the exception of the initial peak. The value of the initial peak force was much higher in the FE model due to the misalignments of the GFRP sheets in the experimental component (with bulges up to 2-3 mm out of plane). This effect was studied in Chapter 3.

In Figure 6.9, the crushing process of the finite element model is shown, and its final state is compared to a tested component. The differences in the crushing mode of the lower zone can be due to the presence of the safety buffers in the real tests and the consequent reduction in the crushing speed.

6.3 Description of the optimization problem

Five metrics were initially considered as candidates to become the objective functions for the optimization problem: the component's mass, the absorbed energy, the specific energy absorption, the initial peak load and the load ratio. All of them are quantities that should be either minimized (m, P_{peak}, LR or maximized (E_{a}, SEA) in a design optimization procedure. Given that these metrics are opposing (e.g. absorbed energy vs. mass), an unconstrained, multi-objective

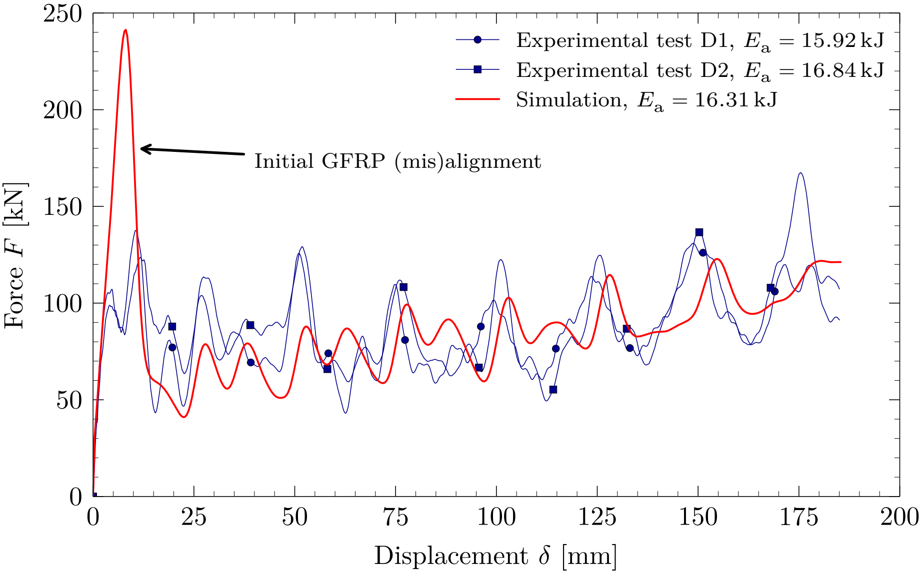

Figure 6.8: Force-displacement curves and absorbed energy of the experimental components D1 and D2 (see Chapter 5), and the finite element model at 10 m/s.

optimization was set out for pairs E_a–m and SEA–P_{peak} for different material configurations. The load ratio was discarded from the optimization given the relative inaccuracy of the surrogate model, which was unable to precisely reproduce the behavior of this function (see values of the likelihood estimators in Section 6.4). It is convenient to indicate here that the algorithm employed looked for the maximum force in the initial 15 % of the filtered force-displacement curves to account, for example, for possible secondary peak force produced by the GFRP plates.

Regarding the design variables, it was considered that the thicknesses of the tube and the GFRP sheets, together with the foam density (strongly related to its yield stresses), were the most interesting aspects of the current design. Even though the supplier provides six different possible densities for the PET foam [217], each one with a different yield stress, this variable was considered to be continuous. The relationship between the foam density and its yield stress in the extrusion direction could be established by a simple linear fit of the products in the brochure (see Figure 6.10). This gave the following expression:

$$\sigma_0^{\mathrm{y}}\,[\mathrm{MPa}] = 0.0021899\rho\,[\mathrm{kg/m^3}] - 0.7219274. \tag{6.20}$$

(a) Finite element model at $\delta =$ 100 mm.

(b) Finite element model at $\delta =$ 200 mm.

(c) Finite element model completely crushed.

(d) Real component.

Figure 6.9: Crushed finite element model and real component. The differences in the crushing mode of the lower zone can be due to the presence of the safety buffers in the real tests and the consequent reduction in the crushing speed.

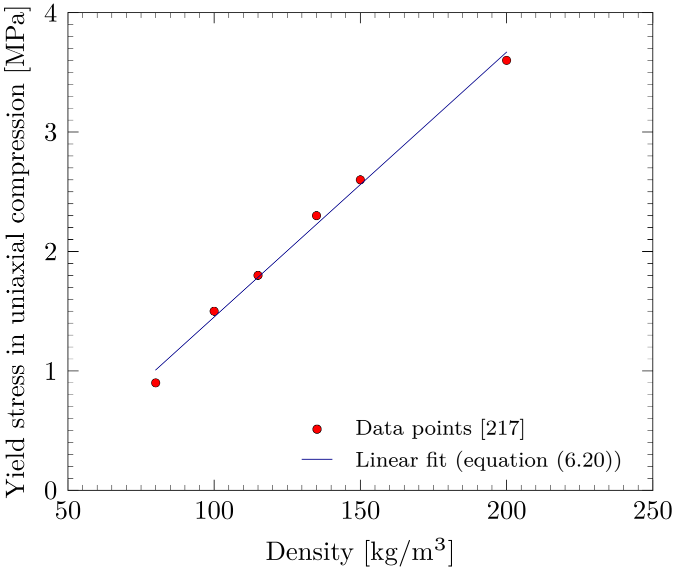

Figure 6.10: Linear fit to the density-yield stress pairs provided for Armaform PET/W AC PET-based foams, load direction parallel to extrusion direction. $R^2 = 0.99416$.

Three different optimization cases were studied:

- Case I consisted of the optimization of the same component described in Chapter 5.
- Case II consisted of the same optimization than case I, but with the foam loaded in its strong direction.
- Case III consisted of the optimization of an steel extrusion filled with PET foam loaded in its strong direction and GFRP, i.e., this case was identical to case II but with a steel cylinder instead of an aluminum cylinder.

The ranges of the design variables are presented in Table 6.6.

In order to build the metamodels of the objective functions, the design space was seeded with 400 sample points following a latin hypercube sampling distribution (LHS). At each sample point, the objective functions were computed and the resulting set was utilized to build a surrogate model for each response function. The computation time for each simulation was 20–30 minutes. Given the good results found in Chapter 4, a multivariate adaptive regression splines (MARS)

Design variable	Lower bound	Upper bound
Tube thickness [mm]	1.00	3.00 or 5.00
GFRP thickness [mm]	1.00	5.00
Foam density [kg/m^3]	80.00	200.00

Table 6.6: Ranges of the design variables for the optimization algorithm. The upper bound of the metal thickness was 3 mm for Case I, this value being later increased in the subsequent cases according to the obtained results.

model was fitted to the sampling results with acceptable likelihood estimators, provided in Section 6.4 for each optimization case. A maximum of 120 MARS bases and a cubic interpolation scheme were used.

The same genetic multi-objective optimization algorithm presented in Chapter 4 [199] was used, with a population size of 300 individuals, a mutation rate of 0.1, a crossover rate of 0.8, 50 elitist individuals and a maximum number of function evaluations equal to 500 000. With this configuration, the execution time of the optimization algorithm was about thirty minutes.

6.4 Results and discussion

6.4.1 Case I: aluminum extrusion, foam loaded in its weak direction

The likelihood of the surrogate model was checked by means of the goodness indicators provided in Table 6.7. A good agreement was achieved for all the proposed functions except the load ratio, in the same vein of what was obtained in Chapter 4.

Objective function	R^2	RMSE	MAE
Absorbed energy	0.9876	0.7374 kJ	0.493 kJ
Mass	0.9999	3.361×10^{-4} kg	1.576×10^{-4} kg
Specific energy absorption	0.9592	0.399 kJ/kg	0.279 kJ/kg
Initial peak load	0.989	2.841 kJ	2.1596 kJ
Load ratio	0.8066	0.537	0.278

Table 6.7: Goodness estimators of the MARS surrogate model fitted to the sample points in optimization case I. RMSE: root-mean-squared error, MAE: mean absolute error.

Pareto fronts considering E_a–m and SEA–P_peak are provided in Figure 6.11 and Figure 6.12, respectively. The values of the objective functions in the design proposed in Chapter 5 are marked with a green star for an easy comparison. It is important to warn the reader about the merely illustrative value of this mark, provided that its values were taken from the experimental quasi-static crushing of the component instead of taking them from the impact tests. This was done because of the limited crushing length in the latter, which did not reach the 245 mm due to the presence of the safety buffers. Furthermore, the numerical value of the peak load was considered here as the reference value, for a more consistent comparison with the remaining –numerical– results.

The obtained results showed some remarkable facts. First, the aluminum extrusion is playing the main role in this design. This can be drawn from Figure 6.11b, where it can be seen that increasing the aluminum thickness is the best way to achieve the optimum performance of the component. Only after this variable reached its upper bound did the remaining variables start to increase, first the foam density and then the GFRP thickness, when the foam density reached a value of 130 kg/m^3, approximately. The relative merits of the aluminum extrusion can also be observed in Figure 6.11a, which shows that the slope of the Pareto front increases rapidly as the aluminum thickness grows, and then increases at a lower rate when this thickness reaches its upper bound and the other materials come into play. A second remarkable fact is that the performance of the design studied in Chapter 5, marked with the green star, can easily be improved in either one way or another:

- Its mass can be reduced by approximately 23 % maintaining the same absorbed energy, by increasing the aluminum thickness up to almost 3 mm and reducing the GFRP thickness and the foam density to their lower bounds.
- Its absorbed energy can be improved by approximately 31 % if the aluminum thickness is increased to 3 mm, the foam density is not modified and the GFRP thickness is reduced to 1.5 mm, approximately.

Regarding the SEA–P_peak front, it can be observed that, in the studied range, the optimum specific energy absorption is always reached with the foam density and the GFRP thickness kept to a minimum, no matter how high SEA is required. Higher SEA values are optimally achieved by increasing the aluminum thickness. It can be also observed that the initial peak force can be significantly reduced in the original design without harming the SEA by minimizing the foam density and the GFRP thickness, and slightly reducing the aluminum thickness too. At this point, it is worth recalling that the initial peak load was measured in the

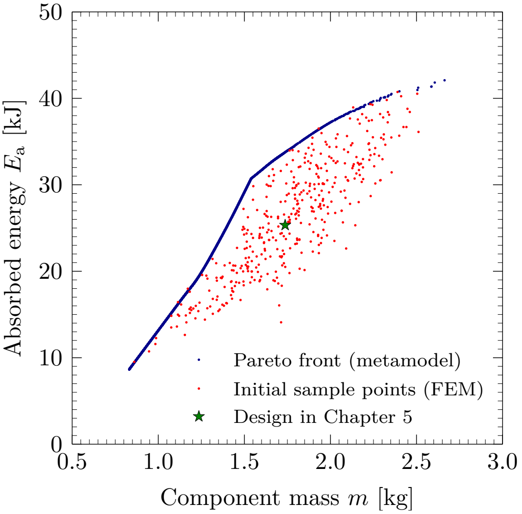

(a) Pareto front for optimization case I considering the absorbed energy and the component's mass as objective functions.

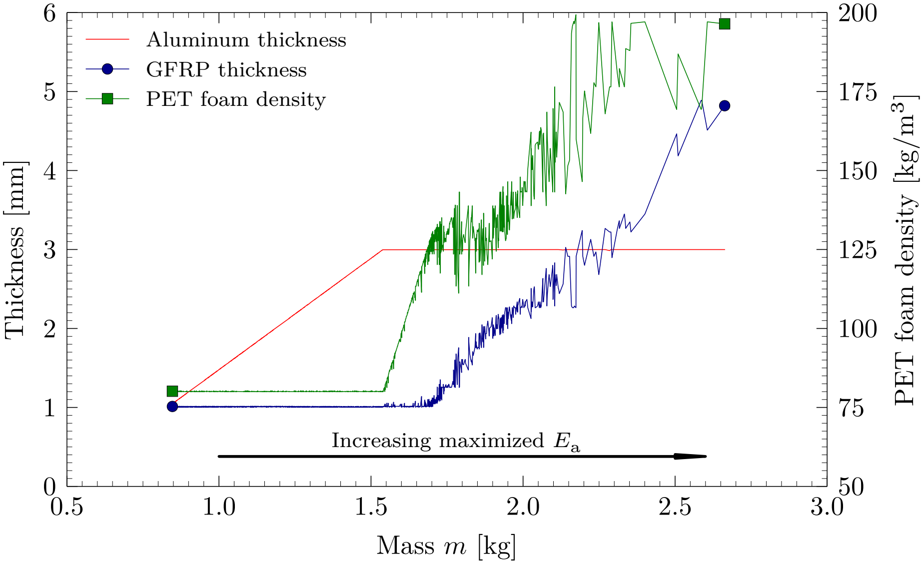

(b) Evolution of the three design variables along the Pareto front. Projection on the mass function.

Figure 6.11: Optimization results for case I considering the absorbed energy E_a and the component mass m as objective functions. Pareto set and evolution of the design variables.

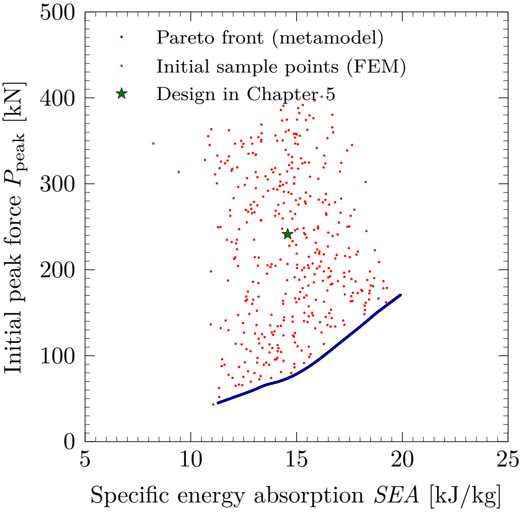

(a) Pareto front for optimization case I considering the initial peak load and the specific energy absorption as objective functions.

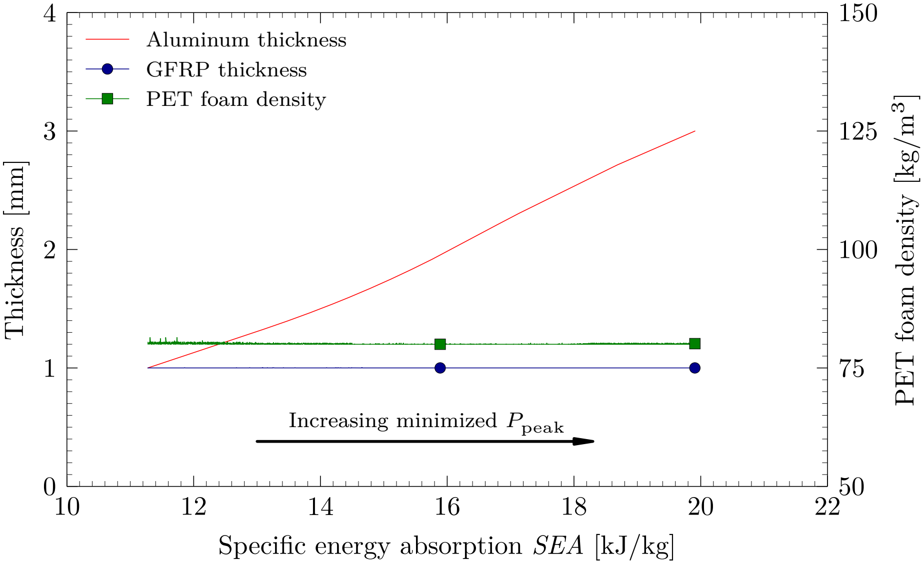

(b) Evolution of the three design variables along the Pareto front. Projection on the specific energy absorption function.

Figure 6.12: Optimization results for case I considering the specific energy absorption SEA and the peak load P_{peak} as objective functions. Pareto set and evolution of the design variables.

first 37 mm of crushing, so this does not necessarily mean that higher forces are not produced at longer crushing distances.

6.4.2 Case II: aluminum extrusion, foam loaded in its strong direction

In cases II and III, the upper bound of the metal thickness was increased to 5 mm given that this variable reached its upper bound in case I. The goodness estimators used to check the accuracy of the surrogate models are provided in Table 6.8. These indicators are in line with those obtained for the optimization case I.

Objective function	R^2	RMSE	MAE
Absorbed energy	0.9595	1.018 kJ	0.674 kJ
Mass	0.9999	4.012×10^{-4} kg	2.857×10^{-4} kg
Specific energy absorption	0.9841	0.475 kJ/kg	0.323 kJ/kg
Initial peak load	0.987	3.6814 kJ	2.7933 kJ
Load ratio	0.8691	0.195	0.116

Table 6.8: Goodness estimators of the MARS surrogate model fitted to the sample points in optimization case II. RMSE: root-mean-squared error, MAE: mean absolute error.

For case II, Pareto fronts are presented in Figures 6.13 and 6.14. Similar conclusions to case I can be drawn from the optimum results regarding the E_{a}–m front: the performance of the part can be improved in either one way or another by reducing the foam density and the GFRP thickness to their lower bounds. The point beyond which it is worth to increase the GFRP thickness appears later in Figure 6.13b than in Figure 6.11b, given that the foam is now more effectively used.

Some differences must be highlighted when it comes to the SEA–P_{peak} optimum sets, compared to what was presented in Figure 6.12. Here, optimum specific energy absorptions are achieved firstly by increasing the foam density (for $13\,\mathrm{kJ/kg} \leq SEA \leq 20\,\mathrm{kJ/kg}$, approximately), if a minimization of the peak load is pursued. For higher values of optimum specific energy absorption minimizing the peak load, the density of the foam should be kept at about $120\,\mathrm{kg/m^3}$, and the aluminum thickness should be progressively increased. Furthermore, the specific energy absorption of the original design can be increased by almost 100 %, keeping the same initial peak load, if the aluminum thickness is increased

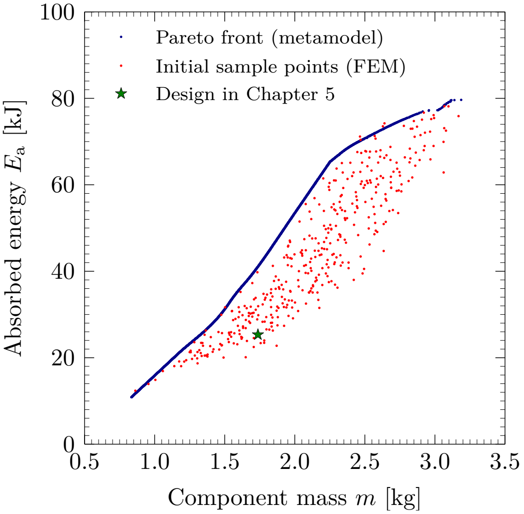

(a) Pareto front for optimization case II considering the absorbed energy and the component's mass as objective functions.

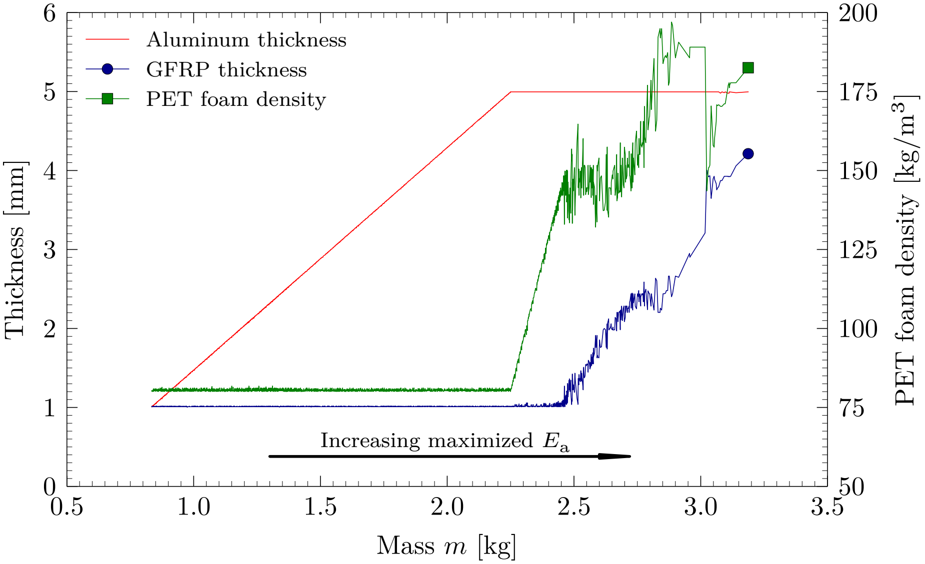

(b) Evolution of the three design variables along the Pareto front. Projection on the mass function.

Figure 6.13: Optimization results for case II considering the absorbed energy E_a and the component mass m as objective functions. Pareto set and evolution of the design variables.

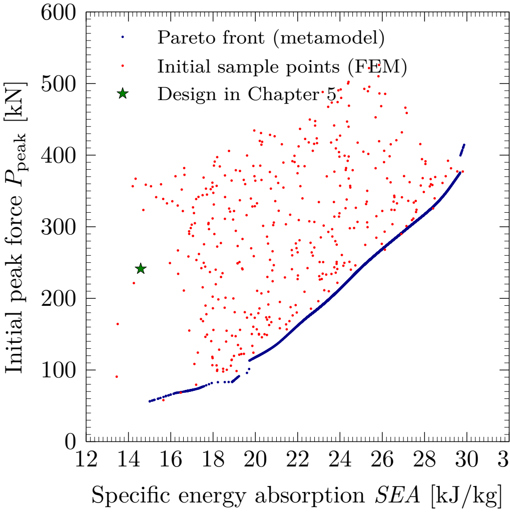

(a) Pareto front for optimization case II considering the specific energy absorption and the initial peak load as objective functions.

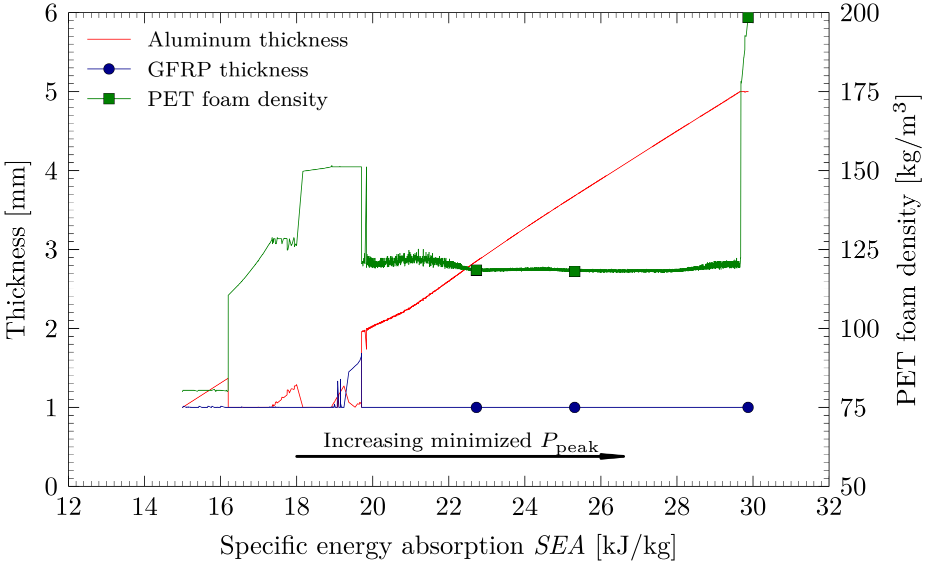

(b) Evolution of the three design variables along the Pareto front. Projection on the specific energy absorption function.

Figure 6.14: Optimization results for case II considering the specific energy absorption SEA and the load ratio LR as objective functions. Pareto set and evolution of the design variables.

to 3.8 mm, the foam density is set to 120 kg/m^3 and the GFRP thickness is reduced to 1 mm.

6.4.3 Case III: steel extrusion, foam loaded in its strong direction

In this last case, the aluminum tube was changed for a steel tube with higher yield stresses, but also higher density. The ranges of the design variables were the same than in case II, and the likelihood indicators are presented in Table 6.9.

Objective function	R^2	RMSE	MAE
Absorbed energy	0.9995	0.9073 kJ	0.667 kJ
Mass	0.9999	1.139×10^{-3} kg	8.789×10^{-4} kg
Specific energy absorption	0.9947	0.278 kJ/kg	0.2111 kJ/kg
Initial peak load	0.9998	3.4177 kJ	2.6312 kJ
Load ratio	0.9115	0.540	0.338

Table 6.9: Goodness estimators of the MARS surrogate model fitted to the sample points in optimization case III. RMSE: root-mean-squared error, MAE: mean absolute error.

For case III, Pareto fronts are provided in Figures 6.15 and 6.16. The results here are quite different from the previous cases: the contribution of the filling materials to the specific energy absorption is now remarkable.

In view of the optimum results obtained in the E_a–m front (Figure 6.15b), for components with a mass between 1.5 and 3.5 kg, the maximum efficiency in absorbed energy is achieved if the strongest foam (200 kg/m^3) is used in combination with 1 mm-thick GFRP plates, and progressively increasing the steel thickness. As shown in Figure 6.15b, for $3.5\,\mathrm{kg} \leq m \leq 6\,\mathrm{kg}$ approximately, the maximum energies for a given mass can be obtained in the same way than cases I and II: reducing the foam density and the GFRP plates to their lower bounds and increasing the steel thickness. Once the steel has reached its upper bound (5 mm), optimum energy absorptions are achieved by increasing the foam density to their upper bound at a first stage, and increasing the GFRP thickness at a later stage.

The GFRP thickness is also kept at its lower bound if the SEA–P_{peak} front is looked into (Figure 6.16). Optimum pairs are achieved mainly if the foam density is set to its upper bound and the steel thickness is then gradually increased, except in a region for $25\,\mathrm{kJ/kg} \leq SEA \leq 28\,\mathrm{kJ/kg}$ approximately, where optimum SEA–P_{peak} pairs are obtained if the foam density is set to its lower bound

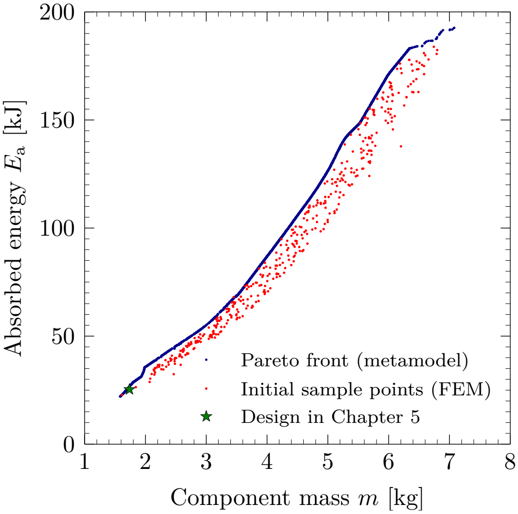

(a) Pareto front for optimization case III considering the absorbed energy and the component's mass as objective functions.

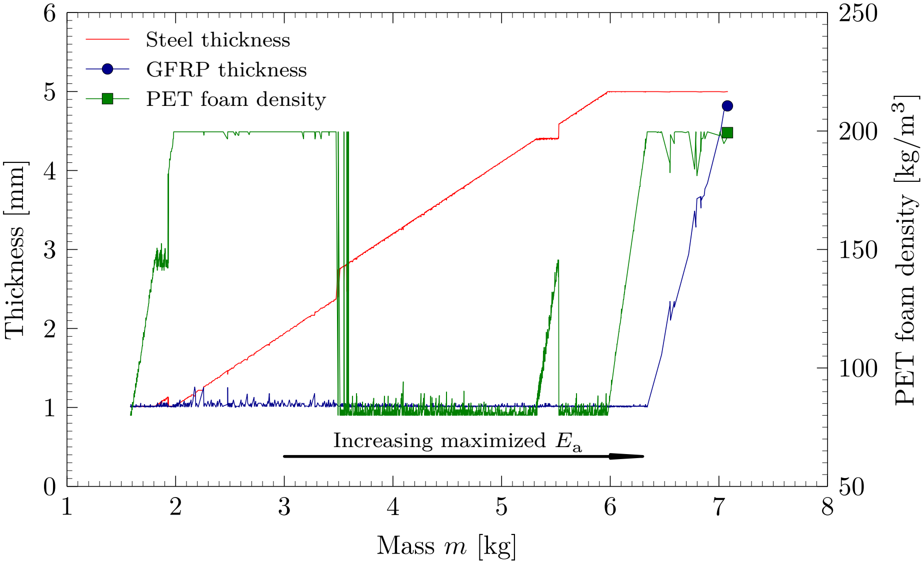

(b) Evolution of the three design variables along the Pareto front. Projection on the mass function.

Figure 6.15: Optimization results for case III considering the absorbed energy E_a and the component mass m as objective functions. Pareto set and evolution of the design variables.

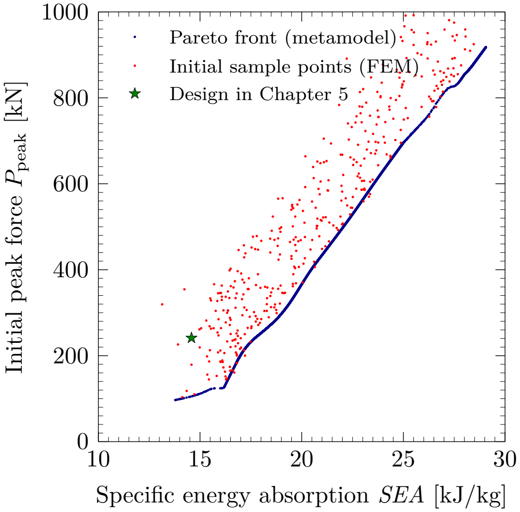

(a) Pareto front for optimization case III considering the specific energy absorption and the initial peak load as objective functions.

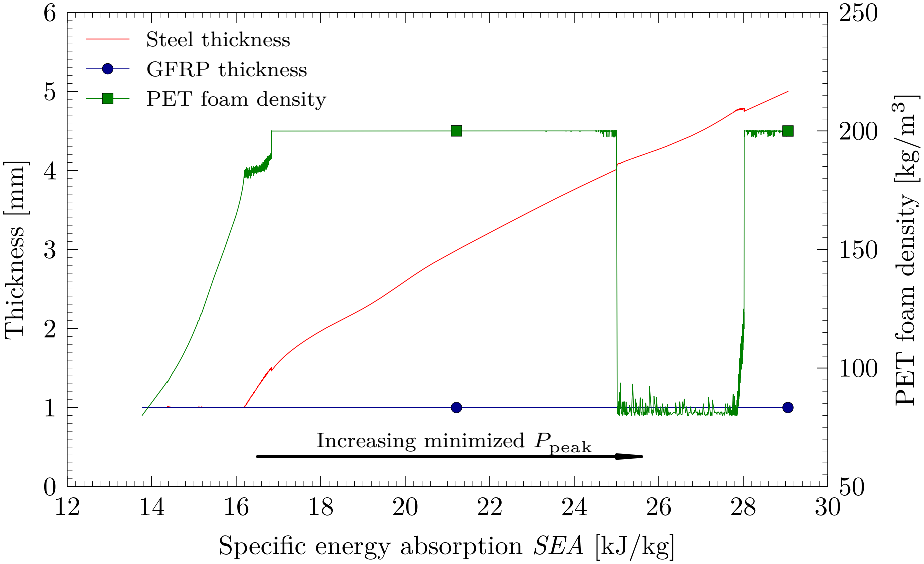

(b) Evolution of the three design variables along the Pareto front. Projection on the specific energy absorption function.

Figure 6.16: Optimization results for case III considering the specific energy absorption SEA and initial peak load P_{peak} as objective functions. Pareto set and evolution of the design variables.

(see Figure 6.16b). From Figure 6.16a, it transpires that the performance of the original design in aluminum can be significantly improved if the tube is changed for a steel cylinder with a smaller thickness, the foam density is increased to $200\,\mathrm{kg/m^3}$ and the GFRP thickness is set to 1 mm.

With the aim of shedding some light on what is happening in the regions of the front where the foam density suddenly drops (see Figures 6.15b and 6.16b), and given that examination of the crushing modes did not provide any conclusive results, an additional optimization was run on the model with the foam density fixed to a value of $200\,\mathrm{kg/m^3}$. This way, the remaining variables were forced to behave as if the foam density did not experience any drop along the front. This analysis resulted on two additional Pareto fronts provided in Figures 6.17, 6.18a and 6.18b, which are plotted together with the results obtained in Case III for a direct comparison.

Regarding the E_{a}–m front, it can be observed that the differences in the Pareto front (Figure 6.17a) arise from a variation in the steel thickness. In fact, it can be also seen that the sudden drop in the foam density in Figure 6.15b was balanced with an increase of the steel thickness of about 0.4 mm. If this drop was not allowed and the foam density was required to stay at $200\,\mathrm{kg/m^3}$, the optimized absorbed energy would be reduced by, approximately, 5-10 %.

A similar result is obtained in the SEA–P_{peak} front, but here the differences between the additional case and Case III are much smaller. Both Pareto fronts are very similar (Figure 6.18a), and if the foam density was required to stay constant at $200\,\mathrm{kg/m^3}$, almost no difference would be observed in the optimum pairs. This difference arises from a very small increase of the steel thickness, as shown in Figure 6.18b.

6.5 Conclusions

This chapter presented the numerical modeling of the crash box experimentally studied in Chapter 5 and its multi-objective optimization using a genetic algorithm. The following conclusions can be drawn:

- The axial crushing of the proposed component was successfully simulated with a numerical model calibrated with the material experimental data. Only a difference in the initial peak load was remarkable, which was caused by the misalignment of the GFRP plates in the experimental tests. The interaction effect appeared in the finite element model too, given that the response was very similar to the experimental behavior.

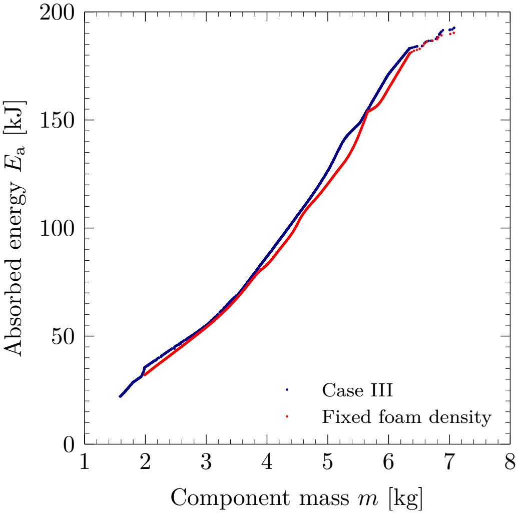

(a) Comparison of the Pareto fronts for optimization case III and for the additional test with fixed foam density considering the absorbed energy and the component's mass as objective functions.

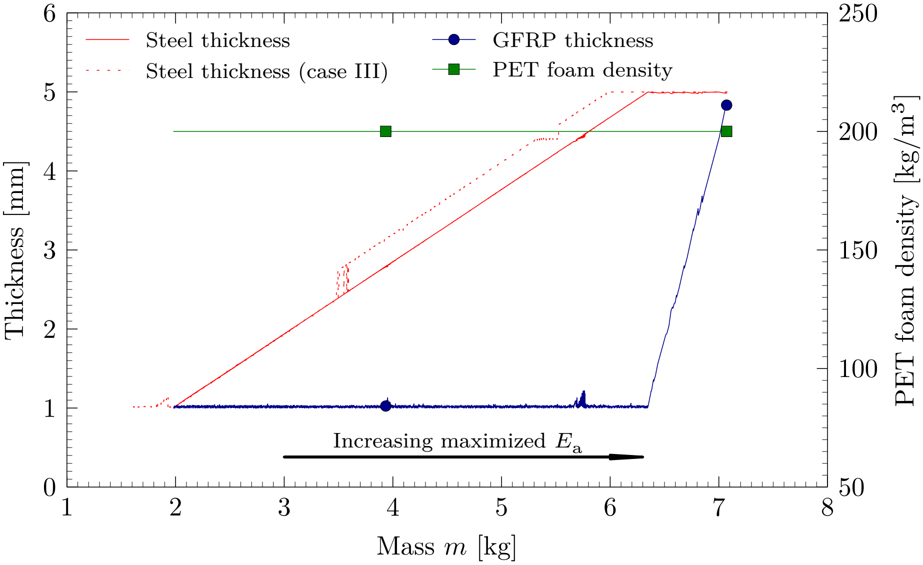

(b) Evolution of the three design variables along the Pareto fronts. Projection on the mass function.

Figure 6.17: Comparison of the optimization results for case III and an additional test with fixed foam density considering the absorbed energy E_a and the component mass m as objective functions. Pareto set and evolution of the design variables.

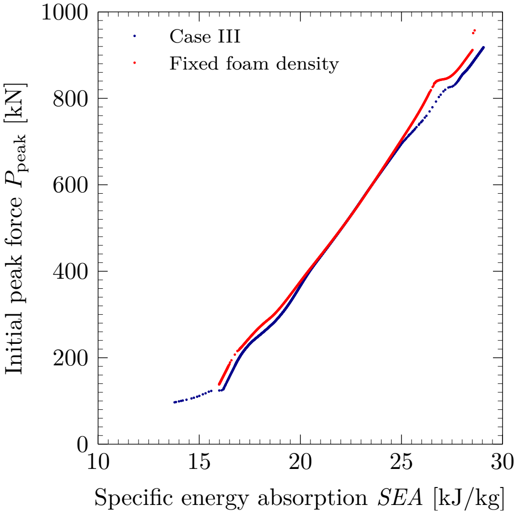

(a) Comparison of the Pareto fronts for optimization case III and for the additional test with fixed foam density considering the specific energy absorption and the initial peak load as objective functions.

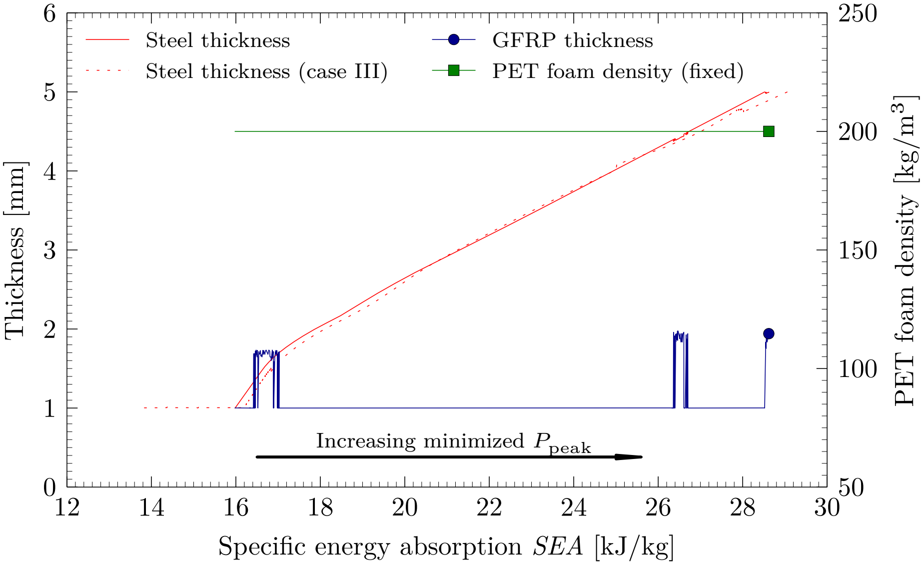

(b) Evolution of the three design variables along the Pareto fronts. Projection on the specific energy absorption function.

Figure 6.18: Comparison of the optimization results for case III and an additional test with fixed foam density considering the specific energy absorption SEA and initial peak load P_{peak} as objective functions. Pareto set and evolution of the design variables.

- Surrogate models constructed with multi-adaptive regression splines accurately represented the response functions, with the single exception of the load ratio, with a minor degree of accuracy. Therefore, these models could be used by the optimization algorithm.

- Three different multi-objective optimization cases were studied, where steel or aluminum tubes were considered. The design variables included shape variables (thickness of tube and plates) and the density of the foam, which is closely related to its crushing strength. In general, the aluminum components performed optimally if the filling materials are close to their lower bounds due to the good characteristics of the AA6063-T5 alloy. However, when it comes to the steel tube, the high-density PET foam had a very significant contribution in terms, for example, of specific energy absorption.

References

[150] BASF. *Ultramid (R) A3WG10 BK00564 Polyamide 66. Product information sheet.* 2012.

[199] J. E. Eddy and K. Lewis. “Effective Generation of Pareto Sets using Genetic Programming”. *Proceedings of ASME Design Engineering Technical Conference* (2001).

[203] H. Zhu, L. Zhu, and J. Chen. “Damage and fracture mechanism of 6063 aluminum alloy under three kinds of stress states”. *Rare Metals* 27.1 (2008), pp. 64–69.

[204] V. Vilamosa. “Behaviour and Modelling of AA6xxx Aluminum Alloys Under a Wide Range of Temperatures and Strain Rates”. PhD thesis. SIMLab (Structural Impact Laboratory), NTNU, 2015.

[206] ISO. *Rigid cellular plastics – Determination of compression properties.* ISO 844:2014. International Organization for Standardization, 2014.

[209] E. Voce. “The relationship between stress and strain for homogeneous deformations”. *Journal of the Institute of Metals* 74 (1948), pp. 537–562.

[210] T. Børvik, O. Hopperstad, T. Berstad, and M. Langseth. “A computational model of viscoplasticity and ductile damage for impact and penetration”. *European Journal of Mechanics - A/Solids* 20.5 (2001), pp. 685–712.

[211] N. Abedrabbo, R. Mayer, A. Thompson, C. Salisbury, M. Worswick, and I. van Riemsdijk. “Crash response of advanced high-strength steel tubes: Experiment and model”. *International Journal of Impact Engineering* 36.8 (2009), pp. 1044–1057.

[212] W. Kolmogorov. “Spannungen Deformationen Bruch”. *Metallurgija* (1970), p. 230.

[213] H. Hooputra, H. Gese, H. Dell, and H. Werner. “A comprehensive failure model for crashworthiness simulation of aluminium extrusions”. *International Journal of Crashworthiness* 9.5 (2004), pp. 449–464.

[214] *ABAQUS 6.13 Documentation.* Dassault Systèmes. Providence Road, Rhode Island. 2014.

[215] V. Deshpande and N. Fleck. “Isotropic constitutive models for metallic foams”. *Journal of the Mechanics and Physics of Solids* 48.6 (2000), pp. 1253–1283.

[216] G. Cowper and P. Symonds. *Strain-hardening and strain-rate effects in the impact loading of cantilever beams.* Division of Applied Mathematics, Brown University, Providence, Rhode Island, USA, 1957.

[217] Armacell. *Armaform PET/W AC, technical data.* 2014.

7

Summary, conclusions and recommendations

This last chapter puts an end to the presented investigation with a short summary, the main conclusions and several recommendations or suggestions for future works.

7.1 Summary

The presented work studied the crashworthiness of some innovative crash box designs based on combinations of metals, composites and cellular materials with the aim of improving the frontal crashworthiness of vehicles. This was achieved by a combination of experimental work, finite element modeling and different optimization algorithms, which provided a better understanding of the performance of the components from an engineering and scientific point of view.

Improvement of the crashworthiness of steel members was achieved with different inner reinforcements in chapter 3. The performance of crash boxes reinforced with a GFRP skeleton and PET-based foam was particularly good compared to the other alternatives. The GFRP-filled tube was optimized in chapter 4 considering its specific energy absorption and its load ratio as simultaneous objective functions in a multi-objective size optimization problem solved with different techniques. In Chapter 5, the PET foam and the GFRP structure were put together inside an aluminum extrusion to be tested experimentally under quasi-static and impact conditions. A very remarkable interaction between foam and GFRP increased the energy absorption of the components. This interaction was quantified with a modification of Hanssen's formulation for aluminum extrusions filled with aluminum foam. A material testing campaign was also carried out for a correct constitutive characterization of the three involved materials.

This led to a calibrated finite element model able to reproduce the behavior of the real components. This design, and a similar one with steel instead of aluminum, were optimized in Chapter 6 using a multi-objective genetic algorithm previously tested in Chapter 4. Results stated the relative merits of each material on the crashworthiness of the component when different objective functions are considered, showing that this bi-material inner reinforcement was particularly suitable for steel extrusions. The obtained Pareto fronts allow the selection of optimum designs for specific requirements of the considered crashworthiness metrics.

7.2 Conclusions

The next conclusions can be drawn from this thesis:

In the study of steel crash boxes reinforced with GFRP, CFRP, PET foam or agglomerated cork, it was shown that:

- Innovative designs in energy absorption were developed in collaboration with CTAG, using materials and geometrical configurations not investigated before. Components were tested under quasi-static and impact conditions, and finite element models were verified against the results.

- The insertion of a GFRP structure inside a steel tube increased its specific energy absorption more than the other materials, closely followed by a PET foam padding. This was proved in quasi-static and impact experimental tests and numerical simulations.

- The behavior of the different materials was represented by the finite element models with an acceptable accuracy. The inclusion of residual strains in the metal tube did not show a relevant influence on the force-displacement results. However, initial imperfections were necessary to reproduce the same collapse mode than the one developed in the experimental tests, besides of allowing a reduction of the initial peak load and match the experimental value.

- The agglomerated cork studied here showed a low increase in specific energy absorption compared to an empty steel tube. Furthermore, its recoverable elastic behavior suggested that this product should be used carefully in energy-absorbing structures, e.g. in areas where this fact is not relevant.

- Considering the results from Chapter 3, the separation between evenly-spaced spot welds should be less than 16.7 % of the component's length for an efficient energy absorption, guarantying that the steel part is progressively crushed. Otherwise, the lobe length increases and the stability of the axial crushing is not guaranteed.

- Foam-filled sections were less sensitive to spot weld spacing due to the constraining or interaction effect between the filler and the extrusion. For this to happen, the foam must be in contact with the steel walls during crushing.

The optimization of the GFRP-filled steel tube gave indications that:

- After the study of different surrogate models, it can be concluded that the functions of specific energy absorption and load ratio could be emulated fairly well with a set of multi-adaptive regression splines (MARS). This allowed the optimization algorithms to perform smoothly in an optimization problem with five variables. The maximum number of MARS bases was obtained from a likelihood analysis of the metamodels.
- Finite element results were sensitive to the parallelization strategy used in the sampling phase. The division of the model into different numbers of subdomains led to differences between 10 and 20 % in the energy absorption of the component. A compromise between results quality and computation time was found for a domain-based strategy in which the model was divided into four sub-domains.
- The specific energy absorption and load ratio of the original design presented in Chapter 3 was improved by near 50 % with the right set of design variables. The shift between the top edge of the steel tube and the reinforcement was essential for the reduction of the load ratios.
- A genetic multi-objective optimization algorithm was tested against a classical Fletcher-Reeves conjugate-gradient method. The genetic strategy was able to find optimum pairs of the objective functions in areas of the metamodel unexplored by the Fletcher-Reeves method.

From the experimental investigation on the crashworthiness of aluminum profiles filled with PET foam and GFRP plates, it was learned that:

- A previous crushing test was done on double-hat hexagonal profiles made of aluminum alloy AA5754-H111 with a thickness of 1 mm joined by double-line laser welding. This solution was not strong enough to withstand the inner pressure of the filler materials due to the weakness of the heat-affected zones. An extrusion of aluminum AA6063-T5 with increased thickness was able to deal with the internal pressures without relevant fracture.

- Extruded aluminum alloy AA6063-T5 exhibited enough ductility to allow a progressive axial crushing of the empty and filled components without relevant fracture. Only some damage was observed in the mode transition from concertina to three-lobe diamond in the empty specimen.
- The absorbed energy of the aluminum extrusions reinforced only with PET foam or only with GFRP was not significantly higher than the absorbed energy of the empty extrusion, given the excellent characteristics of the alloy; but a very remarkable enhancement was indeed produced when all the three materials were combined in a single design. This is explained by the fact that the foam confines the glass fiber plates, improving their performance.
- The energy absorption and the load ratio of the component filled with PET foam and GFRP were improved by almost 100 % compared to that of an empty extrusion. However, the specific energy absorption was slightly lower.
- A significant part of the gain in energy absorption arose from the strong interaction effect between the GFRP plates and the PET foam. Hanssen's formulation was adapted for a tube with two simultaneous fillers to account for this effect. This proved that the PET foam can act as a confinement for the GFRP plates, making the most of their degradation.

And finally, the multi-objective optimization of the component filled with PET foam and GFRP showed that:

- The performance of the component was correctly represented by a calibrated finite element model with adequate constitutive equations for each of the three materials, thanks to the material testing campaign presented in Chapter 5 and appendix A.
- The component's mass and its absorbed energy, specific energy absorption and initial peak load were approximated with a MARS model with a very good degree of accuracy. The load ratio was not considered due to the inaccuracies of all the tested metamodels. The increased number of sample points allowed that the accuracy of the metamodels increased in some regions, which led to smoother and more continuous Pareto fronts.

- Loop parallelization, which involves no sub-divisions of the finite element model, avoided the problem of inconsistency of results presented in Chapter 4, in exchange for a small increase in the computation times.
- The developed optimizations allow the choice of optimum designs adjusted to the real industrial needs, e.g. establishing limits of the peak force and obtaining immediately the system with optimum absorbed energy, specific energy absorption, or other crashworthiness metrics.
- The components built with aluminum performed optimally in terms of specific energy absorption when the thickness of the GFRP plates and the foam density were kept in their lower bounds. However, the optimum specific energy absorptions of the filled steel tube were found in designs where the density of the PET foam was increased to its maximum.

7.3 Recommendations for further works

The scale of the studied problem can be modified to adapt the components for other type of structures, like aircraft or trains. This way, the validity of the results presented in this thesis could be checked for scale consistency. Besides, other types of loading (lateral, oblique,...) could be considered. A change of the load angle can be specially challenging for the metal tube filled with GFRP plates, given its sensitivity to initial geometrical imperfections.

Regarding the crashworthiness of the multi-material parts, it could be interesting to test a design like the one studied in Chapters 5 and 6 but changing the GFRP for metal walls. This is justified by the fact that the GFRP was the material whose contribution was only required after the other two materials reached their upper bounds in the optimization of the part's absorbed energy and specific energy absorption. Furthermore, the use of cork instead foam as a confinement could be tested, emphasizing if the spring-back effect is actually a disadvantage when it comes to occupant protection, and studying it under cyclic loading. For a correct characterization of the cork, samples should be tested also in triaxial compression for different confinement pressures, to match the loading conditions inside the crash box.

High-performance structural adhesives (alone or together with spot welds) could be regarded as a suitable bonding for internally-reinforced cold-formed tubes. Many works exist in the literature about the application of adhesives to energy absorbers made of metal, but no significant contributions can be found on its use in structures withstanding elevated internal pressures during axial crushing. This could solve the issue with the heat-affected zones near the laser weldings experienced in Chapter 5.

About the finite element models, the material testing campaign was quite complete for the represented phenomena. However, high-speed tensile tests on GFRP samples could throw some light on the material's behavior at elevated strain rates. This would require the use of a Split-Hopkinson tensile bar with incident and transmitter bars made of a material with a stress wave speed similar to that of the GFRP, which is quite challenging. The foam model could be also improved taking into account its anisotropy. For this, additional triaxial tests would be required in different directions and for different foam densities.

Further effort could also be done on the optimization part: the load ratio function was not represented by the metamodels as fairly as the other objective functions. It could be useful to find a more suitable approximation for this metric, given its importance.

Regarding the interaction effect, the gaps between the foam triangles and the circular metal walls in Chapters 5 and 6 avoided any relevant interaction between the materials. It could be interesting to test a design in which the foam filler is somehow adjusted to the inner walls of the extrusion, so that the foam–metal interaction effect contributes also to increase the energy absorption of the design.

Related also to the interaction effects, the selection of the C_{avg} parameter as an objective function would indicate the best way improve its contribution, as well as a deeper understanding of its source. For this, the correct friction coefficient between both materials should be obtained, and the GFRP plates should be modeled with solid elements accounting for erosion, so that the penetration of the GFRP fragments into the foam confinement (simulated also with solid, erodible elements) could be properly reproduced.

Appendices

A

Material tests

This appendix describes the laboratory tests carried out to characterize the materials used in some of the components studied in this thesis. Tests descriptions, measurements and results are provided here so that they do not clog the chapters where they are referenced. Some of the tests were carried out with the collaboration of persons whose help is properly acknowledged in the pertinent sections.

A.1 Tensile tests on plane specimens of aluminum alloy AA5754-H111

These tests were conducted with the aim of characterizing the alloy initially selected for the double-hat hexagonal profiles used in Chapter 5. Even though this alloy was not eventually employed, the tests results are provided here for future reference.

According to EN 573-3:2013, AA5754 aluminum alloy has the chemical composition provided in Table A.1. The temper H111 implies some work hardening imparted by shaping processes (cut-to-length line and straightening rollers), but less than required for an H11 temper.

The specimen geometry is depicted in Figure A.1. Specimens were extracted from the same sheets the components were made from, for a more rigorous characterization. The longitudinal direction of the specimens is aligned with the axial direction of the components.

A total of four specimens were tested using a DARTEC M 1000 RK universal test machine with a maximum load of 20 kN at a rate of 1 mm/min. Strain measurements were made with a 10 mm MTS extensometer. Stress-strain curves, depicted in Figure A.2, show a clear Portevin-Le Chatelier (PLC) effect during

Element	Concentration (% by weight)
Mg	2.60-3.60
Mn + Cr	0.10-0.60
Si	0.00-0.40
Fe	0.00-0.40
Cr	0.00-0.30
Zn	0.00-0.20
Ti	0.00-0.15
Others (total)	0.00-0.15
Cu	0.00-0.10
Other (each)	0.00-0.05
Al	Remainder

Table A.1: Chemical composition of AA5754 alloy according to EN 573 specifications.

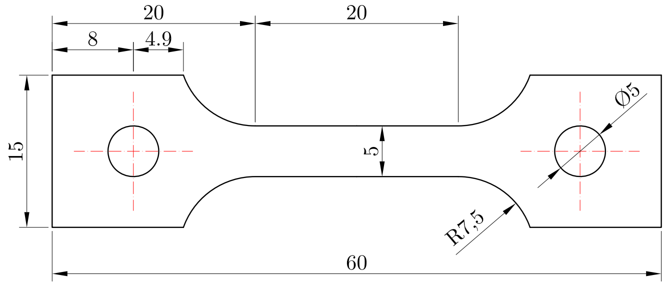

Figure A.1: Dimensions in mm of the AA5754-H111 plane tensile specimens. Nominal thickness is 1 mm.

hardening, which is common in 5xxx aluminum alloys.

In order to quantify the anisotropy of the alloy, specimens were measured at three sections before and after tests. These sections were located at both ends of the specimen's stem (sections A and C) and at its middle point (section B). Plastic strains were obtained in the two directions orthogonal to loading, i.e. width ($\varepsilon_{\mathrm{w}}^{\mathrm{p}}$) and thickness ($\varepsilon_{\mathrm{t}}^{\mathrm{p}}$), and the factor $R = \varepsilon_{\mathrm{w}}^{\mathrm{p}}/\varepsilon_{\mathrm{t}}^{\mathrm{p}}$ was obtained. These measurements and the values of R are provided in Table A.2.

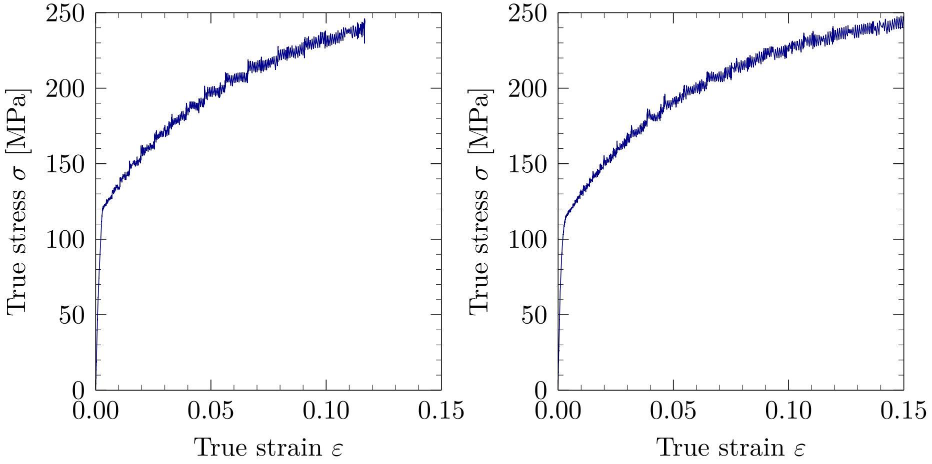

(a) Specimen 1.

(b) Specimen 2.

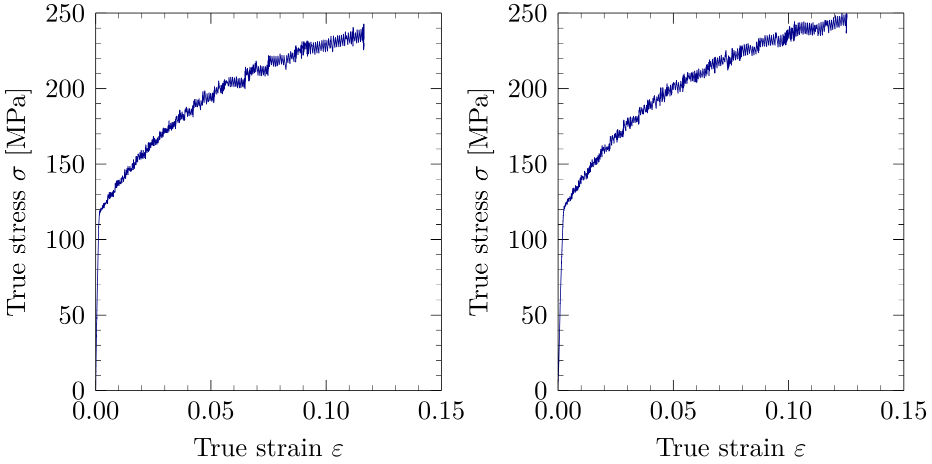

(c) Specimen 3.

(d) Specimen 4.

Figure A.2: Stress-strain curves of plane tensile specimens of aluminum alloy AA5754-H111.

Specimen	Section	t [mm]	w [mm]	t' [mm]	w' [mm]	$\varepsilon_{\mathrm{t}}^{\mathrm{p}}$ [$\times 10^{-2}$]	$\varepsilon_{\mathrm{w}}^{\mathrm{p}}$ [$\times 10^{-2}$]	$R = \varepsilon_{\mathrm{w}}^{\mathrm{p}}/\varepsilon_{\mathrm{t}}^{\mathrm{p}}$
1	A	0.950	5.034	0.882	4.782	−5.006	−7.158	0.699
	B	0.944	5.036	0.884	4.809	−4.508	−6.356	0.709
	C	0.942	5.027	0.888	4.835	−3.819	−5.732	0.666
2	A	1.019	5.023	0.945	4.756	−5.316	−7.262	0.732
	B	1.15	5.025	1.055	4.701	−6.448	−8.261	0.781
	C	1.015	5.048	0.957	4.835	−4.219	−5.714	0.738
3	A	0.978	5.021	0.900	4.697	−6.453	−7.975	0.809
	B	0.952	5.011	0.891	4.779	−4.630	−6.408	0.723
	C	0.955	5.008	0.913	4.756	−5.032	−4.398	1.144
4	A	0.950	5.025	0.891	4.777	−4.935	−6.211	0.795
	B	0.951	5.038	0.882	4.781	−5.101	−7.256	0.703
	C	0.952	5.035	0.890	4.768	−5.303	−6.513	0.814
Mean	A, B, C	0.980	5.028	0.915	4.773	−5.064	−6.604	0.776

Table A.2: Original and deformed thickness and width of the AA5754-H111 plane tensile specimens at three different sections. Anisotropy was quantified by means of the factor R. Measures were taken with an electronic caliper. Nomenclature: t is the initial thickness, w is the original width, t' is the deformed thickness, w' is the deformed width, $\varepsilon_{\mathrm{t}}^{\mathrm{p}}$ is the plastic strain in thickness direction, $\varepsilon_{\mathrm{w}}^{\mathrm{p}}$ is the plastic strain in width direction and R is the anisotropy factor.

A.2 Tensile tests on specimens of AA6063-T5 aluminum alloy

The chemical composition of alloy AA6063 is provided in Table A.3, as specified by the Aluminum Association. The temper T5 implies that the material has been cooled from an elevated-temperature shaping process and naturally aged.

Element	Concentration (% by weight)
Mg	0.45-0.90
Si	0.20-0.60
Fe	0.00-0.35
Others (total)	0.00-0.15
Cr	0.00-0.10
Zn	0.00-0.10
Ti	0.00-0.10
Mn	0.00-0.10
Cu	0.00-0.10
Other (each)	0.00-0.05
Al	Remainder

Table A.3: Chemical composition of AA6063 alloy according to specifications by the Aluminum Association.

A.2.1 Tensile tests on specimens extracted from extruded circular tubes of AA6063-T5 aluminum alloy

Quasi-plane tensile specimens similar to the previously described ones were extracted from the circular tubes so that their longitudinal direction was parallel to the axial direction of the tubes used in Chapters 5 and 6. This implies a certain curvature of the specimens, whose dimensions are provided in Figure A.3.

Tensile tests were run under identical conditions to the experiments on AA5754 alloy, and in the same machine too. As for AA6063-T5 alloy, specimens were airbrushed to acquire sequential images for the application of a digital image correlation (DIC) technique. This data was not eventually used since no relevant fracture was observed on the component tests and, thus, the failure strain of the material was not required for simulations. Figure A.4 shows the test equipment and the specimens employed to test this alloy.

Stress-strain curves are provided in Figure A.5. Compared to AA5754 alloy, this material exhibited a higher initial yield strength and a reduced hardening.

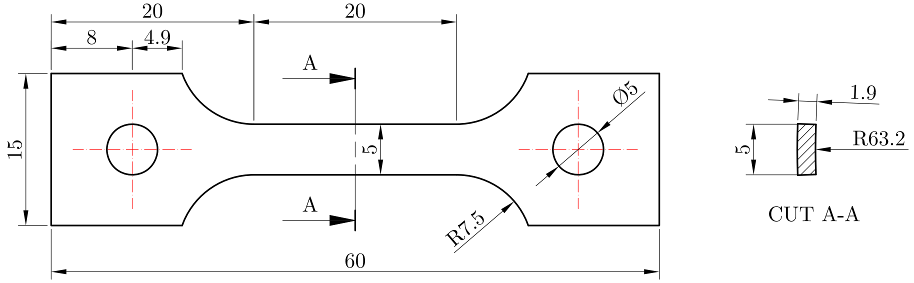

Figure A.3: Dimensions in mm of the AA6063-T5 tensile specimens extracted from the tubes in their longitudinal direction. Nominal thickness is 1.9 mm.

This could be beneficial for its use in crash boxes, provided that materials with reduced hardening develop collapse lobes with a shorter length and thus, more lobes can be formed. Needless to say, this is beneficial as long as the material is ductile enough.

Lateral plastic strains and anisotropy factors R were obtained in the same way than for the AA5754-H111 specimens. Results are provided in Table A.4, where sections affected by necking are marked with an asterisk and excluded from the calculation of the mean values. The latter indicated that this alloy exhibits a slightly higher anisotropy than AA5754-H111.

Specimen	Section	t [mm]	w [mm]	t' [mm]	w' [mm]	$\varepsilon_\mathrm{t}^\mathrm{p}$ [$\times 10^{-2}$]	$\varepsilon_\mathrm{w}^\mathrm{p}$ [$\times 10^{-2}$]	$R = \varepsilon_\mathrm{w}^\mathrm{p}/\varepsilon_\mathrm{t}^\mathrm{p}$
1	A*	1.886	5.022	1.735	4.599	−8.006	−8.423	1.052
	B	1.885	5.023	1.786	4.875	−5.252	−2.946	0.561
	C	1.889	5.030	1.810	4.874	−4.182	−3.101	0.742
2	A	1.891	5.011	1.811	4.839	−4.231	−3.432	0.811
	B	1.893	5.015	1.802	4.885	−4.801	−2.592	0.539
	C	1.899	5.010	1.801	4.797	−4.659	−4.251	0.913
3	A	1.894	5.016	1.812	4.870	−4.329	−2.911	0.672
	B*	1.897	5.024	1.783	4.795	−6.001	−4.558	0.758
	C	1.894	5.016	1.818	4.877	−4.013	−2.771	0.690
Mean	A, B, C	1.891	5.019	1.806	4.863	−4.496	−3.144	0.691

Table A.4: Original and deformed thickness and width of the AA6063-T5 extracted tensile specimens at three different sections. Anisotropy was quantified by means of the factor R. Measures were taken with an electronic caliper. An asterisk indicates that the section was affected by necking, so its results were excluded for the calculation of the mean values. Nomenclature: t is the initial thickness, w is the original width, t' is the deformed thickness, w' is the deformed width, $\varepsilon_\mathrm{t}^\mathrm{p}$ is the plastic strain in thickness direction, $\varepsilon_\mathrm{w}^\mathrm{p}$ is the plastic strain in width direction and R is the anisotropy factor.

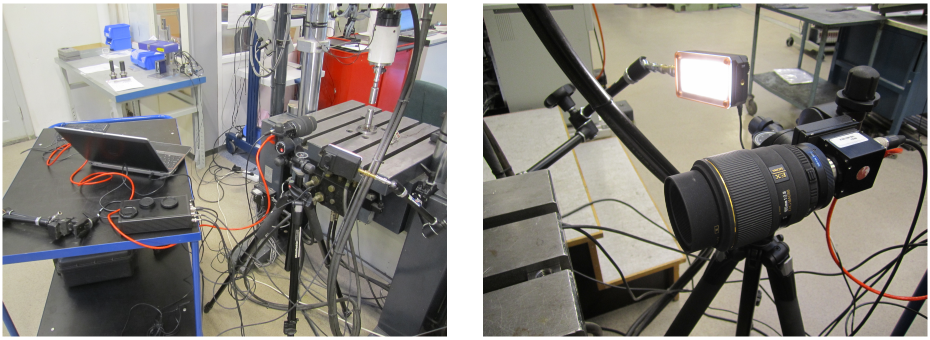

(a) Test set-up: DIC equipment and test rig.

(b) Digital camera for DIC images acquisition.

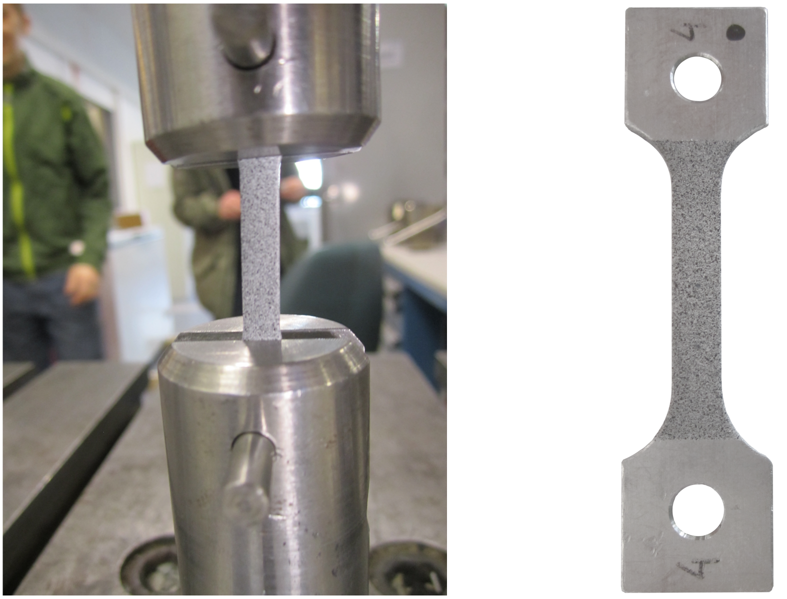

(c) Tensile specimen mounted on the test machine. It will be auto-aligned by the applied load.

(d) Tensile specimen number 4 with a black-white DIC pattern airbrushed on the stem (convex side).

Figure A.4: Pictures of the test equipment and specimens for the tensile tests of AA6063-T5 extracted samples.

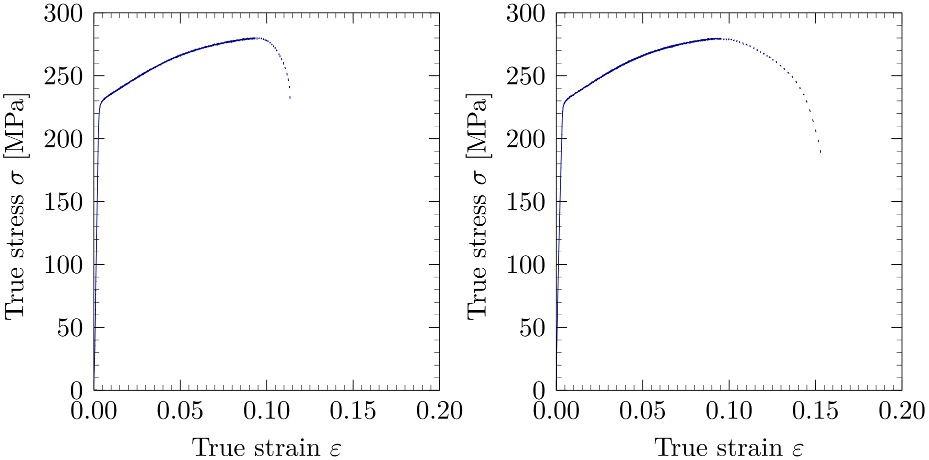

(a) Specimen 1. **(b)** Specimen 2.

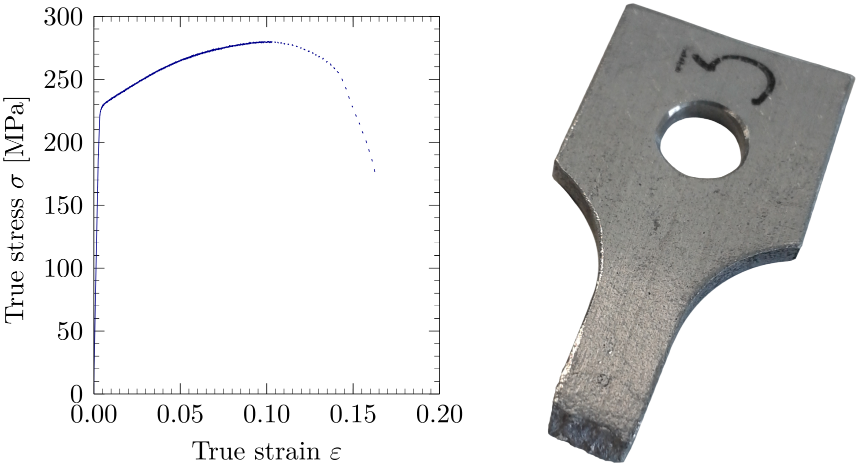

(c) Specimen 3. **(d)** Fracture mode.

Figure A.5: Stress-strain curves of plane tensile specimens of aluminum alloy AA6063-T5. Post-necking data is dotted (extensometer values).

A.2.2 Tensile tests on regular cylindrical specimens extracted from an extruded block of AA6063-T5 aluminum alloy

In order to check how far the extrusion process of the circular tubes studied in Chapters 5 and 6 affects the mechanical properties of the material, tensile tests have also been carried out on three regular cylindrical specimens of AA6063-T5, using the same mahine and instrumentation than AA5754-H11 tests. The geometry of these specimens is provided in Figure A.6.

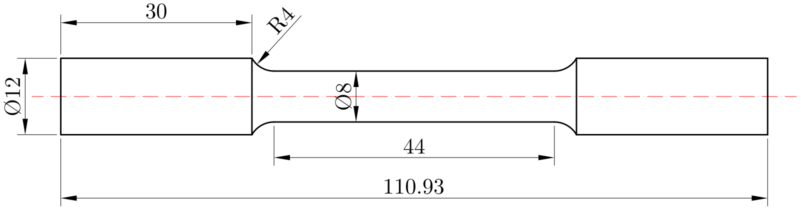

Figure A.6: Geometry of AA6063-T5 regular, cylindrical tensile specimens. Dimensions in millimeters.

Stress-strain curves provided in Figure A.7 show major differences compared to those presented in Figure A.5 for the extruded circular sections. These differences consist of a higher initial yield stress and reduced hardening exhibited by the extracted quasi-plane specimens compared to the regular cylindrical specimens. The fracture mode of the cylindrical specimens is also shown in Figure A.7d.

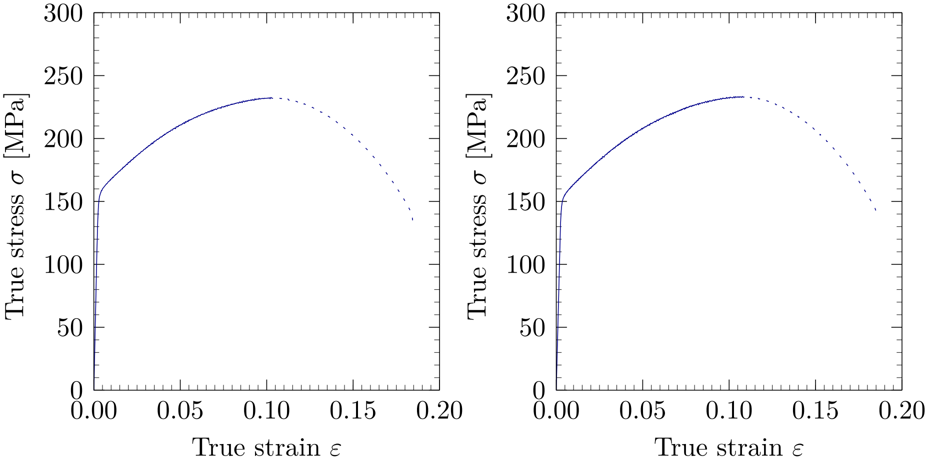

(a) Specimen 1.

(b) Specimen 2.

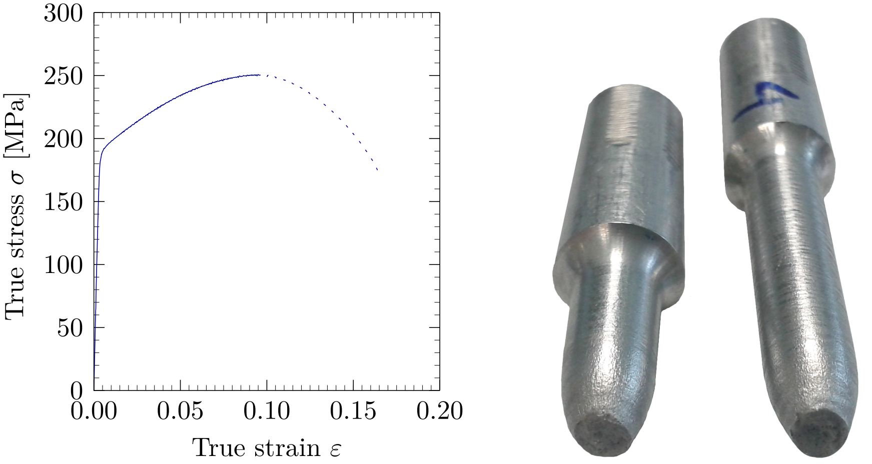

(c) Specimen 3.

(d) Fracture mode.

Figure A.7: Stress-strain curves of cylindrical tensile specimens of aluminum alloy AA6063-T5. Post-necking data is dotted (extensometer values).

A.3 Tensile tests on smooth and notched plane GFRP specimens

A.3.1 Smooth specimens

Plane *dog bone* tensile specimens of Ultramid A3WG10 BK00564 (see Figure A.8) were produced and tested at loading rates of 0.2, 2 and 50 mm/min using an INSTRON 8513 machine and extensometers with an initial length of 50 mm. Tests were conducted at room temperature (25 °C) and at 45 °C, see summary in Table A.5. Stress-strain curves are provided in Figure A.9. The help provided by PhD candidate M. Paredes is acknowledged.

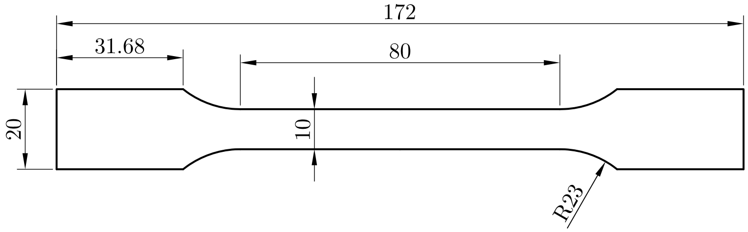

Figure A.8: Dimensions in mm of the smooth GFRP plane tensile specimens.

Specimen	Loading rate	Temperature
TS-1	0.2 mm/min	25 °C
TS-2	2 mm/min	25 °C
TS-3	50 mm/min	25 °C
TS-4	0.2 mm/min	45 °C
TS-5	2 mm/min	45 °C
TS-6	50 mm/min	45 °C

Table A.5: Characteristics of the GFRP smooth tensile specimens.

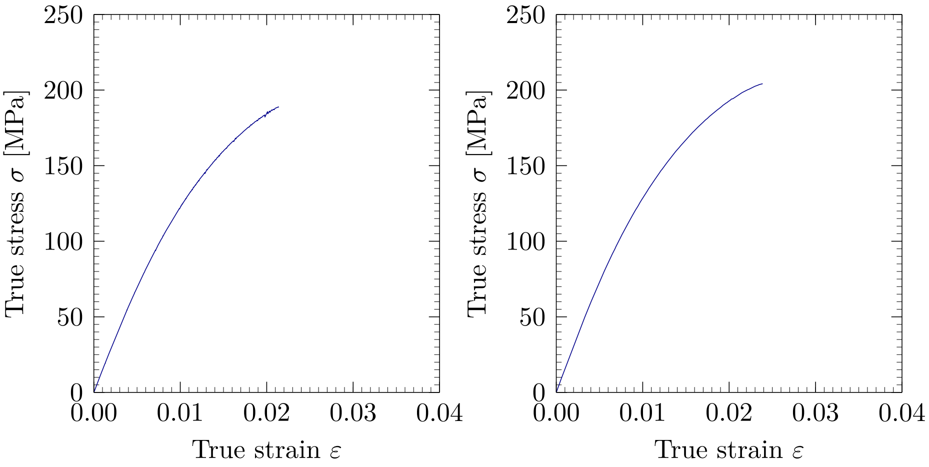

(a) Specimen TS-1.

(b) Specimen TS-2.

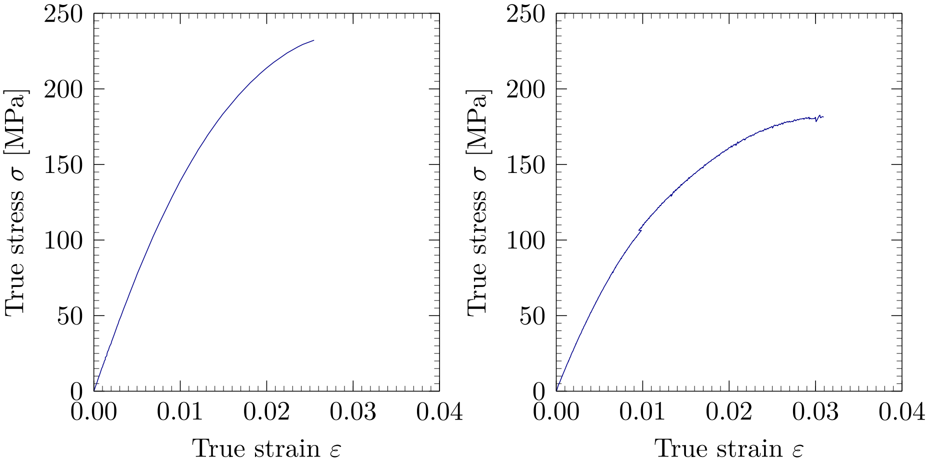

(c) Specimen TS-3.

(d) Specimen TS-4.

Figure A.9: Stress-strain curves of Ultramid A3WG10 BK00564, smooth plane specimens (continues on next page).

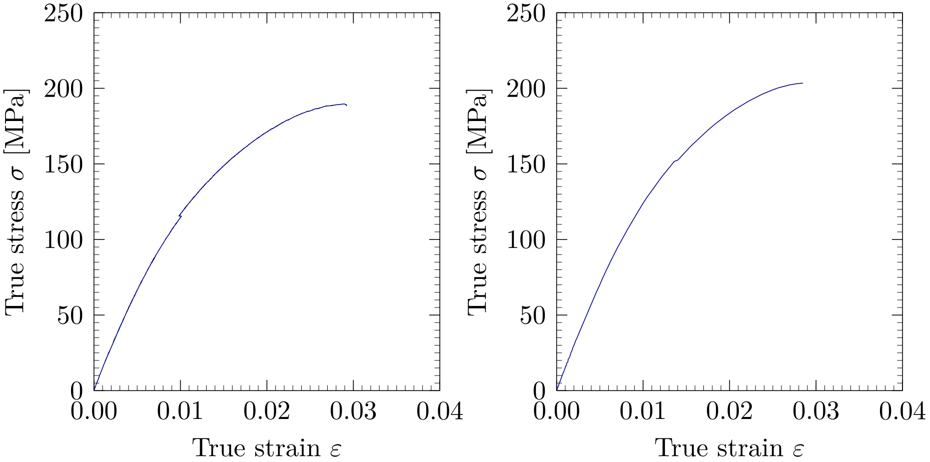

(e) Specimen TS-5. **(f)** Specimen TS-6.

Figure A.9: (cont.) Stress-strain curves of Ultramid A3WG10 BK00564, smooth plane specimens.

A.3.2 Notched specimens

Notches were carved in some smooth tensile specimens identical to the depicted in Figure A.8. These notches consisted on a circular geometry which deviates and concentrates the stresses at the failure point in a way such that the triaxiality ratio takes the desired values of 0.5 and 0.6. The geometries were derived from a finite element analysis which included the material model presented in Chapter 6 without failure, in which special care was taken to conserve at the failure region the same strain rate than the applied in the smooth specimens for the highest loading rate (50 mm/min), resulting on loading rates of 20.30mm/min for $\sigma^* = 0.5$ and 15.67mm/min for $\sigma^* = 0.6$. The geometry of the notches is depicted in Figure A.10. Notched specimens were labeled as shown in Table A.6, and a picture of the specimens is provided in Figure A.10c.

As shown in Figure A.10c, the specimens were airbrushed for DIC, but due to the low strains the noise in the DIC strain field would be too relevant. Stress-strain curves are provided in Figure A.11. The strain values plotted here were measured with an extensometer centered on the notch with a length of 10 mm. These strain measures were used to obtain the strains at the notch section using the detailed finite element model.

The constitutive model requires the equivalent plastic strains at fracture as input data, so these values have been obtained by averaging the values of the

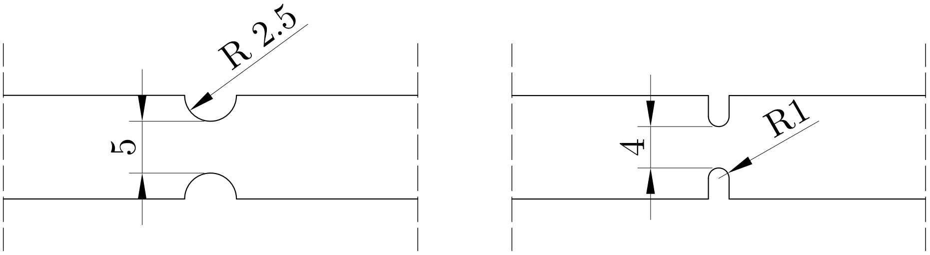

(a) Notch for $\sigma^* = 0.5$. **(b)** Notch for $\sigma^* = 0.6$.

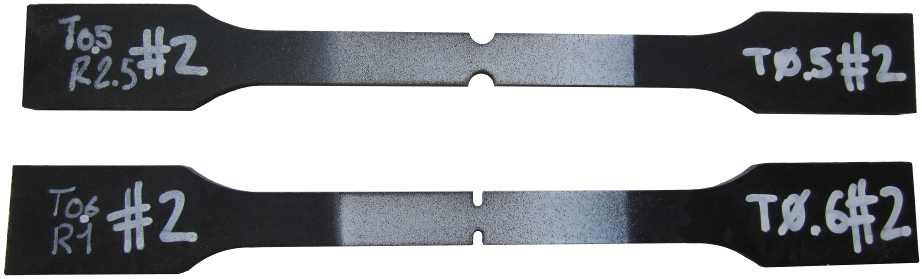

(c) Notched tensile specimens airbrushed for DIC.

Figure A.10: Details of the notches carved in the modified GFRP tensile specimens for σ^*=0.5 and σ^*=0.6, dimensions in millimeters.

Specimen	Loading rate	Triaxiality ratio σ^*
T5-1	20.30 mm/min	0.5
T5-2	20.30 mm/min	0.5
T5-3	20.30 mm/min	0.5
T6-1	15.67 mm/min	0.6
T6-2	15.67 mm/min	0.6
T6-3	15.67 mm/min	0.6

Table A.6: Characteristics of the GFRP notched tensile specimens.

plastic strains in the elements at the failure point. The strain outputs from the finite element code are provided in Figure A.12, and a summary of the total strains and equivalent plastic failure strains is provided in Table A.7.

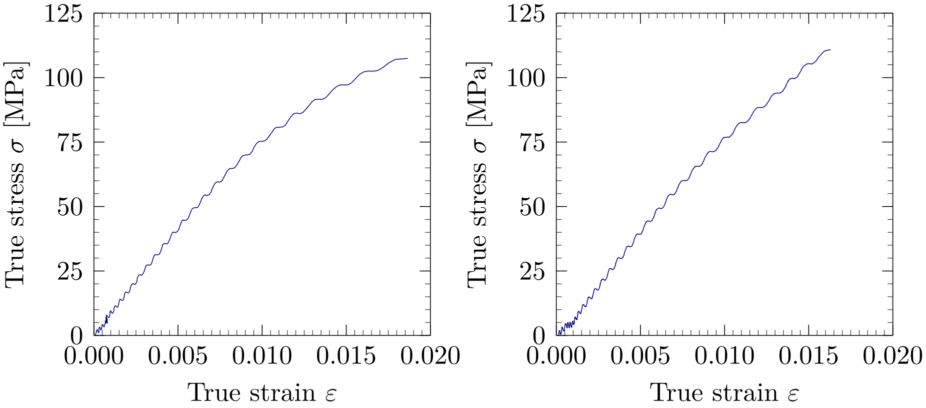

(a) Specimen T5-1. **(b)** Specimen T5-2.

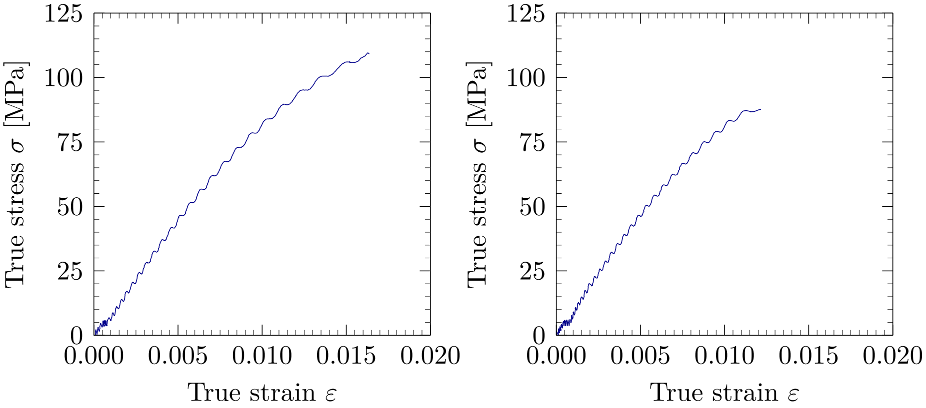

(c) Specimen T5-3. **(d)** Specimen T6-1.

Figure A.11: Stress-strain curves of Ultramid A3WG10 BK00564, notched specimens (see specimens' labels in Table A.6). Vibrations were produced by the test equipment, different than the one used for Figure A.9. Continues on next page.

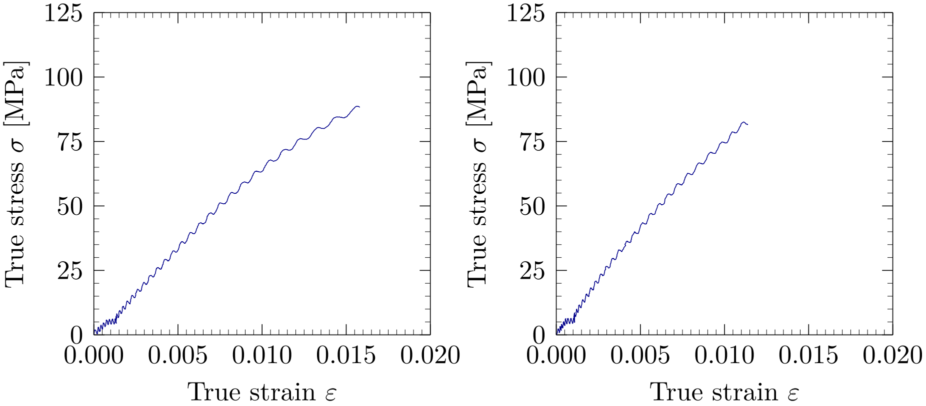

(e) Specimen T6-2. **(f)** Specimen T6-3.

Figure A.11: (cont.) Stress-strain curves of Ultramid A3WG10 BK00564, notched specimens (see specimens' labels in Table A.6). Vibrations were produced by the test equipment, different than the one used for Figure A.9.

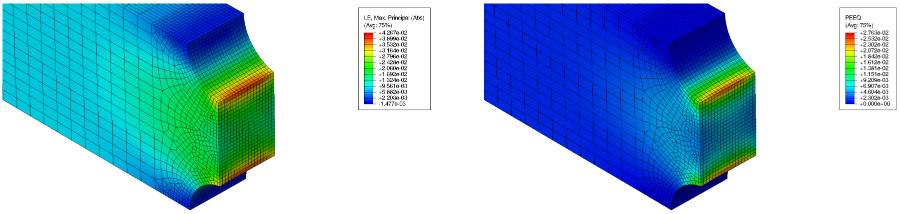

(a) $\sigma^* = 0.5$, total logarithmic strains at fracture.

(b) $\sigma^* = 0.5$, equivalent plastic strains at fracture.

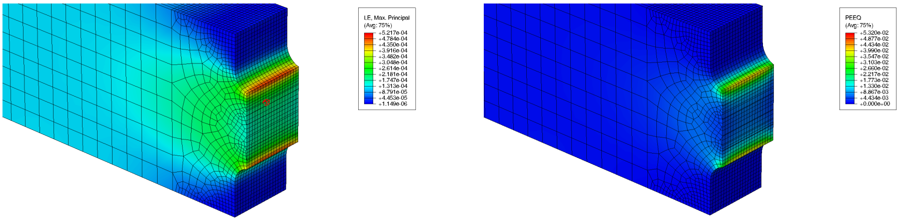

(c) $\sigma^* = 0.6$, total logarithmic strains at fracture.

(d) $\sigma^* = 0.6$, equivalent plastic strains at fracture.

Figure A.12: Cut view of the finite element model of the notched GFRP tensile specimens at the failure point. The values plotted here have been averaged to obtain the failure strain values presented in Table A.7.

$\dot{\varepsilon}$ [s^{-1}]	σ^*	Ultimate true strain ε_D	p_D
3.25×10^{-5}	0.333	2.1360×10^{-2}	0.8544×10^{-2}
3.25×10^{-4}	0.333	2.3836×10^{-2}	1.0682×10^{-2}
8.12×10^{-3}	0.333	2.5439×10^{-2}	1.1019×10^{-2}
8.12×10^{-3}	0.500	2.3280×10^{-2}	1.0092×10^{-2}
8.12×10^{-3}	0.600	2.0137×10^{-2}	0.8461×10^{-2}

Table A.7: Ultimate strains of Ultramid A3WG10 BK00564 for different stress triaxiality ratios and strain rates.

A.4 Compressive tests on cork agglomerate Corecork NL25

Compression tests were performed on cylindrical samples of Corecork NL25 with a diameter of 50.5 mm and a thickness of 12 mm, matching the thickness of the cork layers for components Cc in Chapter 3. Tests were performed using an HBM-C2 5-tonnes load cell with a gain of 2mV/V for the vertical pressure. Two Vishay HS50 LVDTs were attached to the vertical loading device to measure the axial displacement at the top of the specimens, which were put between two sheets of polytetrafluoroethylene (“Teflon”) to minimize friction. A view of the set-up is provided in Figure A.13.

With the aim of analyzing the differences between solid agglomerate and stacked layers of agglomerate, two different specimens were prepared: one consisting of a single cylindrical sample of cork and another one consisting of four cylindrical samples stacked up. Therefore, five cylindrical samples were required, namely C1 (single specimen) and C2, C3, C4, C5 (stacked up). A view of the two specimens is provided in Figure A.14.

Tests were performed at a constant displacement rate of 1.48 mm/min. Engineering and true stress and strains were obtained, considering for the latter a Poisson’s elastic ratio of 0. The exact dimensions of the samples are presented in Table A.8 and the stress-displacement curves are provided in Figure A.15. It is very important to remark that the deformed values of the specimens’ diameters and thicknesses were measured three days after the tests, so that the material was able to partially recover its original shape.

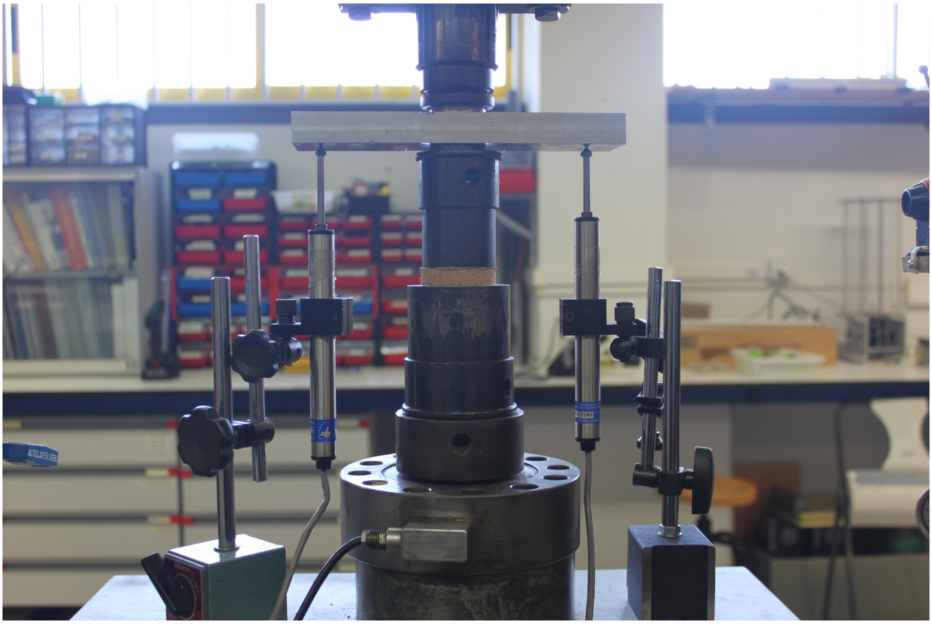

Figure A.13: Test set-up for compression tests on cork samples.

Figure A.14: Single and stacked cork specimens for compression tests.

Sample	D	t	m [g]	D'	t'
C1	50.57 mm	11.87 mm	6.05 g	52.39 mm	9.63 mm
C2	50.36 mm	11.92 mm	5.98 g	52.96 mm	9.58 mm
C3	50.63 mm	11.85 mm	6.19 g	53.82 mm	9.29 mm
C4	50.58 mm	11.85 mm	6.34 g	54.05 mm	9.28 mm
C5	50.63 mm	11.84 mm	6.10 g	53.64 mm	9.57 mm

Table A.8: Dimensions of the cork samples before and three days after testing, allowing strain recovery. D: original diameter, t: original thickness, m: mass, D' deformed post-recovery diameter, t': deformed post-recovery thickness.

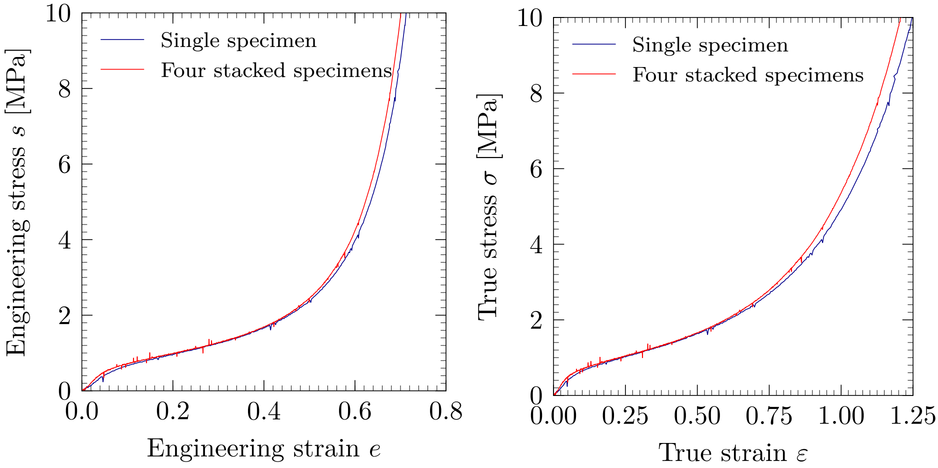

(a) Engineering values. **(b)** True values.

Figure A.15: Experimental compressive stress-strain curves of Corecork NL25.

A.5 Compressive tests on ArmaFORM PET/W AC 135 samples

A.6 Quasi-static compression tests

PET foam is manufactured through an extrusion and welding process, sketched in Figure A.16, which confers an orthotropic behavior to the material. Due to logistic limitations, the material in the crash boxes studied in Chapters 5 and 6 was placed so that the weaker direction of the foam matched the axial direction of the component. This obviously led to a reduction of the absorber's efficiency. However, the material was tested in both (strong and weak) directions so that both behaviors could easily be included in the finite element model in any direction. This allowed us to study the performance of components where the foam was aligned in its strong direction.

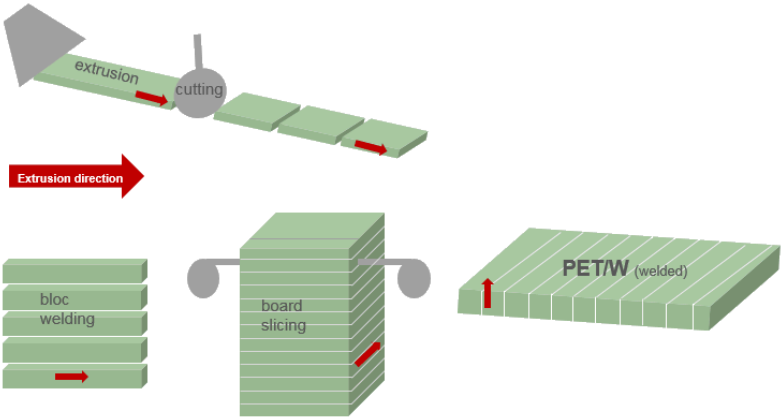

Figure A.16: Production process of ArmaFORM PET/W foams. Kindly provided by Mr. H. Chapelle (ArmaFORM).

Quasi-static compression tests were carried out according to ISO 844:2014 standard. Specimens tested in the strong direction were 100 × 100 × 53 mm, whereas those tested in the weak direction were 50 × 50 × 30 mm. Tests were carried out at different load rates, as described in Table A.9. The author and his supervisors acknowledge the contribution of Dr. I. Pérez and Dr. B. Gómez for their essential help with these tests.

Specimen	Loading rate	Loading direction
FQS-1	1.0 mm/s	Strong
FQS-2	1.5 mm/s	Strong
FQS-3	1.0 mm/s	Strong
FQS-4	0.1 mm/s	Weak
FQS-5	0.5 mm/s	Weak
FQS-6	1.0 mm/s	Weak

Table A.9: Foam specimens for quasi-static compression tests.

Engineering and true stress-strain values were obtained. For collapsible materials with a relevant volume change, the true stresses have to be obtained as

$$\sigma = s \exp\left(-2\nu^{\mathrm{p}}\varepsilon_1\right), \tag{A.1}$$

where s are the engineering stresses, ε_1 are the true strains and ν^{p} is the plastic Poisson's ratio. Results are provided in Figure A.17.

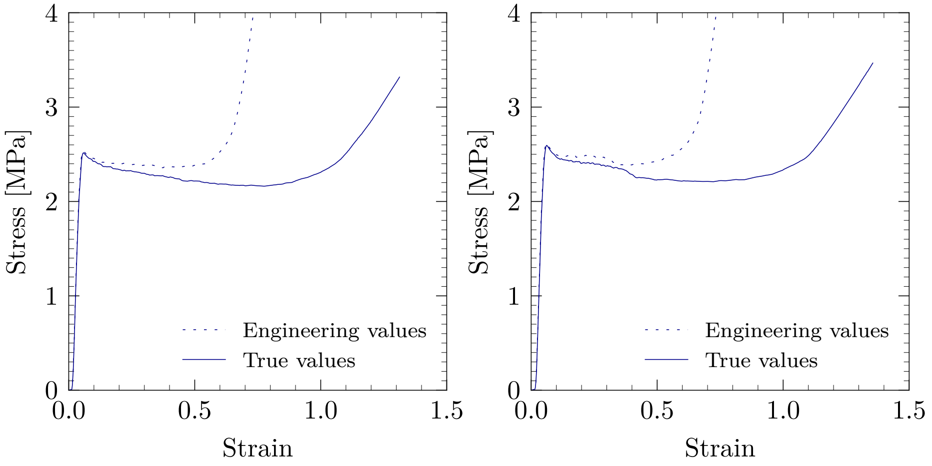

(a) Specimen FQS-1.

(b) Specimen FQS-2.

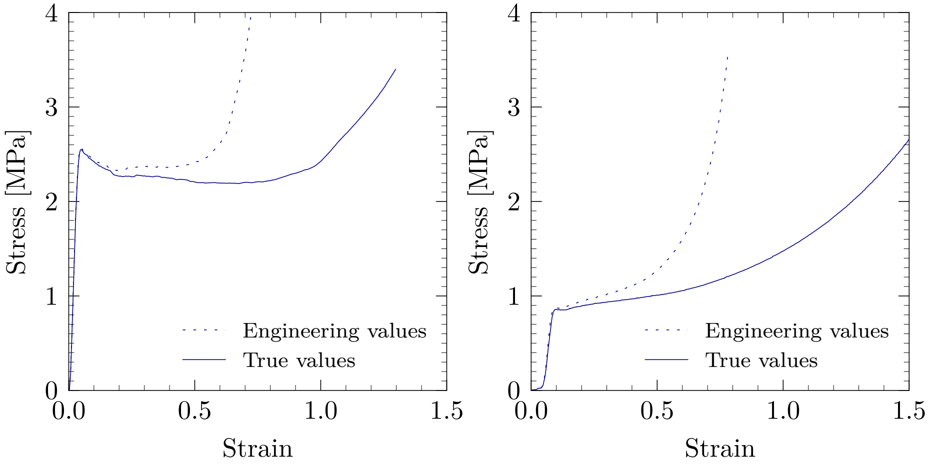

(c) Specimen FQS-3.

(d) Specimen FQS-4.

Figure A.17: Engineering and true stress-strain curves of ArmaFORM PET/W AC 135 (continues on next page).

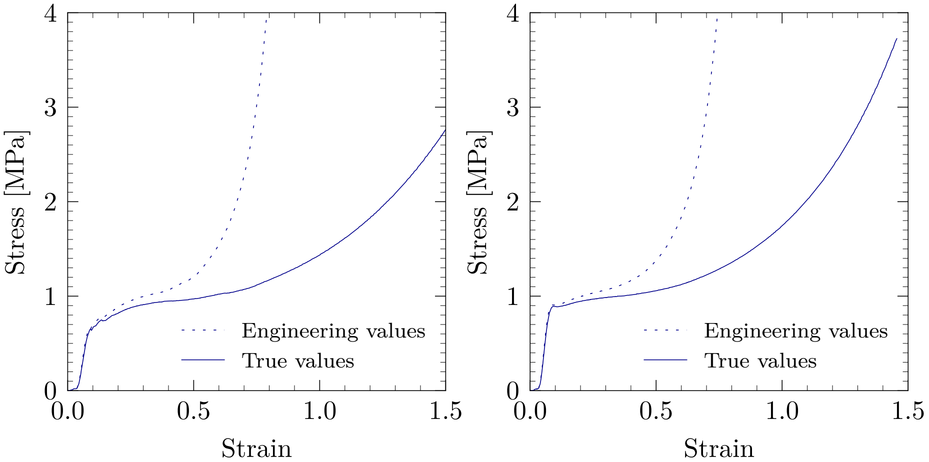

(e) Specimen FQS-5.

(f) Specimen FQS-6.

Figure A.17: (cont.) Engineering and true stress-strain curves of ArmaFORM PET/W AC 135.

A.7 Drop tower tests

Four foam samples were also tested under impact conditions using an INSTRON drop tower. Specimens were 50 × 50 × 40 mm for both loading directions. Some pictures of the test set-up are provided in Figure A.18.

Images from the high-speed camera are offered in Figures A.19 and A.20 and stress-strain curves are presented in Figure A.21. These curves were heavily influenced by stress waves traveling along the test equipment and the load cell. Specimens FDT-1 and FDT-2 were impacted along their weak direction, and specimens FDT-3 and FDT-4 were impacted along their strong direction. Impact speed was 6.88 m/s for all tests, and the striker mass was 8 kg.

(a) INSTRON drop tower. **(b)** Detail of the impact area.

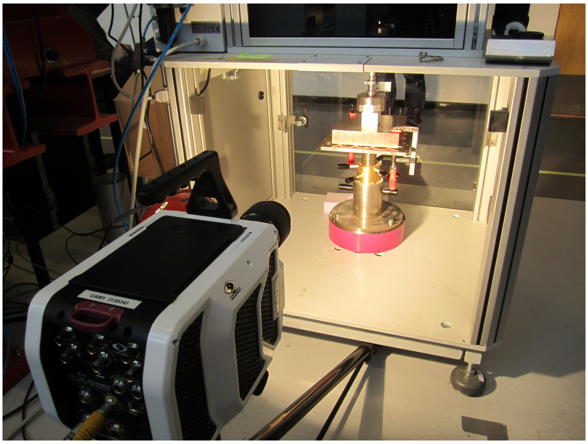

(c) High-speed Phantom camera for image acquisition.

Figure A.18: Drop tower tests on PET foam samples: set-up.

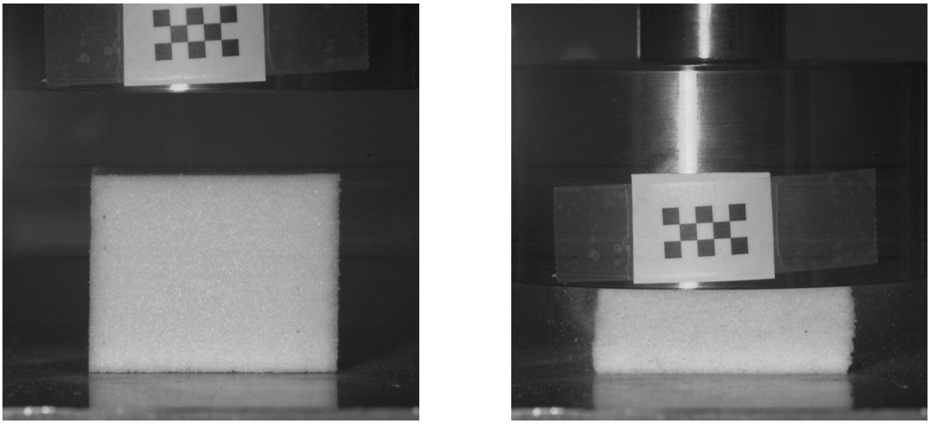

(a) Specimen FDT-1 before impact at 6.88 m/s.

(b) Specimen FDT-1 1560 µs after impact.

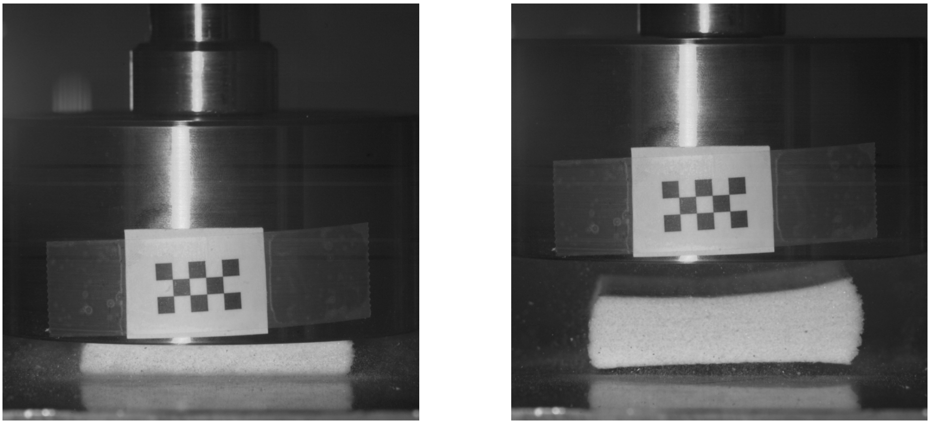

(c) Specimen FDT-1 at its maximum compression.

(d) Specimen FDT-1 after impact and spring-back.

Figure A.19: Drop tower tests on PET foam sample FDT-1, loaded in its weak direction.

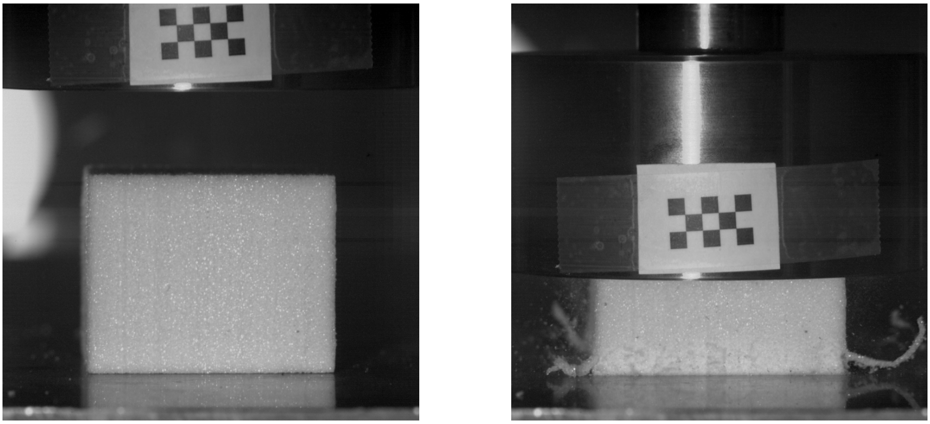

(a) Specimen FDT-3 before impact at 6.88 m/s.

(b) Specimen FDT-3 1560 μs after impact.

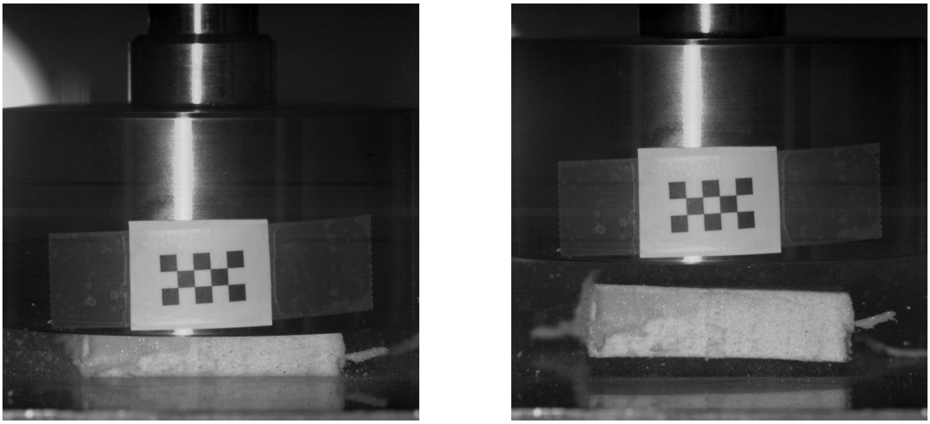

(c) Specimen FDT-3 at its maximum compression.

(d) Specimen FDT-3 after impact and spring-back.

Figure A.20: Drop tower tests on PET foam sample FDT-3, loaded in its strong direction.

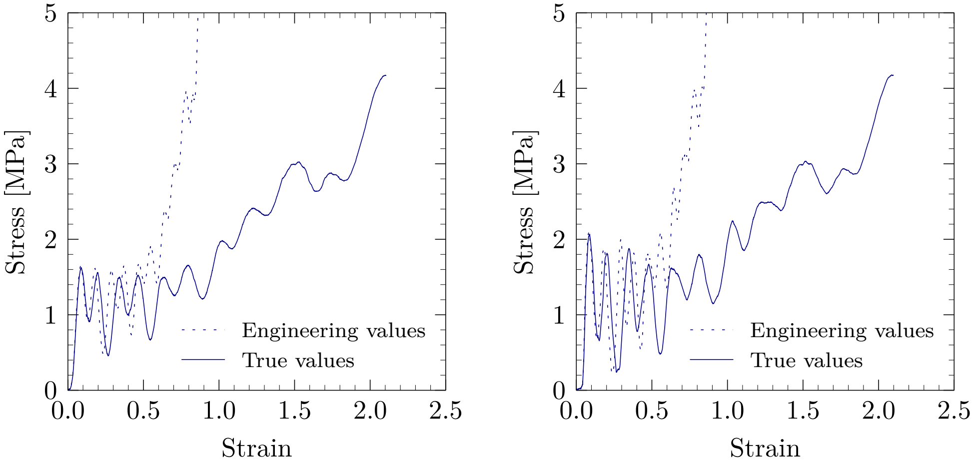

(a) Specimen FDT-1.

(b) Specimen FDT-2.

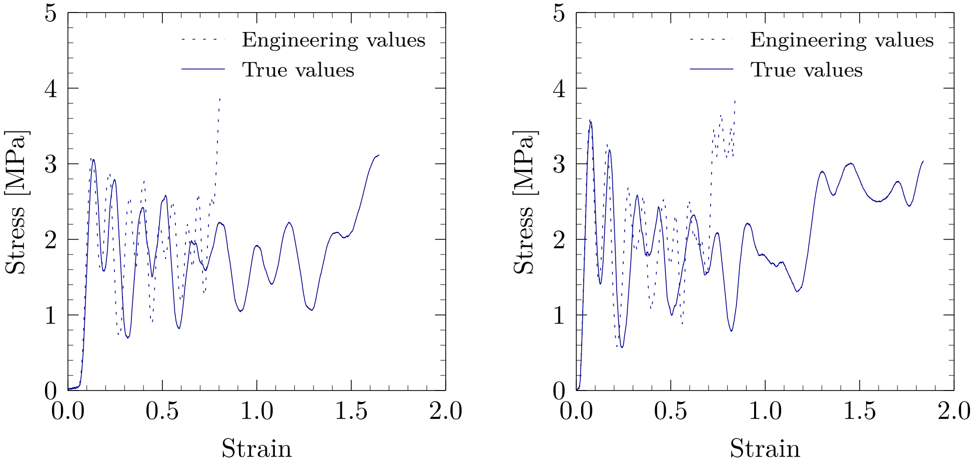

(c) Specimen FDT-3.

(d) Specimen FDT-4.

Figure A.21: Raw stress-strain curves of ArmaFORM PET/W AC 135 specimens subjected to a drop tower test.

A.7.1 Triaxial compressive tests on cylindrical specimens of ArmaFORM PET/W AC 135

With the aim of obtaining the values for the crushable foam model in Chapter 6, triaxial compression tests were performed on foam samples for different confinement pressures. The author thanks Dr. J. Delgado for his valuable contribution to this section.

The test set-up consisted of a confinement cell with an inner membrane where the specimens were placed, and a vertical actuator to apply the vertical pressure. A Hoek-Franklin cell with hydraulic oil HV46 was used for the confinement pressure, and a HBM-C2 5-tonnes load cell with a gain of 2mV/V for the vertical pressure. Two LVDT Vishay HS50 extensometers were attached to the vertical loading device to measure the axial displacement at the top of the specimen. A Micromeasurements D4 device was used for the data acquisition and the system control software was Servosis PCD 2K. Tests were performed at a room temperature of 24.6 degrees Celsius. The set-up is presented in Figure A.22.

Cylindrical specimens were extracted from foam blocks so that their longitudinal axis was orthogonal to the extrusion direction, according to the dimensions depicted in Figure A.23a. Specimens were confined at a certain pressure (less than the yield strength) and then axially compressed. A total of six specimens were tested with initial confinement pressures of 0, 250, 500, 700, 900 and 1200 kPa, labeled T9, T8, T6, T5, T10 and T3, respectively. The two last specimens were not considered for calculations since the material yielded before the axial load was applied, i.e. the yield surface was already expanded. The opposite tests were not performed (keeping an axial pressure constant and increasing the confinement), given the difficulty of computing an equivalent radial strain to be compared with the axial true strain of 0.3 (see below). This led to an unexplored region in the yield surface.

Two previous calibrations had to be run in order to obtain reliable results from the tests, one for the vertical actuator and another one to obtain the deformation of the confinement membrane, which has to be subtracted if volumetric strains want to be computed.

At the first stage, a relation between the pump pressure and the applied vertical load had to be established. This was done with a linear regression of pressure-force pairs obtained in this calibration stage. Figure A.24 shows the goodness of the fit

$$F_{\mathrm{v}} = AP + B \tag{A.2}$$

for A = 0.32597 and B = -0.08477, F_{v} and P being the vertical load and vertical pressure, respectively.

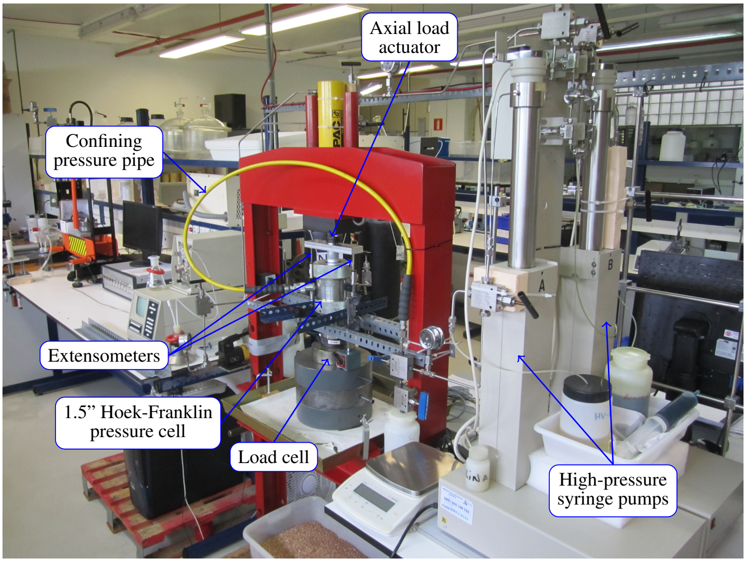

(a) Test device.

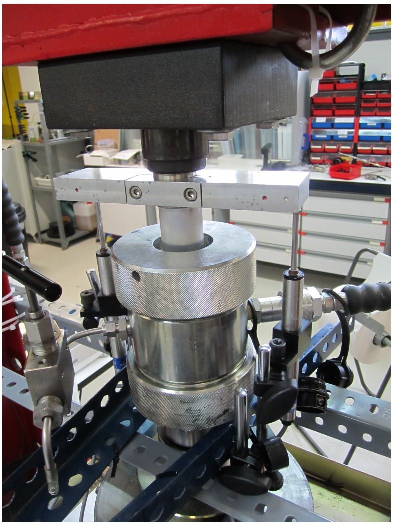

(b) Detail of the confinement cell.

Figure A.22: Test device for triaxial compression.

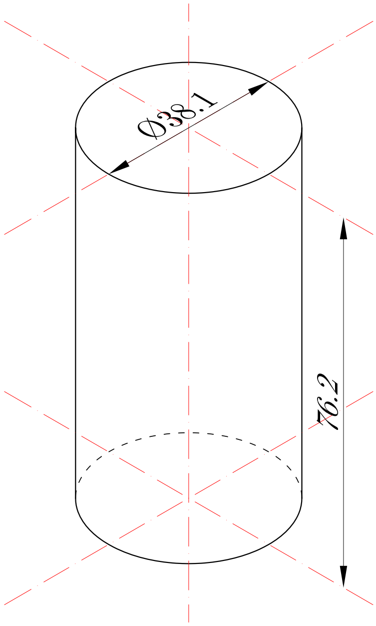

(a) Dimensions in millimeters of the foam specimens for the triaxial tests. The extrusion direction is orthogonal to the longitudinal axis.

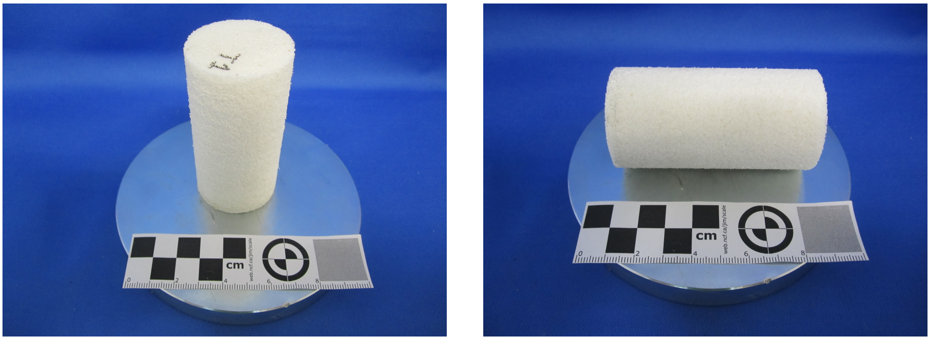

(b) Foam specimen for triaxial compression test.

(c) Foam specimen for triaxial compression test.

Figure A.23: Foam specimens for triaxial compression tests.

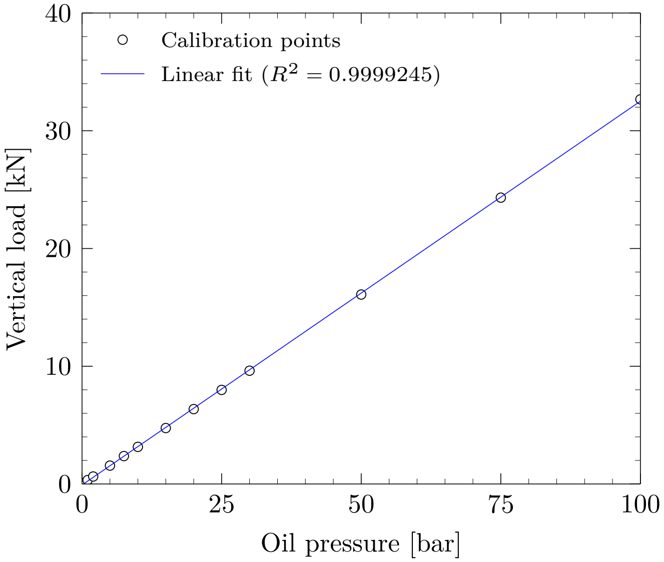

Figure A.24: Linear fit to calibration points for the vertical actuator of the triaxial test.

The second stage consisted of introducing a steel cylinder into the cell and increasing the lateral pressure. If it is assumed that the deformations in the steel cylinder are negligible compared to the deformation of the membrane, an expression relating the confinement pressure and the volumetric change of the membrane can be obtained. Two load-unload cycles up to a lateral pressure of 15 bar were done, and the resulting volume-pressure curve was approximated by means of the following expression:

$$\Delta V \approx \sum_{i=1}^{2} C_i \left[1 - \exp\left(-D_i P\right)\right], \tag{A.3}$$

where ΔV is the volume change due to the deformation of the membrane. Best fit was obtained for $C_1 = 405.06\,\mathrm{ml}$, $C_2 = 10.59\,\mathrm{ml}$, $D_1 = 0.000416$ and $D_2 = 0.6560$. Original measurements and fit are presented in Figure A.25.

A view of the tested specimens and one undeformed sample (specimen labeled T12) is provided in Figure A.26. Notice that the anisotropy of the material in the radial direction produced that specimen T3 adopted an ellipse-like shape.

According to ABAQUS documentation, the ratio of the uniaxial yield stress

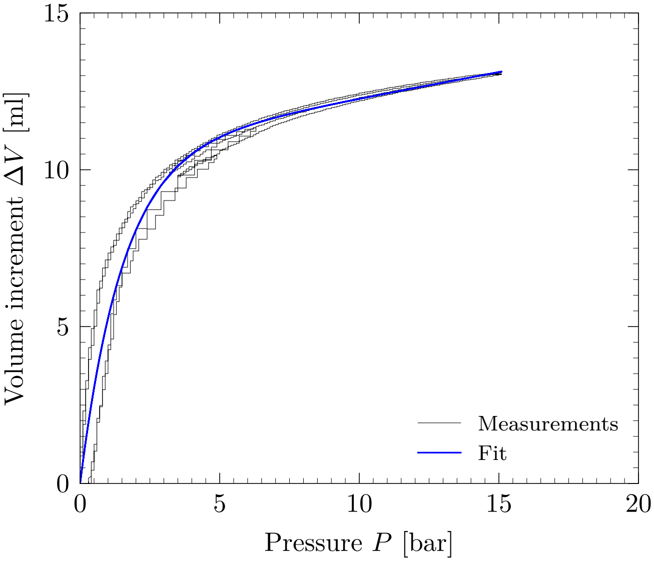

Figure A.25: Volume-pressure curves for the measurement of the membrane compressibility.

to the hydrostatic yield stress should be obtained from the plateau region in the stress-strain curves. For consistency with Chapter 5, the stress corresponding to a true strain of 0.3 was used. Figure A.27 shows the true stress-strain curves for different confinement pressures. Notice that specimen T10 was not valid for comparison given that it reached the yielding point under lateral pressure before the axial load started. This generated a reduction of the cross-sectional area, and therefore, the plotted stresses are much smaller than the real ones. Stresses at $\varepsilon = 0.3$ are presented in Table A.10.

Specimen	Initial confinement pressure [kPa]	Axial stress at $\varepsilon = 0.3$ [kPa]
T9	0	982.98
T8	250	1105.68
T6	500	1410.12
T5	700	1432.46
T10	900	Not valid
T3	1200	Not valid

Table A.10: Evolution of the yield stress at $\varepsilon = 0.3$ for different lateral confinement pressures.

Figure A.26: ArmaFORM PET/W AC 135 foam specimens tested in triaxial compression with increasing confinement pressure from left to right, and non-tested specimen (T12) for comparison. Specimens T10 and T3 yielded before the axial load was applied, and the material anisotropy in the radial direction can be observed clearly.

The ratio k_c for the constitutive model was estimated as:

$$k_\mathrm{c} = \frac{\sigma_{0.3,T9}}{\max\left(\sigma_{0.3}\right)}. \tag{A.4}$$

By doing so, a value of $k_\mathrm{c} = 0.686$ was obtained. An alternative is to assume an elliptical yield surface and fit an adequate ellipse to the obtained data, assuming also that the major axis of the ellipse lies on the hydrostatic line ($\sigma_\mathrm{v} = \sigma_\mathrm{lat}$). This led to a yield stress in hydrostatic compression equal to 1383.3 kPa, which gives $k_\mathrm{c} = 0.708$. Both results are quite similar, but the second one was adopted for being considered more accurate.

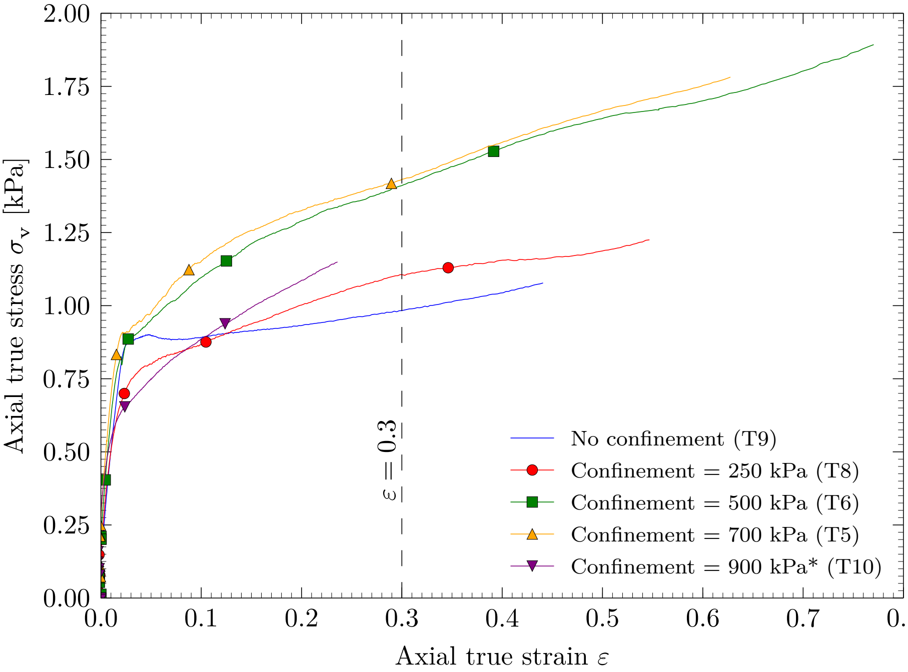

Figure A.27: True axial stress-strain curves obtained from the triaxial compression tests. The curve for 900 kPa of confinement was discarded since the specimen reached yielding in the radial direction.

B

Microscopic structure of AA6063-T5 extrusion, GFRP and PET-based foam

This appendix contains pictures of the three materials employed in Chapters 5 and 6 as seen through a scanning electron microscope (SEM). These images were obtained in cooperation with Dr. Ada Castro at SAI (Servizos de Investigación) facilities in Universidade da Coruña.

B.1 AA6063-T5 aluminum alloy

Tensile tests have been performed on cylindrical and plane specimens. The plane specimens were extracted from the circular extrusions, as described in Chapter 5. Cylindrical specimens of alloy AA6063-T5 failed in a ductile, circular cup-cone pattern. Figure B.1 shows the failure surface at different zoom rates. Some dimples generated by the presence of crystal grains can be clearly observed. The tensile specimens cut from the AA6063-T5 extrusions failed in a ductile, 45° pattern. Figure B.2 shows a progressive zooming of the top view of the failure surface.

B.2 Ultramid A3WG10 BK00564

This material is made of a poliamide matrix (40 %) and short, randomly-oriented glass fibers (60 %). The sample of the fracture surface of a tensile specimen was covered with gold particles (sputter-coating) to improve its electrical conductibility. Figure B.3 offers a progressive zooming over the fracture surface.

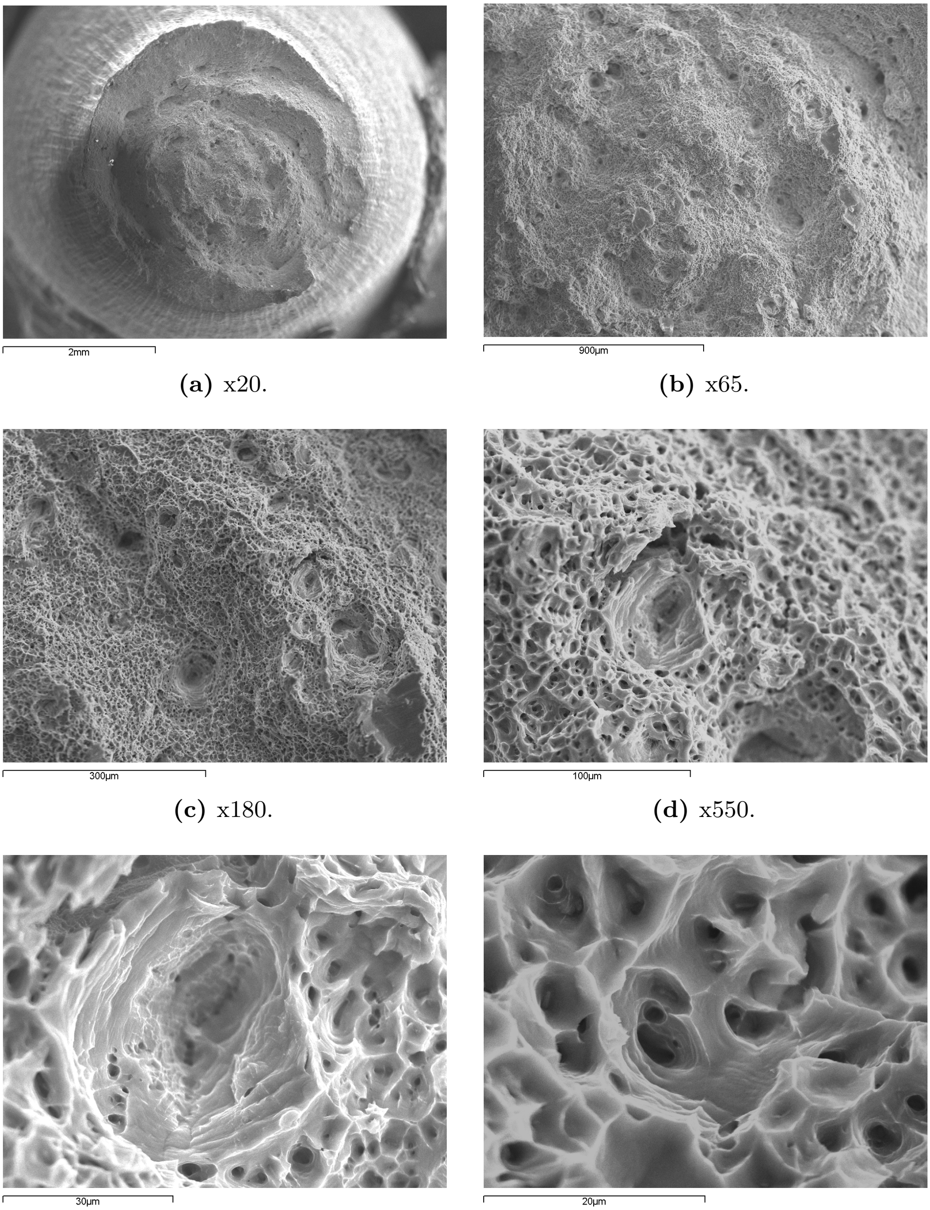

(a) x20.

(b) x65.

(c) x180.

(d) x550.

(e) x1500.

(f) x3000.

Figure B.1: SEM images of the cup-cone fracture surface of a AA6063-T5 cylindrical tensile specimen (top view).

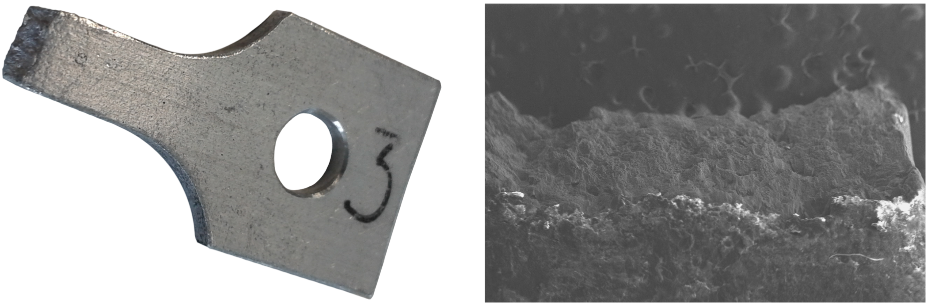

(a) Digital camera. **(b)** x27.

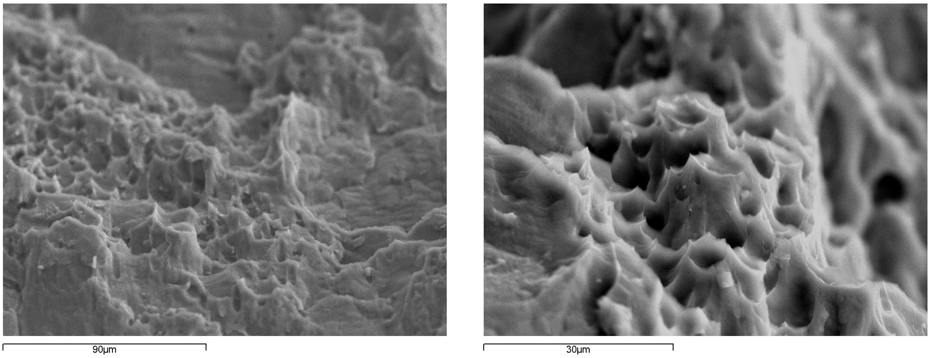

(c) x600. **(d)** x1700.

Figure B.2: Digital camera and SEM images of the fracture surface of a AA6063-T5 extracted tensile specimen.

B.3 ArmaFORM PET/W AC 135

Like GFRP, foam samples have been also sputter-coated in gold to improve their electrical conductivity. Samples have been extracted in two directions in order to check if the orthotropic properties are somehow related to the cell structure. In the view of the pictures, cells are stretched in the extrusion direction, which confers an increased stiffness to the material when loads are applied in this direction. Besides, we can appreciate the presence of a second polymer constituting a secondary colloidal phase in form of well-differentiable particles inserted in the main phase (see for instance Figures B.4e, B.5e and B.5f).

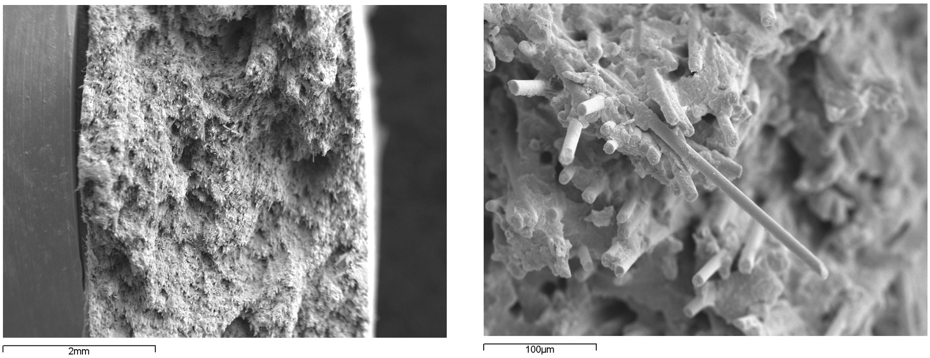

(a) Fracture surface, x20.

(b) Chopped glass fibers, x300.

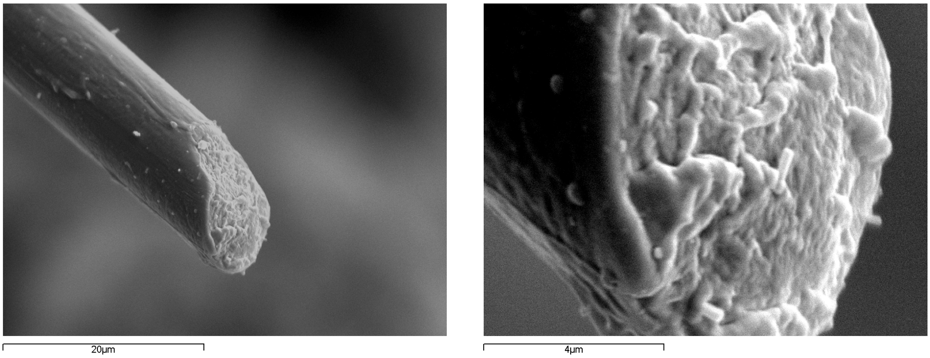

(c) Detail of a fractured single glass fiber, x2700.

(d) Fracture surface on a single fiber, x12000.

Figure B.3: SEM images of the fracture surface of an Ultramid A3WG10 BK00564 tensile specimen.

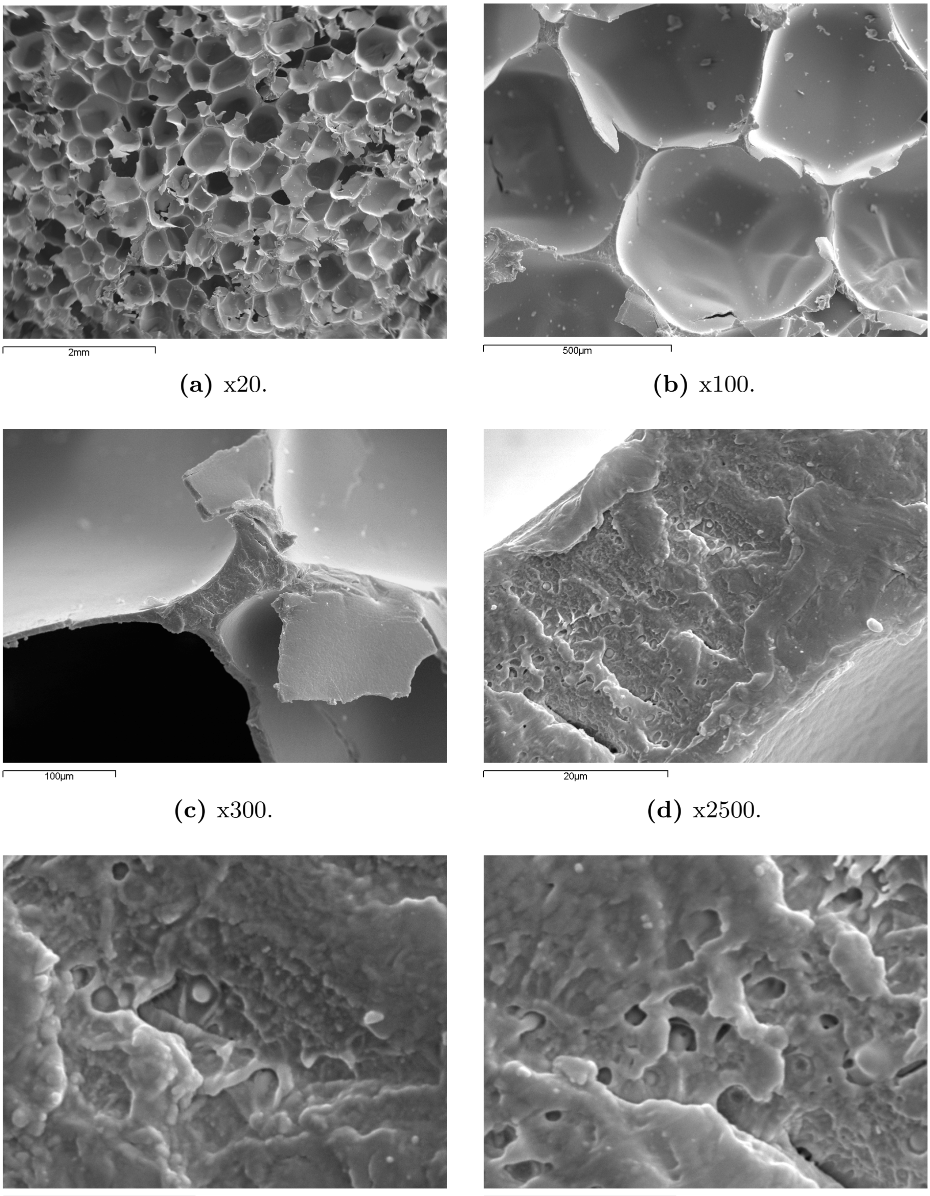

(a) x20.

(b) x100.

(c) x300.

(d) x2500.

(e) x8500.

(f) x8500.

Figure B.4: SEM images of ArmaFORM PET/W AC 135. The depicted surface is orthogonal to the extrusion direction.

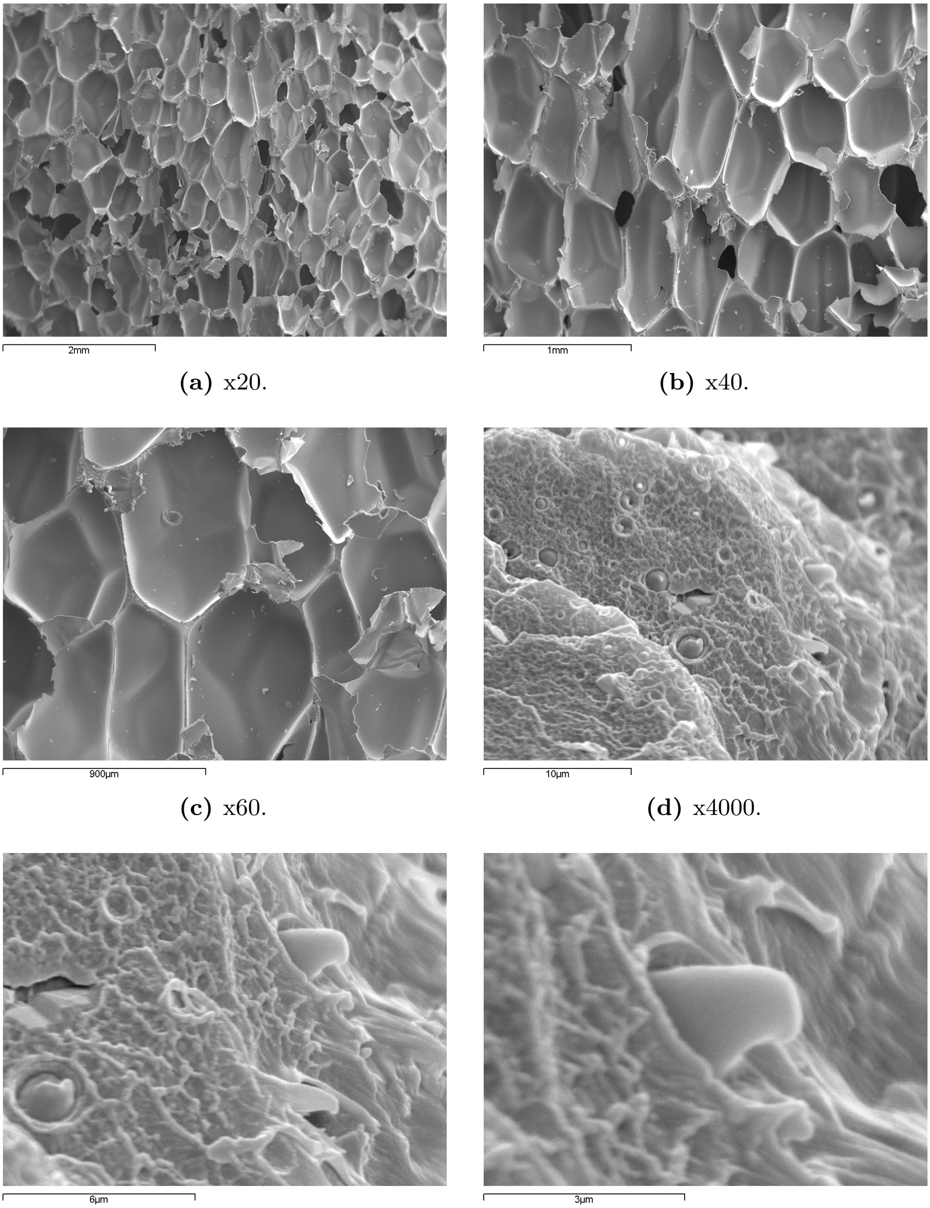

(a) x20.

(b) x40.

(c) x60.

(d) x4000.

(e) x8500.

(f) x18000.

Figure B.5: SEM images of ArmaFORM PET/W AC 135. The extrusion direction is parallel to the largest page margin.

C

Material datasheets

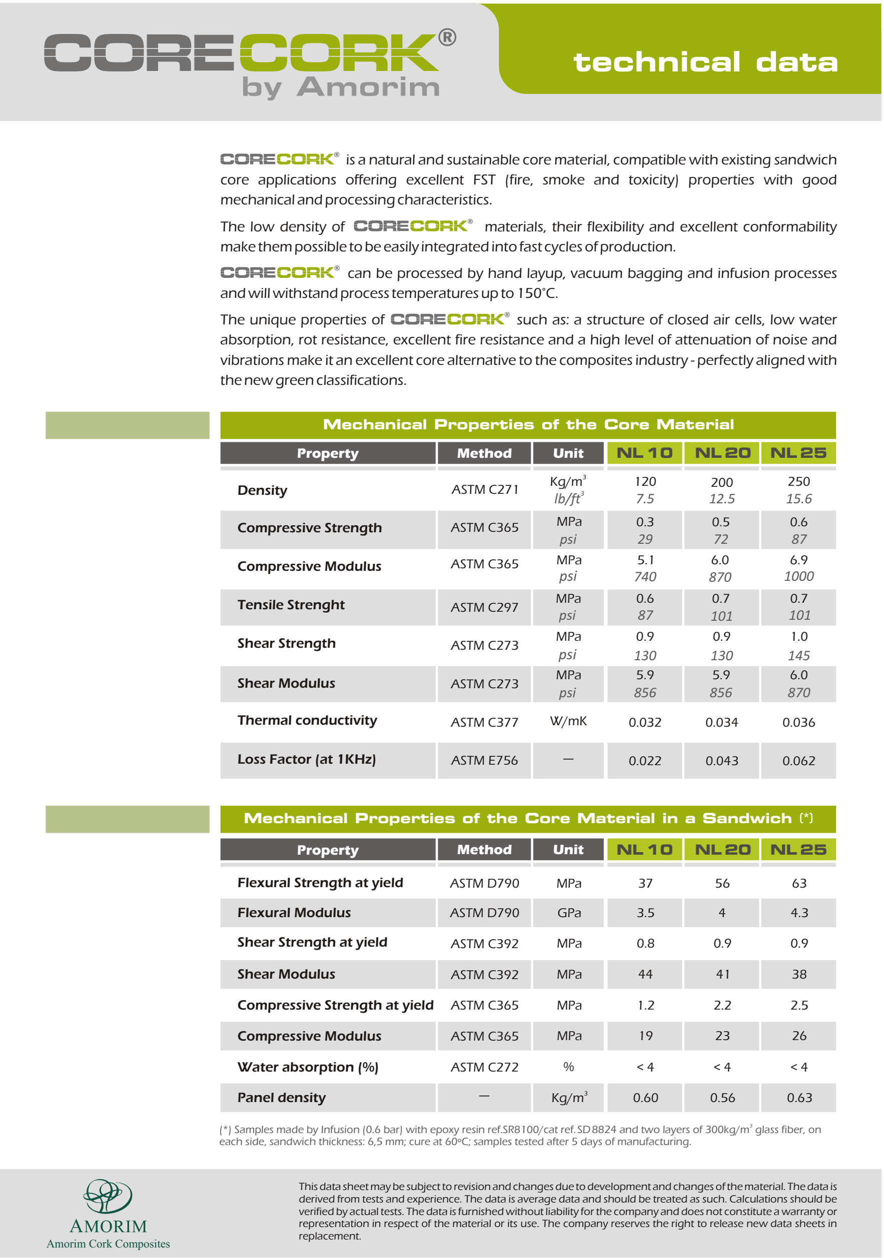

CORECORK® by Amorim

technical data

CORECORK® is a natural and sustainable core material, compatible with existing sandwich core applications offering excellent FST (fire, smoke and toxicity) properties with good mechanical and processing characteristics.

The low density of CORECORK® materials, their flexibility and excellent conformability make them possible to be easily integrated into fast cycles of production.

CORECORK® can be processed by hand layup, vacuum bagging and infusion processes and will withstand process temperatures up to 150°C.

The unique properties of CORECORK® such as: a structure of closed air cells, low water absorption, rot resistance, excellent fire resistance and a high level of attenuation of noise and vibrations make it an excellent core alternative to the composites industry - perfectly aligned with the new green classifications.

Mechanical Properties of the Core Material

Property	Method	Unit	NL 10	NL 20	NL 25
Density	ASTM C271	Kg/m^3 *lb/ft^3*	120 *7.5*	200 *12.5*	250 *15.6*
Compressive Strength	ASTM C365	MPa *psi*	0.3 *29*	0.5 *72*	0.6 *87*
Compressive Modulus	ASTM C365	MPa *psi*	5.1 *740*	6.0 *870*	6.9 *1000*
Tensile Strenght	ASTM C297	MPa *psi*	0.6 *87*	0.7 *101*	0.7 *101*
Shear Strength	ASTM C273	MPa *psi*	0.9 *130*	0.9 *130*	1.0 *145*
Shear Modulus	ASTM C273	MPa *psi*	5.9 *856*	5.9 *856*	6.0 *870*
Thermal conductivity	ASTM C377	W/mK	0.032	0.034	0.036
Loss Factor (at 1KHz)	ASTM E756	—	0.022	0.043	0.062

Mechanical Properties of the Core Material in a Sandwich (*)

Property	Method	Unit	NL 10	NL 20	NL 25
Flexural Strength at yield	ASTM D790	MPa	37	56	63
Flexural Modulus	ASTM D790	GPa	3.5	4	4.3
Shear Strength at yield	ASTM C392	MPa	0.8	0.9	0.9
Shear Modulus	ASTM C392	MPa	44	41	38
Compressive Strength at yield	ASTM C365	MPa	1.2	2.2	2.5
Compressive Modulus	ASTM C365	MPa	19	23	26
Water absorption (%)	ASTM C272	%	< 4	< 4	< 4
Panel density	—	Kg/m^3	0.60	0.56	0.63

(*) Samples made by Infusion (0.6 bar) with epoxy resin ref.SR8100/cat ref.SD 8824 and two layers of 300kg/m^3 glass fiber, on each side, sandwich thickness: 6,5 mm; cure at 60ºC; samples tested after 5 days of manufacturing.

AMORIM
Amorim Cork Composites

This data sheet may be subject to revision and changes due to development and changes of the material. The data is derived from tests and experience. The data is average data and should be treated as such. Calculations should be verified by actual tests. The data is furnished without liability for the company and does not constitute a warranty or representation in respect of the material or its use. The company reserves the right to release new data sheets in replacement.

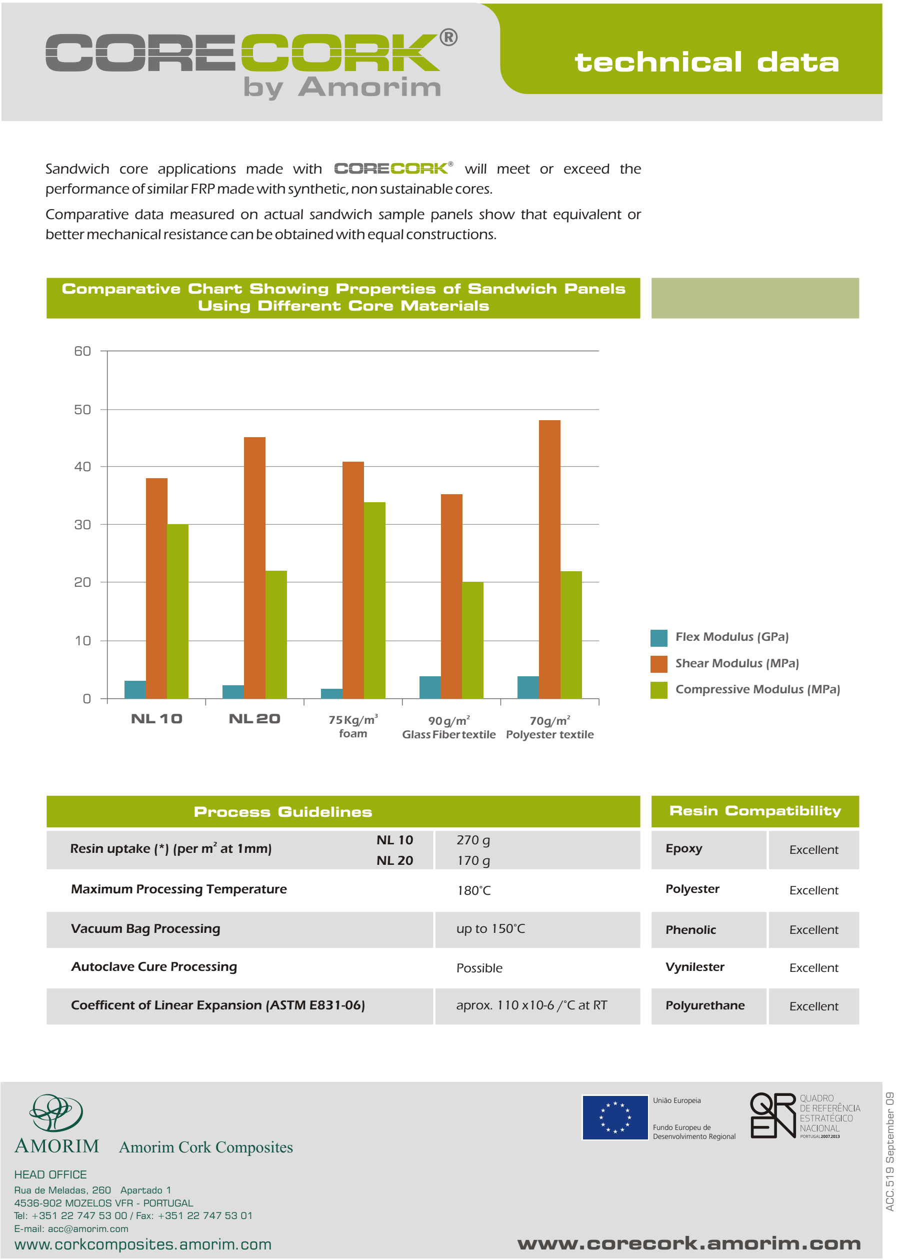

CORECORK® by Amorim

technical data

Sandwich core applications made with CORECORK® will meet or exceed the performance of similar FRP made with synthetic, non sustainable cores.

Comparative data measured on actual sandwich sample panels show that equivalent or better mechanical resistance can be obtained with equal constructions.

Comparative Chart Showing Properties of Sandwich Panels Using Different Core Materials

Process Guidelines		
Resin uptake (*) (per m² at 1mm)	NL 10 NL 20	270 g 170 g
Maximum Processing Temperature		180°C
Vacuum Bag Processing		up to 150°C
Autoclave Cure Processing		Possible
Coefficent of Linear Expansion (ASTM E831-06)		aprox. 110 x10-6 /°C at RT

Resin Compatibility	
Epoxy	Excellent
Polyester	Excellent
Phenolic	Excellent
Vynilester	Excellent
Polyurethane	Excellent

AMORIM Amorim Cork Composites

União Europeia
Fundo Europeu de Desenvolvimento Regional

QUADRO DE REFERÊNCIA ESTRATÉGICO NACIONAL
PORTUGAL 2007.2013

HEAD OFFICE
Rua de Meladas, 260 Apartado 1
4536-902 MOZELOS VFR - PORTUGAL
Tel: +351 22 747 53 00 / Fax: +351 22 747 53 01
E-mail: acc@amorim.com
www.corkcomposites.amorim.com

www.corecork.amorim.com

ACC.519 September 09

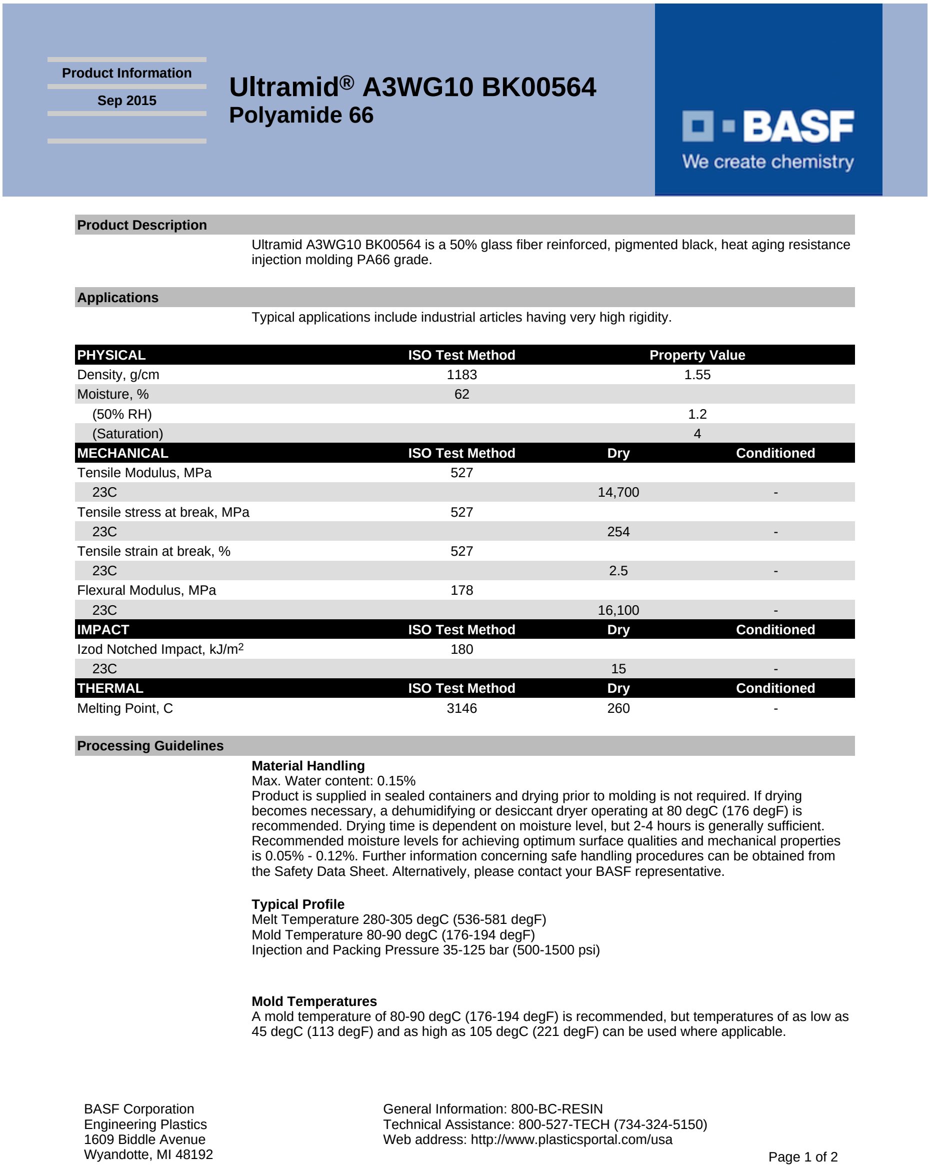

Product Information

Sep 2015

Ultramid® A3WG10 BK00564
Polyamide 66

BASF
We create chemistry

Product Description

Ultramid A3WG10 BK00564 is a 50% glass fiber reinforced, pigmented black, heat aging resistance injection molding PA66 grade.

Applications

Typical applications include industrial articles having very high rigidity.

PHYSICAL	ISO Test Method	Property Value
Density, g/cm	1183	1.55
Moisture, %	62	
(50% RH)		1.2
(Saturation)		4

MECHANICAL	ISO Test Method	Dry	Conditioned
Tensile Modulus, MPa	527		
23C		14,700	-
Tensile stress at break, MPa	527		
23C		254	-
Tensile strain at break, %	527		
23C		2.5	-
Flexural Modulus, MPa	178		
23C		16,100	-

IMPACT	ISO Test Method	Dry	Conditioned
Izod Notched Impact, kJ/m^2	180		
23C		15	-

THERMAL	ISO Test Method	Dry	Conditioned
Melting Point, C	3146	260	-

Processing Guidelines

Material Handling
Max. Water content: 0.15%
Product is supplied in sealed containers and drying prior to molding is not required. If drying becomes necessary, a dehumidifying or desiccant dryer operating at 80 degC (176 degF) is recommended. Drying time is dependent on moisture level, but 2-4 hours is generally sufficient. Recommended moisture levels for achieving optimum surface qualities and mechanical properties is 0.05% - 0.12%. Further information concerning safe handling procedures can be obtained from the Safety Data Sheet. Alternatively, please contact your BASF representative.

Typical Profile
Melt Temperature 280-305 degC (536-581 degF)
Mold Temperature 80-90 degC (176-194 degF)
Injection and Packing Pressure 35-125 bar (500-1500 psi)

Mold Temperatures
A mold temperature of 80-90 degC (176-194 degF) is recommended, but temperatures of as low as 45 degC (113 degF) and as high as 105 degC (221 degF) can be used where applicable.

BASF Corporation
Engineering Plastics
1609 Biddle Avenue
Wyandotte, MI 48192

General Information: 800-BC-RESIN
Technical Assistance: 800-527-TECH (734-324-5150)
Web address: http://www.plasticsportal.com/usa

Ultramid® A3WG10 BK00564

Pressures
Injection pressure controls the filling of the part and should be applied for 90% of ram travel. Packing pressure affects the final part and can be used effectively in controlling sink marks and shrinkage. It should be applied and maintained until the gate area is completely frozen off.

Back pressure can be utilized to provide uniform melt consistency and reduce trapped air and gas. Minimal back pressure should be utilized to prevent glass breakage.

Fill Rate
Fast fill rates are recommended to ensure uniform melt delivery to the cavity and prevent premature freezing. Surface appearance is directly affected by injection rate.

Note

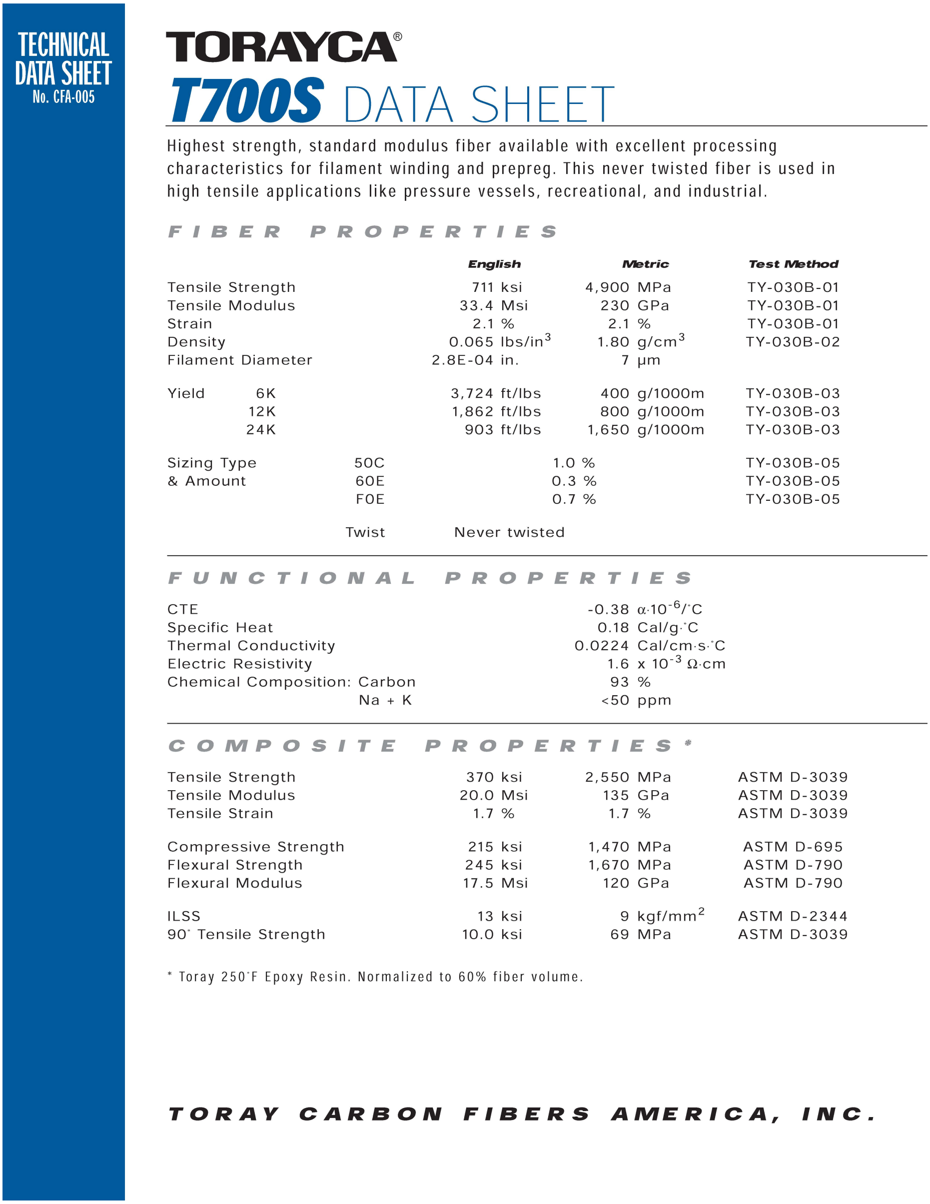

TECHNICAL
DATA SHEET
No. CFA-005

TORAYCA®
T700S DATA SHEET

Highest strength, standard modulus fiber available with excellent processing characteristics for filament winding and prepreg. This never twisted fiber is used in high tensile applications like pressure vessels, recreational, and industrial.

FIBER PROPERTIES

		English	Metric	Test Method
Tensile Strength		711 ksi	4,900 MPa	TY-030B-01
Tensile Modulus		33.4 Msi	230 GPa	TY-030B-01
Strain		2.1 %	2.1 %	TY-030B-01
Density		0.065 lbs/in^3	1.80 g/cm^3	TY-030B-02
Filament Diameter		2.8E-04 in.	7 μm	
Yield	6K	3,724 ft/lbs	400 g/1000m	TY-030B-03
	12K	1,862 ft/lbs	800 g/1000m	TY-030B-03
	24K	903 ft/lbs	1,650 g/1000m	TY-030B-03
Sizing Type & Amount	50C		1.0 %	TY-030B-05
	60E		0.3 %	TY-030B-05
	F0E		0.7 %	TY-030B-05
	Twist	Never twisted		

FUNCTIONAL PROPERTIES

CTE	-0.38 $\alpha \cdot 10^{-6}/^\circ\text{C}$
Specific Heat	0.18 Cal/g·°C
Thermal Conductivity	0.0224 Cal/cm·s·°C
Electric Resistivity	1.6 x 10^{-3} Ω·cm
Chemical Composition: Carbon	93 %
Na + K	<50 ppm

COMPOSITE PROPERTIES*

	English	Metric	Test Method
Tensile Strength	370 ksi	2,550 MPa	ASTM D-3039
Tensile Modulus	20.0 Msi	135 GPa	ASTM D-3039
Tensile Strain	1.7 %	1.7 %	ASTM D-3039
Compressive Strength	215 ksi	1,470 MPa	ASTM D-695
Flexural Strength	245 ksi	1,670 MPa	ASTM D-790
Flexural Modulus	17.5 Msi	120 GPa	ASTM D-790
ILSS	13 ksi	9 kgf/mm^2	ASTM D-2344
90° Tensile Strength	10.0 ksi	69 MPa	ASTM D-3039

* Toray 250°F Epoxy Resin. Normalized to 60% fiber volume.

TORAY CARBON FIBERS AMERICA, INC.

T700S

COMPOSITE PROPERTIES**

Tensile Strength	355 ksi	2,450 MPa	ASTM D-3039
Tensile Modulus	18.0 Msi	125 GPa	ASTM D-3039
Tensile Strain	1.7 %	1.7 %	ASTM D-3039
Compressive Strength	230 ksi	1,570 MPa	ASTM D-695
Compressive Modulus	--- Msi	--- GPa	ASTM D-695
In-Plane Shear Strength	14 ksi	98 MPa	ASTM D-3518
ILSS	15.5 ksi	11 kgf/mm^2	ASTM D-2344
90° Tensile Strength	10.0 ksi	70 MPa	ASTM D-3039

** Toray Semi-Toughened 350°F Epoxy Resin. Normalized to 60% fiber volume.

See Section 4 for Safety & Handling information. The above properties do not constitute any warranty or guarantee of values. These values are for material selection purposes only. For applications requiring guaranteed values, contact our sales and technical team to establish a material specification document.

PACKAGING

The table below summarizes the tow sizes, twists, sizing types, and packaging available for standard material. Other bobbin sizes may be available on a limited basis.

Tow Sizes	Twist[1]	Sizing	Bobbin Net Weight (kg)	Bobbin Type[2]	Bobbin Size (mm)					Spools per Case	Case Net Weight (kg)
					a	**b**	**c**	**d**	**e**		
6K	C	50C	2.0	*III*	76.5	82.5	280	140	252	12	24
12K	C	50C	6.0	*III*	76.5	82.5	280	200	252	4	24
	C	60E	6.0	*III*	76.5	82.5	280	200	252	4	24
	C	F0E	6.0	*III*	76.5	82.5	280	200	252	4	24
24K	C	50C	6.0	*III*	76.5	82.5	280	200	252	4	24
	C	60E	6.0	*III*	76.5	82.5	280	200	252	4	24
	C	F0E	6.0	*III*	76.5	82.5	280	200	252	4	24

[1] **Twist** A: Twisted yarn B: Untwisted yarn made from a twisted yarn through an untwisting process C: Never twisted yarn

[2] **Bobbin Type** See Diagram below

TYPE I

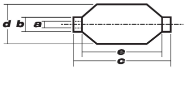

TYPE II

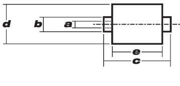

TYPE III

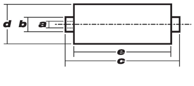

TORAY CARBON FIBERS AMERICA, INC.

6 Hutton Centre Drive, Suite #1270, Santa Ana, CA 92707 TEL: (714) 431-2320 FAX: (714) 424-0750
Sales@Toraycfa.com Technical@Toraycfa.com www.torayusa.com

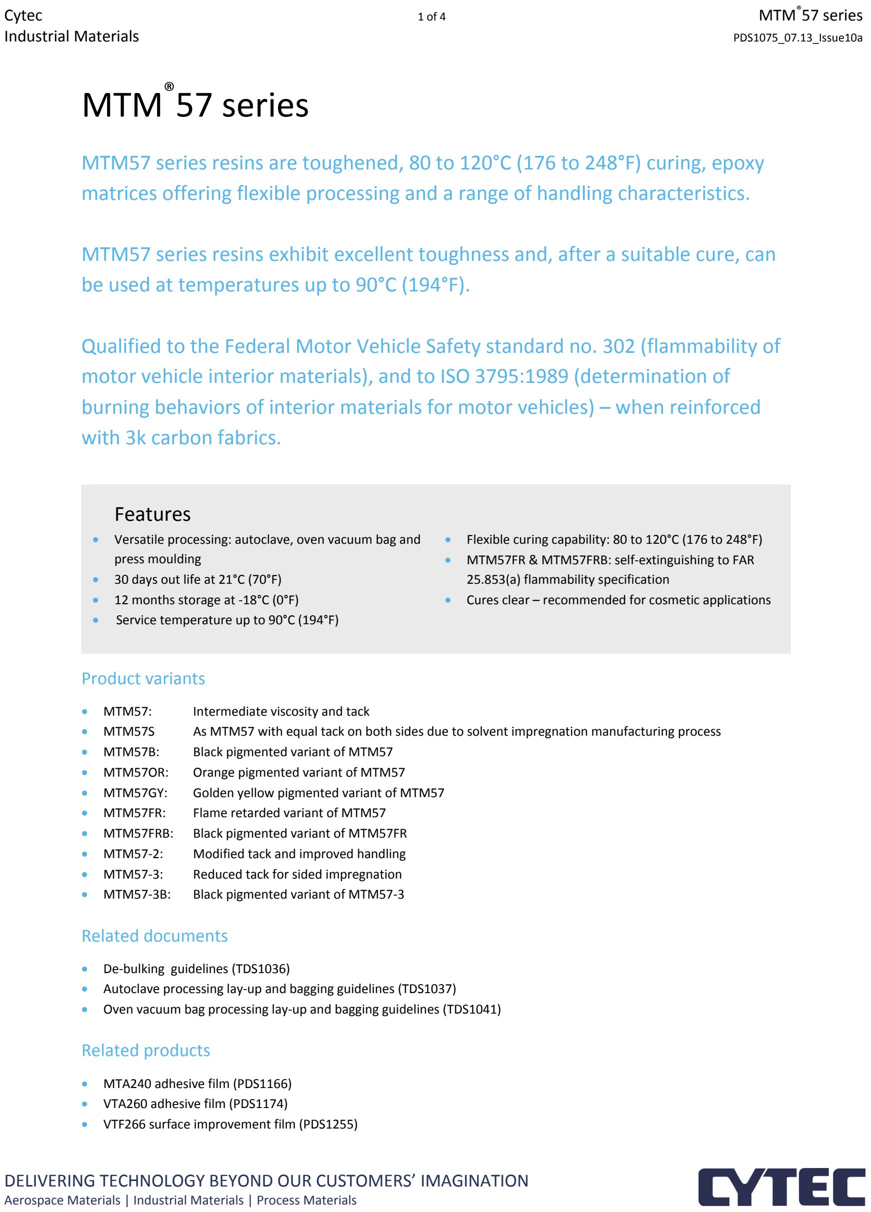

MTM® 57 series

MTM57 series resins are toughened, 80 to 120°C (176 to 248°F) curing, epoxy matrices offering flexible processing and a range of handling characteristics.

MTM57 series resins exhibit excellent toughness and, after a suitable cure, can be used at temperatures up to 90°C (194°F).

Qualified to the Federal Motor Vehicle Safety standard no. 302 (flammability of motor vehicle interior materials), and to ISO 3795:1989 (determination of burning behaviors of interior materials for motor vehicles) – when reinforced with 3k carbon fabrics.

Features

- Versatile processing: autoclave, oven vacuum bag and press moulding
- 30 days out life at 21°C (70°F)
- 12 months storage at -18°C (0°F)
- Service temperature up to 90°C (194°F)
- Flexible curing capability: 80 to 120°C (176 to 248°F)
- MTM57FR & MTM57FRB: self-extinguishing to FAR 25.853(a) flammability specification
- Cures clear – recommended for cosmetic applications

Product variants

MTM57:	Intermediate viscosity and tack
MTM57S	As MTM57 with equal tack on both sides due to solvent impregnation manufacturing process
MTM57B:	Black pigmented variant of MTM57
MTM57OR:	Orange pigmented variant of MTM57
MTM57GY:	Golden yellow pigmented variant of MTM57
MTM57FR:	Flame retarded variant of MTM57
MTM57FRB:	Black pigmented variant of MTM57FR
MTM57-2:	Modified tack and improved handling
MTM57-3:	Reduced tack for sided impregnation
MTM57-3B:	Black pigmented variant of MTM57-3

Related documents

- De-bulking guidelines (TDS1036)
- Autoclave processing lay-up and bagging guidelines (TDS1037)
- Oven vacuum bag processing lay-up and bagging guidelines (TDS1041)

Related products

- MTA240 adhesive film (PDS1166)
- VTA260 adhesive film (PDS1174)
- VTF266 surface improvement film (PDS1255)

Cure cycle

Oven vacuum bag cure

Vacuum bag pressure	Minimum of 980mbar (29"Hg)*
Ramp rate	1 to 3°C (1.8 to 5.4°F)/minute
Recommended cure cycle	1 hour at 120°C, +5/-0°C (248°F, +9/-0°F)
Cool down	Maximum of 3°C (5.4°F)/minute to 60°C (140°F)

*This is the ideal vacuum level, however, it is recognised that it is not always possible to attain. If in doubt, please contact our technical support staff for advice.

Autoclave cure

Vacuum bag pressure	Minimum of 980mbar (29"Hg)*
Autoclave pressure	6.2 bar (90 psi)**
Ramp rate	1 to 3°C (1.8 to 5.4°F)/minute
Recommended cure cycle	1 hour at 120°C, +5/-0°C (248°F, +9/-0°F)
Cool down	Maximum of 3°C (5.4°F)/minute to 60°C (140°F)

*This is the ideal vacuum level, however, it is recognised that it is not always possible to attain. If in doubt, please contact our technical support staff for advice.

**If producing sandwich panels, apply the maximum pressure allowable for the honeycomb type.

Press cure

Mould tools should restrain the flow sufficiently under moulding conditions to avoid fabric or fibre distortion.

Press pressure	Minimum of 2.8 bar (40 psi)
Ramp rate	A suitable rate (dependant on mould tooling)
Recommended cure cycle	1 hour at 120°C, +5/-0°C (248°F, +9/-0°F)
Cool down	A suitable rate (dependant on mould tooling) to 60°C (140°F)

Note:

- Demoulding at the cure temperature may be possible if the tooling is suitably designed. A specific trial is recommended.

Alternative cure cycles

Temperature	Duration
80°C (176°F)	12 hours
100°C (212°F)	3 hours

Post-cure

In applications demanding maximum temperature or environmental resistance, it is essential that the component is post-cured to fully develop the glass transition temperature.

Ramp rate	0.3°C (0.5°F)/minute
Post-cure cycle	2 hours at 120°C -0/+5°C (248°F -0/+9°F)*
Cool down	Maximum of 3°C (5.4°F)/minute to 60°C (140°F)

* Temperature must be measured by the lagging thermocouple attached to the part.

Notes:

- Parts may be loaded into a pre-heated oven or heated at 3°C (5.4°F)/minute to the initial cure temperature.
- Large components should be adequately supported to avoid distortion.

Cytec
Industrial Materials

3 of 4

MTM®57 series
PDS1075_07.13_Issue10a

Physical properties

Test	Sample conditions		Results
Cured resin density	1 hour at 120°C (248°F)	MTM57, MTM57B, MTM57-2, MTM57-3 & MTM57-3B	1.19 g/cm^3
		MTM57FR & MTM57FRB	1.38 g/cm^3
DMA E' onset Tg	12 hours at 80°C (176°F), dry 3 hours at 100°C (212°F), dry 1 hour at 120°C (248°F), dry		100°C (212°F) 120°C (248°F) 125°C (260°F)

Dynamic viscosity at 2°C (3.6°F)/minute

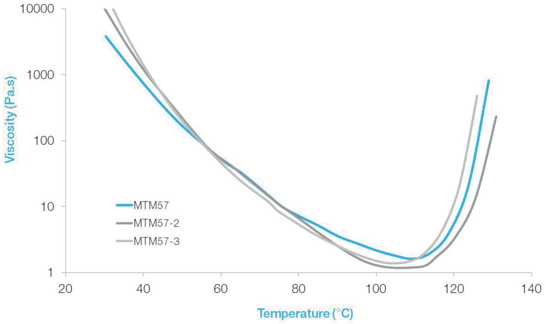

Availability

MTM57 series prepregs are available in a wide range of reinforcing fabrics and unidirectional tapes, including glass, carbon, aramid and hybrids. Materials can be supplied in fully and ZPREG partially-impregnated formats.

Note:
It is possible, when using combinations of the MTM57 series and certain carbon fibre reinforcements, for discolouration of the resin matrix to occur. Therefore, where the intended end application is for a cosmetic product, customers are advised to consult a Cytec sales representative for specific advice on fibre selection when placing an order for material.

Storage

Out life* at 21°C (70°F)	30 days
Storage at -18°C (0°F)	12 months from date of manufacture

*Out life refers to accumulated time out of the freezer before the part is cured.

Note:
The actual freezer storage life and out life are dependent on a number of factors, including; fibre type, format and application. For certain formats, it may be possible for the storage life and out life to be longer than stated. Please contact our technical support staff for advice.

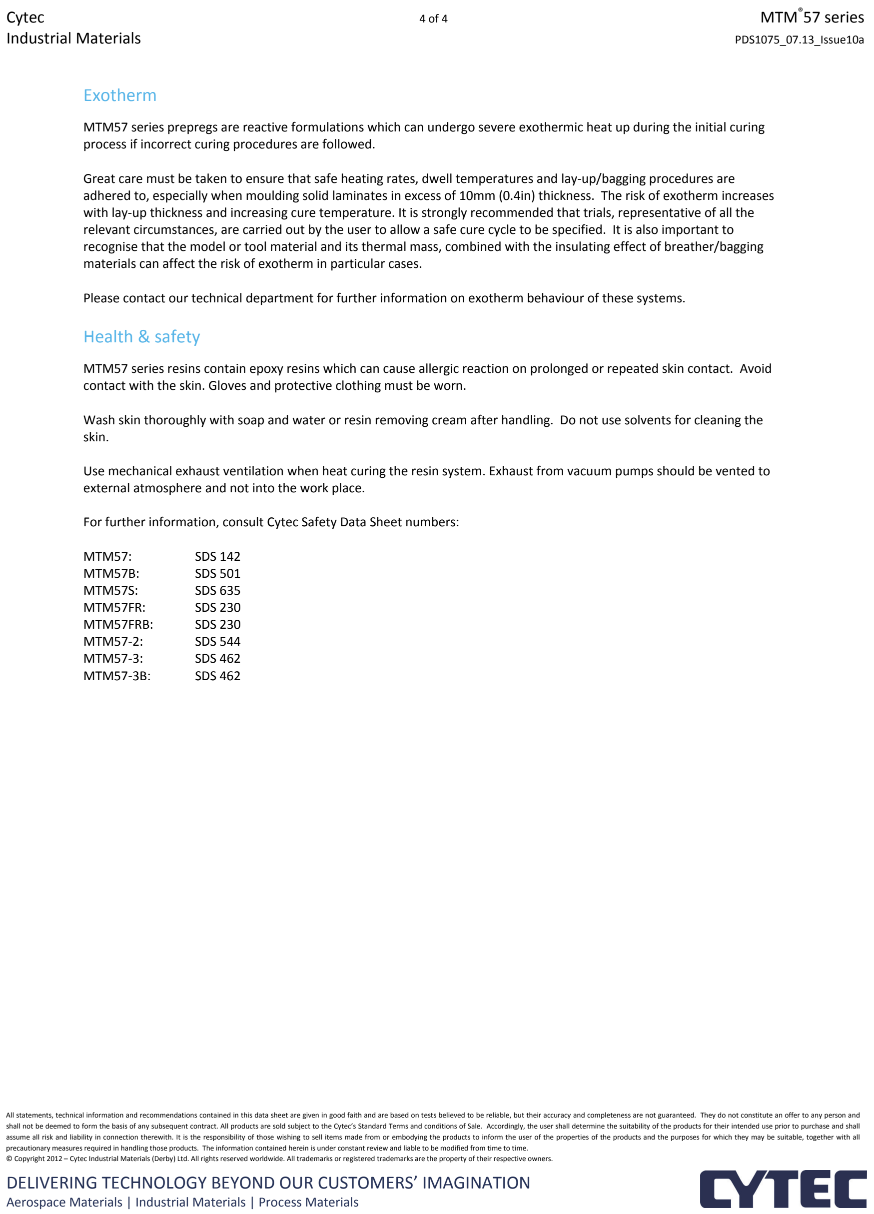

Exotherm

MTM57 series prepregs are reactive formulations which can undergo severe exothermic heat up during the initial curing process if incorrect curing procedures are followed.

Great care must be taken to ensure that safe heating rates, dwell temperatures and lay-up/bagging procedures are adhered to, especially when moulding solid laminates in excess of 10mm (0.4in) thickness. The risk of exotherm increases with lay-up thickness and increasing cure temperature. It is strongly recommended that trials, representative of all the relevant circumstances, are carried out by the user to allow a safe cure cycle to be specified. It is also important to recognise that the model or tool material and its thermal mass, combined with the insulating effect of breather/bagging materials can affect the risk of exotherm in particular cases.

Please contact our technical department for further information on exotherm behaviour of these systems.

Health & safety

MTM57 series resins contain epoxy resins which can cause allergic reaction on prolonged or repeated skin contact. Avoid contact with the skin. Gloves and protective clothing must be worn.

Wash skin thoroughly with soap and water or resin removing cream after handling. Do not use solvents for cleaning the skin.

Use mechanical exhaust ventilation when heat curing the resin system. Exhaust from vacuum pumps should be vented to external atmosphere and not into the work place.

For further information, consult Cytec Safety Data Sheet numbers:

MTM57:	SDS 142
MTM57B:	SDS 501
MTM57S:	SDS 635
MTM57FR:	SDS 230
MTM57FRB:	SDS 230
MTM57-2:	SDS 544
MTM57-3:	SDS 462
MTM57-3B:	SDS 462

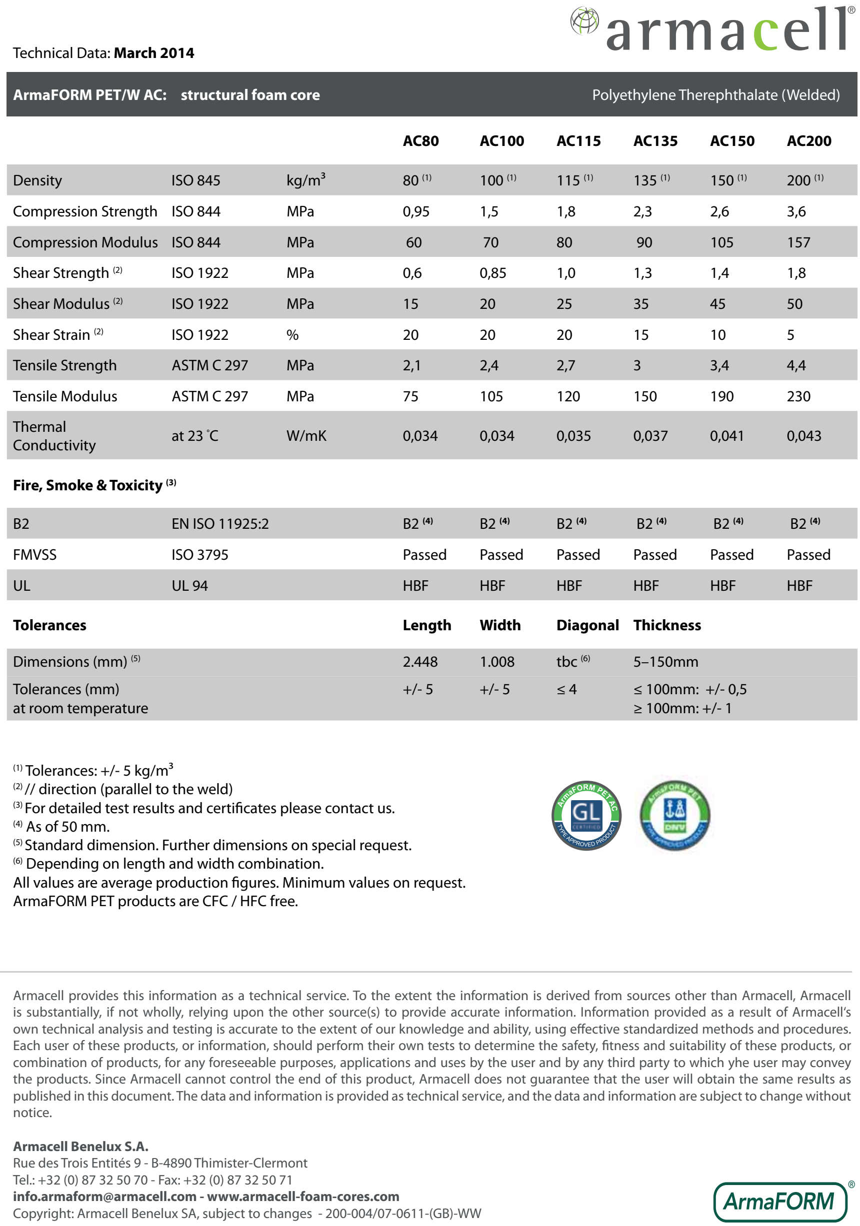

Technical Data: **March 2014**

ArmaFORM PET/W AC: structural foam core Polyethylene Therephthalate (Welded)

			AC80	AC100	AC115	AC135	AC150	AC200
Density	ISO 845	kg/m^3	80 (1)	100 (1)	115 (1)	135 (1)	150 (1)	200 (1)
Compression Strength	ISO 844	MPa	0,95	1,5	1,8	2,3	2,6	3,6
Compression Modulus	ISO 844	MPa	60	70	80	90	105	157
Shear Strength (2)	ISO 1922	MPa	0,6	0,85	1,0	1,3	1,4	1,8
Shear Modulus (2)	ISO 1922	MPa	15	20	25	35	45	50
Shear Strain (2)	ISO 1922	%	20	20	20	15	10	5
Tensile Strength	ASTM C 297	MPa	2,1	2,4	2,7	3	3,4	4,4
Tensile Modulus	ASTM C 297	MPa	75	105	120	150	190	230
Thermal Conductivity	at 23 °C	W/mK	0,034	0,034	0,035	0,037	0,041	0,043

Fire, Smoke & Toxicity (3)

B2	EN ISO 11925:2	B2 (4)	B2 (4)	B2 (4)	B2 (4)	B2 (4)	B2 (4)
FMVSS	ISO 3795	Passed	Passed	Passed	Passed	Passed	Passed
UL	UL 94	HBF	HBF	HBF	HBF	HBF	HBF

Tolerances	**Length**	**Width**	**Diagonal**	**Thickness**
Dimensions (mm) (5)	2.448	1.008	tbc (6)	5–150mm
Tolerances (mm) at room temperature	+/- 5	+/- 5	≤ 4	≤ 100mm: +/- 0,5 ≥ 100mm: +/- 1

(1) Tolerances: +/- 5 kg/m^3
(2) // direction (parallel to the weld)
(3) For detailed test results and certificates please contact us.
(4) As of 50 mm.
(5) Standard dimension. Further dimensions on special request.
(6) Depending on length and width combination.
All values are average production figures. Minimum values on request.
ArmaFORM PET products are CFC / HFC free.

Armacell Benelux S.A.
Rue des Trois Entités 9 - B-4890 Thimister-Clermont
Tel.: +32 (0) 87 32 50 70 - Fax: +32 (0) 87 32 50 71
info.armaform@armacell.com - www.armacell-foam-cores.com

D

National Spanish patent ES-2.386.269.B1

⑲ OFICINA ESPAÑOLA DE
PATENTES Y MARCAS

ESPAÑA

⑪ Número de publicación: **2 386 269**

㉑ Número de solicitud: 201200682

(51) Int. Cl.:

B60R 19/18 (2006.01)

⑫ PATENTE DE INVENCIÓN B1

㉒ Fecha de presentación: **21.06.2012** ㊸ Fecha de publicación de la solicitud: **14.08.2012** Fecha de la concesión: **01.07.2013** ㊺ Fecha de publicación de la concesión: **11.07.2013**	(73) Titular/es: **FUNDACIÓN PARA LA PROMOCIÓN DE LA INNOVACIÓN, INVEST. Y DESARROLLO TECNOLÓGICO EN LA INDUSTRIA DE AUTOMOCIÓN DE GALICIA (100.0%)** **Polígono Industrial a Granxa Calle A parcelas 249-250** **36400 O Porriño (Pontevedra) ES** (72) Inventor/es: **TIELAS MACÍA, Alberto;** **ÁLVAREZ DE FRANCISCO, Isabel;** **LEDO BAÑOBRE, Raquel;** **COSTAS PIÑÓ, Miguel y** **ROMERA RODRÍGUEZ, Luis Esteban**

(54) Título: **Sistema hibrído metal-composite para absorción de energía en choque**

(57) Resumen:
Sistema híbrido metal-composite para absorción de energía en choque que tiene forma de barra que tiene: una carcasa (1) metálica; un núcleo (2) de relleno de material composite configurado para absorber energía y para aumentar una absorción de energía de la carcasa (1) por medio de una deformación en un eje transversal (10) de la carcasa (1).

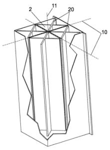

FIG. 1A

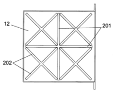

FIG. 1B

ES 2 386 269 B1

Aviso: Se puede realizar consulta prevista por el art. 37.3.8 LP.

SISTEMA HÍBRIDO METAL-COMPOSITE PARA ABSORCIÓN DE ENERGÍA EN CHOQUE

Campo de la invención

La presente invención se encuadra en el sector del transporte, más concretamente en lo relativo a piezas con componente estructural para absorción de energía en choque.

Antecedentes de la invención

Se define el habitáculo de seguridad de un vehículo como la zona interior de la carrocería o estructura del vehículo donde viajan los ocupantes. En caso de choque, este se daña pero debe deformarse lo menos posible. Para ello, la carrocería del vehículo contiene elementos cuya función es la de absorber energía en el choque y evitar que esta se transmita al habitáculo.

El concepto de absorción de energía es utilizado en numerosos campos y en particular en el "crash" de automóvil. Existen diversas soluciones de estructuras que permiten absorber energía, siendo una de ellas la absorción por deformación del material. Esta deformación puede ser elástica (con retorno) o plástica (permanente).

Se considera que el sistema de absorción de choque de un automóvil comprende las piezas del vehículo dedicadas a "consumir" la energía durante un choque, principalmente en un choque de alta velocidad. Así, el sistema de absorción delantero puede comprender una viga transversal que se apoya sobre los extremos de los largueros de la caja en blanco –traducción de la expresión inglesa BIW (Body In White) usada en todo el sector de automoción para referirse a la carrocería o estructura metálica del vehículo- a través de absorbedores de choque.

El principal objetivo de los constructores automovilísticos es alcanzar la relación óptima entre absorción de energía y peso del vehículo. En todos los vehículos podemos encontrar elementos que participan en la disipación de la energía recibida por efecto de un impacto. Estos elementos forman vías de esfuerzo, que dependiendo de la estrategia de los constructores toman una forma u otra (hay fabricantes que reparten el esfuerzo por la zona inferior del vehículo y por la zona media, otros derivan una parte a la zona alta,...). Algunos elementos comunes a todos los constructores son el parachoques, la viga frontal y los largueros, entre otros, mientras que otros tipos de refuerzos o absorbedores pueden estar o no presentes.

Los largueros son parte fundamental del comportamiento global del vehículo en un choque frontal. Los diversos fabricantes diseñan el sistema delantero del vehículo para conseguir una deformación controlada y asegurar la integridad del habitáculo. Algunos constructores usan diferentes tipos de acero de alto límite elástico en los componentes de la zona delantera para disipar energía mediante deformación y aceros de alta resistencia en la zona central para conseguir rigidez. Otros constructores, utilizan numerosas piezas de aluminio en lugar de acero, consiguiendo mayores deformaciones con menor peso.

Los diferentes fabricantes del sector automovilístico trabajan en diversas líneas de investigación para mejorar el comportamiento global del vehículo en caso de choque, intentando al mismo tiempo reducir el peso. En este sentido existen un número considerable de patentes con el objetivo de conseguir una mayor absorción de energía, por ejemplo ES2295533T3, ES2334259T3, ES2325347A1 y ES2331190T3, ES2251670T3 entre muchas otras.

Todas las soluciones actuales para largueros tienen un punto en común, y es que están basadas en estructuras metálicas, ya sea en acero o aluminio. La presente invención aporta como novedad el hecho de desarrollar una estructura híbrida metal composite, de modo que se saque provecho de las mejores características de cada material.

Descripción de la invención

La invención tiene por objeto un sistema de absorción de energía de impacto en choque que puede ser un choque delantero de automóvil, destinado a ser montado en el lugar de los largueros tradicionales. La absorción de la energía se produce por la deformación de los materiales que trabajan a compresión y rotura.

De este modo, se conseguirá una absorción de energía mejorada respecto a la actual, permitiendo aligerar el resto de la estructura del automóvil sin perjuicio de la seguridad de los ocupantes.

El sistema comprende por una parte metálica, es decir un larguero similar a los actuales (perfil metálico de sección cuadrada) y que forma un cuerpo hueco y un núcleo de material composite. El material compuesto desempeña la función de núcleo absorbedor de energía, mientras que la parte metálica sirve para mantener la estabilidad de la estructura del vehículo y seguir desempeñando su función como vía de esfuerzo principal. Una de las características es que el núcleo de material composite sea un componente en si mismo, de modo que pueda ser introducido fácilmente (adaptando la geometría) sin introducir modificaciones sustanciales en el proceso de fabricación del vehículo. Lo que se consigue con el sistema híbrido es, por un lado, mejorar la absorción de energía debido al trabajo realizado por el material composite, y por otro lado, se provoca que el acero trabaje de modo diferente a como lo hace en solitario, ya que el hecho de tener un núcleo provoca que también se deforme en el eje transversal y no solo en el longitudinal (a mayor deformación, mayor absorción de energía).

El núcleo interno absorbedor de energía puede realizarse de diversos materiales, entre otros:

- Termoplástico.
- Resina epoxi + fibra de carbono.
- Espumas estructurales (PET, PVC, corcho).

La unión entre el tubo metálico y el núcleo puede realizarse mediante adhesivos estructurales o por encastre.

Breve descripción de los dibujos

A continuación se pasa a describir de manera muy breve una serie de dibujos que ayudan a comprender mejor la invención y que se relacionan expresamente con una realización de dicha invención que se presenta como un ejemplo no limitativo de ésta.

La Figura 1A muestra una perspectiva con un corte para mostrar el interior y la Figura 1B muestra una planta de un sistema de la invención con láminas o placas planas que forman una celosía. Esta geometría puede utilizarse cuando el material del núcleo es termoplástico.

La Figura 2A muestra una perspectiva con un corte para mostrar el interior de un sistema de la invención con láminas o placas onduladas. Esta geometría puede utilizarse cuando el material del núcleo es resina epoxi y fibra de carbono.

La Figura 3 muestra una perspectiva con un corte para mostrar el interior de un sistema de la invención con planchas transversales al eje longitudinal de la barra. Esta geometría puede utilizarse cuando el material del núcleo es espuma.

La Figura 4 muestra los resultados obtenidos de un ensayo de compresión realizado en una máquina universal de ensayos con una célula de carga de 100 kN. La gráfica representa el comportamiento de un sistema similar al actual, solamente de acero (gráfica de trazo grueso) y un sistema híbrido acero-termoplástico (las gráficas de trazo fino corresponden a sistemas híbridos con dos materiales termoplásticos diferentes).

La Figura 5 muestra la colocación de cinco capas con una configuración -45/45/0/90/ud/0/90/-45/45 para formar la placa/lámina ondulada mostrada en la parte inferior de dicha figura. La denominación ud significa unidireccional.

Dicha gráfica representa la fuerza aplicada (Newton), frente al desplazamiento (mm) para un ensayo de compresión en estático. El área comprendida debajo de cada gráfica corresponde a la energía absorbida y claramente los sistemas híbridos consiguen una mayor absorción que el sistema de metal. El comportamiento en estático es extrapolable al comportamiento en dinámico, ya que la capacidad de absorción de energía (resistencia) de los materiales utilizados, aumenta con la velocidad de impacto, siendo esto una característica intrínseca del material.

<u>Descripción detallada de un modo de realización</u>

Una realización de la invención se refiere a un sistema híbrido metal-composite para absorción de energía en choque que tiene forma de barra que comprende:

1a) una carcasa (1) metálica;

1b) un núcleo (2) de relleno de material composite configurado para absorber energía y para aumentar una absorción de energía de la carcasa (1) por medio de una deformación en un eje transversal (10) de la carcasa (1).

Conforme a otras características de la invención:

2. El núcleo (2) comprende una pluralidad de láminas (20) orientadas según un eje longitudinal (11) de la carcasa (1).

3. Las láminas (20) son planas. Las láminas o placas (20) pueden ser rectangulares. La estructura nervada interior puede construirse mediante encastrado de placas termoplásticas realizadas mediante proceso de inyección. Conforme a una realización de la invención, el sistema comprende una pluralidad de láminas/placas primarias (201), las que definen unas cavidades (12) entre las láminas/placas primarias (201) y la carcasa (1), y una pluralidad de láminas/placas secundarias (202), las que ocupan las cavidades. Las láminas/placas primarias (201) y las láminas/placas secundarias (202) pueden tener un espesor de 2mm. Esta geometría puede construirse posicionando y encastrando las placas por facilidad de construcción, pero también puede inyectarse el componente como geometría única.

4. Las láminas (20) son onduladas. Las láminas o placas (20) pueden ser fabricadas por moldeo en prensa de placas epoxi Carbono en base a un impregnado unidireccional o bidireccional. Las láminas o placas (20) pueden ser posicionadas en el interior de la carcasa (1) mediante un posicionador.

5. Las láminas (20) son paralelas. La disposición de las láminas (20) en paralelo puede ser a su vez en concordancia, cuando la distancia entre ondulaciones se mantiene constante, o en contraposición, cuando la distancia entre ondulaciones varía. La figura 2A muestra una disposición en contraposición donde valles y picos de las ondulaciones son enfrentados, obteniendo una distancia mínima entre una primera lámina y una segunda lámina, y una distancia máxima entre una segunda lámina y una tercera lámina.

6. Las láminas (20) tienen un espesor comprendido entre 1,8 y 2mm.

7. Las láminas (20) tienen una configuración de capas 0/90/+45/-45/0/-45/+45/90/0. La figura 5 muestra una configuración de capas -45/45/0/90/ud/0/90/-45/45. En caso de usar tejido bidireccional, las capas son apiladas girada cada una 45º respecto a la anterior y usando típicamente 5 capas. En caso de tejido unidireccional, la segunda capa se posiciona girada 90º respecto a la primera (para simular lo que sería un tejido bidireccional), la tercera sería posicionada girada 45º y así sucesivamente, obteniendo un total de 9 capas.

8. El núcleo (2) comprende una pluralidad de planchas (21) transversales al eje longitudinal (11) de la carcasa (1).

9. Las láminas (20) tienen un espesor comprendido entre 10 y 14mm. En una realización de la invención, el espesor es 12mm.

10. No hay unión entre láminas (20) y la carcasa (1).

11. No hay unión entre las láminas (20).

12. El núcleo interno (2) comprende una composición seleccionada entre: termoplástico; resina epoxi y fibra de carbono; espuma estructural.

REIVINDICACIONES

1. Sistema híbrido metal-composite para absorción de energía en choque que tiene forma de barra **caracterizado por que** comprende:

1a) una carcasa (1) metálica;

1b) un núcleo (2) de relleno de material composite configurado para absorber energía y para aumentar una absorción de energía de la carcasa (1) por medio de una deformación en un eje transversal (10) de la carcasa (1).

2. Sistema híbrido metal-composite para absorción de energía en choque según la reivindicación 1 **caracterizado por que** el núcleo (2) comprende una pluralidad de láminas (20) orientadas según un eje longitudinal (11) de la carcasa (1).

3. Sistema híbrido metal-composite para absorción de energía en choque según la reivindicación 2 **caracterizado por que** las láminas (20) son planas.

4. Sistema híbrido metal-composite para absorción de energía en choque según la reivindicación 2 **caracterizado por que** las láminas (20) son onduladas.

5. Sistema híbrido metal-composite para absorción de energía en choque según cualquiera de las reivindicaciones 3-4 **caracterizado por que** las láminas (20) son paralelas.

6. Sistema híbrido metal-composite para absorción de energía en choque según cualquiera de las reivindicaciones 4-5 **caracterizado por que** las láminas (20) tienen un espesor comprendido entre 1,8 y 2mm.

7. Sistema híbrido metal-composite para absorción de energía en choque según cualquiera de las reivindicaciones 4-6 **caracterizado por que** las láminas (20) tienen una configuración de capas 0/90/+45/-45/0/-45/+45/90/0.

8. Sistema híbrido metal-composite para absorción de energía en choque según la reivindicación 1 **caracterizado por que** el núcleo (2) comprende una pluralidad de planchas (21) transversales al eje longitudinal (11) de la carcasa (1).

9. Sistema híbrido metal-composite para absorción de energía en choque según la reivindicación 8 **caracterizado por que** las láminas (20) tienen un espesor comprendido entre 10 y 14mm.

10. Sistema híbrido metal-composite para absorción de energía en choque según cualquiera de las reivindicaciones 1-9 **caracterizado por que** no hay unión entre láminas (20) y la carcasa (1).

11. Sistema híbrido metal-composite para absorción de energía en choque según cualquiera de las reivindicaciones 1-10 **caracterizado por que** no hay unión entre las láminas (20).

12. Sistema híbrido metal-composite para absorción de energía en choque según cualquiera de las reivindicaciones 1-11 **caracterizado por que** el núcleo interno (2) comprende una composición seleccionada entre: termoplástico; resina epoxi y fibra de carbono; espuma estructural.

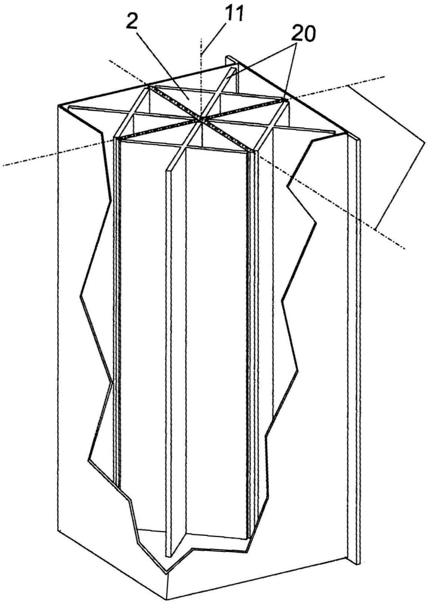

FIG. 1A

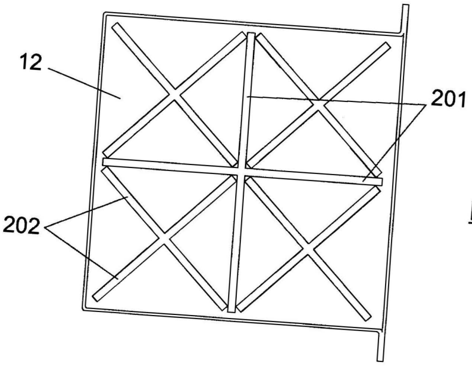

FIG. 1B

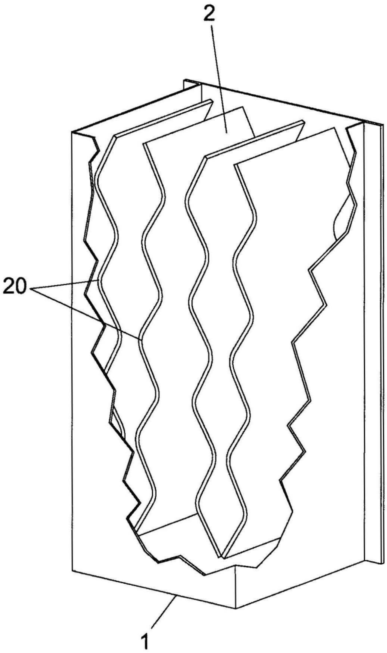

FIG. 2

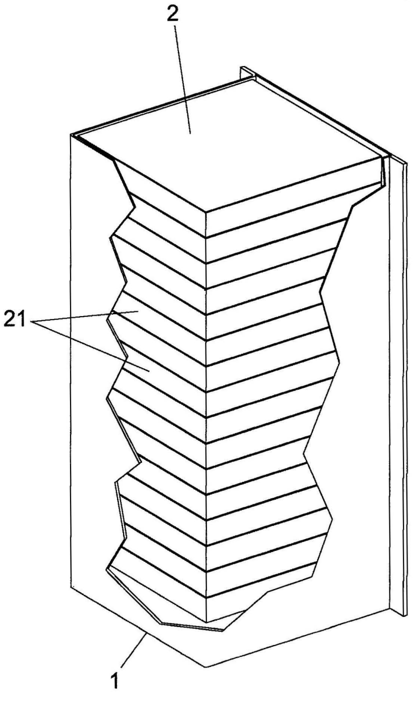

FIG. 3

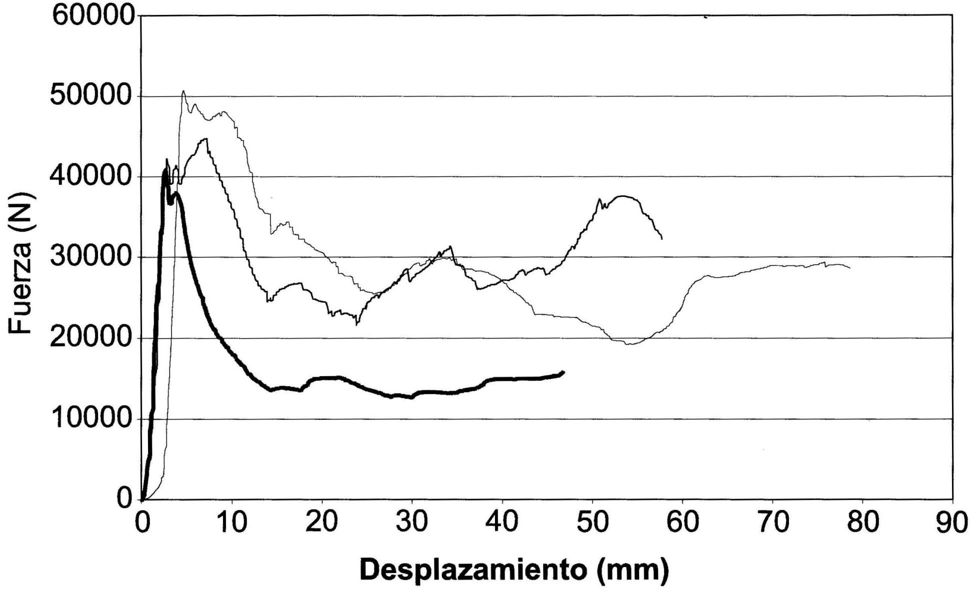
Fuerza (N)
60000
50000
40000
30000
20000
10000
0
0
10
20
30
40
50
60
70
80
90
Desplazamiento (mm)

FIG. 4

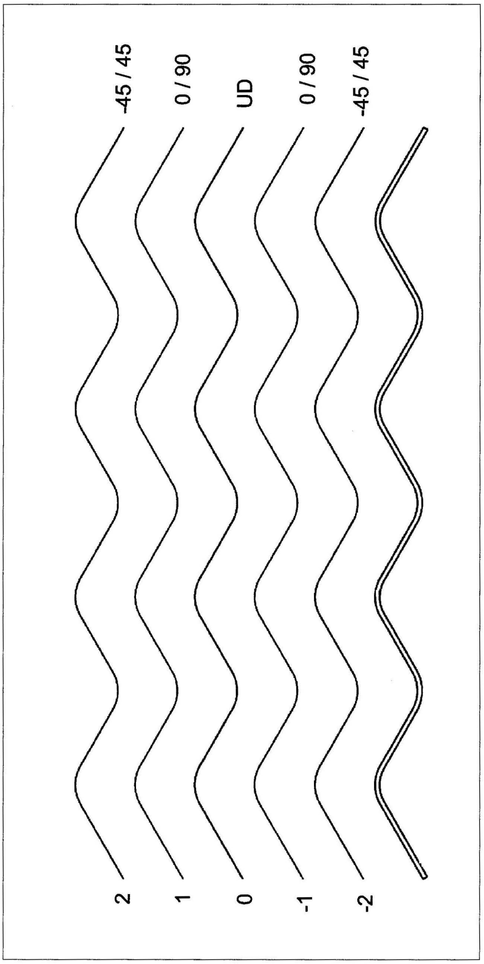

FIG. 5

OFICINA ESPAÑOLA
DE PATENTES Y MARCAS

ESPAÑA

㉑ N.º solicitud: 201200682

㉒ Fecha de presentación de la solicitud: 21.06.2012

㉜ Fecha de prioridad:

INFORME SOBRE EL ESTADO DE LA TECNICA

(51) **Int. Cl. :** ***B60R19/18*** (2006.01)

DOCUMENTOS RELEVANTES

Categoría	(56) **Documentos citados**	**Reivindicaciones afectadas**
X	US 4961603 A (CARPENTER RONALD A) 09/10/1990, resumen; columna 3, línea 31 - columna 5, línea 30; figuras.	1
Y		2-6,8-9,12
Y	US 2005287371 A1 (CHAUDHARI TANSEN D ET AL.) 29/12/2005, resumen; párrafos [0004 - 0024]; reivindicaciones 1-33; figuras.	2-6,8-9,12
A	US 6511109 B1 (SCHULTZ JOHN P ET AL.) 28/01/2003, columna 2, línea 40 - columna 4, línea 26; figuras.	1
A	US 2008001416 A1 (CHAUDHARI TANSEN DHANANJAY ET AL.) 03/01/2008, resumen; párrafo [0020]; figuras.	1
A	US 5746419 A (MCFADDEN JAMES ROBERT ET AL.) 05/05/1998, todo el documento.	2

Categoría de los documentos citados

X: de particular relevancia
Y: de particular relevancia combinado con otro/s de la misma categoría
A: refleja el estado de la técnica

O: referido a divulgación no escrita
P: publicado entre la fecha de prioridad y la de presentación de la solicitud
E: documento anterior, pero publicado después de la fecha de presentación de la solicitud

El presente informe ha sido realizado

☒ para todas las reivindicaciones ☐ para las reivindicaciones nº:

Fecha de realización del informe	**Examinador**	**Página**
01.08.2012	**O. G. Rucián Castellanos**	1/4

INFORME DEL ESTADO DE LA TÉCNICA

Nº de solicitud: 201200682

Documentación mínima buscada (sistema de clasificación seguido de los símbolos de clasificación)

B60R

Bases de datos electrónicas consultadas durante la búsqueda (nombre de la base de datos y, si es posible, términos de búsqueda utilizados)

INVENES, EPODOC

OPINIÓN ESCRITA

Nº de solicitud: 201200682

Fecha de Realización de la Opinión Escrita: 01.08.2012

Declaración

Novedad (Art. 6.1 LP 11/1986)	Reivindicaciones	1-12	**SI**
	Reivindicaciones		**NO**
Actividad inventiva (Art. 8.1 LP11/1986)	Reivindicaciones	7,10,11	**SI**
	Reivindicaciones	1-6,8-9,12	**NO**

Se considera que la solicitud cumple con el requisito de aplicación industrial. Este requisito fue evaluado durante la fase de examen formal y técnico de la solicitud (Artículo 31.2 Ley 11/1986).

Base de la Opinión.-

La presente opinión se ha realizado sobre la base de la solicitud de patente tal y como se publica.

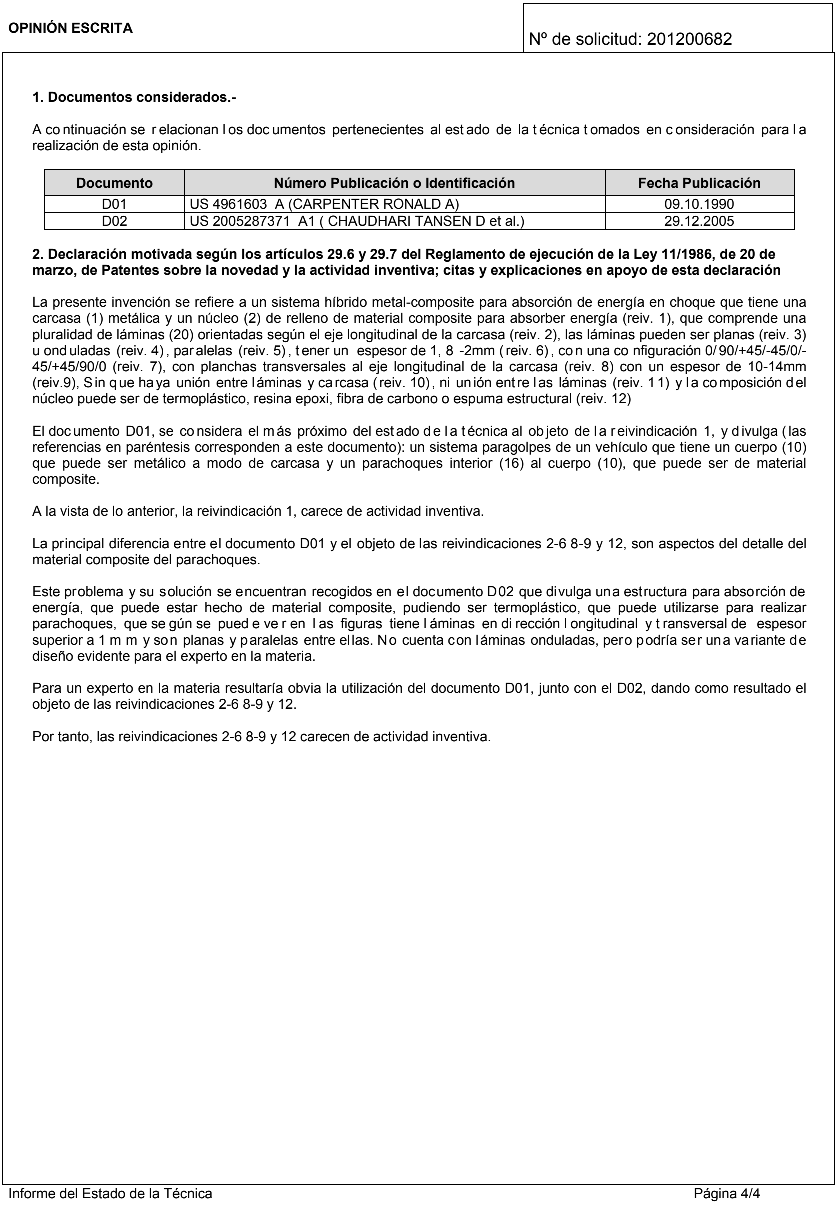

OPINIÓN ESCRITA

Nº de solicitud: 201200682

1. Documentos considerados.-

A continuación se relacionan los documentos pertenecientes al estado de la técnica tomados en consideración para la realización de esta opinión.

Documento	Número Publicación o Identificación	Fecha Publicación
D01	US 4961603 A (CARPENTER RONALD A)	09.10.1990
D02	US 2005287371 A1 (CHAUDHARI TANSEN D et al.)	29.12.2005

2. Declaración motivada según los artículos 29.6 y 29.7 del Reglamento de ejecución de la Ley 11/1986, de 20 de marzo, de Patentes sobre la novedad y la actividad inventiva; citas y explicaciones en apoyo de esta declaración

La presente invención se refiere a un sistema híbrido metal-composite para absorción de energía en choque que tiene una carcasa (1) metálica y un núcleo (2) de relleno de material composite para absorber energía (reiv. 1), que comprende una pluralidad de láminas (20) orientadas según el eje longitudinal de la carcasa (reiv. 2), las láminas pueden ser planas (reiv. 3) u onduladas (reiv. 4), paralelas (reiv. 5), tener un espesor de 1,8-2mm (reiv. 6), con una configuración 0/90/+45/-45/0/-45/+45/90/0 (reiv. 7), con planchas transversales al eje longitudinal de la carcasa (reiv. 8) con un espesor de 10-14mm (reiv.9), Sin que haya unión entre láminas y carcasa (reiv. 10), ni unión entre las láminas (reiv. 11) y la composición del núcleo puede ser de termoplástico, resina epoxi, fibra de carbono o espuma estructural (reiv. 12)

El documento D01, se considera el más próximo del estado de la técnica al objeto de la reivindicación 1, y divulga (las referencias en paréntesis corresponden a este documento): un sistema paragolpes de un vehículo que tiene un cuerpo (10) que puede ser metálico a modo de carcasa y un parachoques interior (16) al cuerpo (10), que puede ser de material composite.

A la vista de lo anterior, la reivindicación 1, carece de actividad inventiva.

La principal diferencia entre el documento D01 y el objeto de las reivindicaciones 2-6 8-9 y 12, son aspectos del detalle del material composite del parachoques.

Este problema y su solución se encuentran recogidos en el documento D02 que divulga una estructura para absorción de energía, que puede estar hecho de material composite, pudiendo ser termoplástico, que puede utilizarse para realizar parachoques, que según se puede ver en las figuras tiene láminas en dirección longitudinal y transversal de espesor superior a 1 mm y son planas y paralelas entre ellas. No cuenta con láminas onduladas, pero podría ser una variante de diseño evidente para el experto en la materia.

Para un experto en la materia resultaría obvia la utilización del documento D01, junto con el D02, dando como resultado el objeto de las reivindicaciones 2-6 8-9 y 12.

Por tanto, las reivindicaciones 2-6 8-9 y 12 carecen de actividad inventiva.

E

Extended summary in Spanish

In accordance with the University regulations approved in 2012, an extended summary of this thesis is presented in Spanish.

E.1 Introducción y objetivos

Esta tesis se enmarca en el campo de investigación del comportamiento de estructuras de absorción de energía frente a cargas de impacto. En particular, los elementos estructurales investigados tienen unas dimensiones que los hacen adecuados para su uso en vehículos de carretera, aunque los resultados son aplicables a cualquier otro tipo de vehículo o sistema estructural.

En este caso, se estudiaron componentes cuya función es absorber parte de la energía cinética en caso de colisión frontal, por lo que se ubican en la parte delantera del vehículo. Tradicionalmente estos elementos consisten en tubos de acero o, más recientemente, aluminio. En caso de que una colisión sea considerablemente severa, estos tubos se aplastan de forma progresiva y controlada en su dirección longitudinal, disipando energía por fenómenos plásticos en los metales. Sin embargo, en el presente estudio se han considerado varias combinaciones de materiales de distinta naturaleza para su uso con estos fines. En particular, se han estudiado tubos metálicos reforzados internamente con estructuras de fibra de vidrio o carbono, una espuma en base a tereftalato de polietileno o un aglomerado de corcho. Estos diseños se han ensayado experimental y computacionalmente, y se han sometido a procesos de optimización estructural no sólo para obtener los diseños óptimos, sino también para profundizar en el comportamiento de los distintos materiales y sus interacciones.

Esta tesis contribuye, por lo tanto, con el análisis del comportamiento frente a impacto de estructuras novedosas, incluyendo modelos validados de elementos finitos, una metodología de optimización adecuada y el estudio de la interacción entre algunos materiales destacados.

E.2 Metodología y resultados

El análisis y el diseño de estructuras de absorción de impactos es, sin duda, uno de los problemas más desafiantes de ingeniería. Esto es debido a la presencia simultánea de varios procesos de naturaleza compleja y difícil simulación, como son los fenómenos de plasticidad y plegado de metales a distintas velocidades de solicitación, la fractura en partes metálicas o en materiales compuestos y el aplastamiento de materiales celulares como el corcho o las espumas sintéticas. Desde el punto de vista computacional, las dificultades se multiplican dada la magnitud de las deformaciones que experimentan estos componentes y la velocidad a la que éstas suceden, así como la dificultad de simular adecuadamente el comportamiento de cada material, prestando especial atención a aquellas características o propiedades más relevantes para el problema y planteando hipótesis o suposiciones en aquellas de menor importancia. Por todo esto, se han utilizado unas metodologías muy específicas tanto para el análisis experimental y computacional de los componentes como para su optimización.

En primer lugar se ha analizado y valorado el comportamiento frente a impacto de tubos metálicos de pared delgada rellenos de diferentes materiales: placas de materiales compuestos (fibra de vidrio o carbono), bloques de espuma sintética o bloques de aglomerado de corcho. Este trabajo se realizó en colaboración con el Centro Tecnolóxico de Automoción de Galicia (CTAG) en el marco del proyecto “Hybrid Body”, dando como resultado artículos de investigación, comunicaciones a congresos internacionales y una patente. Este estudio consistió en ensayos experimentales cuasi-estáticos y a impacto, y simulaciones computacionales del comportamiento de los diferentes diseños. Los componentes que incorporaron placas de fibra de vidrio mostraron un mejor comportamiento que los demás atendiendo a métricas comúnmente utilizadas en impacto estructural, por ello se sometieron a un estudio paramétrico para determinar mejor su comportamiento variando los espesores de sus elementos. Adicionalmente, se estudió el efecto de la distribución de los puntos de soldadura en el comportamiento frente a impacto de todas las combinaciones de materiales anteriormente descritas, dando lugar a algunas reglas de diseño útiles.

A continuación se procedió a optimizar la respuesta de los componentes consistentes en un tubo de acero reforzado internamente con una estructura de termoplástico de fibra de vidrio. Para ello se seleccionaron variables de diseño que se consideraron relevantes: espesores de las distintas partes y alguna modificación geométrica de la sección. La aplicación de algoritmos de optimización a este tipo de problemas presenta dos grandes dificultades: el coste computacional de cada evaluación de las funciones objetivo y su no-linealidad. Además, las respuestas están afectadas hasta cierto punto por el ruido numérico derivado de las propias simulaciones. Por todo ello se decidió emplear una metodología de optimización apoyada en modelos subrogados, que reemplacen las evaluaciones de los modelos de elementos finitos por evaluaciones de aproximaciones hechas mediante diferentes modelos de más fácil manejo. Estos modelos deben ser suficientemente flexibles para representar con suficiente grado de detalle las no-linealidades de las funciones, además de suavizar en cierta medida el ruido numérico del modelo de elementos finitos. Con estos objetivos en mente, se evaluaron metamodelos de diferente naturaleza: polinómicos, procesos Gaussianos (o kriging) y regresión de splines adaptativas multivariadas (MARS), siendo los últimos los que demostraron una mayor eficacia. Los modelos fueron ajustados a muestreos representativos paralelizados del modelo de elementos finitos, tomando como respuestas aquellas funciones objetivo seleccionadas para la optimización. En relación a esta optimización, dos estrategias de diferente naturaleza fueron evaluadas: un método de gradiente conjugado y un algoritmo genético, ambos adaptados para el caso de optimizaciones multiobjetivo. Si bien el método de gradiente conjugado es el único de los dos cuyas soluciones son óptimos en el sentido estricto, el algoritmo genético fue capaz de llegar a áreas de los modelos subrogados que no fueron exploradas por el anterior, obteniendo algunos óptimos adicionales. Estos diseños óptimos fueron representados en frentes de Pareto, que permiten escoger el diseño óptimo de acuerdo a las necesidades o criterios requeridos. Los resultados del trabajo descrito en este párrafo también fueron convenientemente publicados en un artículo de revista de gran impacto.

En relación al diseño optimizado, consistente en placas de termoplástico de fibra de vidrio colocadas en el interior de un tubo metálico, se observó que la respuesta frente a impactos se podría mejorar considerablemente con algún sistema de confinamiento del material compuesto. Esto evitaría que fragmentos de termoplástico considerablemente grandes que aún podrían degradarse más se desprendiesen de la estructura, desaprovechando su contribución. Para este fin se consideró que la espuma de tereftalato de polietileno estudiada anteriormente podría contribuir de forma notable. Por tanto, se planteó un nuevo diseño en el que las placas estuvieran embebidas en esta espuma y se sustituyó el tubo exterior de acero por uno de aluminio AA5754-H111, cambiando también su geometría a una hexagonal, de mayor eficiencia. Sin embargo, aparecieron graves problemas con el método de unión de las dos chapas de aluminio para formar el tubo dada la dificultad para soldar correctamente este material. La solución adoptada, una doble línea de soldadura láser, generó debilidades en la zona afectada por el calor del proceso que propiciaron que los componentes se abriesen al ser aplastados debido a la presión interior ejercida por los refuerzos de fibra y espuma. Como alternativa a esta solución, se optó por un tubo circular extruido en aleación AA6063-T5, de espesor algo mayor al anterior. Esta solución funcionó adecuadamente al carecer de zonas débiles, y los refuerzos interiores demostraron mejorar la respuesta frente a impactos del tubo. Además, se prestó especial atención a la interacción entre los distintos materiales. De particular influencia en los resultados fue la interacción entre las placas de fibra y la espuma, cuya contribución a los niveles de absorción de energía fue muy considerable. Este fenómeno se cuantificó por medio de una modificación de la fórmula de Hanssen para tubos de aluminio rellenos de espuma de aluminio, de forma que ahora considerase la presencia de dos refuerzos simultáneos que interactúan entre sí. El trabajo descrito en este párrafo y parte del siguiente se realizó durante una estancia de investigación de seis meses en el Structural Impact Laboratory (SIMLab) de la NTNU en Trondheim, Noruega, bajo la supervisión del profesor Magnus Langseth y el investigador postdoctoral David Morin. De lo descrito en este párrafo resultó, además, otro artículo de investigación publicado en una revista de gran impacto.

Por último, se procedió a optimizar el diseño anterior utilizando el modelo subrogado y el algoritmo de optimización seleccionados con anterioridad. Se realizó una campaña de ensayos de materiales con el objetivo de caracterizar correctamente aquéllas propiedades de cada material más relevantes para este tipo de aplicaciones. En particular se realizaron ensayos de tracción a distintas velocidades y estados triaxiales, ensayos de compresión uniaxial cuasi-estáticos y en torre de caída y ensayos de compresión confinada (ensayos triaxiales). Con fines comparativos, se optimizó también un segundo modelo en el que el tubo exterior de aluminio se sustituyó por uno de acero de características similares. En esta optimización, además de los espesores de la extrusión metálica y las placas de termoplástico, se consideró como variable de diseño la densidad de la espuma. Esta densidad está directamente relacionada con su resistencia a compresión, de acuerdo con los datos proporcionados por el fabricante. De la optimización se desprende que este tipo de refuerzos es particularmente útil para estructuras de acero, en especial, si la densidad de la espuma se incrementa en relación con lo anterior. Se obtuvieron frentes de Pareto para ambos diseños y diferentes funciones objetivo y se analizó la variación de las variables de diseño a lo largo de los frentes, lo que puso de manifiesto la eficiencia y utilidad de esta metodología.

E.3 Conclusiones

Del trabajo anterior se pueden extraer las siguientes conclusiones:

En el estudio de componentes metálicos reforzados con fibra de carbono o vidrio, espuma de tereftalato de polietileno o aglomerado de corcho se observó que:

- Se desarrollaron diseños innovadores para la absorción de energía de impacto en colaboración con CTAG, utilizando materiales y geometrías que no habían sido investigadas con anterioridad. Los componentes se ensayaron en condiciones cuasi-estáticas y de impacto, y se desarrollaron y validaron modelos de elementos finitos que reproducen de forma aceptable los resultados experimentales.
- El refuerzo de tubos de acero con una estructura de termoplástico de fibra de vidrio incrementó su absorción específica de energía más que los demás materiales, seguida de cerca por un relleno de espuma sintética. Estos resultados fueron demostrados en ensayos experimentales y numéricos.
- El comportamiento de los diferentes materiales fue reproducido por los modelos de elementos finitos con una precisión razonable. El hecho de considerar deformaciones residuales no mostró una gran repercusión en los resultados, sin embargo, las imperfecciones iniciales sí fueron necesarias para reproducir los mismos modos de colapso observados en los ensayos experimentales, además de que permitieron reducir el pico inicial de carga para coincidir con el experimental.
- El aglomerado de corcho analizado en esta tesis produjo un incremento relativamente bajo en los niveles de absorción específica de energía comparado con el tubo de acero vacío. Además, su comportamiento elástico recuperable sugirió que este producto se debería usar con precaución en estructuras dedicadas a la absorción de energía, por ejemplo, en áreas donde este hecho no sea relevante.
- A la vista de los resultados del Capítulo 3, la separación entre puntos de soldadura equidistantes debería ser menor de un 16.7 % de la longitud del tubo para una absorción de energía eficiente, garantizando que la parte de acero se pliega progresivamente. En caso contrario, la longitud de plegado se incrementa y la estabilidad del aplastamiento axial se ve comprometida.
- Las secciones rellenas de espuma fueron menos sensibles al espaciado entre puntos de soldadura debido al efecto de interacción o confinamiento entre el relleno y el tubo. Para que esto suceda, la espuma debe estar en contacto con las paredes metálicas durante el aplastamiento.

La optimización del tubo reforzado con termoplástico de fibra de vidrio indicó que:

- Después de aplicar diferentes modelos subrogados, puede concluirse que las funciones de absorción específica de energía y relación de carga pudieron ser emuladas razonablemente bien con un conjunto de splines adaptativas multivariadas (MARS). Esto permitió una ejecución adecuada de los algoritmos de optimización en un problema con cinco variables. El número máximo de funciones base de MARS se determinó con un análisis de la bondad de los metamodelos.

- Los resultados del modelo de elementos finitos mostraron sensibilidad al esquema de paralelización empleado en la fase de muestreo. La división del modelo en un número diferente de submodelos produjo diferencias de entre un 10 y un 20 % en la energía absorbida por el mismo componente. Se encontró un equilibrio entre la calidad de los resultados y el tiempo de computación para una división en cuatro subdominios.

- La absorción específica de energía y la relación de carga del diseño original estudiado en el Capítulo 3 se mejoró casi un 50 % con los valores óptimos de las variables de diseño. El decalaje entre la parte superior del tubo de acero y el refuerzo fue esencial para conseguir una reducción de las relaciones de carga.

- Se compararon un algoritmo genético multiobjetivo y el método de gradiente conjugado de Fletcher-Reeves. La alternativa metaheurística fue capaz de encontrar pares óptimos de las funciones objetivo en zonas del metamodelo que no fueron exploradas por el algoritmo de Fletcher-Reeves.

A partir de la investigación experimental del comportamiento frente a impactos de perfiles de aluminio reforzados con espuma sintética y placas de termoplástico simultáneamente se aprendió que:

- Se realizó un análisis previo sobre secciones hexagonales de doble sombrero hechas en aleación AA5754-H111 con un espesor de 1 mm unidas por un doble cordón de soldadura láser. Esta solución no fue lo suficientemente resistente para soportar las presiones internas de los refuerzos debido a la debilidad de las zonas afectadas por el calor. Una extrusión en aleación AA6063-T5 con un espesor superior fue capaz de soportar estas presiones internas sin fracturas relevantes.

- La extrusión de aluminio en aleación AA6063-T5 mostró una ductilidad suficiente para permitir el colapso progresivo de componentes vacíos y rellenos sin fracturas relevantes. Sólo se observaron daños menores en la transición del modo de concertina al de diamante de tres puntas, en el tubo vacío.

- La energía absorbida por los diseños reforzados únicamente con espuma sintética o con termoplástico no fue significativamente mayor que la de la sección vacía, dadas las excelentes propiedades de esta aleación; pero se observó una mejora muy notable cuando los tres materiales se combinaron en un único diseño. Esto se explica por el hecho de que la espuma confina las placas de termoplástico, mejorando su aprovechamiento.
- La energía absorbida y la relación de carga del componente relleno con espuma de tereftalato de polietileno y fibra de vidrio se mejoró entorno a un 100 % comparado con la de un tubo vacío. Sin embargo, la absorción específica fue sensiblemente más baja.
- Una gran parte del incremento en la energía absorbida se debió a la fuerte interacción entre las placas de termoplástico y la espuma. La formulación de Hanssen se adaptó para un tubo con dos rellenos simultáneos, de forma que se tenga en cuenta este efecto. Esto demostró que la espuma de tereftalato de polietileno puede ser utilizada como un sistema de confinamiento de las placas, aprovechando al máximo su degradación.

Por último, la optimización multiobjetivo del componente reforzado con espuma y fibra mostró que:

- El comportamiento del componente fue fielmente representado por un modelo de elementos finitos calibrado con las ecuaciones constitutivas adecuadas para cada uno de los tres materiales, gracias a la campaña de ensayos de materiales presentada en el Capítulo 5 y el Apéndice A.
- La masa del diseño y su absorción de energía, absorción específica de energía y pico inicial de fuerza fueron aproximadas por un modelo de MARS con una excelente correlación con los resultados del modelo de elementos finitos. No se consideró como función objetivo la relación de carga debido a las imprecisiones de todos los metamodelos estudiados. Un muestreo más exhaustivo permitió una mejora de la precisión de los metamodelos, lo que condujo a frentes de Pareto más suaves y más continuos.
- La paralelización en bucle, que no conlleva divisiones del modelo de elementos finitos, evitó el problema de la inconsistencia de resultados descrito en el Capítulo 4, a cambio de un incremento asumible en los tiempos de cálculo.
- Las optimizaciones llevadas a cabo permiten escoger diseños óptimos ajustados a las necesidades reales de la industria, por ejemplo, estableciendo límites en los picos de la fuerza de aplastamiento y obteniendo inmediatamente el sistema con la máxima absorción de energía, absorción específica u otras métricas.

- Los componentes construidos en aluminio mostraron un comportamiento óptimo cuando los espesores de las placas de termoplástico y la densidad de la espuma se redujeron al mínimo. Sin embargo, la absorción específica óptima del tubo de acero reforzado se logró en diseños en los que la densidad de la espuma se incrementa a su máximo.

E.4 Líneas futuras de investigación

La escala del problema puede ser modificada para adaptar los diseños para otro tipo de estructuras, como aeronaves o trenes. De esta forma, la validez de los resultados presentados en esta tesis podría ser comprobada a otras escalas. Además, se podrían considerar otros tipos de cargas (laterales, oblicuas,...). Un cambio en el ángulo del impacto puede ser especialmente problemático para los tubos rellenos de placas de material compuesto, dada su sensibilidad a las imperfecciones geométricas iniciales.

En lo relativo al comportamiento frente a impactos de los componentes multimaterial, sería interesante analizar un diseño como el propuesto en los Capítulos 5 y 6 pero sustituyendo el termoplástico por paredes metálicas. Esto se justifica por el hecho de que el termoplástico fue el material cuya contribución hizo falta sólo cuando los otros dos materiales alcanzaron sus límites superiores en la optimización de la energía absorbida y la absorción específica. Además, se podría considerar utilizar corcho en lugar de espuma como confinamiento, con especial énfasis en la comprobación de si el efecto rebote es en realidad una desventaja cuando se trata de la protección de los ocupantes, y estudiándolo bajo cargas cíclicas. Para una correcta caracterización del corcho, las muestras deberían ser sometidas también a ensayos triaxiales a diferentes presiones de confinamiento, para reproducir el comportamiento ante diferentes condiciones de carga en el interior del componente.

Se podrían considerar adhesivos de altas prestaciones como uniones para estos tubos. Existen en la literatura muchos trabajos acerca de la aplicación de adhesivos a dispositivos de absorción de impactos hechos de metal, pero no hay contribuciones relevantes en lo relativo a su uso en estructuras que tengan que soportar presiones internas elevadas durante el colapso axial. Esto podría resolver el problema con las zonas afectadas por el calor experimentado en el Capítulo 5.

Acerca de los modelos de elementos finitos, la campaña de ensayos de materiales fue bastante completa para los fenómenos representados. Sin embargo, ensayos de tracción a alta velocidad en muestras del termoplástico podrían servir para caracterizar este material correctamente a velocidades de deformación elevadas. Esto requeriría el uso de una barra de tracción Split-Hopkinson con barras de entrada y salida hechas de un material en el que las ondas de tensiones viajen a una velocidad similar a como lo hacen en el termoplástico, lo cual es bastante complicado. El modelo de la espuma también podría mejorarse considerando su ortotropía. Para esto, se requerirían ensayos triaxiales adicionales en diferentes direcciones y para distintas densidades de la espuma.

Se podría realizar un esfuerzo adicional en la parte de optimización: la función de relación de carga no fue representada por los metamodelos con tanta precisión como las demás. Podría resultar de utilidad encontrar una aproximación más adecuada para esta métrica, dada su importancia.

En lo relativo al efecto de interacción, los huecos entre los prismas de espuma y las paredes cilíndricas de metal en los Capítulos 5 y 6 evitaron que se desarrollara una interacción relevante entre los materiales. Podría ser interesante ensayar un diseño en el que el relleno de espuma se ajustase de alguna forma a las paredes internas de la extrusión, de forma que el efecto de interacción espuma–metal contribuyese también a la absorción de energía del sistema.

También relacionado con lo anterior, el parámetro C_{avg} podría ser considerado una función objetivo, de forma que se obtuviera la mejor forma de aumentar su contribución, además de entenderse mejor su origen. Para esto, debería obtenerse el coeficiente de rozamiento exacto entre espuma y fibra, y las placas de termoplástico deberían ser modeladas con elementos sólidos considerando erosión, de forma que se reprodujese fielmente la penetración de los fragmentos de termoplástico en el confinamiento de espuma (simulado también con elementos sólidos erosionables).

F

Extended summary in Galician

In accordance with the University regulations approved in 2012, an extended summary of this thesis is presented in Galician.

F.1 Introdución e obxectivos

Esta tese enmárcase no campo de investigación do comportamento de estruturas de absorción de enerxía fronte a cargas de impacto. En particular, os elementos estruturais investigados teñen unhas dimensións que os fan adecuados para o seu uso en vehículos de estrada, aínda que os resultados son aplicables a calquera outro tipo de vehículo ou sistema estrutural.

Neste caso, estudáronse compoñentes cuxa función é absorber parte da enerxía cinética en caso de colisión frontal, polo que se sitúan na parte dianteira do vehículo. Tradicionalmente estes elementos consisten en tubos de aceiro ou, máis recentemente, aluminio. No caso de que unha colisión sexa considerablemente severa, estes tubos esmáganse de forma progresiva e controlada na súa dirección lonxitudinal, disipando enerxía por fenómenos plásticos nos metais. Con todo, no presente estudo consideráronse varias combinacións de materiais de distinta natureza para o seu uso con estes fins. En particular, estudáronse tubos metálicos reforzados internamente con estruturas de fibra de vidro ou carbono, unha escuma en base a tereftalato de polietileno ou un aglomerado de cortiza. Estes deseños ensaiáronse experimental e computacionalmente, e sometéronse a procesos de optimización estrutural non só para obter os deseños óptimos, senón tamén para profundar no comportamento dos distintos materiais e as súas interaccións.

Esta tese contribúe, por tanto, coa análise do comportamento fronte a impacto de estruturas novidosas, incluíndo modelos validados de elementos finitos, unha metodoloxía de optimización adecuada e o estudo da interacción entre algúns materiais salientables.

F.2 Metodoloxía e resultados

A análise e o deseño de estruturas de absorción de impactos é, sen dúbida, un dos problemas máis desafiantes de enxeñería. Isto é debido á presenza simultánea de varios procesos de natureza complexa e difícil simulación, como son os fenómenos de plasticidade e encartado de metais a distintas velocidades de solicitación, a fractura en partes metálicas ou en materiais compostos e o esmagamento de materiais celulares coma a cortiza ou as escumas sintéticas. Desde o punto de vista computacional, as dificultades multiplícanse dada a magnitude das deformacións que experimentan estes compoñentes e a velocidade á que estas suceden, así como a dificultade de simular axeitadamente o comportamento de cada material, prestando especial atención a aquelas características ou propiedades máis relevantes para o problema e adoptando hipóteses ou suposicións naquelas de menor importancia. Por todo isto, utilizáronse unhas metodoloxías moi específicas tanto para a análise experimental e computacional dos compoñentes coma para a súa optimización.

En primeiro lugar analizouse e valorouse o comportamento fronte a impacto de tubos metálicos de parede delgada recheos de diferentes materiais: placas de materiais compostos (fibra de vidro ou carbono), bloques de escuma sintética ou bloques de aglomerado de cortiza. Este traballo realizouse en colaboración co Centro Tecnolóxico de Automoción de Galicia (CTAG) no marco do proxecto “Hybrid Body”, dando como resultado artigos de investigación, comunicacións a congresos internacionais e unha patente. Este estudo consistiu en ensaios experimentais cuasi-estáticos e a impacto, e simulacións computacionais do comportamento dos diferentes deseños. Os compoñentes que incorporaron placas de fibra de vidro mostraron un mellor comportamento que os demais atendendo a métricas comunmente empregadas en impacto estrutural, por iso se someteron a un estudo paramétrico para determinar mellor o seu comportamento variando os espesores dos seus elementos. Adicionalmente, estudouse o efecto da distribución dos puntos de soldadura no comportamento fronte a impacto de todas as combinacións de materiais anteriormente descritas, dando lugar a algunhas regras de deseño útiles.

A continuación procedeuse a optimizar a resposta dos compoñentes consistentes nun tubo de aceiro reforzado internamente cunha estrutura de termoplástico de fibra de vidro. Para iso seleccionáronse variables de deseño que se consideraron relevantes: espesores das distintas partes e algunha modificación xeométrica da sección. A aplicación de algoritmos de optimización a este tipo de problemas presenta dúas grandes dificultades: o custo computacional de cada avaliación das funcións obxectivo e a súa non-linealidade. Ademais, as respostas están afectadas ata certo punto polo ruído numérico derivado das propias simulacións. Por todo iso decidiuse empregar unha metodoloxía de optimización apoiada en modelos subrogados, que substitúan as avaliacións dos modelos de elementos finitos por avaliacións de aproximacións feitas mediante diferentes modelos de máis fácil manexo. Estes modelos deben ser suficientemente flexibles para representar con suficiente grao de detalle as non-linealidades das funcións, ademais de suavizar en certa medida o ruído numérico do modelo de elementos finitos. Con estes obxectivos en mente, avaliáronse metamodelos de diferente natureza: polinómicos, procesos Gaussianos (ou kriging) e regresión de splines adaptativas multivariadas (MARS), sendo os últimos os que demostraron unha maior eficacia. Os modelos foron axustados a mostraxes representativas paralelizadas do modelo de elementos finitos, tomando como respostas aquelas funcións obxectivo seleccionadas para a optimización. No tocante a esta optimización, dúas estratexias de diferente natureza foron avaliadas: un método de gradiente conxugado e un algoritmo xenético, ambos adaptados para o caso de optimizacións multiobxectivo. Aínda que o método de gradiente conxugado é o único dos dous cuxas solucións son óptimos no sentido estrito, o algoritmo xenético foi capaz de chegar a áreas dos modelos subrogados que non foron exploradas polo anterior, obtendo algúns óptimos adicionais. Estes deseños óptimos foron representados en frontes de Pareto, que permiten escoller o deseño óptimo de acordo ás necesidades ou criterios requiridos. Os resultados do traballo descrito neste parágrafo tamén foron convenientemente publicados nun artigo de revista de grande impacto.

En relación ao deseño optimizado, consistente en placas de termoplástico de fibra de vidro colocadas no interior dun tubo metálico, observouse que a resposta fronte a impactos poderíase mellorar considerablemente con algún sistema de confinamento do material composto. Isto evitaría que fragmentos de termoplástico considerablemente grandes que aínda poderían degradarse máis se desprendesen da estrutura, desaproveitando a súa contribución. Para este fin considerouse que a escuma de tereftalato de polietileno estudada anteriormente podería contribuír de forma notable. Por tanto, expúxose un novo deseño no que as placas estivesen embebidas nesta escuma e substituíuse o tubo exterior de aceiro por un de aluminio AA5754-H111, mudando tamén a súa xeometría a unha hexagonal, de maior eficiencia. Con todo, apareceron graves problemas co método de unión das dúas chapas de aluminio para formar o tubo dada a dificultade para soldar correctamente este material. A solución adoptada, unha dobre liña de soldadura láser, xerou debilidades na zona afectada pola calor do proceso que propiciaron que os compoñentes se abrisen ao ser esmagados debido á presión interior exercida polos reforzos de fibra e escuma. Coma alternativa a esta solución, optouse por un tubo circular extruido en aliaxe AA6063-T5, de espesor algo maior ao anterior. Esta solución funcionou axeitadamente ao carecer de zonas débiles, e os reforzos interiores demostraron mellorar a resposta fronte a impactos do tubo. Ademais, prestouse especial atención á interacción entre os distintos materiais. De particular influencia nos resultados foi a interacción entre as placas de fibra e a escuma, cuxa contribución aos niveis de absorción de enerxía foi moi considerable. Este fenómeno cuantificouse por medio dunha modificación da fórmula de Hanssen para tubos de aluminio recheos de escuma de aluminio, de forma que agora considerase a presenza de dous reforzos simultáneos que interactúan entre si. O traballo descrito neste parágrafo e parte do seguinte realizouse durante unha estancia de investigación de seis meses no Structural Impact Laboratory (SIMLab) da NTNU en Trondheim, Noruega, baixo a supervisión do profesor Magnus Langseth e o investigador postdoctoral David Morin. Do descrito neste parágrafo resultou, ademais, outro artigo de investigación publicado nunha revista de grande impacto.

Por último, procedeuse a optimizar o deseño anterior empregando o modelo subrogado e o algoritmo de optimización seleccionados con anterioridade. Realizouse unha campaña de ensaios de materiais co obxectivo de caracterizar correctamente aquelas propiedades de cada material máis relevantes para este tipo de aplicacións. En particular realizáronse ensaios de tracción a distintas velocidades e estados triaxiales, ensaios de compresión uniaxial cuasi-estáticos e en torre de caída e ensaios de compresión confinada (ensaios triaxiales). Con fins comparativos, optimizouse tamén un segundo modelo no que o tubo exterior de aluminio substituíuse por un de aceiro de características similares. Nesta optimización, ademais dos espesores da extrusión metálica e as placas de termoplástico, considerouse coma variable de deseño a densidade da escuma. Esta densidade está directamente ligada á súa resistencia a compresión, de acordo cos datos proporcionados polo fabricante. Da optimización despréndese que este tipo de reforzos é particularmente útil para estruturas de aceiro, en especial, se a densidade da escuma incrementase en relación co anterior. Obtivéronse frontes de Pareto para ambos deseños e diferentes funcións obxectivo e analizouse a variación das variables de deseño ao longo das frontes, o que puxo de manifesto a eficiencia e utilidade desta metodoloxía.

F.3 Conclusións

No estudo de compoñentes metálicos reforzados con fibra de carbono ou vidro, escuma de tereftalato de polietileno ou aglomerado de cortiza observouse que:

- Desenvolvéronse deseños innovadores para a absorción de enerxía de impacto en colaboración con CTAG, utilizando materiais e xeometrías que non foran investigadas con anterioridade. Os compoñentes ensaiáronse en condicións cuase-estáticas e de impacto, e desenvolvéronse e validaron modelos de elementos finitos que reproducen de forma aceptable os resultados experimentais.

- O reforzo de tubos de aceiro cunha estrutura de termoplástico de fibra de vidro incrementou a súa absorción específica de enerxía máis que os demais materiais, seguida de preto por un recheo de escuma sintética. Estes resultados foron demostrados en ensaios experimentais e numéricos.

- O comportamento dos diferentes materiais foi reproducido polos modelos de elementos finitos cunha precisión razoable. O feito de considerar deformacións residuais non mostrou unha gran repercusión nos resultados, con todo, as imperfeccións iniciais si foron necesarias para reproducir os mesmos modos de colapso observados nos ensaios experimentais, ademais de que permitiron reducir o pico inicial de carga para coincidir co experimental.

- O aglomerado de cortiza analizada nesta tese produciu un incremento relativamente baixo nos niveis de absorción específica de enerxía comparado co tubo de aceiro baleiro. Ademais, o seu comportamento elástico recuperable suxeriu que este produto deberíase usar con precaución en estruturas adicadas á absorción de enerxía, por exemplo, en áreas onde este feito non sexa relevante.

- Á vista dos resultados do Capítulo 3, a separación entre puntos de soldadura equidistantes debería ser menor dun 16.7 % da lonxitude do tubo para unha absorción de enerxía eficiente, garantindo que a parte de aceiro plégase progresivamente. En caso contrario, a lonxitude de encartado incrementase e a estabilidade do esmagamento axial vese comprometida.

- As seccións recheas de escuma foron menos sensibles ao espaciado entre puntos de soldadura debido ao efecto de interacción ou confinamento entre o recheo e o tubo. Para que isto suceda, a escuma debe estar en contacto coas paredes metálicas durante o esmagamento.

A optimización do tubo reforzado con termoplástico de fibra de vidro indicou que:

- Despois de aplicar diferentes modelos subrogados, pode concluírse que as funcións de absorción específica de enerxía e relación de carga puideron ser emuladas razoablemente ben cun conxunto de splines adaptativas multivariadas (MARS). Isto permitiu unha execución adecuada dos algoritmos de optimización nun problema con cinco variables. O número máximo de funcións bases de MARS determinouse cunha análise da bondade dos metamodelos.

- Os resultados do modelo de elementos finitos mostraron sensibilidade ao esquema de paralelización empregado na fase de mostraxe. A división do modelo nun número diferente de submodelos produciu diferenzas de entre un 10 e un 20 % na enerxía absorbida polo mesmo compoñente. Atopouse un equilibrio entre a calidade dos resultados e o tempo de computación para unha división en catro subdominios.
- A absorción específica de enerxía e a relación de carga do deseño orixinal estudado no Capítulo 3 mellorouse case un 50 % cos valores óptimos das variables de deseño. A decalaxe entre a parte superior do tubo de aceiro e o reforzo foi esencial para conseguir unha redución das relacións de carga.
- Comparáronse un algoritmo xenético multiobxectivo e o método de gradiente conxugado de Fletcher-Reeves. A alternativa metaheurística foi capaz de atopar pares óptimos das funcións obxectivo en zonas do metamodelo que non foron exploradas polo algoritmo de Fletcher-Reeves.

A partir da investigación experimental do comportamento fronte a impactos de perfís de aluminio reforzados con escuma sintética e placas de termoplástico simultaneamente aprendeuse que:

- Realizouse unha análise previa sobre seccións hexagonais de dobre chapeu feitas en aliaxe AA5754-H111 cun espesor de 1 mm unidas por un dobre cordón de soldadura láser. Esta solución non foi o suficientemente resistente para soportar as presións internas dos reforzos debido á debilidade das zonas afectadas pola calor. Unha extrusión en aliaxe AA6063-T5 cun espesor superior foi capaz de soportar estas presións internas sen fracturas relevantes.
- A extrusión de aluminio en aliaxe AA6063-T5 mostrou unha ductilidade suficiente para permitir o colapso progresivo de compoñentes baleiros e recheos sen fracturas relevantes. Só se observaron danos menores na transición do modo de concertina ao de diamante de tres puntas, no tubo baleiro.
- A enerxía absorbida polos deseños reforzados unicamente con escuma sintética ou con termoplástico non foi significativamente maior que a da sección baleira, dadas as excelentes propiedades desta aliaxe; pero observouse unha mellora moi notable cando os tres materiais se combinaron nun único deseño. Isto explícase polo feito de que a escuma confina as placas de termoplástico, mellorando o seu aproveitamento.

- A enerxía absorbida e a relación de carga do compoñente recheo con escuma de tereftalato de polietileno e fibra de vidro mellorouse entorno a un 100 % comparado coa dun tubo baleiro. Con todo, a absorción específica foi sensiblemente máis baixa.
- Unha gran parte do incremento na enerxía absorbida debeuse á forte interacción entre as placas de termoplástico e a escuma. A formulación de Hanssen adaptouse para un tubo con dous recheos simultáneos, de forma que se teña en conta este efecto. Isto demostrou que a escuma de tereftalato de polietileno pode ser utilizada como un sistema de confinamento das placas, aproveitando ao máximo a súa degradación.

Por último, a optimización multiobxectivo do compoñente reforzado con escuma e fibra mostrou que:

- O comportamento do compoñente foi fielmente representado por un modelo de elementos finitos calibrado coas ecuacións constitutivas adecuadas para cada un dos tres materiais, grazas á campaña de ensaios de materiais presentada no Capítulo 5 e no Apéndice A.
- A masa do deseño e a súa absorción de enerxía, absorción específica de enerxía e pico inicial de forza foron aproximadas por un modelo de MARS cunha excelente correlación cos resultados do modelo de elementos finitos. Non se considerou como función obxectivo a relación de carga debido ás imprecisións de todos os metamodelos estudados. Unha mostraxe máis exhaustiva permitiu unha mellora da precisión dos metamodelos, o que conduciu a frontes de Pareto máis suaves e máis continuos.
- A paralelización en bucle, que non implica divisións do modelo de elementos finitos, evitou o problema da inconsistencia de resultados descrito no Capítulo 4, a cambio dun incremento asumible nos tempos de cálculo.
- As optimizacións levadas a cabo permiten escoller deseños óptimos axustados ás necesidades reais da industria, por exemplo, establecendo límites nos picos da forza de esmagamento e obtendo inmediatamente o sistema coa máxima absorción de enerxía, absorción específica ou outras métricas.
- Os compoñentes construídos en aluminio mostraron un comportamento óptimo cando os espesores das placas de termoplástico e a densidade da escuma se reduciron ao mínimo. Con todo, a absorción específica óptima do tubo de aceiro reforzado logrouse en deseños nos que a densidade da escuma increméntase ao seu máximo.

F.4 Liñas futuras de investigación

A escala do problema pode ser modificada para adaptar os deseños para outro tipo de estruturas, como aeronaves ou trens. Desta forma, a validez dos resultados presentados nesta tese podería ser comprobada a outras escalas. Ademais, poderíanse considerar outros tipos de cargas (laterais, oblicuas,...). Un cambio no ángulo do impacto pode ser especialmente problemático para os tubos recheos de placas de material composto, dada a súa sensibilidade ás imperfeccións xeométricas iniciais.

No relativo ao comportamento fronte a impactos dos compoñentes multimaterial, sería interesante analizar un deseño como o proposto nos Capítulos 5 e 6 pero substituíndo o termoplástico por paredes metálicas. Isto xustifícase polo feito de que o termoplástico foi o material cuxa contribución fixo falta só cando os outros dous materiais alcanzaron os seus límites superiores na optimización da enerxía absorbida e a absorción específica. Ademais, poderíase considerar utilizar cortiza en lugar de escuma como confinamento, con especial énfase na comprobación de se o efecto rebote é en realidade unha desvantaxe cando se trata da protección dos ocupantes, e estudándoo baixo cargas cíclicas. Para unha correcta caracterización da cortiza, as mostras deberían ser sometidas tamén a ensaios triaxiais a diferentes presións de confinamento, para reproducir o comportamento ante diferentes condicións de carga no interior do compoñente.

Poderíanse considerar adhesivos de altas prestacións como unións para estes tubos. Existen na literatura moitos traballos acerca da aplicación de adhesivos a dispositivos de absorción de impactos feitos de metal, pero non hai contribucións relevantes no relativo ao seu uso en estruturas que teñan que soportar presións internas elevadas durante o colapso axial. Isto podería resolver o problema coas zonas afectadas pola calor experimentado no Capítulo 5.

Acerca dos modelos de elementos finitos, a campaña de ensaios de materiais foi bastante completa para os fenómenos representados. Con todo, ensaios de tracción a alta velocidade en mostras do termoplástico poderían servir para caracterizar este material correctamente a velocidades de deformación elevadas. Isto requiriría o uso dunha barra de tracción Split-Hopkinson con barras de entrada e saída feitas dun material no que as ondas de tensións viaxen a unha velocidade similar a como o fan no termoplástico, o cal é bastante complicado. O modelo da escuma tamén se podería mellorar considerando a súa ortotropía. Para isto, requiriríanse ensaios triaxiais adicionais en diferentes direccións e para distintas densidades da escuma.

Poderíase realizar un esforzo adicional na parte de optimización: a función de relación de carga non foi representada polos metamodelos con tanta precisión como as demais. Podería resultar de utilidade atopar unha aproximación máis adecuada para esta métrica, dada a súa importancia.

No tocante ao efecto de interacción, os ocos entre os prismas de escuma e as paredes cilíndricas de metal nos Capítulos 5 e 6 evitaron que se desenvolvese unha interacción relevante entre os materiais. Podería ser interesante ensaiar un deseño no que o recheo de escuma se axustáse dalgún xeito ás paredes internas da extrusión, de forma que o efecto de interacción escuma–metal contribuíse tamén á absorción de enerxía do sistema.

Tamén relacionado co anterior, o parámetro C_{avg} podería ser considerado unha función obxectivo, de forma que se obtivese a mellor forma de aumentar a súa contribución, ademais de entenderse mellor a súa orixe. Para isto, debería obterse o coeficiente de rozamento exacto entre escuma e fibra, e as placas de termoplástico deberían ser modeladas con elementos sólidos considerando erosión, de forma que se reproducise fielmente a penetración dos fragmentos de termoplástico no confinamento de escuma (simulado tamén con elementos sólidos erosionables).

Bibliography

[1] National Highway Traffic Safety Administration - NHTSA. *Early estimate of motor vehicle traffic fatalities for the first half (January-June) of 2013.* Tech. rep. U.S. Department of Transportation, 2013.

[2] National Highway Traffic Safety Administration - NHTSA. *Fatalities in Frontal Crashes despite Seat Belts and Air Bags.* Tech. rep. U.S. Department of Transportation, 2009.

[3] *Frontal Impact Testing Protocol, Version 6.0.* European New Car Assessment Programme (Euro NCAP), 2012.

[4] *Full Width Rigid Barrier.* `http://www.euroncap.com/en/vehicle-safety/the-ratings-explained/adult-occupant-protection/full-width-rigid-barrier/`.

[5] J. De Kanter. "Energy absorption of monolithic and fibre reinforced aluminium cylinders". PhD thesis. Faculty of Aerospace Engineering - Delft University of Technology, 2006.

[6] G. Nagel. "Impact and energy absorption of straight and tapered rectangular tubes". PhD thesis. School of Civil Engineering, Queensland University of Technology, 2005.

[7] *Image of the Honda ACE system.* `http://www.quazoo.com/q/Advanced_Compatibility_Engineering`.

[8] *Image of the body-in-white of an Audi A8, 2011 version.* `http://www.boronextrication.com/2010/04/29/2010-audi-a8-uk-body-structure/`.

[9] *Detail of the body-in-white of an Audi A8, 2011 version.* `https://www.audi-mediacenter.com/en/photos/detail/audi-ultra-lightweight-construction-9223`.

[10] M. Costas, J. Díaz, L. Romera, S. Hernández, and A. Tielas. “Static and dynamic axial crushing analysis of car frontal impact hybrid absorbers”. *International Journal of Impact Engineering* 62 (2013), pp. 166–181.

[11] M. Costas, J. Díaz, L. Romera, and S. Hernández. “A multi-objective surrogate-based optimization of the crashworthiness of a hybrid impact absorber”. *International Journal of Mechanical Sciences* 88 (2014), pp. 46–54.

[12] M. Costas, D. Morin, M. Langseth, L. Romera, and J. Díaz. “Axial crushing of aluminum extrusions filled with PET foam and GFRP. An experimental investigation”. *Thin-Walled Structures* 99 (2016), pp. 45–57.

[13] J. Paz, J. Díaz, L. Romera, and M. Costas. “Crushing analysis and multi-objective crashworthiness optimization of GFRP honeycomb-filled energy absorption devices”. *Finite Elements in Analysis and Design* 91 (2014), pp. 30–39.

[14] M. Cid Montoya, M. Costas, J. Díaz, L. Romera, and S. Hernández. “A multi-objective reliability-based optimization of the crashworthiness of a metallic-GFRP impact absorber using hybrid approximations”. *Structural and Multidisciplinary Optimization* 52 (2015), pp. 827–843.

[15] J. Paz, J. Díaz, L. Romera, and M. Costas. “Size and shape optimization of aluminum tubes with GFRP honeycomb reinforcements for crashworthy aircraft structures”. *Composite Structures* 133 (2015), pp. 499–507.

[16] M. Costas, J. Díaz, L. Romera, S. Hernández, and R. Ledo. “Influence of welded joints on the crashworthiness response of hybrid structural elements”. In: *SAE 2013 World Congress and Exhibition, paper 13B-0036/2013-01-0755.* 2013.

[17] M. Costas, L. Romera, J. Díaz, S. Hernández, and A. Tielas. “Computational and experimental analysis of a hybrid car impact absorber”. In: *Computational Methods and Experimental Measurements XVI, WIT Press, C.A. Brebbia, G. M. Carlomagno and S. Hernandez (eds.)* 2013, pp. 367–378.

[18] L. Romera, J. Paz, M. Costas, J. Díaz, and S. Hernández. “Crashworthiness response of honeycomb metallic-GFRP energy abpsortion devices”. In: *HPSM/OPTI 2014, The 2014 International Conference on High Performance and Optimum Design of Structures and Materials.* 2014.

[19] J. Díaz, M. Costas, L. Romera, J. Paz, and S. Hernández. “Surrogate-based multi-objective optimization of glass-fiber - steel crash absorbers”. In: *35th FISITA World Automotive Congress, Maastrich (Netherlands).* 2014.

[20] L. Romera, M. Costas, J. Díaz, J. Paz, and S. Hernández. “Reduction of the frontal crash peak forces in a car using size optimization tools”. In: *35th FISITA World Automotive Congress, Maastrich (Netherlands).* 2014.

[21] M. Langseth. *Lecture notes on impact dynamics.* Structural impact laboratory, NTNU, Trondheim (Norway), 2005.

[22] H. W. Henn. “Crash tests and the head injury criterion”. *Teaching mathematics and its applications* 17.4 (1998), pp. 162–170.

[23] G. Lu and T. X. Yu. *Energy absorption of structures and materials.* Woodhead Publishing, Cambridge (UK), 2003.

[24] N. Jones. *Structural Impact.* Second edition. Cambridge University Press, Cambridge (UK), 2011.

[25] K.-H. Lin and G. T. Mase. “An assessment of add-on energy absorbing devices for vehicle crashworthiness”. *Journal of Engineering Materials and Technology, Transactions ASME* 112.4 (1990), pp. 406–411.

[26] A. Hanssen, M. Langseth, and O. Hopperstad. “Static and dynamic crushing of circular aluminum extrusions with aluminum foam filler”. *International Journal of Impact Engineering* 24.5 (2000), pp. 475–507.

[27] N. Jones. “Energy-absorbing effectiveness factor”. *International Journal of Impact Engineering* 37.6 (2010), pp. 754–765.

[28] A. Mallock. “Note on the instability of tubes subjected to end pressure, and on the folds in a flexible material”. *Proceedings of the Royal Society of London. Series A, Containing Papers of a Mathematical and Physical Character* 81.549 (1908), pp. 388–393.

[29] A. Pugsley. “The large-scale crumpling of cylindrical columns”. *The Quarterly Journal of Mechanics and Applied Mathematics* 13.1 (1958), pp. 1–9.

[30] J. M. Alexander. “An approximate analysis of the collapse of thin cylindrical shells under axial loading”. *Quarterly Journal of Mechanics and Applied Mathematics* 13.1 (1960), pp. 10–15.

[31] A. Pugsley. “On the crumpling of thin tubular struts”. *The Quarterly Journal of Mechanics and Applied Mathematics* 32.1 (1979), pp. 1–7.

[32] T. Wierzbicki. *Optimum design of integrated front panel against crash.* Tech. rep. Report for Ford Motor Company, Vehicle Dept., 1983.

[33] W. Abramowicz and N. Jones. “Dynamic axial crushing of circular tubes”. *International Journal of Impact Engineering* 2.3 (1984), pp. 263–281.

[34] W. Abramowicz and N. Jones. “Dynamic progressive buckling of circular and square tubes”. *International Journal of Impact Engineering* 4.4 (1986), pp. 243–270.

[35] T. Wierzbicki and U. Bhat. “A moving hinge solution for axysimmetric crushing of tubes”. *International Journal of Mechanical Sciences* 83.3 (1986), pp. 135–151.

[36] T. Wierzbicki, U. Bhat, and W. Abramowicz. “Alexander revisited - A two folding elements model of progressive crushing of tubes”. *International Journal of Solids and Structures* 29.24 (1992), pp. 1269–1288.

[37] R. Grzebieta. “An alternative method for determining the behaviour of round stocky tubes subjected to an axial crush load”. *Thin-Walled Structures* 9.1-4 (1990), pp. 61–89.

[38] A. Singace, H. Elsobky, and T. Reddy. “On the eccentricity factor in the progressive crushing of tubes”. *International Journal of Solids and Structures* 32.24 (1995), pp. 3589–3602.

[39] A. Singace and H. Elsobky. “Further experimental investigation on the eccentricity factor in the progressive crushing of tubes”. *International Journal of Solids and Structures* 33.24 (1996), pp. 3517–3538.

[40] N. Gupta and R. Velmurugan. “An analysis of axi-symmetric axial collapse of round tubes”. *Thin-Walled Structures* 22.4 (1995), pp. 261–274.

[41] S. Guillow, G. Lu, and R. Grzebieta. “Quasi-static axial compression of thin-walled circular aluminium tubes”. *International Journal of Mechanical Sciences* 43.9 (2001), pp. 2103–2123.

[42] A. Pugsley. “The crumpling of tubular structures under impact conditions”. *Proceedings of the Symposium on the use of aluminium in railway rolling stock* (1960), pp. 33–41.

[43] T. Wierzbicki and W. Abramowicz. “On the crushing mechanics of thin-walled structures”. *Journal of Applied Mechanics* 50.4a (1983), pp. 727–734.

[44] M. White and N. Jones. “Experimental quasi-static axial crushing of top-hat and double-hat thin-walled sections”. *International Journal of Mechanical Sciences* 41.2 (1999), pp. 179–208.

[45] V. Tarigopula, M. Langseth, O. Hopperstad, and A. Clausen. “Axial crushing of thin-walled high-strength steel sections”. *International Journal of Impact Engineering* 32.5 (2006), pp. 847–882.

[46] A. Mamalis, D. Manolakos, G. Vieghlan, and W. Johnson. “On the crumpling of thin plastic closed top-hat sections by compressive loadings”. *International Journal of Vehicle Design* 9.6 (1988), pp. 675–685.

[47] A. Mamalis, D. Manolakos, G. Vieghlan, and S. Minarecioglou. “The inextensional axial collapse of thin plastic double top-hat sections”. *International Journal of Vehicle Design* 10.3 (1989), pp. 269–279.

[48] M. White, N. Jones, and W. Abramowicz. “A theoretical analysis for the quasi-static axial crushing of top-hat and double-hat thin-walled sections”. *International Journal of Mechanical Sciences* 41.2 (1999), pp. 209–233.

[49] F. Schneider and N. Jones. “Influence of spot-weld failure on crushing of thin-walled structural sections”. *International Journal of Mechanical Sciences* 45.12 (2003), pp. 2061–2081.

[50] W. Abramowicz and T. Wierzbicki. “Axial crushing of multicorner sheet metal columns”. *Journal of Applied Mechanics, Transactions ASME* 56.1 (1989), pp. 113–120.

[51] W. Chen and D. Nardini. “Experimental study of crush behaviour of sheet aluminium foam-filled sections”. *International Journal of Crashworthiness* 5.4 (2000), pp. 447–468.

[52] W. Chen and T. Wierzbicki. “Relative merits of single-cell, multi-cell and foam-filled thin-walled structures in energy absorption”. *Thin-Walled Structures* 39.4 (2001), pp. 287–306.

[53] H.-S. Kim. “New extruded multi-cell aluminum profile for maximum crash energy absorption and weight efficiency”. *Thin-Walled Structures* 40.4 (2002), pp. 311–327.

[54] X. Zhang, G. Cheng, and H. Zhang. “Theoretical prediction and numerical simulation of multi-cell square thin-walled structures”. *Thin-Walled Structures* 44.11 (2006), pp. 1185–1191.

[55] A. Alavi Nia and M. Parsapour. “An investigation on the energy absorption characteristics of multi-cell square tubes”. *Thin-Walled Structures* 68 (2013), pp. 26–34.

[56] Z. Tang, S. Liu, and Z. Zhang. “Analysis of energy absorption characteristics of cylindrical multi-cell columns”. *Thin-Walled Structures* 62 (2013), pp. 75–84.

[57] T. Tran, S. Hou, X. Han, W. Tan, and N. Nguyen. “Theoretical prediction and crashworthiness optimization of multi-cell triangular tubes”. *Thin-Walled Structures* 82 (2014), pp. 183–195.

[58] H. Yin, G. Wen, Z. Liu, and Q. Qing. “Crashworthiness optimization design for foam-filled multi-cell thin-walled structures”. *Thin-Walled Structures* 75 (2014), pp. 8–17.

[59] P. Thornton and P. Edwards. “Energy absorption in composite tubes”. *Journal of Composite Materials* 16.6 (1982), pp. 521–545.

[60] G. L. Farley. “Energy absorption of composite materials”. *Journal of Composite Materials* 17.3 (1983), pp. 267–279.

[61] P. Thornton. “The crush behavior of glass fiber reinforced plastic sections”. *Composites Science and technology* 27 (1986), pp. 199–223.

[62] G. L. Farley. “Effect of fiber and matrix maximum strain on the energy absorption of composite materials”. *Journal of Composite Materials* 20.4 (1986), pp. 322–334.

[63] G. L. Farley. “Effect of specimen geometry on the energy absorption capability of composite materials”. *Journal of Composite Materials* 20.4 (1986), pp. 390–400.

[64] J. Price and D. Hull. “Axial crushing of glass fibre-polyester composite cones”. *Composites Science and technology* 28 (1987), pp. 211–230.

[65] D. Hull. “A unified approach to progressive crushing of fibre-reinforced composite tubes”. *Composites Science and Technology* 40.4 (1991), pp. 377–421.

[66] G. L. Farley and R. M. Jones. “Crushing characteristics of continuous fiber-reinforced composite tubes”. *Journal of Composite Materials* 26.1 (1992), pp. 37–50.

[67] G. L. Farley. “The effect of fiber and matrix maximum strain on the energy absorption of composite materials”. *Journal of Composite Materials* 20 (1986), pp. 322–334.

[68] H. Hamada, J. Coppola, D. Hull, Z. Maekawa, and H. Sato. “Comparison of energy absorption of carbon/epoxy and carbon/PEEK composite tubes”. *Composites* 23.4 (1992), pp. 245–252.

[69] H. Hamada, S. Ramakrishna, and H. Satoh. “Crushing mechanism of carbon fibre/PEEK composite tubes”. *Composites* 26.11 (1995), pp. 749–755.

[70] A. Mamalis, Y. Yuan, and G. Viegelahn. “Collapse of thin-wall composite sections subjected to high speed axial loading”. *International Journal of Vehicle Design* 13.5-6 (1992), pp. 564–579.

[71] A. Mamalis, D. Manolakos, G. Demosthenous, and M. Ioannidis. “Axial collapse of thin-walled fibreglass composite tubular components at elevated strain rates”. *Composites Engineering* 4.6 (1994), pp. 653–677.

[72] A. Mamalis, D. Manolakos, G. Demosthenous, and M. Ioannidis. “The static and dynamic axial collapse of fibreglass composite automotive frame rails”. *Composite Structures* 34.1 (1996), pp. 77–90.

[73] A. Mamalis, D. Manolakos, G. Demosthenous, and M. Ioannidis. “Energy absorption capability of fibreglass composite square frusta subjected to static and dynamic axial collapse”. *Thin-Walled Structures* 25.4 (1996), pp. 269–295.

[74] A. Mamalis, D. Manolakos, G. Demosthenous, and M. Ioannidis. “Analytical modelling of the static and dynamic axial collapse of thin-walled fibreglass composite conical shells”. *International Journal of Impact Engineering* 19.5–6 (1997), pp. 477–492.

[75] A. Mamalis, D. Manolakos, M. Ioannidis, and D. Papapostolou. “Crashworthy characteristics of axially statically compressed thin-walled square CFRP composite tubes: Experimental”. *Composite Structures* 63.3-4 (2004), pp. 347–360.

[76] A. Mamalis, D. Manolakos, M. Ioannidis, and D. Papapostolou. “On the response of thin-walled CFRP composite tubular components subjected to static and dynamic axial compressive loading: experimental”. *Composite Structures* 69.4 (2005), pp. 407–420.

[77] A. Mamalis, D. Manolakos, M. Ioannidis, and D. Papapostolou. “The static and dynamic axial collapse of CFRP square tubes: Finite element modelling”. *Composite Structures* 74.2 (2006), pp. 213–225.

[78] G. Jacob, J. Fellers, J. Starbuck, and S. Simunovic. “Crashworthiness of automotive composite material systems”. *Journal of Applied Polymer Science* 92.5 (2004), pp. 3218–3225.

[79] C. Bisagni, G. Di Pietro, L. Fraschini, and D. Terletti. “Progressive crushing of fiber-reinforced composite structural components of a formula one racing car”. *Composite Structures* 68.4 (2005), pp. 491–503.

[80] H. Ghasemnejad, B. Blackman, H. Hadavinia, and B. Sudall. “Experimental studies on fracture characterisation and energy absorption of GFRP composite box structures”. *Composite Structures* 88.2 (2009), pp. 253–261.

[81] H. Hadavinia and H. Ghasemnejad. “Effects of mode-I and mode-II interlaminar fracture toughness on the energy absorption of CFRP twill/weave composite box sections”. *Composite Structures* 89.2 (2009), pp. 303–314.

[82] S. Ochelski and P. Gotowicki. “Experimental assessment of energy absorption capability of carbon-epoxy and glass-epoxy composites”. *Composite Structures* 87.3 (2009), pp. 215–224.

[83] H. Ghasemnejad and A. Hadavinia H.and Aboutorabi. “Effect of delamination failure in crashworthiness analysis of hybrid composite box structures”. *Materials & Design* 31.3 (2010), pp. 1105–1116.

[84] J. Bouchet, E. Jacquelin, and P. Hamelin. “Static and dynamic behavior of combined composite aluminium tube for automotive applications”. *Composites Science and Technology* 60 (2000), pp. 1891–1900.

[85] A. Mamalis, D. Manolakos, G. Demosthenous, and W. Johnson. "Axial plastic collapse of thin bi-material tubes as energy dissipating systems". *International Journal of Impact Engineering* 11.2 (1991), pp. 185–196.

[86] E. Hanefi and T. Wierzbicki. "Axial resistance and energy absorption of externally reinforced metal tubes". *Composites Part B: Engineering* 27.5 (1996), pp. 387–394.

[87] H.-W. Song, Z.-M. Wan, Z.-M. Xie, and X.-W. Du. "Axial impact behavior and energy absorption efficiency of composite wrapped metal tubes". *International Journal of Impact Engineering* 24.4 (2000), pp. 385–401.

[88] X. Wang and G. Lu. "Axial crushing force of externally fibre-reinforced metal tubes". *Proceedings of the Institution of Mechanical Engineers, Part C: Journal of Mechanical Engineering Science* 216.9 (2002), pp. 863–874.

[89] K. Shin, J. Lee, K. Kim, M. Song, and J. Huh. "Axial crush and bending collapse of an aluminum/GFRP hybrid square tube and its energy absorption capability". *Composite Structures* 57.1-4 (2002), pp. 279–287.

[90] M. Bambach and M. Elchalakani. "Plastic mechanism analysis of steel SHS strengthened with CFRP under large axial deformation". *Thin-Walled Structures* 45.2 (2007), pp. 159–170.

[91] M. Bambach, M. Elchalakani, and X. Zhao. "Composite steel–CFRP SHS tubes under axial impact". *Composite Structures* 87.3 (2009), pp. 282–292.

[92] M. Bambach, H. Jama, and M. Elchalakani. "Static and dynamic axial crushing of spot-welded thin-walled composite steel–CFRP square tubes". *International Journal of Impact Engineering* 36.9 (2009), pp. 1083–1094.

[93] M. Bambach. "Axial capacity and crushing of thin-walled metal, fibre–epoxy and composite metal–fibre tubes". *Thin-Walled Structures* 48.6 (2010), pp. 440–452.

[94] M. Bambach. "Axial capacity and crushing behavior of metal–fiber square tubes – Steel, stainless steel and aluminum with CFRP". *Composites Part B: Engineering* 41.7 (2010), pp. 550–559.

[95] H. Kim, D. Shin, J. Lee, and J. Kwon. "Crashworthiness of aluminum/CFRP square hollow section beam under axial impact loading for crash box application". *Composite Structures* 112.1 (2014), pp. 1–10.

[96] P. H. Thornton. "Energy absorption by foam filled structures". *SAE Technical Paper 800081* (1980).

[97] B. Lampinen and R. Jeryan. "Effectiveness of polyurethane foam in energy absorbing structures". *SAE Technical Paper 820494* (1983).

[98] S. Reid, T. Reddy, and M. Gray. “Static and dynamic axial crushing of foam-filled sheet metal tubes”. *International Journal of Mechanical Sciences* 28.5 (1986), pp. 295–322.

[99] S. Reid and T. Reddy. “Axial crushing of foam-filled tapered sheet metal tubes”. *International Journal of Mechanical Sciences* 28.10 (1986), pp. 643–656.

[100] T. Reddy and R. Wall. “Axial compression of foam-filled thin-walled circular tubes”. *International Journal of Impact Engineering* 7.2 (1988), pp. 151–166.

[101] W. Abramowicz and T. Wierzbicki. “Axial crushing of foam-filled columns”. *International Journal of Mechanical Sciences* 30.3-4 (1988), pp. 263–271.

[102] M. Seitzberger, F. Rammerstorfer, H. Degischer, and R. Gradinger. “Crushing of axially compressed steel tubes filled with aluminium foam”. *Acta Mechanica* 125.1-4 (1997), pp. 93–105.

[103] A. Singace and H. El-Sobky. “Behaviour of axially crushed corrugated tubes”. *International Journal of Mechanical Sciences* 39.3 (1997), pp. 249–268.

[104] M. Langseth, O. Hopperstad, and A. Hanssen. “Crash behaviour of thin-walled aluminium members”. *Thin-Walled Structures* 32.1-3 (1998), pp. 127–150.

[105] S. Santosa and T. Wierzbicki. “Crash behavior of box columns filled with aluminum honeycomb or foam”. *Computers and Structures* 68.4 (1998), pp. 343–367.

[106] A. Hanssen, M. Langseth, and O. Hopperstad. “Static and dynamic crushing of square aluminum extrusions with aluminum foam filler”. *International Journal of Impact Engineering* 24.4 (2000), pp. 347–383.

[107] A. Hanssen, M. Langseth, and O. Hopperstad. “Static and dynamic crushing of circular aluminium extrusions with aluminium foam filler”. *International Journal of Mechanical Sciences* 24.4 (2000), pp. 475–570.

[108] A. Hanssen, M. Langseth, and O. Hopperstad. “Optimum design for energy absorption of square aluminum columns with aluminum foam filler”. *International Journal of Mechanical Sciences* 43.1 (2001), pp. 153–176.

[109] S. Santosa, T. Wierzbicki, A. Hanssen, and M. Langseth. “Experimental and numerical studies of foam-filled sections”. *International Journal of Impact Engineering* 24.5 (2000), pp. 509–534.

[110] M. Seitzberger, F. Rammerstorfer, R. Gradinger, H. Degischer, M. Blaimschein, and C. Walch. “Experimental studies on the quasi-static axial crushing of steel columns filled with aluminium foam”. *International Journal of Solids and Structures* 37.30 (2000), pp. 4125–4147.

[111] W. Chen and T. Wierzbicki. “Relative merits of single-cell, multi-cell and foam-filled thin-walled structures in energy absorption”. *Thin-Walled Structures* 39.4 (2001), pp. 287–306.

[112] T. Børvik, O. Hopperstad, A. Reyes, M. Langseth, G. Solomos, and T. Dyngeland. “Empty and foam-filled circular aluminium tubes subjected to axial and oblique quasi-static loading”. *International Journal of Crashworthiness* 8.5 (2003), pp. 481–494.

[113] A. Reyes, O. Hopperstad, and M. Langseth. “Aluminum foam-filled extrusions Subjected to oblique loading: experimental and numerical study”. *International Journal of Solids and Structures* 41.5-6 (2004), pp. 1645–1675.

[114] S. Meguid, M. Attia, and A. Monfort. “On the crush behaviour of ultralight foam-filled structures”. *Materials and Design* 25.3 (2004), pp. 183–189.

[115] L. Aktay, A. Toksoy, and M. Güden. “Quasi-static axial crushing of extruded polystyrene foam-filled thin-walled aluminum tubes: Experimental and numerical analysis”. *Materials and Design* 27.7 (2006), pp. 556–565.

[116] Z. Ahmad and D. Thambiratnam. “Crushing response of foam-filled conical tubes under quasi-static axial loading”. *Materials and Design* 30.7 (2009), pp. 2393–2403.

[117] H. Zarei and M. Kröger. “Crashworthiness optimization of empty and filled aluminum crash boxes”. *International Journal of Crashworthiness* 12.3 (2007), pp. 255–264.

[118] S. Hou, Q. Li, S. Long, X. Yang, and W. Li. “Crashworthiness design for foam filled thin-wall structures”. *Materials and Design* 30.6 (2009), pp. 2024–2032.

[119] J. Bi, H. Fang, Q. Wang, and X. Ren. “Modeling and optimization of foam-filled thin-walled columns for crashworthiness designs”. *Finite Elements in Analysis and Design* 46.9 (2010), pp. 698–709.

[120] G. Sun, G. Li, S. Hou, S. Zhou, W. Li, and Q. Li. “Crashworthiness design for functionally graded foam-filled thin-walled structures”. *Materials Science and Engineering A* 527.7-8 (2010), pp. 1911–1919.

[121] S. Hou, X. Han, G. Sun, S. Long, W. Li, X. Yang, and Q. Li. “Multiobjective optimization for tapered circular tubes”. *Thin-Walled Structures* 49.7 (2011), pp. 855–863.

[122] Y. Zhang, G. Sun, Z. Li G.and Luo, and Q. Li. “Optimization of foam-filled bitubal structures for crashworthiness criteria”. *Materials and Design* 38 (2012), pp. 99–109.

[123] X. Song, G. Sun, G. Li, W. Gao, and Q. Li. "Crashworthiness optimization of foam-filled tapered thin-walled structure using multiple surrogate models". *Structural and Multidisciplinary Optimization* 47.2 (2013), pp. 221–231.

[124] G. Zheng, S. Wu, G. Sun, G. Li, and Q. Li. "Crushing analysis of foam-filled single and bitubal polygonal thin-walled tubes". *International Journal of Mechanical Sciences* 87 (2014), pp. 226–240.

[125] J. Lin, X. Wang, C. Fang, and X. Huang. "Collapse loading and energy absorption of fiber-reinforced conical shells". *Composites Part B: Engineering* 74 (2015), pp. 178–189.

[126] S. P. Silva, M. A. Sabino, E. M. Fernandes, V. M. Correlo, L. F. Boesel, and R. L. Reis. "Cork: properties, capabilities and applications". *International Materials Reviews* 50.6 (2005), pp. 345–365.

[127] C. Gameiro and J. Cirne. "Dynamic axial crushing of short to long circular aluminium tubes with agglomerate cork filler". *International Journal of Mechanical Sciences* 49.9 (2007), pp. 1029–1037.

[128] I. Alcántara, F. Teixeira-Dias, and M. Paulino. "Cork composites for the absorption of impact energy". *Composite Structures* 95 (2013), pp. 16–27.

[129] M. Paulino and F. Teixeira-Dias. "An energy absorption performance index for cellular materials - Development of a side-impact cork padding". *International Journal of Crashworthiness* 16.2 (2011), pp. 135–153.

[130] Y. Tay, C. Lim, and H. Lankarani. "A finite element analysis of high-energy absorption cellular materials in enhancing passive safety of road vehicles in side-impact accidents". *International Journal of Crashworthiness* 19.3 (2014), pp. 288–300.

[131] F. Fernandes, R. Pascoal, and R. Alves de Sousa. "Modelling impact response of agglomerated cork". *Materials and Design* 58 (2014), pp. 499–507.

[132] R. Jardin, F. Fernandes, A. Pereira, and R. Alves de Sousa. "Static and dynamic mechanical response of different cork agglomerates". *Materials and Design* 68 (2015), pp. 121–126.

[133] S. Sánchez-Sáez, S. García-Castillo, E. Barbero, and J. Cirne. "Dynamic crushing behaviour of agglomerated cork". *Materials and Design* 65 (2015), pp. 743–748.

[134] T. Wierzbicki. "Crushing analysis of metal honeycombs". *International Journal of Impact Engineering* 1.2 (1983), pp. 157–174.

[135] Y. Yasui. "Dynamic axial crushing of multi-layer honeycomb panels and impact tensile behavior of the component members". *International Journal of Impact Engineering* 24.6 (2000), pp. 659–671.

[136] H. Zhao and G. Gary. “Crushing behaviour of aluminium honeycombs under impact loading”. *International Journal of Impact Engineering* 21.10 (1998), pp. 827–836.

[137] L. J. Gibson and M. F. Ashby. *Cellular solids, structure and properties*. Second edition. Cambridge University Press, Cambridge (UK), 1997.

[138] *ABAQUS 6.14 Documentation*. Dassault Systèmes. Providence Road, Rhode Island. 2014.

[139] W. Abramowicz. “Thin-walled structures as impact energy absorbers”. *Thin-Walled Structures* 41.2-3 (2003), pp. 91–107.

[140] D. Karagiozova, M. Alves, and N. Jones. “Inertia effects in axisymmetrically deformed cylindrical shells under axial impact”. *International Journal of Impact Engineering* 24.10 (2000), pp. 1083–1115.

[141] Z. Kazanc and K.-J. Bathe. “Crushing and crashing of tubes with implicit time integration”. *International Journal of Impact Engineering* 42 (2012), pp. 80–88.

[142] T. Belytschko, W. K. Liu, B. Moran, and K. I. Elkhodary. *Nonlinear finite elements for continua and structures*. Second edition. John Wiley & Sons, Hoboken (New Jersey, USA), 2014.

[143] R. Courant, K. Friedrichs, and H. Lewy. “Über die partiellen differenzengleichungen der mathematischen physik”. *Mathematische Annalen* 100.1 (1928), pp. 32–74.

[144] M. Costas, J. Díaz, L. Romera, S. Hernández, and R. Ledo. “Influence of welded joints on the crashworthiness response of hybrid structural elements”. *SAE Technical Papers* 2 (2013).

[145] M. Costas, L. E. Romera, J. Díaz, S. Hernández, and A. Tielas. “Computational and experimental analysis of a hybrid car impact absorber”. *Computational Methods and Experimental Measurements XVI* 55 (2013).

[146] *ABAQUS 6.11 Documentation*. Dassault Systèmes. Providence Road, Rhode Island. 2011.

[147] J. Seidt. “EOD material characterization, supplemental reports: constitutive and fracture models for ASTM A36 hot rolled steel”. *Battelle Technical report prepared for the Naval Explosive Ordenance Disposal Technology Division, Columbus, Ohio* (2005).

[148] X. Zhang and H. Zhang. “Experimental and numerical investigation on crush resistance of polygonal columns and angle elements”. *Thin-Walled Structures* 57 (2012), pp. 25–36.

[149] Y. Xiang, Q. Wang, Z. Fan, and H. Fang. "Optimal crashworthiness design of a spot-welded thin-walled hat section". *Finite Elements in Analysis and Design* 42 (2006), pp. 846–855.

[150] BASF. *Ultramid (R) A3WG10 BK00564 Polyamide 66. Product information sheet.* 2012.

[151] E. Totry, J. Molina-Aldareguía, C. González, and J. Llorca. "Effect of fiber, matrix and interface properties on the in-plane shear deformation of carbon-fiber reinforced composites". *Composites Science and Technology* 70.6 (2010), pp. 970–980.

[152] F. Garattoni. "Crashworthiness and composite materials: development of an experimental test method for the energy absorption determination and implementation of the relative numerical model". PhD thesis. Universitá di Bologna, 2011.

[153] Z. Haszin. "Failure criteria for unidirectional fiber composites". *Journal of Applied Mechanics, Transactions ASME* 47.2 (1980), pp. 329–334.

[154] Z. Hashin. "Fatigue failure criteria for unidirectional fiber composites". *Journal of Applied Mechanics, Transactions ASME* 48.4 (1981), pp. 846–852.

[155] S. Jose, K. Kuma, M. Jana, and G. Rao. "Interlaminar fracture toughness of a cross-ply laminate and its constituent sub-laminates". *Composites Science and Technology* 61.8 (2001), pp. 1115–1122.

[156] V. Deshpande and N. Fleck. "Isotropic constitutive models for metallic foams". *Journal of the Mechanics and Physics of Solids* 48.6–7 (2000), pp. 1253–1283.

[157] J. Zhang, N. Kikuchi, V. Li, A. Yee, and G. Nusholtz. "Constitutive modeling of polymeric foam material subjected to dynamic crash loading". *International Journal of Impact Engineering* 21.5 (1998), pp. 369–386.

[158] A. Micuzzi and G. Elvira. "Caracterización computacional de placas de espuma de poliestireno expandido bajo cargas dinámicas de impacto". In: *IBEROMET XI, X CONAMET/SAM.* 2010.

[159] M. Paulino, F. Teixeira-Dias, C. Gameiro, and J. Cirne. "Hyperelastic and dynamical behaviour of cork and its performance in energy absorption devices and crashworthiness applications". *International Journal of Materials Engineering Innovation* 1.2 (2009), pp. 197–234.

[160] C. Gameiro, J. Cirne, and G. Gary. "Experimental study of the quasi-static and dynamic behaviour of cork under compressive loading". *Journal of Materials Science* 42.12 (2007), pp. 4316–4324.

[161] S. P. Silva, M. A. Sabino, E. M. Fernandes, V. M. Correlo, L. F. Boesel, and R. L. Reis. "Cork: properties, capabilities and applications". *International Materials Reviews* 50.6 (2005), pp. 345–365.

[162] C. Gameiro, J. Cirne, V. Miranda, J. Pinho-Da-Cruz, and F. Teixeira-Dias. "Dynamic behaviour of cork and cork-filled aluminium tubes: Numerical simulation and innovative applications". *Holzforschung* 61.4 (2007), pp. 400–405.

[163] V. Sokolinsky, K. Indermuehle, and J. Hurtado. "Numerical simulation of the crushing process of a corrugated composite plate". *Composites Part A: Applied Science and Manufacturing* 42.9 (2011), pp. 1119–1126.

[164] C. Nex and R. Smith. "Impact performance of model spot welded stainless steel structures". *Experimental Mechanics* (1998).

[165] F. Schneider and N. Jones. "Influence of spot-weld failure on crushing of thin-walled structural sections". *International Journal of Mechanical Sciences* 45 (2003), pp. 2061–2081.

[166] L. Peroni, M. Avalle, and G. Belingardi. "Comparison of the energy absorption capability of crash boxes assembled by spot-weld and continuous joining techniques". *International Journal of Impact Engineering* 36 (2009), pp. 498–511.

[167] J. Paz, J. Díaz, L. Romera, and M. Costas. "Crushing analysis and multi-objective crashworthiness optimization of GFRP honeycomb-filled energy absorption devices". *Finite Elements in Analysis and Design* 91 (2014), pp. 30–39.

[168] M. Cid Montoya, M. Costas, J. Díaz, L. Romera, and S. Hernández. "A multi-objective reliability-based optimization of the crashworthiness of a metallic-GFRP impact absorber using hybrid approximations". *Structural and Multidisciplinary Optimization* 52.4 (2015), pp. 827–843.

[169] K. Yamazaki and J. Han. "Maximization of the crushing energy absorption of tubes". *Structural Optimization* 16.1 (1998), pp. 37–46.

[170] P. Marklund and L. Nilsson. "Optimization of a car body component subjected to side impact". *Structural and Multidisciplinary Optimization* 21.5 (2001), pp. 383–392.

[171] J. Sobieszczanski-Sobieski, S. Kodiyalam, and R. Yang. "Optimization of car body under constraints of noise, vibration, and harshness (NVH), and crash". *Structural and Multidisciplinary Optimization* 22.4 (2001), pp. 295–306.

[172] T. Jansson, L. Nilsson, and M. Redhe. “Using surrogate models and response surfaces in structural optimization - With application to crashworthiness design and sheet metal forming”. *Structural and Multidisciplinary Optimization* 25.2 (2003), pp. 129–140.

[173] S. Hou, Q. Li, S. Long, X. Yang, and W. Li. “Design optimization of regular hexagonal thin-walled columns with crashworthiness criteria”. *Finite Elements in Analysis and Design* 43.6-7 (2007), pp. 555–565.

[174] E. Acar, M. Guler, B. Gereker, M. Cerit, and B. Bayram. “Multi-objective crashworthiness optimization of tapered thin-walled tubes with axisymmetric indentations”. *Thin-Walled Structures* 49.1 (2011), pp. 94–105.

[175] X. Gu, G. Sun, G. Li, L. Mao, and Q. Li. “A Comparative study on multiobjective reliable and robust optimization for crashworthiness design of vehicle structure”. *Structural and Multidisciplinary Optimization* (2013), pp. 1–16.

[176] M. Kiani, I. Gandikota, A. Parrish, K. Motoyama, and M. Rais-Rohani. “Surrogate-based optimisation of automotive structures under multiple crash and vibration design criteria”. *International Journal of Crashworthiness* (2013).

[177] *SAE Standard J211: Instrumentation for Impact Test.* Society of Automotive Engineers.

[178] M. Huang. *Vehicle Crash Mechanics.* CRC Press, Boca Raton, USA, 2002.

[179] V. Eglājs and P. Audze. “New approach to the design of multifactor experiments”. *Problems of Dynamics and Strengths* (in Russian) (1977), pp. 104–107.

[180] M. McKay, R. Beckman, and W. Conover. “A comparison of three methods for selecting values of input variables in the analysis of output from a computer code”. *Technometrics* 21.2 (1979), pp. 239–245.

[181] J. Iman R.L.; Helton and J. Campbell. “An approach to sensitivity analysis of computer models, Part 1. Introduction, input variable selection and preliminary variable assessment”. *Journal of Quality Technology* 13.3 (1981), pp. 174–183.

[182] J. H. Friedman. “Multivariate adaptive regression splines”. *Annals of Statistics* 19 (1991), pp. 1–141.

[183] R. Fletcher and C. M. Reeves. “Function minimization by conjugate gradients”. *The Computer Journal* 7.2 (1964), pp. 149–154.

[184] R. Haftka and Z. Gürdal. *Elements of Structural Optimization.* Third edition. Springer Netherlands, 1991.

[185] W. Karush. “Minima of Functions of Several Variables with Inequalities as Side Constraints”. MA thesis. Dept. of Mathematics, Univ. of Chicago, Chicago, Illinois., 1939.

[186] H. Kuhn and A. Tucker. “Nonlinear programming”. *Proceedings of 2nd Berkeley Symposium* (1951), pp. 481–492.

[187] R. Fletcher. *Unconstrained Optimization. Practical Methods of Optimization.* John Wiley & Sons, Chichester, 1981.

[188] P. Gill. *Practical Optimization.* Academic Press, London, 1982.

[189] I. Griva, S. Nash, and A. Sofer. *Linear and Nonlinear Optimization.* Second edition. Society for Industrial Mathematics, Philadelphia, 2008.

[190] B. Adams, L. Bauman, W. Bohnhoff, K. Dalbey, M. Ebeida, J. Eddy, M. Eldred, P. Hough, K. Hu, J. Jakeman, L. Swiler, and V. D. *DAKOTA, A Multilevel Parallel Object-Oriented Framework for Design Optimization, Parameter Estimation, Uncertainty Quantification, and Sensitivity Analysis: Version 5.3.1 User's Manual.* Sandia National Laboratories. December 2009. Updated April 2013.

[191] *ABAQUS 6.12 Documentation.* Dassault Systèmes. Providence Road, Rhode Island. 2012.

[192] J. Holland. *Adaptation in natural and artificial systems.* University of Michigan Press, Michigan, USA, 1975.

[193] D. Goldberg. *Genetic algorithms in search, optimization and machine learning.* Addison-Wesley Longman Publishing, Boston, USA, 1989.

[194] M. Mitchell. *An introduction to genetic algorithms.* MIT Press, Cambridge, USA, 1998.

[195] W. Chen, M. Wiecek, and J. Zhang. “Quality utility: a compromise programming approach to robust designs”. *ASME journal of mechanical design* 121 (1999), pp. 179–187.

[196] I. Das and J. Dennis. “A closer look at drawbacks of minimizing weighted sums of objectives for Pareto set generation in multicriteria optimization problems”. *Structural optimization* 14 (1997), pp. 63–69.

[197] A. Messac, J. Sundararaj, R. Tappeta, and J. Renaud. “The ability of objective functions to generate points on non-convex Pareto frontiers”. *AIAA journal* 38 (2000), pp. 1084–1091.

[198] A. Messac, E. Melachrinoudis, and C. Sukam. “Aggregate objective functions and Pareto frontiers: required relationships and practical implications”. *Optimization and engineering* 1 (2000), pp. 171–188.

[199] J. E. Eddy and K. Lewis. “Effective Generation of Pareto Sets using Genetic Programming”. *Proceedings of ASME Design Engineering Technical Conference* (2001).

[200] K. Deb, R. Tiwary, M. Dixit, and J. Dutta. “Finding trade-off solutions close to KKT points using evolutionary multi-objective optimization”. *Proceedings of the congress on evolutionary computation* (2007), pp. 2109–2116.

[201] F. Wang, Y. Mo, J. Lv, F. Huang, and Q. He. “Numerical studies on STFD-HAT sections under axial dynamic impact”. *Thin-Walled Structures* 82 (2014), pp. 105–114.

[202] A. Castro and C. Prado. “Study of the root droplets in high thickness hybrid welding”. MA thesis. Dept. of Engineering Sciences and Mathematics, Luleå University of Technology, Sweeden, 2011.

[203] H. Zhu, L. Zhu, and J. Chen. “Damage and fracture mechanism of 6063 aluminum alloy under three kinds of stress states”. *Rare Metals* 27.1 (2008), pp. 64–69.

[204] V. Vilamosa. “Behaviour and Modelling of AA6xxx Aluminum Alloys Under a Wide Range of Temperatures and Strain Rates”. PhD thesis. SIMLab (Structural Impact Laboratory), NTNU, 2015.

[205] BASF. *Ultramid (R) A3WG10 BK00564 Polyamide 66. Product information sheet.* 2015.

[206] ISO. *Rigid cellular plastics – Determination of compression properties.* ISO 844:2014. International Organization for Standardization, 2014.

[207] A. Hanssen, T. Auestad, T. Tryland, and M. Langseth. “The kicking machine: A device for impact testing of structural components”. *International Journal of Crashworthiness* 8 (2003), pp. 385–392.

[208] M. Kristoffersen. “Impact against X65 offshore pipelines”. PhD thesis. SIMLab (Structural Impact Laboratory), NTNU, 2014.

[209] E. Voce. “The relationship between stress and strain for homogeneous deformations”. *Journal of the Institute of Metals* 74 (1948), pp. 537–562.

[210] T. Børvik, O. Hopperstad, T. Berstad, and M. Langseth. “A computational model of viscoplasticity and ductile damage for impact and penetration”. *European Journal of Mechanics - A/Solids* 20.5 (2001), pp. 685–712.

[211] N. Abedrabbo, R. Mayer, A. Thompson, C. Salisbury, M. Worswick, and I. van Riemsdijk. “Crash response of advanced high-strength steel tubes: Experiment and model”. *International Journal of Impact Engineering* 36.8 (2009), pp. 1044–1057.

[212] W. Kolmogorov. “Spannungen Deformationen Bruch”. *Metallurgija* (1970), p. 230.

[213] H. Hooputra, H. Gese, H. Dell, and H. Werner. “A comprehensive failure model for crashworthiness simulation of aluminium extrusions”. *International Journal of Crashworthiness* 9.5 (2004), pp. 449–464.

[214] *ABAQUS 6.13 Documentation.* Dassault Systèmes. Providence Road, Rhode Island. 2014.

[215] V. Deshpande and N. Fleck. “Isotropic constitutive models for metallic foams”. *Journal of the Mechanics and Physics of Solids* 48.6 (2000), pp. 1253–1283.

[216] G. Cowper and P. Symonds. *Strain-hardening and strain-rate effects in the impact loading of cantilever beams.* Division of Applied Mathematics, Brown University, Providence, Rhode Island, USA, 1957.

[217] Armacell. *Armaform PET/W AC, technical data.* 2014.